



Reverberation Chambers and the Measurement of Antenna Characteristics

by

Stephen J. Boyes

Submitted in accordance with the requirements for the award of the
degree of Doctor of Philosophy of the University of Liverpool

February 2013

Copyright

Copyright © 2013 Stephen J. Boyes. All rights reserved.

The copyright of this thesis rests with the author. Copies (by any means) either in full, or of extracts, may not be made without prior written consent from the author.

*The courses of his youth promised him not, and be assured you'll find a difference, as we his
subjects have in wonder found, between the promise of his greener days, and these he
masters now....*

Henry V.... William Shakespeare

To my Parents and Grandparents: Thank you for all your efforts and for your support.

To my Brother: Thank you for the inspiration and the drive to succeed.

Table of Contents

<i>Copyright</i>	i
<i>Table of Contents</i>	iii - vii
<i>Acronyms</i>	viii
<i>Acknowledgements</i>	ix
<i>List of Publications</i>	x - xi
<i>Abstract</i>	xii - xiii
Chapter 1: Introduction	1
1.1 Background	1 - 3
1.2 Research Motivation	3 - 5
1.3 Organisation of Thesis	6 - 7
1.4 References	7 - 9
Chapter 2: Reverberation Chamber Cavity Theory	10
2.1 Introduction	10
2.2 Cavity Modes and Electromagnetic Fields	10 - 21
2.3 Mode Stirring Techniques	21
2.3.1 Mechanical Stirring	21 - 22
2.3.2 Polarisation Stirring	23
2.3.3 Platform & Position Stirring	24
2.3.4 Frequency Stirring	24
2.4 Plane Wave Angle of Arrival	25 - 28

2.5	Average Mode Bandwidths	28 - 30
2.6	Chamber Quality (Q) Factor	30 - 34
2.7	Statistical Forms	34 - 36
2.7.1	Statistical Method of Analysis	36 - 37
2.7.2	Statistical Distribution of Measured Magnitudes	37 - 39
2.7.3	Statistical Distribution of Complex Samples	40 - 42
2.7.4	Statistical Distribution of Measured Power	43 - 45
2.7.5	Statistical Distribution of Measured Phase	45 - 47
2.7.6	Concluding Remarks	48 - 49
2.8	Line of Sight Elements	49 - 56
2.9	References	56 - 58
Chapter 3: Textile Antenna Efficiency Performance		59
3.1	Introduction	59 - 61
3.2	Definitions: Antenna Efficiency	61 - 62
3.3	Definitions: Single Band Textile Antennas	62 - 63
3.4	Measurement Procedures	63 - 66
3.5	Measurement Investigation	66
3.5.1	Free Space Performance	67 - 71
3.5.2	On-Body Chest (0 mm) Performance	71 - 80
3.5.3	Bent Elbow (0 mm) Performance	80 - 82
3.5.4	On-Body Back (0 mm) Performance	82 - 84
3.5.5	On-Body Chest (20 mm) Performance	85 - 88

3.6	Theoretical & Simulated Evidence	88 - 89
3.7	Summary	90
3.8	Definitions: Dual Band Textile Antennas	90 - 92
3.9	Measurement Procedures	92 - 93
3.10	Measurement Investigation	93
	3.10.1 Free Space Performance	93 - 96
	3.10.2 On-Body Chest (0 mm) Performance	96 - 100
	3.10.3 On-Body Back (0 mm) Performance	100 - 103
3.11	Theoretical & Simulated Evidence	103 - 104
3.12	Measurement Uncertainty	104 - 108
3.13	Conclusion	109 - 110
3.14	References	110 - 112
Chapter 4: Multiport & Array Antennas		113
4.1	Introduction	113 - 114
4.2	Definitions: Single Element Dual Feed PIFAs	115 - 118
4.3	Measurement Parameters	118 - 119
4.4	Diversity Gain from Cdf	120 - 125
4.5	Diversity Gain from Correlation	125 - 130
4.6	Channel Capacity	130 - 131
4.7	Embedded Element Efficiency	132 - 137
4.8	Summary	137

4.9	Definitions: Conventional Array Antennas	138 - 139
4.10	Measurement Parameters	140
4.10.1	All-Excited Measurement Parameters	140
4.10.2	Power Divider Measurement Parameters	141 - 142
4.11	Deduction of New Equation	142 - 143
4.12	Measurement Results	144
4.12.1	Power Divider Measurement Results	144 - 145
4.12.2	Antenna Array Measurement Results	145 - 147
4.13	Measurement Uncertainty	147 - 148
4.14	Conclusion	148 - 149
4.15	References	149 - 151
Chapter 5: Improved Mechanical Stirrer Designs		152
5.1	Introduction	152 - 155
5.2	Design Methodology	155 - 157
5.3	Numerical Analysis	157 - 159
5.3.1	Effect of the Number of Cuts	159 - 161
5.3.2	Effect of the Periodicity of the Cuts	161 - 164
5.3.3	Effect of the Shape of the Cuts	164 - 168
5.3.4	Complex Nature of the Cuts	169 - 172
5.3.5	Variation in Paddle Dimensions	172 - 175
5.4	Comments on Practical Validation	175 - 176
5.5	Measurement Parameters for Validation	176 - 177

5.6	Measurement Results	178
5.6.1	Standard Vs New Design: Unloaded Chamber	179 - 186
5.6.2	Standard Vs New Design: Loaded Chamber	186 - 190
5.7	Conclusion	190 - 192
5.8	References	192 - 193
Chapter 6: Contributions & Future Work		194
6.1	Thesis Summary	194 - 195
6.2	Future Work	195 - 197
6.3	Key Contributions	197 - 198
6.4	References	198
<i>Appendix A1</i>		199 - 203
<i>Appendix A2</i>		204 - 208
<i>Appendix A3</i>		209 - 213
<i>Appendix A4</i>		214 - 219

Acronyms

AC	Anechoic Chamber
AoA	Angle of Arrival
AUT	Antenna under Test
DUT	Device under Test
EMC	Electromagnetic Compatibility
EMI	Electromagnetic Interference
ISM	Industrial Scientific & Medical
LOS	Line of Sight
MIMO	Multiple Input Multiple Output
NLOS	Non Line of Sight
OTA	Over the Air
PIFA	Planar Inverted F Antenna
RC	Reverberation Chamber
SNR	Signal to Noise Ratio
WC	Wheeler Cap
WLAN	Wireless Local Area Network

Acknowledgements

Reflecting on the culmination of three years of hard work, I am grateful to very many people. First and foremost my sincere and upmost gratitude must be extended to my research supervisor Professor Yi Huang. I thank you for giving me the opportunity to test myself at the highest level, not to mention all the invaluable comments and advice which guided me towards a successful conclusion. I also thank you for making me feel very much at home in the research group, and I hope I have repaid the faith you showed in me all those years ago now.

I would also like to recognise the major contribution played by my parents and grandparents. Your support and sacrifice made life a lot easier for me and I am eternally grateful for everything you have done. This work is for you. I would also like to express my gratitude to my brother Ian, who, probably unbeknown to him, provided me with a great deal of inspiration and instilled a drive and desire to succeed.

Thanks must also be paid to my colleagues in the research group; in particular to Hassan Chattha and Neda Khiabani for many fruitful discussions in a work related context, but also for allowing me to develop an understanding and appreciation of different cultures and their mannerisms.

Finally, I would also like to acknowledge the part played by the many different research groups with whom I have shared such successful collaboration. Particular thanks to Professor Anthony Brown and Dr Yongwei (David) Zhang from the University of Manchester, and to Professor Guy Vandenbosch and Mr Ping Jack Soh from the Katholieke Universiteit Leuven in Belgium. I have enjoyed getting to know you personally and working with you all.

List of Publications

Journal Publications

- [1] **S. J. Boyes**, P. J. Soh, Y. Huang, G. A. E. Vandenbosch, “Measurement & Performance of Textile Antenna Efficiency on Human Subjects in a Reverberation Chamber”, *IEEE Transactions Antennas & Propagation*, vol. 61, no. 2, 2013.
- [2] **S. J. Boyes**, P. J. Soh, G. A. E. Vandenbosch, Y. Huang, “On-Body Performance of Dual Band Textile Antennas”, *IET Microwaves Antennas & Propagation*, pp. 1-8, 2012.
- [3] P. J. Soh, **S. J. Boyes**, G. A. E. Vandenbosch, Y. Huang, S. L. Ooi, “On-Body Characterization of Dual Band All-Textile PIFA”, *Progress in Electromagnetics Research (PIER)*, vol. 129, pp. 517-539, 2012.
- [4] H. T. Chattha, Y. Huang, **S. J. Boyes**, Y. Zhu, “Polarization and Pattern Diversity Based Dual Feed Planar Inverted F Antenna”, *IEEE Transactions on Antennas & Propagation*, vol. 60, no. 3, pp. 1532-1539, 2012.
- [5] N. Khiabani, Y. Huang, Y. Shen, **S. J. Boyes**, “Efficiency Calculation of THz Photoconductive Antennas in a Pulsed System”, *IEEE Transactions on Antennas & Propagation*, accepted for publication January 2013.
- [6] **S. J. Boyes**, Y. Zhang, Y. Huang and A. K. Brown, “A Method to De-embed External Power Dividers of All-Excited Antenna Arrays in Reverberation Chamber”, *IEEE Antenna & Wireless Propagation Letters*, vol. 11, pp. 1418 - 1421, 2012.
- [7] H. T. Chattha, Y. Huang, M. K. Ishfaq, **S. J. Boyes**, “A Comprehensive Parametric Study of Planar Inverted-F Antenna,” *Scientific Research Wireless Engineering and Technology*, vol. 3, no. 1, pp. 1–11, 2012.
- [8] **S. J. Boyes**, Y. Huang, “Mechanical Stirrer Designs in Reverberation Chambers: A Review of Current Thinking”, *IEEE Transactions on Antennas & Propagation*, under peer review.

- [9] **S. J. Boyes**, Y. Huang, N. Khiabani, “Improved Performance of Mechanical Stirrer Designs in Reverberation Chambers”, *IEEE Transactions on Antennas & Propagation*, under peer review.

Conference Publications

- [1] **S. J. Boyes**, Y. Huang, N. Khiabani, “Repeatability Assessment of UWB Antenna Efficiency in Reverberation Chambers”, *ICUWB 2010 Conference*, vol.1, pp 78-81, 2010.
- [2] Y. Huang, Y. Lu, **S. J. Boyes**, H.T Chattha, N. Khiabani, “Wideband Antenna Efficiency Measurements”, *In Proc. IWAT 2010 Conference*, pp 1-4, 2010.
- [3] Y. Huang, T. H. Loh, L. J. Foged, **S. J. Boyes** et al, “Broadband Antenna Measurement Comparisons”, *In Proc. EuCAP 2010*, April, 2010.
- [4] N. Khiabani, Y. Huang, Y. Shen, D. Li, **S. J. Boyes**, “Substrate Thickness Effects on the Performance of PC Antennas”, *In Proc. 3rd China-Europe Workshop on Millimetre Waves & THz Technologies*, Sept 2010.
- [5] **S. J. Boyes**, Y. Huang, H. T. Chattha, “Comparison of Diversity Gain Performance of Single Element Dual Feed PIFAs with Assorted MIMO Antennas”, *In Proc. IWAT 2011 Conference*, Hong Kong, 2011
- [6] **S. J. Boyes**, Y. Huang, N. Khiabani, “Improved Rayleigh Field Statistic in Reverberation Chambers from Modified Mechanical Stirring Paddles”, *In Proc. LAPC 2011*.
- [7] Y. Huang, Y. Lu, **S. J. Boyes**, “Ground Plane Effects & Measurement of Portable Planar Broadband Antennas”, *In Proc. IEEE APS Conf. Antennas & Propagation in Wireless Communications*, Sept 2011.
- [8] Y. Huang, Y. Lu, **S. J. Boyes**, “Source Stirred Chamber/Cap Method for Antenna Efficiency Measurements”, *In Proc. EuCAP 2011*.
- [9] **S. J. Boyes**, P. J. Soh, Y. Huang, G. A. E. Vandenbosch, N. Khiabani, “Repeatability & Uncertainty Evaluations of On-Body Textile Antenna Efficiency Measurements in Reverberation Chamber”, *In Proc. LAPC 2012*.

Abstract

Over the past ten years, Reverberation Chambers (RC) have emerged as a promising facility for the measurement of antenna characteristics for the wireless communications industry. The RC has begun to diverge from its initial purpose of performing Electromagnetic Compatibility (EMC) measurements, as conceived by H. A. Mendes back in 1968. Unlike the Anechoic Chamber (AC) however, the RC facility and measurement protocols are relatively in their infancy whose standardisation is yet to be finalised. The purpose of this thesis is to present a further study into reverberation chambers and their associated measurement procedures, aimed at smoothing the transition into a fully standardised and accepted facility within the measurement industry. This thesis is comprised of three main investigation areas.

The first area under investigation concerns single port textile antennas designed for use in the on-body communications role. The purpose of this investigation is twofold: (1) to chart the efficiency and impedance matching performance of the antennas in both free space and on-body roles to completely characterise their performance, and (2) to devise and configure operational procedures for the measurement of antenna characteristics on human subjects using the RC.

Two separate varieties of textile antenna are subject to investigation; the first consists of two antennas with an equally small ground plane designed for use in the Industrial Scientific and Medical (ISM) 2.45 GHz band. The second variety also consists of two separate antennas that have a larger ground plane size and are designed to offer a dual band characteristic; to operate at 2.45 GHz and 5.2 GHz respectively.

The results for the smaller ground plane sized antennas show that in free space conditions, the textile antenna constructed from the higher conductivity textile material exhibits a greater level of efficiency which is expected. However, when placed on-body, the antenna with the lower conductivity textile material remarkably outperforms the antenna with the higher conductivity material which is contrary to expectations; this represents new and important knowledge. The results for the larger ground plane sized textile antennas conform completely to expectations. That is, the higher conductivity material outperformed the lower conductivity material in both free space and on-body roles. Comparing both cases, further new knowledge can be concluded in the fact that in addition to the conductivity of the textile material, the ground plane dimensions is also of crucial importance.

The second area under investigation concerns multiport (array) antennas. This area is subdivided into two sections to chart a distinction between multiport antennas designed for Multiple Input Multiple Output (MIMO) applications and more conventional array antennas that are not. The first section concerns the complete practical verification of two new dual feed Planar Inverted F Antennas (PIFAs). Results show that both antennas yield a high level of diversity gain and channel capacity (close to the theoretical maximums) and very low correlation between the two feeds despite the antennas small size. Furthermore, the antennas are also proved to be highly efficient at the desired frequency of operation. Comparing all performance results, it is possible to conclude that due to the small size and excellent performance of the new designs, they could be useful in more practical and commercial applications than larger sized elements that currently exist.

The second section focuses upon more conventional larger sized array antennas used for radio astronomy applications. In this thesis, a series of power dividers is used to emulate a realistic ‘all - excited’ scenario, but the power divider approach has a consequence in that it will give rise to an external power loss that is not attributed to the antenna array. A new equation is developed in this work that allows for the accurate efficiency determination of the array and the de-embedding of the power divider in one. It is shown that the new equation can make this whole process simpler and straightforward to accomplish whilst maintaining accuracy.

The final area under investigation concerns the design of reverberation chambers. The most common of the mode stirring techniques used in reverberation chambers is via the rotation or movement of electrically large metallic paddles inside the chamber known as ‘Mechanical Stirring’. In this thesis, a technique based upon a meanderline principle is used to cut slots into the mechanical stirring paddles to increase the current path length (induced when a wave hits the metallic surface) and thereby increase the electrical size of the paddle. New paddle designs for reverberation chambers are designed and verified. It is shown that the overall paddle dimensions do not need to be increased in size, meaning that the working volume of the chamber can remain as large as possible. The results show that the new designs exhibit enhanced performance over and above conventional paddle designs at lower modal numbers, meaning that any chamber will be able to better perform at frequencies where fewer modes exist. Results also show that at higher frequencies, the slot cuts do not adversely affect the chambers higher frequency performance. This work therefore has the potential to forge a new way of thinking when it comes to the design of mechanical stirrers in RC’s.

Chapter 1: Introduction

1.1 Background

The concept of the Reverberation Chamber (RC) was first proposed by H. A. Mendes back in 1968 as a novel means for electromagnetic field strength measurements [1]. The RC can be characterised as an electrically large shielded metallic enclosure which is designed to work in an ‘over-mode’ condition (i.e. many modes). Although proposed back in 1968, it took time for the facility to gain universal acceptance. However, by the 1980’s and in particular the 1990’s, their use for performing Electromagnetic Compatibility (EMC) and Electromagnetic Interference (EMI) measurements was well established [2-11]. It was in this role that the facility was known for a long time.

If we fast forward to the present day, it is clear that the role and function of wireless technology in everyday life has reached unprecedented levels as compared to 20 - 30 years ago. For this to occur, it has meant that antenna designs and their application have had to evolve also. But how has the RC come to the fore to be proposed and used for antenna measurements, diverging away from its earlier intended use? To answer this question, we must partly examine the nature of antenna designs and their operational use.

Traditionally, antennas have always been orientated, and their communication channels configured in a Line of Sight (LOS) manner. For example, we have terrestrial antennas mounted on roof tops, and other directive types of antenna that are employed in satellite communications. The characterisation of these types of antenna for use in LOS communications are wholly defined by use of an equivalent free space approach which is typified by the Anechoic Chamber (AC) [12]. In a real applicational environment, reflection, scattering and diffraction may still exist to a certain extent, which brings about the creation of additional wave paths within the communication channel. Nonetheless, the AC is still the preferred environment to characterise these types of antennas, as their radiation patterns (and other subsequent parameters of interest) are of prime importance in this LOS scenario.

When we consider the modern mobile terminal, (i.e. the mobile phone) these do not operate under the premise of a LOS scenario. The antennas inside mobile phones seldom ‘see’ the base station and are expected to work perfectly in Non Line of Sight (NLOS) environments. This type of environment gives rise to signals that will be readily exposed to reflections caused by large smooth objects, diffraction effects caused by the edges of sharp objects, and scattering effects caused by small or irregular objects [12]. When these effects occur, they

will cause the creation of additional wave paths which will eventually add at the receiving side. These wave contributions have independent complex amplitudes (i.e. magnitude and phase information), such that at recombination, they may add constructively or destructively or anything in between these extremes [12].

The wave paths and their complex amplitudes are also subject to rapid changes with time, with the terminal moving or parts of the environment (communication channel) changing. This brings about variations in the signal at the receiver and is commonly referred to as fading [12]. The largest variations occur when there is a complete block on the LOS which is more accurately referred to as small scale fading, as opposed to large scale fading which is usually applied to variations only in the distance from the transmitter or due to part shadowing [12].

As it is important to characterise any antenna in a manner befitting its operational scenario or intended use to accurately reflect the performance merits, another facility is thus required that can emulate this type of fading environment.

When the regulations of the American Federal Communications Commission (FCC) released the unlicensed use of the Ultra Wide-Band (UWB) frequency band between 3.1 GHz and 10.6 GHz in 2002 [13], a vast amount of interest and industrial/academic research followed. The RC offered little compunction or restriction concerning large operational frequencies whilst also allowing for a vast range of antenna types and sizes, something, for example, the Wheeler Cap procedure [14] isn't always suited for when measuring antenna efficiencies [14].

Financial implications have also played a part in the subsequent rise to prominence of the RC. With the construction and operation of an AC (here we will only specifically compare with far field anechoic chambers), large amounts of anechoic absorber must be purchased to line the walls in order to suppress reflections, and this can be expensive. The RC requires no such absorber, leaving the walls purely metallic to encourage reflections which represents a cost saving. Furthermore, if one was to compare the relative size of each facility against the lowest frequency of operation, it is possible to conclude that the RC can be constructed smaller in size than its AC counterpart - again offering a potential cost saving.

The RC is a unique, stand alone facility in the sense that it will allow a user full control over the time frame and uncertainty inherent in a given measurement, distinguishing itself from any other facility. The operational principles for the RC allows for the measurement resolution to be clearly defined which in turn controls the overall measurement time.

Mathematical procedures can be defined which link the expected uncertainty to the resolution and thus the time frame. Therefore, before a measurement commences all the parameters can be defined accordingly.

Perhaps one of the more important factors that have lead to the RC's increasing popularity (and subsequent proposal) concerns the ease of measurement. Due to its unique operation of multiple reflected waves, the angle of arrival of these waves reaching any receiving antenna is uniformly distributed over three dimensional space [15]. What this effectively means is that the angle of arrival and wave polarisation is equally probable which can simplify the characterisation of antennas, because in such an environment, their performance is then insensitive to their orientation.

1.2 Research Motivation

Although much research has been performed on RCs over the past decade, the facility and the measurement procedures for antennas can be relatively considered to be in their infancy. Much published work exists from Chalmers University of Technology, the National Institute of Standards and Technology (NIST), the National Physics Laboratory (NPL), and many other groups in the U.K, France, Germany and indeed worldwide, whose work concerning reverberation chambers should be rightfully acknowledged.

There is however a necessity for continued research. Notwithstanding that much work concerning the efficiency deduction of single port metallic antennas had been completed, the avenue of on-body communications coupled with the development of the textile antenna provided an interesting area. The characterisation of textile antenna efficiency in free space conditions in a RC was recently performed in [16]; however, simulated or WC methods have been often employed to depict the performance of such antennas in an on-body role [17, 18]. Measurement prediction of antenna performance in close proximity to a user is a necessary task to determine exactly how the antenna behaves and what power losses are liable to exist, but this can be a challenging issue; some researchers therefore prefer to adopt the use of phantoms as opposed to human test subjects [19]. The absence of knowledge concerning the efficiency performance of textile antennas on human subjects, coupled with the lack of detailed measurement procedures concerning how to measure, and the effect of measuring antenna quantities using human subjects in a RC [20] was an interesting proposition which supplied the motivation to investigate this area.

The characterisation of Multiple Input Multiple Output (MIMO) channels and the measurement of multiport antennas for MIMO applications had also begun to receive treatment [21-23]. However, the antennas employed were usually quite large in dimension [22], dipole based [24], or often configured utilising spatial diversity as their means of reducing mutual coupling between two or more feeds [25]. The Planar Inverted F Antenna (PIFA) is well known from many concurrent studies [26-29] and there exists a large demand to use these types of antennas for MIMO applications. This is to allow for an increase of data rates, and also to combat the shallow fading minima evident from multipath propagation environments. A new design of PIFA (the single element dual feed PIFA) was proposed at Liverpool in 2010, with the aim of creating a miniaturised MIMO antenna based on a PIFA topology that could be successfully employed in a telecommunications capacity.

Initially however, the antennas were only characterised theoretically and numerically with limited experimental results; therefore the initial motivation was to fully characterise them practically. A secondary motivation for this work existed in the fact that these novel antennas employed only pattern and polarisation diversity techniques to reduce the correlation between two very closely spaced feeds. Practical research was therefore necessary to benchmark the performance of these smaller antennas against existing larger designs in literature, aimed at validating the PIFA's potential, and also to prove that the isolation techniques employed were successful in eliminating any detrimental performance effects so they could be accepted and employed in an Industrial capacity.

The characterisation of larger array antennas, not employed in a MIMO capacity, was an interesting proposition. As previously stated, it is important to characterise any antenna in a manner befitting their operational scenario or intended use to accurately reflect their performance merits; thus the characterisation of these larger arrays requires different measurement protocols to be developed and configured. Essentially this meant that the use of power dividers is required to actively excite all array elements at the same time to attempt to mimic their realistic mode of operation. To the best of this author's knowledge, only one example of such work exists in RC's; see [30]. The subtle problem of employing power dividers in such a capacity is that power losses exist that need to be accounted for and de-embedded from the array to ensure accurate results. It was realised that the procedures and techniques in [30] could be simplified somewhat which provided the motivation to develop a new equation that could de-embed the losses of the power divider and calculate the efficiency performance of the array in one.

Research into the design and operation of stirring mechanisms within reverberation chambers has attracted a lot of interest [31-36]. Dedicated small sized chambers now exist on the market whose purpose is geared mainly to characterise small terminal antennas [37]. All reverberation chambers use mode stirring techniques; however, the smaller sized facilities can be found to have additional automated turntables inside (used to perform platform stirring), made possible because the antenna devices they are designed to measure do not weigh very much and are small in size. For the larger RC, they offer slightly more flexibility when it comes to the size of an antenna under test that can be measured; however, it is possible to state that perhaps more emphasis is placed on ‘Mechanical Stirring’ in the larger chambers to stir the modes, particularly so when the antenna under test is large in size. In this thesis, the focus is solely placed upon larger sized reverberation chambers.

What is clear is that whether the RC is large or small, the performance in that facility will decrease when the number of modes available to be excited becomes sparse. This is an obvious consequence of the size of the facility, but it can be argued that it is also a consequence on the performance of the mode stirring tools in the facility. To explain further, when it comes to the design of mechanical stirring paddles in the RC, they should be appropriately sized with respect to wavelength to ensure they can adequately interact with and be able to ‘stir’ excited modes. However, many pertinent questions still remain regarding these paddles:

- 1) What is the optimum design?
- 2) How can their performance be improved, particularly at larger wavelengths?
- 3) How best to design these paddles?
- 4) How best to validate the paddle/chamber performance?

This has provided a natural motivation to attempt to answer these questions and design better performing mechanical stirring paddles. The work is aimed at eventually reaching an optimum design of reverberation chamber which up till now has proved elusive.

1.3 Organisation of the Thesis

The contents of this thesis are organised in the following manner.

Chapter 2 is issued to review and discuss the theoretical foundations of the RC, underpinning its use as a facility for antenna measurements. This chapter is important as many of the concepts later relied upon will have their theoretical base established in this chapter.

Chapter 3 presents the complete efficiency and impedance matching characterisation of four single port textile antennas for on-body communications, analysed in both free space and on-body roles. New knowledge is obtained regarding the performance of these devices and the subsequent reasons for that performance are also conclusively discussed. This chapter will also present detailed measurement procedures of how to measure performance quantities on human beings using an RC, as well as thoroughly documenting the effect of using human beings instead of substitute phantoms to fill the gaps in knowledge as previously discussed.

Chapter 4 concerns multiport (array) antennas. The chapter is subdivided into two parts to chart a distinction between multiport antennas specifically designed for MIMO applications and conventional array antennas, developed for use in other applications.

The first part of this chapter deals with the full practical validation of two new single element dual feed PIFAs. In this, the measurement procedures are comprehensively discussed, after which all results pertinent to the investigation are issued. The results serve to examine the miniaturisation of these devices and the impact on performance; aimed to benchmark and prove the designs operational quality despite remaining compact in size.

The second part of Chapter 4 concerns the efficiency characterisation of a new large sized array antenna for use in radio astronomy applications. Full detailed measurement procedures are documented concerning the array measurement, coupled with the use of power dividers. The loss deduction of the power dividers is depicted before the development of the new equation to characterise the efficiency of the entire array and de-embed the power divider loss is developed. It is shown that the measurement procedures are accurate, straightforward and the new equation is simple to employ without any drawbacks in accuracy.

Chapter 5 analyses the design of new mechanical stirrer designs for RC's. A review of existing work is presented before the design strategy and methodology is issued. A numerical approach is undertaken to create the designs before being transferred into practice. A discussion is then presented concerning the appropriate means of validating the

performance of reverberation chambers, before the final results are issued proving the superior nature of the new designs as compared to standard designs of mechanical stirring paddles. It is shown that the measurement verification is more thorough and accurate than existing procedures, and that the strategy and the new designs have the potential to improve chamber performance with minimal associated costs and for no increase in the physical size.

1.4 References

- [1] H. A. Mendes, "A New Approach to Electromagnetic Field-Strength Measurements in Shielded Enclosures," *Wescon Tech. Papers*, August 1968.
- [2] G. H. Koepke and J. M. Ladbury, "New electric field expressions for EMC testing in a reverberation chamber," in *Digital Avionics Systems Conference, 1998. Proceedings., 17th DASC. The AIAA/IEEE/SAE*, 1998, pp. D53/1-D53/6 vol.1.
- [3] Y. Huang, "Asymmetric reverberation chambers for EMC measurements," in *Electromagnetic Compatibility, 1999. EMC York 99. International Conference and Exhibition on (Conf. Publ. No. 464)*, 1999, pp. 65-69.
- [4] D. A. Hill, "Spatial correlation function for fields in a reverberation chamber," *Electromagnetic Compatibility, IEEE Transactions on*, vol. 37, p. 138, 1995.
- [5] J. Page, "Stirred mode reverberation chambers for EMC emission measurements and radio type approvals or organised chaos," in *Electromagnetic Compatibility, 1994., Ninth International Conference on*, 1994, pp. 313-320.
- [6] P. F. Wilson and M. T. Ma, "Techniques for measuring the electromagnetic shielding effectiveness of materials. II. Near-field source simulation," *Electromagnetic Compatibility, IEEE Transactions on*, vol. 30, pp. 251-259, 1988.
- [7] L. Scott, "Mode-stir measurement techniques for EMC theory and operation," in *Antenna Measurements (Ref. No. 1998/254), IEE Colloquium on*, 1998, pp. 8/1-8/7.
- [8] T. H. Lehman, G. J. Freyer, M. L. Crawford, and M. O. Hatfield, "Recent developments relevant to implementation of a hybrid TEM cell/reverberation chamber HIRF test facility," in *Digital Avionics Systems Conference, 1997. 16th DASC., AIAA/IEEE*, 1997, pp. 4.2-26-30 vol.1.
- [9] G. J. Freyer, T. H. Lehman, J. M. Ladbury, G. H. Koepke, and M. O. Hatfield, "Verification of fields applied to an EUT in a reverberation chamber using statistical theory," in *Electromagnetic Compatibility, 1998. 1998 IEEE International Symposium on*, 1998, pp. 34-38 vol.1.
- [10] M. O. Hatfield, M. B. Slocum, E. A. Godfrey, and G. J. Freyer, "Investigations to extend the lower frequency limit of reverberation chambers," in *Electromagnetic Compatibility, 1998. 1998 IEEE International Symposium on*, 1998, pp. 20-23 vol.1.
- [11] Y. Huang and D. J. Edwards, "A novel reverberating chamber: the source-stirred chamber," in *Electromagnetic Compatibility, 1992., Eighth International Conference on*, 1992, pp. 120-124.
- [12] P. S. Kildal, *Foundations of antennas: A unified approach*: Studentlitteratur, 2000.

- [13] F. C. Commission, "Revision of Part 15 of the Commission's Rules regarding Ultra-Wideband Transmission Systems, First Report and Order," *ET Docket 98-153, FCC 02-48*, pp. pp. 1–118, Feb.14, 2002.
- [14] Y. Lu, Y. Huang, and H. T. Chattha, "Effects of Wheeler cap loss on wideband antenna efficiency measurement results," in *Antenna Technology, 2009. iWAT 2009. IEEE International Workshop on*, 2009, pp. 1-4.
- [15] K. Rosengren and P. S. Kildal, "Study of distributions of modes and plane waves in reverberation chambers for the characterization of antennas in a multipath environment," *Microwave and Optical Technology Letters*, vol. 30, pp. 386-391, 2001.
- [16] P. J. Soh, G. A. E. Vandenbosch, X. Chen, P. S. Kildal, S. L. Ooi, and H. Aliakbarian, "Wearable textile antennas' efficiency characterization using a reverberation chamber," in *Antennas and Propagation (APSURSI), 2011 IEEE International Symposium on*, 2011, pp. 810-813.
- [17] M. Mantash, A. C. Tarot, S. Collardey, and K. Mahdjoubi, "Investigation of Flexible Textile Antennas and AMC Reflectors," *International Journal of Antennas and Propagation*, vol. 2012, pp. 1-10, 2012.
- [18] M. A. R. Osman, M. K. A. Rahim, N. A. Samsuri, M. K. Elbasheer, and M. E. Ali, "Textile UWB Antenna Bending and Wet Performances," *International Journal of Antennas and Propagation*, vol. 2012, pp. 1-12, 2012.
- [19] P. S. Kildal, "Measurements of mobile phone antennas in small reverberation chambers," *Automatika*", vol. 43, p. 63–68, 2002.
- [20] G. A. Conway, W. G. Scanlon, C. Orlenius, and C. Walker, "In situ measurement of UHF wearable antenna radiation efficiency using a reverberation chamber," *Antennas and Wireless Propagation Letters, IEEE*, vol. 7, pp. 271-274, 2008.
- [21] X. Chen, "Spatial correlation and ergodic capacity of MIMO channel in reverberation chamber," *International Journal of Antennas and Propagation*, vol. 2012, pp. 1-7, 2012.
- [22] P. S. Kildal, K. Rosengren., "Correlation and capacity of MIMO systems and mutual coupling, radiation efficiency, and diversity gain of their antennas, Simulations and measurements in a reverberation chamber," *IEEE Communications Magazine*, vol. 42, pp. 104-112, Dec 2004.
- [23] A. Diallo, P. Le Thuc, R. Starajf, G. Kossiavas, M. Franzen, P. S. Kildal, "Evaluation of the performances of several four-antenna systems in a reverberation chamber," *In. Proc. EuCap 2007*, 2007.
- [24] A. Khaleghi, "Diversity techniques with parallel dipole antennas: radiation pattern analysis," *Progress In Electromagnetics Research B*, vol. 64, pp. 23-42, 2006.
- [25] X. Chen, Y. Gao, C. Parini, Y. Zhinong, , "Study of a dual-element PIFA array for MIMO terminals," in *Antennas and Propagation Society International Symposium 2006, IEEE*, 2006, pp. 309-312.
- [26] D. M. Nashaat, H. A. Elsadek, and H. Ghali, "Single Feed Compact Quad-Band PIFA Antenna for Wireless Communication Applications," *Antennas and Propagation, IEEE Transactions on*, vol. 53, pp. 2631-2635, 2005.

- [27] Y. T. Jean-Charles and V. Ungvichian, "The effects of an additional shorting stub on PIFA performance," in *Electromagnetic Compatibility and 19th International Zurich Symposium on Electromagnetic Compatibility, 2008. APEMC 2008. Asia-Pacific Symposium on*, 2008, pp. 558-561.
- [28] H. T. Chattha, Y. Huang, Y. Lu, and Z. M. Huang, "A study of parameter changes on the characteristics of planar inverted-F antenna," in *Antennas and Propagation, 2009. EuCAP 2009. 3rd European Conference on*, 2009, pp. 370-373.
- [29] H. T. Chattha, Y. Huang, M. K. Ishfaq, and S. J. Boyes, "Bandwidth enhancement techniques for planar inverted-F antenna," *Microwaves, Antennas & Propagation, IET*, vol. 5, pp. 1872-1879, 2011.
- [30] M. V. Ivashina, M. Kehn, P. S. Kildal, and R. Maaskant, "Decoupling Efficiency of a Wideband Vivaldi Focal Plane Array Feeding a Reflector Antenna," *Antennas and Propagation, IEEE Transactions on*, vol. 57, pp. 373-382, 2009.
- [31] C. L. Holloway, D. A. Hill, J. M. Ladbury, and G. Koepke, "Requirements for an effective reverberation chamber: unloaded or loaded," *Electromagnetic Compatibility, IEEE Transactions on*, vol. 48, pp. 187-194, 2006.
- [32] D. I. Wu and D. C. Chang, "The effect of an electrically large stirrer in a mode-stirred chamber," *Electromagnetic Compatibility, IEEE Transactions on*, vol. 31, pp. 164-169, 1989.
- [33] Y. Huang, Z. Jie Tao, and L. Ping, "A novel method to examine the effectiveness of a stirrer," in *Electromagnetic Compatibility, 2005. EMC 2005. 2005 International Symposium on*, 2005, pp. 556-561.
- [34] J. Clegg, A. C. Marvin, J. F. Dawson, and S. J. Porter, "Optimization of stirrer designs in a reverberation chamber," *Electromagnetic Compatibility, IEEE Transactions on*, vol. 47, pp. 824-832, 2005.
- [35] K. R. Goldsmith and P. A. Johnson, "Design, construction, computational EM modelling, and characterisation of an aircraft sized reverberation chamber and stirrer," in *Digital Avionics Systems Conference, 1998. Proceedings., 17th DASC. The AIAA/IEEE/SAE*, 1998, pp. D55/1-D55/8 vol.1.
- [36] Y. Huang, N. Abumustafa, Q. G. Wang, and X. Zhu, "Comparison of Two Stirrer Designs for a New Reverberation Chamber," in *Environmental Electromagnetics, The 2006 4th Asia-Pacific Conference on*, 2006, pp. 450-453.
- [37] P. S. Kildal, X. Chen, C. Orlenius, M. Franzen, and C. S. L. Patane, "Characterization of Reverberation Chambers for OTA Measurements of Wireless Devices: Physical Formulations of Channel Matrix and New Uncertainty Formula," *Antennas and Propagation, IEEE Transactions on*, vol. 60, pp. 3875-3891, 2012.

Chapter 2: Reverberation Chamber Cavity Theory

2.1 Introduction

Grounding in the theoretical principles concerning reverberation chambers is important and essential for any practical undertaking to be completed accurately. The overall field of electromagnetics that contains the foundations of reverberation chamber cavity theory is a well studied and classical area, and we owe much to authors such as Harrington [1], Balanis [2], Jackson [3], Kraus [4] and more recently Hill [5] for their pioneering work in this area. We should also not forget the contribution made by James Clark Maxwell who provided the unified theory and equations that made work in the entire field possible, and Henrich Hertz who practically validated Maxwell's theorems by demonstrating the existence of electromagnetic radiation.

The purpose of this chapter is to present a review into some of the more important theoretical concepts that uphold and support the RC's use for antenna measurements. This chapter is intended to underpin the concepts and techniques that will later be referred to and relied upon in more practically orientated chapters. The chapter is by no means exhaustive and will attempt to draw upon many of the accepted theoretical concepts published over the last 60 years. This author does not claim any credit for the accepted concepts discussed in this chapter; all the theoretical work is appropriately cited. This author will however discuss and apply the theoretical theorems specifically around the rectangular RC facility at the University of Liverpool, where all of the work in this thesis was completed.

2.2 Cavity Modes and Electromagnetic Fields

It is well known that a metallic rectangular empty cavity is resonant when its dimensions satisfy the condition [5]:

$$k_{mnp}^2 = \left(\frac{m\pi}{a}\right)^2 + \left(\frac{n\pi}{b}\right)^2 + \left(\frac{p\pi}{d}\right)^2 \quad (2.1)$$

where: $k = 2\pi/\lambda$, λ = the wavelength; m , n and p are integer numbers and a , b and d are the chamber dimensions.

For convenience, (2.1) can also be expressed as (2.2).

$$k_{mnp}^2 = k_x^2 + k_y^2 + k_z^2 \quad (2.2)$$

Where:

$$k_x = \left(\frac{m\pi}{a} \right), k_y = \left(\frac{n\pi}{b} \right), k_z = \left(\frac{p\pi}{d} \right) \quad (2.3)$$

It is stated that the simplest method to construct the resonant modes for a rectangular cavity is to derive modes that are Transverse Electric (TE) or Transverse Magnetic (TM) to one of the three axis [5]. The standard convention in this sense is normally chosen to be the z axis with respect to Fig. 2.1.

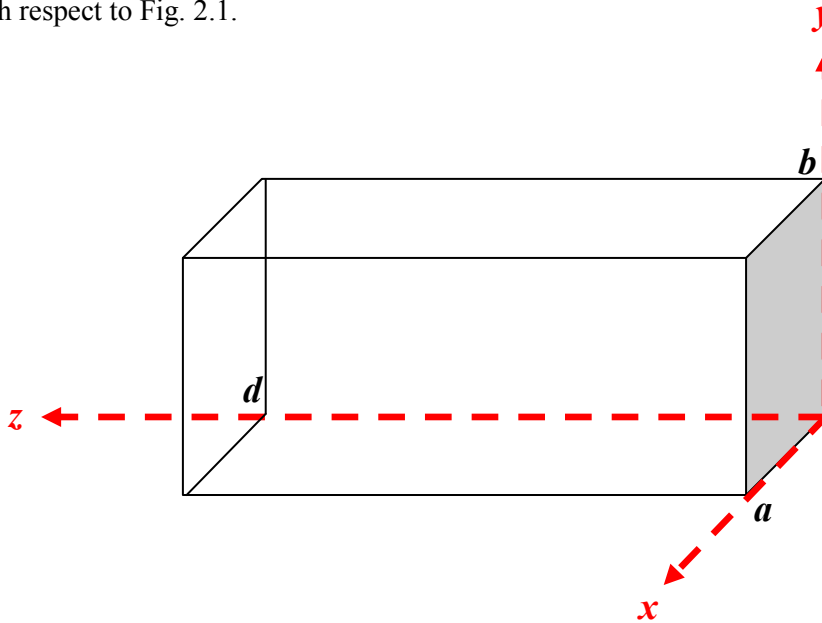


Fig. 2.1: Rectangular cavity principle axis

The TE modes are referred to as magnetic modes as the E_z field component is zero. Similarly, the TM modes are referred to as electric modes as the H_z field component is also zero [5]. The corresponding fields can be given as follows, beginning first with the TM components.

$$E_{zmn}^{TM} = E_O \sin\left(\frac{m\pi}{a}x\right) \sin\left(\frac{n\pi}{b}y\right) \cos\left(\frac{p\pi}{d}z\right) \quad (2.4)$$

where: E_O is a constant with units of V/m [5]. The transverse components can be issued now as:

$$E_{xmn}^{TM} = \frac{k_x k_z E_O}{k_{mnp}^2 - k_z^2} \cos\left(\frac{m\pi}{a}x\right) \sin\left(\frac{n\pi}{b}y\right) \sin\left(\frac{p\pi}{d}z\right) \quad (2.5)$$

$$E_{ymnp}^{TM} = \frac{k_y k_z E_O}{k_{mnp}^2 - k_z^2} \sin\left(\frac{m\pi}{a}x\right) \cos\left(\frac{n\pi}{b}y\right) \sin\left(\frac{p\pi}{d}z\right) \quad (2.6)$$

The z component of the magnetic field is zero (owing to the definition of the TM mode), and the transverse components of the magnetic field can be given as [5]:

$$H_{xmn}^{TM} = -\frac{i\omega_{mnp}\epsilon k_y E_O}{k_{mnp}^2 - k_z^2} \sin\left(\frac{m\pi}{a}x\right) \cos\left(\frac{n\pi}{b}y\right) \cos\left(\frac{p\pi}{d}z\right) \quad (2.7)$$

$$H_{ymnp}^{TM} = \frac{i\omega_{mnp}\epsilon k_x E_O}{k_{mnp}^2 - k_z^2} \cos\left(\frac{m\pi}{a}x\right) \sin\left(\frac{n\pi}{b}y\right) \cos\left(\frac{p\pi}{d}z\right) \quad (2.8)$$

where: ϵ is the permittivity of the media inside the cavity and ω is the angular frequency. By virtue that E_{zmn}^{TM} be non-zero (Eq. 2.4), the allowable values of the mode coefficients are $m = 1, 2, 3, \dots; n = 1, 2, 3, \dots; p = 0, 1, 2, 3, \dots;$

The TE (magnetic modes) can be derived in an equivalent manner. The z component of the magnetic field satisfies the scalar Helmholtz equation and the boundary conditions are such that the following is prevalent:

$$H_{zmn}^{TE} = H_O \cos\left(\frac{m\pi}{a}x\right) \cos\left(\frac{n\pi}{b}y\right) \sin\left(\frac{p\pi}{d}z\right) \quad (2.9)$$

where: H_O is a constant of units A/m. The eigenvalues and axial wave numbers are the same as given in Equations (2.1) to (2.3). The transverse components can now be issued as [5]:

$$H_{xmn}^{TE} = -\frac{H_O k_x k_y}{k_{mnp}^2 - k_z^2} \sin\left(\frac{m\pi}{a}x\right) \cos\left(\frac{n\pi}{b}y\right) \cos\left(\frac{p\pi}{d}z\right) \quad (2.10)$$

$$H_{ymnp}^{TE} = \frac{H_O k_y k_z}{k_{mnp}^2 - k_z^2} \cos\left(\frac{m\pi}{a}x\right) \sin\left(\frac{n\pi}{b}y\right) \sin\left(\frac{p\pi}{d}z\right) \quad (2.11)$$

The z component of the electric field is zero by definition of a TE mode and the transverse components of the electric field can be stated as [5]:

$$E_{xmn}^{TE} = -\frac{i\omega_{mnp}\mu k_y H_O}{k_{mnp}^2 - k_z^2} \cos\left(\frac{m\pi}{a}x\right) \sin\left(\frac{n\pi}{b}y\right) \sin\left(\frac{p\pi}{d}z\right) \quad (2.12)$$

$$E_{ymnp}^{TE} = \frac{i\omega_{mnp}\mu k_x H_O}{k_{mnp}^2 - k_z^2} \sin\left(\frac{m\pi}{a}x\right) \cos\left(\frac{n\pi}{b}y\right) \sin\left(\frac{p\pi}{d}z\right) \quad (2.13)$$

The allowable mode coefficients in this regard are $m = 0, 1, 2, 3, \dots$; $n = 0, 1, 2, 3, \dots$; and $p = 1, 2, 3, \dots$; with the only exception that $m = n = 0$ is not allowed.

The resonant frequencies with respect to each individual set of mode coefficients can be deduced by (2.14), adopting the earlier defined notation.

$$f_{mnp} = \frac{1}{2\sqrt{\mu\epsilon}} \sqrt{\left(\frac{m}{a}\right)^2 + \left(\frac{n}{b}\right)^2 + \left(\frac{p}{d}\right)^2} \quad (2.14)$$

where: μ, ϵ relates to the permeability and the permittivity of the medium inside the cavity respectively.

When assessing the number of modes that are present in a given cavity, three common methods exist. The first is based on what is termed ‘mode counting’ which can be performed by the repeated solution of (2.1) for both TE and TM modes, giving the total number of modes present with eigenvalues less than or equal to k (a practical limit for the propagation of modes). The second method is by an approximation referred to as ‘Weyl’s formula’ [5], which is valid for cavities of general shape and is given in (2.15).

$$N = \frac{8\pi}{3} (a \times b \times d) \frac{f^3}{c^3} \quad (2.15)$$

where: N is the number of modes, f is the frequency in Hz and c is the wave speed in the cavity medium (m/s).

The third method is an extension to Weyl’s formula specific to rectangular cavities [5] and is stated in (2.16).

$$N = \frac{8\pi}{3} (a \times b \times d) \frac{f^3}{c^3} - (a + b + d) + \frac{1}{2} \quad (2.16)$$

A comparison of the modal numbers present in the University of Liverpool RC (dimensions of $a = 3.6$ m, $b = 4$ m and $d = 5.8$ m) by all three methods is shown in Fig. 2.2.

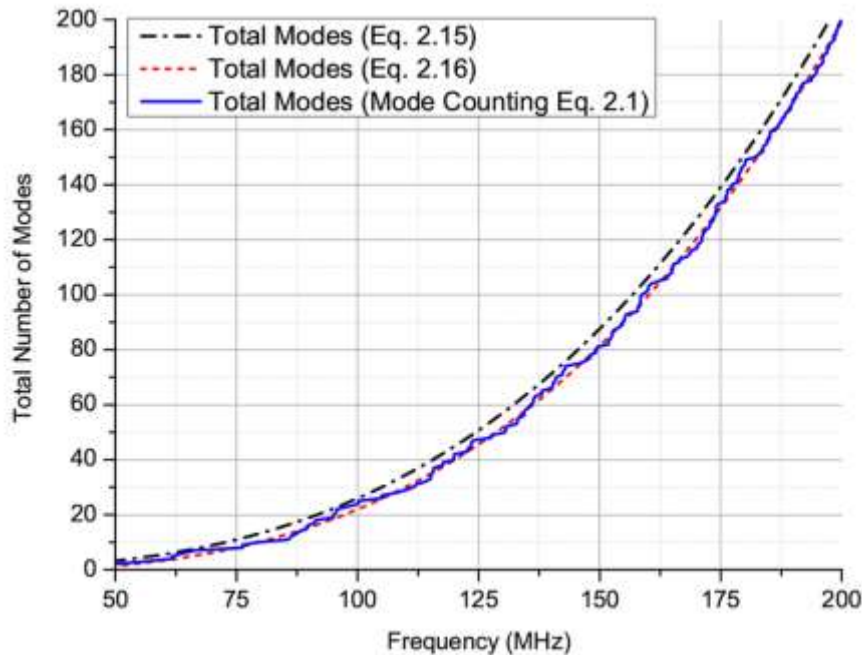


Fig. 2.2: Mode numbers Vs frequency for the University of Liverpool RC

From Fig. 2.2 we see that the extra terms in (2.16) improve the agreement obtained with the numerical mode counting as opposed to using the original Weyl's formula in (2.15). For increasing frequency it is seen that the number of modes increases with respect to the cavity volume and the third power of frequency.

The mode density is another important parameter to be able to assess. This quantity charts the amount of modes available in a small bandwidth about a given frequency [5]. This quantity can be found by differentiating (2.16) and is issued in (2.17) after consultation with [5].

$$D_S(f) = 8\pi(a \times b \times d) \frac{f^2}{c^3} - \frac{a + b + d}{c} \quad (2.17)$$

A plot of the mode density per megahertz Vs frequency can be viewed in Fig. 2.3. From Fig. 2.3 we see that the chamber has a mode density of at least one mode per megahertz from 116 MHz upwards. A low mode density in any given chamber means that chamber would not have adequate performance, as the mode density is too small to obtain spatial field uniformity [5].

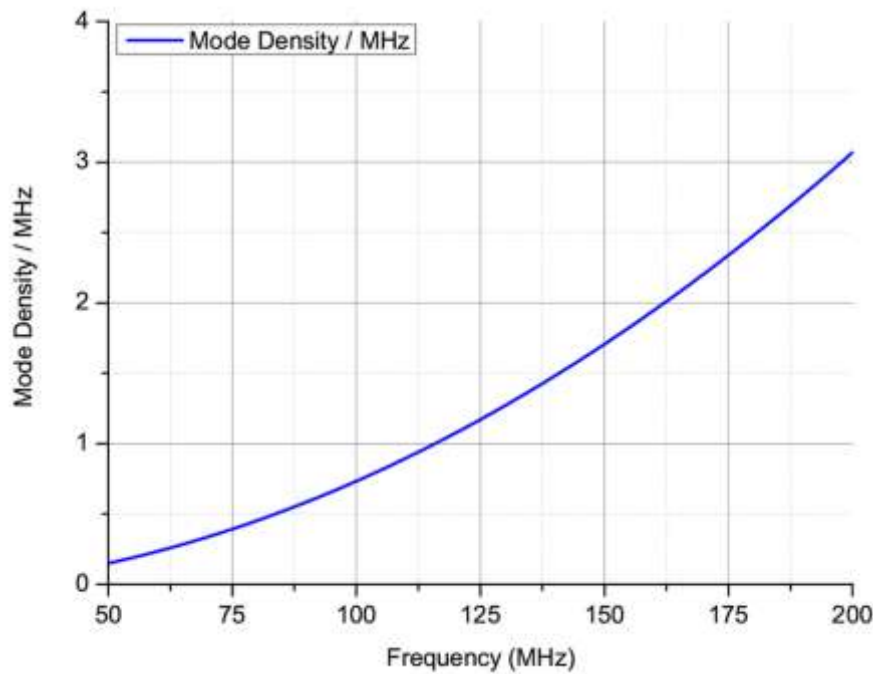


Fig. 2.3: Mode density / MHz Vs frequency in the University of Liverpool RC

Knowledge of the modal condition inside any given RC is important. It can be seen from equations (2.4) to (2.13), that the fields inside a given cavity can be depicted in terms of resonant modes and their subsequent integer coefficients (m , n and p) satisfying the boundary conditions at the walls of the chamber. In operational practice, different modes are required to be excited in order to promote a sufficient change in the field distribution (to achieve spatial uniformity). The first five allowable modes in the University of Liverpool RC can be seen in Table I.

Table I: The first five resonant modes in University of Liverpool RC

Distinct mode	$m \ n \ p$	Resonant frequency (MHz)
1	0 1 1	45.55
2	1 0 1	49.04
3	1 1 0	56.06
4	1 1 1	61.73
5	0 1 2	63.89

It is advantageous to be able to calculate and visualise the fields created inside a given chamber by the excitation of resonant modes. However, different from the prior field equations in (2.4) to (2.13), it is advantageous to visualise these fields in a ‘non-empty’ chamber; that is, with a realistic excitation involved. This provides confidence to be able to interpret the conditions inside the chamber and link them to operational conditions that are witnessed in practice. With respect to the modes and the subsequent fields, it is known from [6] that:

- a) The ElectroMagnetic (EM) fields inside a rectangular chamber outside of the source area are purely the superposition of all TE and TM modes generated within it. In the source area, an extra term needs to be added from the contribution of other hybrid modes.
- b) For a current with any polarisation inside the chamber, an electric field with three components may be generated. This essentially means that a signal transmitted by an antenna with one polarisation can be received by an antenna with any polarisation.
- c) Modes inside the chamber can be controlled by the choice of the polarisation and location of the excitation source.

In [6], a computationally efficient series of equations based on cavity Green’s functions was derived in order to study the resultant electric field inside shielded enclosures. The resulting electric field (E) was deduced using (2.18), (2.19) and (2.20).

$$E = \frac{1}{j\omega\epsilon} \int_{source} \underline{G} \cdot J(x', y', z') dv' \quad (2.18)$$

where: $J(x', y', z')$ = the excitation current, ω is the angular frequency in radians and \underline{G} = dyadic Green’s function.

$$E = \frac{1}{j\omega\epsilon} \int_{source} [G_{xy}\hat{x} + G_{yy}\hat{y} + G_{zy}\hat{z}] J(x', y', z') dv' \quad (2.19)$$

$$\begin{aligned}
G = & \sum_{p=0}^{\infty} \sum_{m=0}^{\infty} \frac{2\epsilon_{0m}}{da\alpha \sin \alpha b} \sin k_z z' \cos k_x x' \\
& \left\{ \begin{array}{l} \left\{ \begin{array}{l} k_z k_x \cos k_z z \sin k_x x \frac{\sin \alpha y \sin \alpha(b-y')}{\sin \alpha y' \sin \alpha(b-y)} \end{array} \right\} y < y' \hat{z}\hat{x} \\ \left\{ \begin{array}{l} \left(k_x^2 - k^2 \right) \sin k_z z \cos k_x x \frac{\sin \alpha y \sin \alpha(b-y')}{\sin \alpha y' \sin \alpha(b-y)} \end{array} \right\} y > y' \hat{x}\hat{x} \end{array} \right\} \\
& \left\{ \begin{array}{l} \left\{ \begin{array}{l} + k_x \alpha \sin k_z z \sin k_x x \frac{\cos \alpha y \sin \alpha(b-y')}{-\sin \alpha y' \cos \alpha(b-y)} \end{array} \right\} y < y' \hat{y}\hat{x} \\ \left\{ \begin{array}{l} \left(k_y^2 - k^2 \right) \sin k_x x \cos k_y y \frac{\sin \beta z \sin \beta(d-z')}{\sin \beta z' \sin \beta(d-z)} \end{array} \right\} z < z' \hat{x}\hat{y} \\ \left\{ \begin{array}{l} \left(k_y^2 - k^2 \right) \sin k_x x \cos k_y y \frac{\sin \beta z \sin \beta(d-z')}{\sin \beta z' \sin \beta(d-z)} \end{array} \right\} z > z' \hat{y}\hat{y} \end{array} \right\} \\
& + \sum_{m=0}^{\infty} \sum_{n=0}^{\infty} \frac{2\epsilon_{0n}}{ab\beta \sin \beta d} \sin k_x x' \cos k_y y' \\
& \left\{ \begin{array}{l} \left\{ \begin{array}{l} k_x k_y \cos k_x x \sin k_y y \frac{\sin \beta z \sin \beta(d-z')}{\sin \beta z' \sin \beta(d-z)} \end{array} \right\} z < z' \hat{x}\hat{y} \\ \left\{ \begin{array}{l} + k_y \beta \sin k_x x \sin k_y y \frac{\cos \beta z \sin \beta(d-z')}{-\sin \beta z' \cos \beta(d-z)} \end{array} \right\} z < z' \hat{z}\hat{y} \end{array} \right\} \\
& + \sum_{n=0}^{\infty} \sum_{p=0}^{\infty} \frac{2\epsilon_{0p}}{bd\gamma \sin \gamma a} \sin k_y y' \cos k_z z' \\
& \left\{ \begin{array}{l} \left\{ \begin{array}{l} k_y k_z \cos k_y y \sin k_z z \frac{\sin \gamma x \sin \gamma(a-x')}{\sin \gamma x' \sin \gamma(a-x)} \end{array} \right\} x < x' \hat{y}\hat{z} \\ \left\{ \begin{array}{l} + \left(k_z^2 - k^2 \right) \sin k_y y \cos k_z z \frac{\sin \gamma x \sin \gamma(a-x')}{\sin \gamma x' \sin \gamma(a-x)} \end{array} \right\} x < x' \hat{z}\hat{z} \\ \left\{ \begin{array}{l} + k_z \gamma \sin k_y y \sin k_z z \frac{\cos \gamma x \sin \gamma(a-x')}{-\sin \gamma x' \cos \gamma(a-x)} \end{array} \right\} x < x' \hat{x}\hat{z} \end{array} \right\} \quad (2.20)
\end{aligned}$$

where: $\epsilon_{0n} = \begin{cases} 1 & \text{when } n=0, \\ 2 & \text{when } n \neq 0, \end{cases}$, $\alpha = \sqrt{k^2 - k_z^2 - k_x^2}$, $\beta = \sqrt{k^2 - k_x^2 - k_y^2}$ and

$$\gamma = \sqrt{k^2 - k_y^2 - k_z^2}.$$

Assuming a y polarised unit current (with respect to the principle axis defined in Fig. 2.1), and with reference to (2.18), (2.19) and (2.20), the resultant electric field can be obtained using (2.21).

$$\begin{aligned}
 E = & \frac{1}{j\omega\epsilon} \sum_{m=0}^{\infty} \sum_{n=0}^{\infty} \frac{2\epsilon_{0n}}{ab\beta \sin \beta d} \sin k_x x' \cos k_y y' \\
 & \left\{ \begin{array}{l} \left\{ \begin{array}{l} k_x k_y \cos k_x x \sin k_y y \sin \beta z \sin \beta(d-z') \\ \sin \beta z' \sin \beta(d-z) \end{array} \right\} z < z' \hat{x} \\ \left\{ \begin{array}{l} + (k_y^2 - k_x^2) \sin k_x x \cos k_y y \sin \beta z \sin \beta(d-z') \\ \sin \beta z' \sin \beta(d-z) \end{array} \right\} z > z' \hat{y} \end{array} \right\} \\
 & \left\{ \begin{array}{l} \left\{ \begin{array}{l} + k_y \beta \sin k_x x \sin k_y y \cos \beta z \sin \beta(d-z') \\ - \sin \beta z' \cos \beta(d-z) \end{array} \right\} z < z' \hat{z} \\ \left\{ \begin{array}{l} + k_y \beta \sin k_x x \sin k_y y \cos \beta z \sin \beta(d-z') \\ - \sin \beta z' \cos \beta(d-z) \end{array} \right\} z > z' \hat{z} \end{array} \right\}
 \end{aligned} \quad (2.21)$$

The following plots depict a series of E_y field distributions on an xz plane, resulting from a uniform current excitation within the University of Liverpool RC. The field distributions are charted as a function of frequency. The observation location (y) selected in all plots is equal to $b/2$; that is the mid-point in height of the chamber.

The program code written to perform this task was developed by Y. Huang in [6] and disclosed to this author with permission for use in [7]. The co-ordinate locations for the source in all plots are $x_1 = 0.4$ m, $x_2 = 0.5$ m, $y_1 = 1.35$ m, $y_2 = 1.4$ m and $z = 0.5$ m, which situates the source towards one corner of the chamber in the principle x axis, and locates the source between 1.35 m and 1.4 m high from the chamber floor. These selections have been made because this is the typical source location chosen in the chamber during practical measurements, as will be seen in later chapters.

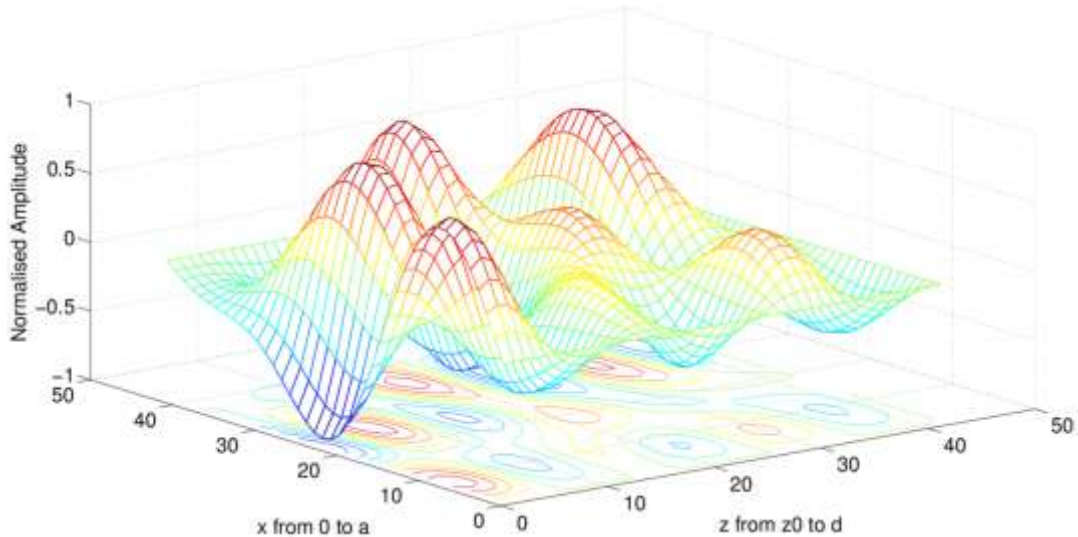


Fig. 2.4: Normalised E_y Field distribution in University of Liverpool RC at 200 MHz

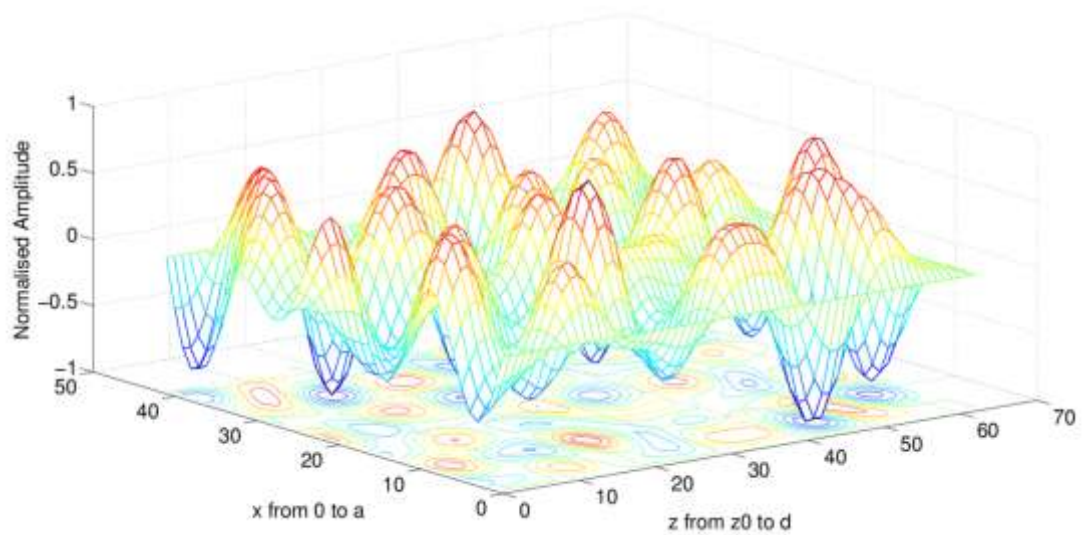


Fig. 2.5: Normalised E_y Field distribution in University of Liverpool RC at 400 MHz

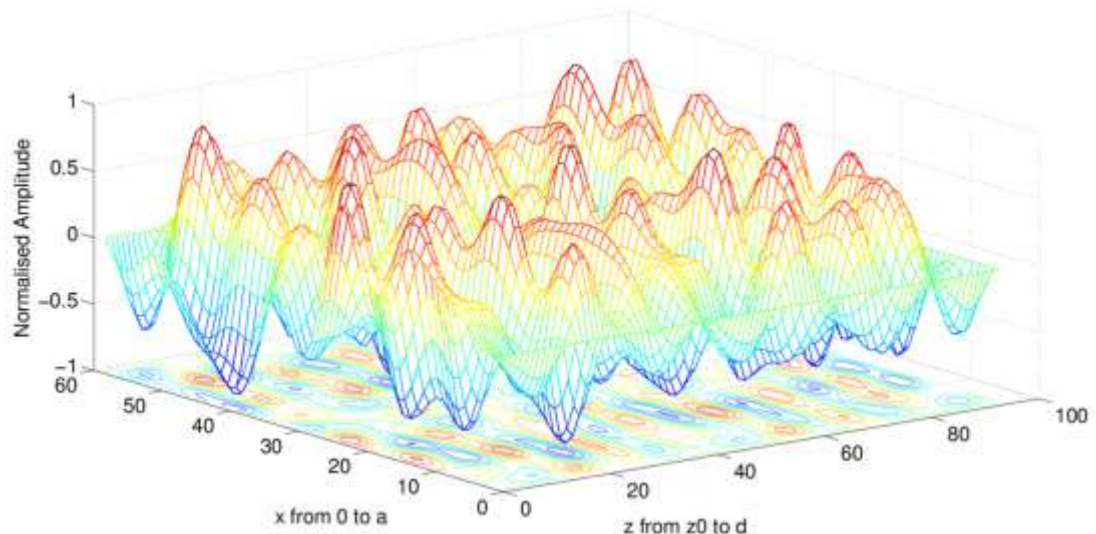


Fig. 2.6: Normalised E_y Field distribution in University of Liverpool RC at 600 MHz

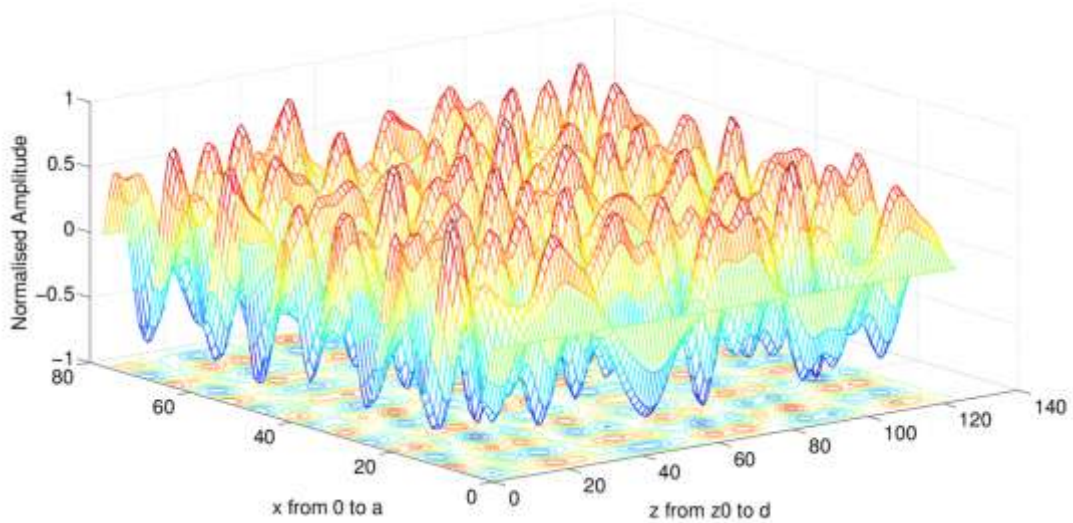


Fig. 2.7: Normalised E_y Field distribution in University of Liverpool RC at 800 MHz

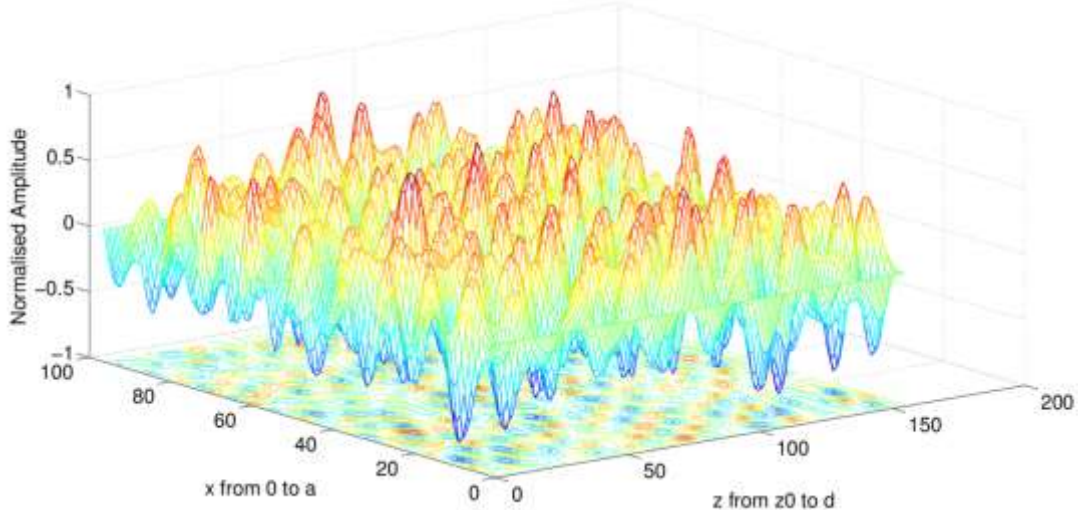


Fig. 2.8: Normalised E_y Field distribution in University of Liverpool RC at 1000 MHz

From Figs. 2.4 to 2.8 we see that the fields are formed in the screened chamber as a result of standing waves that have a sine and cosine dependence. As frequency increases we also see that the fields vary in a more complex manner. From point to point in the screened chamber (at all frequencies depicted here) we see the magnitude of the field has significantly different values.

This is not the desired property for operation in the chamber. If an antenna was to be placed in such a field distribution during a given measurement, then the amount of power it would receive would be dependent upon the location in which that antenna was situated. Any results therefore would not necessarily be repeatable and/or correct. In practice, a uniform

field in the chamber is desired to undertake measurements such that repeatable and correct results could be potentially obtained.

2.3 Mode Stirring Techniques

The reverberation chamber is a unique facility as it employs ‘mode stirring’ techniques to deal with the nature of the fields in the chamber. The purpose of these techniques is to be able to render the fields statistically uniform and isotropic on average; in achieving this, we could potentially situate a receiving antenna in the chamber in different locations and orientations and receive the same average power level. This would go some way to ensuring statistically repeatable measurements. The question now is: What are these techniques and how are they implemented?

2.3.1 Mechanical Stirring

This mode stirring technique is perhaps considered to be the most common technique employed to permute the fields inside a reverberation chamber. The action of mechanical stirring is performed by the rotation or movement of electrically large paddles or plates situated inside the chamber, whose design is usually configured to be non-symmetric and arbitrarily shaped. The paddles can be configured to rotate or move in a step-wise or continuous manner and upon each rotation or movement, the boundary conditions for the electromagnetic field inside the chamber are changed [8].

The effect of changing the boundary conditions for the field means that the ‘peaks’ and ‘nulls’ evident from the field distributions in Figs. 2.4 to 2.8 will change as a function of (observation) location. This means that the field distribution can be rendered statistically homogeneous and isotropic on average from many stirrer increments, provided that the field location is situated approximately $\lambda/2$ (where λ is the wavelength in metres) from the chamber boundaries (e.g. walls) [9]. The rotation or movement from the paddles also gives rise to a statistical environment which is advantageous for antenna measurements in the facility. More on the statistical aspects can be found later in this chapter.

An example of mechanical stirrer design in the University of Liverpool RC can be viewed in Fig. 2.9.



As can be seen in Fig. 2.9, two principle sets of paddles exist; one set mounted about a central rotational shaft from the floor to the roof, the other mounted about a central rotational shaft at ceiling height from near to the front wall to the back wall. The requirement for two sets of paddles arises from any potential change in the polarisation of any reflected waves inside the chamber, regardless of source polarisation. This way, both linear polarisation characteristics emitting from the source should be effectively stirred; helping to ensure that the polarisation characteristic of a wave arriving at the receiver has, on average, a desired equal probability and hence can be considered un-polarised (no dominance one way or another). The paddles are typically sized and as such are designed to operate where they can be considered ‘electrically large’; that is, they are at least comparable with respect to the wavelength of operation and the cavity can generally be considered to be over-moded. When this is not the case, the paddles performance in significantly changing the field distribution will diminish - this is a limitation of the process.

2.3.2 Polarisation Stirring

Despite the adoption of the two principle sets of mechanical stirring paddles and the theoretical validation concerning the un-polarised nature of the reverberation chamber, a bias can potentially exist in practice. It was reported in [10, 11] that a different amount of TE and TM modes could potentially be excited during measurements, which subsequently manifests itself as a difference in the received power with respect to different receive antenna polarisations inside the chamber. In [10], when discussed purely from a modal and wave perspective, investigations were present that cited differences of anything between 3 – 9 dB could be evident.

This mode stirring technique advocates that both vertical and horizontal (assuming linear polarisation) transmit polarisations be measured and both measured results averaged to remove any effect of bias, regardless of the receive antennas polarisation. That is, it aims to ensure that no ‘polarisation imbalance’ exists as it can represent a serious source of measurement uncertainty.

In addition, a polarisation imbalance could also be prevalent as a result of different performances in the vertical and horizontal mechanical stirrer paddles; hence, they have a different efficiency in permuting the fields in the chamber (stirrer efficiency). This necessitates that the design of mechanical stirrer paddles be carefully and rigorously conducted as we will see in chapter five.

In practice, a large number of samples are also normally required to obtain accurate average values. It stands to reason that the more samples one has to form an average, the more accurate that average value will be. Therefore, this technique is also useful in generating an additional number of measurement samples and should be used in conjunction with the mechanical stirring aspect previously defined.

In conclusion, a systematic polarisation imbalance in practice could be caused by the excitation of different amounts of TE and TM modes, in addition to having mechanical stirrer paddles with different stirrer efficiencies. The technique of measuring two transmit polarisations regardless of the receive antennas orientation can remove the problem [10]. The technique can also be a useful method in generating an additional number of measurement samples, required for accuracy purposes.

2.3.3 Platform and Position Stirring

Platform stirring advocates the movement of an Antenna under Test (AUT) or Device under Test (DUT) to various different locations in the chamber by means of a turntable, and an overall average is taken from measured samples at each individual location. This technique was devised in [12] as a means of improving accuracy in a small reverberation chamber, and necessitates that the movement distance to different receive locations should be no less than $\lambda/2$, to avoid progressive samples obtained from different locations being correlated (thus independent). Position stirring is essentially the same procedure. However, this technique does not employ the use of a turntable; instead relying on the physical movement of an AUT/DUT to different test locations inside a given chamber. The advantage of these procedures is that it has been shown to improve accuracy in measurements by giving rise to an additional number of independent measurements for use in the averaging process.

2.3.4 Frequency Stirring

Frequency or electronic stirring advocates the taking of a further average from acquired measurements in an RC, by the use of an algorithm in the post processing stage. The frequency stirring application has been discussed at length (albeit for a 2D cavity) in [5] as a means of improving the spatial uniformity of fields and decreasing the interaction between a line source and the chamber walls.

The application advocates that the smoothing bandwidth (defined as the total number of points in a given window from which to take a further successive average) should decrease for an increase in frequency (increase in modal density) in a given chamber. Hence, a higher level of frequency stirring is required at lower modal densities because it is more difficult to achieve field uniformity in a sparse modal environment for reasons previously discussed.

A degree of care is normally required when performing frequency stirring as by taking too large an average (large smoothing bandwidth) can result in the loss of frequency resolution in any measured data. For example, when measuring the radiation efficiencies or complex reflection coefficients in a reverberation chamber, the amount of frequency stirring is usually chosen to be much less than the absolute operating bandwidths of the antenna in order to avoid this problem. This technique is typically always used in order to obtain smooth and precise results.

2.4 Plane Wave Angle of Arrival

The purpose of this sub-section is to theoretically examine the Angle of Arrival (AoA) nature of plane waves inside the University of Liverpool RC. This section is important to be able to verify because if we could confirm the characteristics of the propagation scenario, it would go some way to demonstrating the RC's suitability as a multipath emulator for mobile communications, and also theoretically demonstrate the earlier claim (from chapter 1) that a multiple reflected wave environment allows for a simplification in the antennas' characterisation, as the performance is insensitive to the orientation.

With respect to Eqns. (2.1), (2.2), (2.4) and (2.9), it has been shown [13] that we can represent the sine and cosine terms as exponentials via Euler's relationship and express the product in the form of (2.22).

$$\begin{aligned}
 & \cos(u) \cdot \cos(v) \cdot \sin(w) \\
 &= A_{mnp}^{TE} \cdot \frac{e^{ju} + e^{-ju}}{2} \cdot \frac{e^{jv} + e^{-jv}}{2} \cdot \frac{e^{jw} - e^{-jw}}{2i} \\
 &= \text{const} \cdot \left\{ e^{ju+jv+jw} + e^{ju-jv+jw} + e^{-ju+jv+jw} + e^{-ju-jv+jw} \right. \\
 &\quad \left. - e^{-ju+jv-jw} - e^{ju-jv-jw} - e^{-ju+jv-jw} - e^{-ju-jv-jw} \right\} \quad (2.22) \\
 &= \text{const} \cdot \sum e^{\pm ju \pm jv \pm jw}
 \end{aligned}$$

In turn, the specific forms of E_z in (2.4) and H_z in (2.9) can be represented as (2.23).

$$\begin{cases} H_z^{TE} = \text{const} \cdot \sum e^{-jk\hat{k} \cdot r} \\ E_z^{TM} = \text{const} \cdot \sum e^{-jk\hat{k} \cdot r} \end{cases} \quad (2.23)$$

where:

$$r = x\hat{x} + y\hat{y} + z\hat{z}, \hat{k} = \{k_x\hat{x} + k_y\hat{y} + k_z\hat{z}\}/k \text{ and } k_x = \pm \frac{m\pi}{a}, k_y = \pm \frac{n\pi}{b}, k_z = \pm \frac{p\pi}{d}$$

The crucial terms above are the \pm signs that need to be permuted in order to obtain different plane wave terms [13]. Each term above is thus seen to represent an individual plane wave propagating in the \hat{k} direction, meaning that (2.23) symbolises a sum of eight plane waves for both TE and TM modes. The only exception here is when one of the indices is zero; only four plane waves are then evident. Once the allowable and existing modes have been

calculated using (2.14) for both TE and TM modes, the corresponding angle of arrival of the plane waves can be calculated from (2.24).

$$\varphi = \arctan\left(\frac{k_y}{k_x}\right), \theta = \arctan\left(\frac{\sqrt{k_x^2 + k_y^2}}{k_z}\right) \quad (2.24)$$

Fig. 2.10 depicts a series of figures concerning the angle of arrival of plane waves in the University of Liverpool RC as a function of frequency. The lines displayed on each three dimensional traces represent the incoming arrival towards an origin (in this case a fictitious unit sphere), and the small patches can be thought of as parts of the associated wavefronts [13] - a simplification in order to visualise.

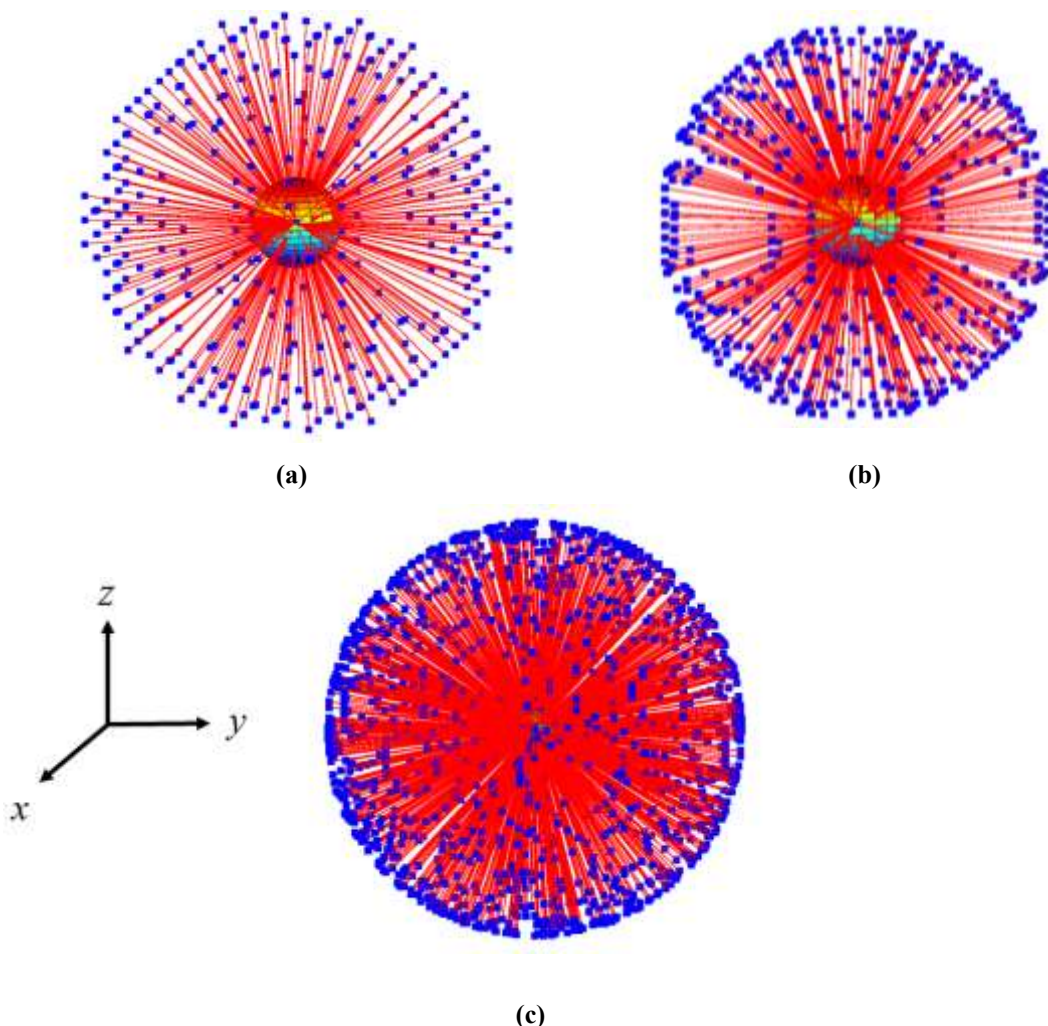


Fig. 2.10: Plane wave angle of arrival - (a) 200 - 225 MHz, (b) 400 - 410 MHz and (c) 900 - 905 MHz

From Fig. 2.10 it can be seen that the angle of arrival comes from every conceivable direction over the unit sphere. With increasing frequency it can be seen that a higher density of waves are apparent in a smaller band each time. The exact statistical nature of such plots was provided in [13], confirming a uniform distribution of angle of arrivals exists providing enough modes are excited (sufficiently large band). A uniform distribution of angle of arrivals means that a plane wave (with subsequent polarisation) will arrive from any direction over the unit sphere with an equal probability. This is how measurement procedures in the RC are simplified, as then it should not matter how a receive antenna is orientated and the subsequent direction of its radiation pattern.

A table concerning the number of modes and subsequent number of plane waves in various sub-bands in the University of Liverpool RC is provided in Table II, and confirms that for increasing frequency we have an ever richer number of modes and plane waves available.

Table II: The number of modes and plane waves in University of Liverpool RC

Frequency sub-bands (MHz)	Number of modes	Number of plane waves
200-225	87	620
400-410	122	924
900-910	643	4992
1940-1950	1866	14776
2400-2410	1930	15384

Real environments it should be stressed will subtly differ from the isotropic nature of the RC. An antenna operating in a real environment may have a preferred orientation, and in outdoor environments they may have a larger probability of waves coming from close to horizontal [14]. Real environments are also stated to have a larger amount of vertically polarised waves as most base stations are vertically polarised, representing a ‘cross polarised power discrimination’ (XPD), which can differ in different real environments [14]. For measurements in real environments this can be problematic, as any results obtained will then be a function of the environment in which they were undertaken and may not be repeatable.

The specific advantage of the RC is that statistically repeatable results have been demonstrated [15], outweighing the fact that the RC isotropic environment has no true

counterpart in reality. However, it can be argued that if a terminal in a real environment is used with arbitrary orientations, then it can approach what is witnessed in the RC [14]. With respect to the specific modes that will be excited in the chamber and the subsequent number of plane waves during measurements, in practice this will depend upon the value of the ‘mode bandwidth’.

2.5 Average Mode Bandwidths

In a RC, theoretically a mode will only be excited when a source excites the chamber at a frequency corresponding to the exact frequency of the resonant mode [13]. This would imply however that the Q (Quality) factor of the mode is infinite [13]. In reality, the mode Q factor is finite in value and the mode will exhibit a certain ‘bandwidth’- this implies that the modes do not have an infinite cut-off and this gives rise to the ‘bandwidth’ term. The bandwidth can be defined as: ‘*The bandwidth over which the excited power in a particular cavity mode with resonance frequency f_0 is larger than half the excited power at f_0* ’ [11].

The ‘average mode bandwidth’ (Δf) is the average of the mode bandwidths of all the modes excited about an excitation frequency (f), meaning that at a given (f), modes may be excited in the range [13]:

$$f - \Delta f / 2 \leq f_{res} \leq f + \Delta f / 2 \quad (2.25)$$

where: $\Delta f = f / Q$ and Q = the chamber Q factor. The theory and definitions here are analogous to the theory and definitions that can be found in [16]. Therefore, the average mode bandwidth can be found from knowledge of the measured chamber Q factor or it can be deduced from (2.26) and (2.27) after consultation with [11].

$$\Delta f = \frac{c^3 \times \eta_{RAD_TX} \times \eta_{RAD_RX}}{16\pi^2 V f^2 G_{net}} \quad (2.26)$$

where: V = the inside volume of the chamber, η_{RAD_TX} is the radiation efficiency of the transmitting antenna (defined as the total radiated power to net power accepted by the antenna) and η_{RAD_RX} is the radiation efficiency of the receiving antenna. G_{net} can be found from (2.27).

$$G_{net} = \frac{\langle |S_{21}|^2 \rangle}{(1 - |S_{11}|^2) \times (1 - |S_{22}|^2)} \quad (2.27)$$

where: $\langle \rangle$ symbolises the average of the scattering parameters, S_{21} is the transmission coefficient, and the two terms in the denominator represent the mismatch efficiencies of the transmitting and receiving antennas respectively.

Fig. 2.11 depicts both the measured average mode bandwidth in an ‘empty’ scenario (just containing transmit and receive antennas) and a ‘loaded’ scenario in the University of Liverpool chamber (dimensions $a = 3.6$ m, $b = 4$ m and $d = 5.8$ m). In both scenarios the receiving antenna is a log periodic antenna, and the transmitting antenna is a large Vivaldi antenna; both with known efficiency values. In the ‘loaded’ configuration, the chamber has been loaded with two pieces of anechoic absorber in two corners of the chamber to illustrate the effect this has on the average mode bandwidth. The average mode bandwidth is important to know because in measurement situations it governs the channel characteristics in the chamber. For example, it can control whether the fading channel is frequency flat or frequency selective. A further discussion on the channel characteristics with a view to measurements can be found in [17]. The average mode bandwidth and thus the channel characteristics can be controlled by ‘loading’ the chamber as the results of Fig. 2.11 suggest.

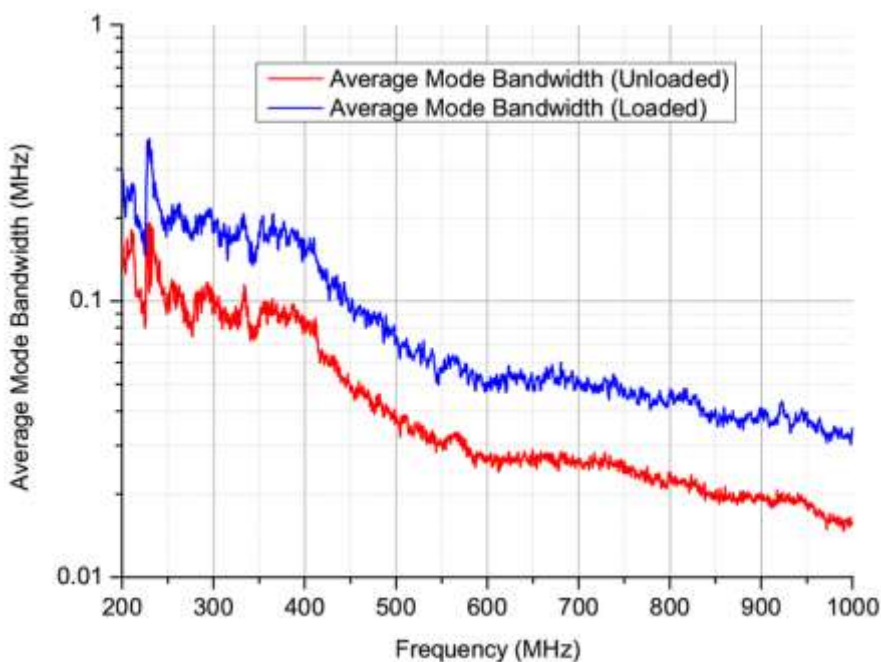


Fig. 2.11: Measured average mode bandwidths in University of Liverpool RC

From Fig. 2.11 it can be seen that the average mode bandwidth is slightly decreasing in size for increasing frequency, albeit in a relatively small scale. Fig. 2.11 would suggest that the window in which subsequent modes can be excited grows smaller at higher frequencies. This should not be too problematic however, as the small mode bandwidth will be offset by the high mode density that exists at higher frequencies, meaning that many modes can still be excited. The values of the average mode bandwidth are smaller here as compared with [18], which is a consequence in part of the difference between very large and small reverberation chambers. The curves do not appear to be entirely smooth because they have been deduced using measured data with a finite number of points (718 measured samples).

Further, the decreasing trend of the plot would also suggest that the Q factor of the chamber would increase for increasing frequency from the relation stated under (2.25). This aspect (Q factor) we will move on to assess next.

2.6 Chamber Quality (Q) Factor

It is well known that the Q factor describes the rate at which a system at resonance loses energy due to its conversion to other forms (e.g. heat). As previously defined in section 2.5, when considering a single resonance, a low Q system will have a large bandwidth and will dissipate energy very rapidly. When we think of an RC, it is a multimode facility, but the concept of the Q factor is still important as it describes information as to the overall losses that exist within the facility for a given set up.

The reference works on the reverberation chamber Q factor was published by Corona in 1980 [19] and Hill in 1994 [20]. Hill picked up from Corona's earlier work and proceeded to derive in detail the multiple mechanisms that contribute to a chambers' total Q factor. Hill defined five separate loss terms to exist:

- 1) Wall losses (Q_1)
- 2) Losses due to aperture leakage (Q_2)
- 3) Losses due to absorption in any loading objects in the chamber (Q_3)
- 4) Antenna losses (Q_4)
- 5) Losses due to water vapour absorption (Q_5 but only at frequencies > 18 GHz).

In terms of the mathematics, the total Q factor (Q) and separate loss mechanisms can be briefly summarised as follows [20].

$$Q = \omega U_s / P_d \quad (2.28)$$

where: U_s = steady state energy and P_d = power dissipated.

$$U_s = WV \quad (2.29)$$

where: V = volume of the cavity and W = energy density.

$$W = \epsilon_0 E^2 \quad (2.30)$$

where: ϵ_0 = permittivity of the medium in the cavity (free space) and E = RMS electric field.

The power density (S_c) in the cavity can also be expressed as (2.31).

$$S_c = \frac{E^2}{\eta_0} \quad (2.31)$$

where: η_0 = intrinsic impedance of the medium in the cavity.

The separate loss terms (Q_1) to (Q_4) from [20] can be stated as (2.32), (2.33), (2.34) and (2.35) respectively.

$$Q_1 = \frac{3V}{2\mu_r S \delta} \quad (2.32)$$

where: $\delta = \sqrt{\frac{1}{\pi f \mu_w \sigma_w}}$, $\mu_r = \frac{\mu_w}{\mu_o}$. μ_w and σ_w are the permeability and conductivity of the wall material respectively, δ is the skin depth and S is the cavity surface area.

$$Q_2 = \frac{2\pi V}{\lambda \langle \sigma_a \rangle} \quad (2.33)$$

where: $\langle \sigma_a \rangle$ = averaged absorption cross section of the medium loading the chamber. For irregular shaped objects, this term could be complex to solve analytically. A measurement procedure to deduce this term can be found in [21].

$$Q_3 = \frac{4\pi V}{\lambda \langle \sigma_i \rangle} \quad (2.34)$$

where: $\langle \sigma_i \rangle$ = average transmission cross section of any apertures.

$$Q_4 = \frac{16\pi^2 V}{m\lambda^3} \quad (2.35)$$

where: m = the impedance mismatch factor ($m = 1$ for a matched load).

In steady state conditions, the power transmitted into the chamber (P_t) is required to be equal to the power dissipated by the loss mechanisms that may exist in a given chamber configuration. Therefore:

$$P_t = P_d \quad (2.36)$$

By substituting (2.28), (2.29), (2.31) into (2.36), the power density in the cavity can be re-written as (2.37).

$$S_c = \frac{\lambda Q P_t}{2\pi V} \quad (2.37)$$

By use of an impedance matched antenna, the received power (P_r) is stated in [20] to be a product of the effective area $\lambda^2 / 8\pi$ and the received power can be expressed as (2.38).

$$P_r = \frac{\lambda^3 Q}{16\pi^2 V} P_t \quad (2.38)$$

Solving (2.38) in terms of Q yields the chamber Q factor in terms of the measured power ratio (P_r / P_t). Thus (2.39) represents a commonly used measured approach to obtain the chamber Q factor [20]. The equation assumes well matched and highly efficient antennas.

$$Q = \frac{16\pi^2 V}{\lambda^3} \times \frac{P_r}{P_t} \quad (2.39)$$

where:

$$\frac{P_r}{P_t} = \frac{\langle |S_{21}|^2 \rangle}{(1 - \langle |S_{11}|^2 \rangle)(1 - \langle |S_{22}|^2 \rangle)} \quad (2.40)$$

The terms $(|S_{11}|)$ and $(|S_{22}|)$ represent the reflection coefficients of the transmitting and receiving antennas respectively. In (2.40) they are assumed to be acquired in an AC. Furthermore, (2.40) also assumes that any cable losses are neglectable as a result of calibrating the system.

An alternative representation of the loss terms in (2.32) to (2.35), derived in terms of the average mode bandwidth instead of Q of the modes can be found in [22]. As stated earlier, this is also a representative means of establishing the Q factor of a given chamber. Fig. 2.12 depicts the measured Q factor of the University of Liverpool RC in both unloaded and loaded scenarios. The results have been acquired from measured data with a finite number of measured samples (718); hence they are not entirely smooth.

A result derived from the average mode bandwidth method is also supplied for comparison in Fig. 2.13.

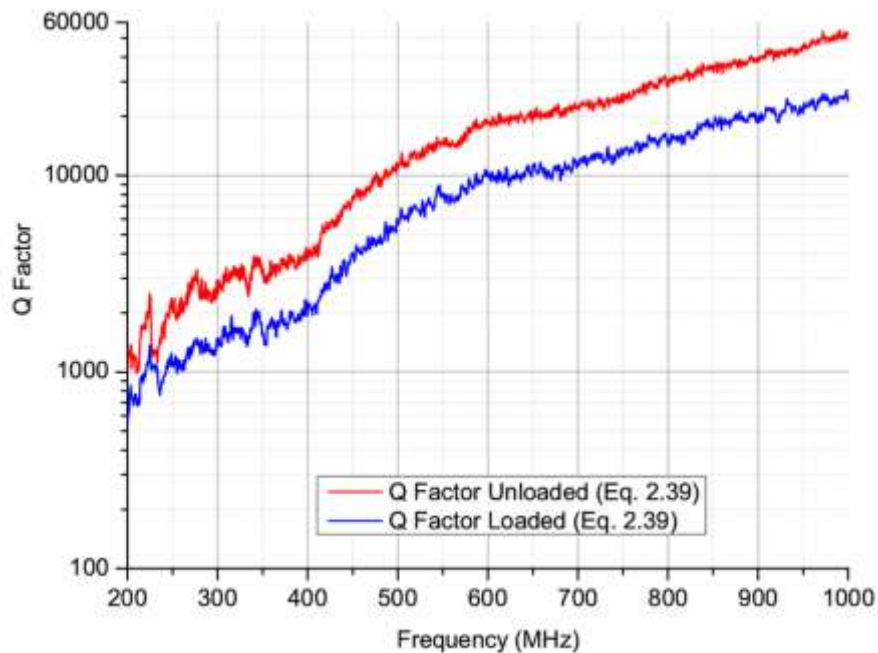


Fig. 2.12: Measured Q factor University of Liverpool RC from (2.39)

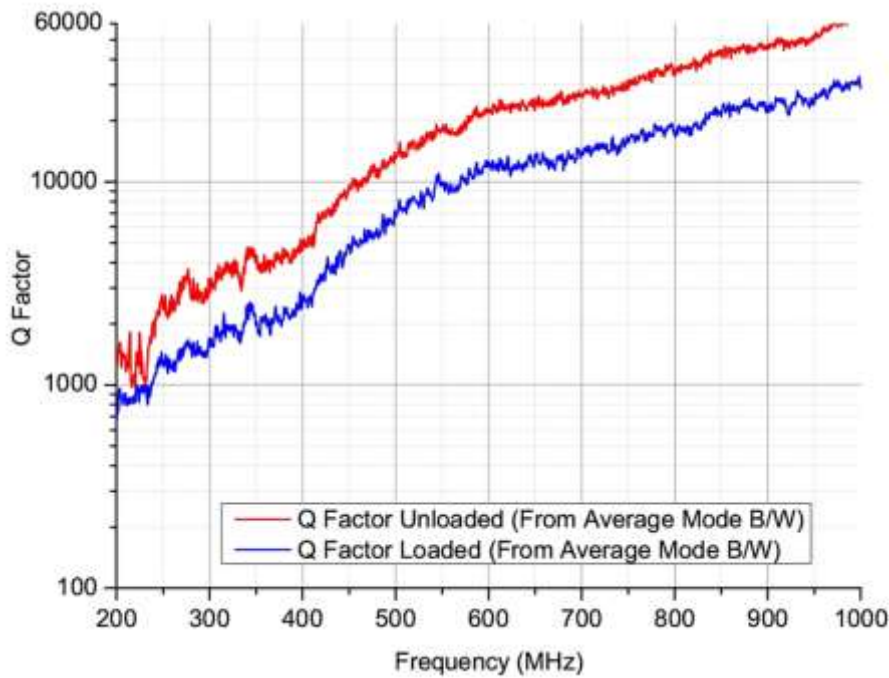


Fig. 2.13: Measured Q factor University of Liverpool RC from average mode bandwidths

Comparing Fig. 2.12 and 2.13 we can see that both methods yield similar values for the chamber Q factor. Further, from this similarity, it is possible to conclude that the average mode bandwidth values from Fig. 2.11 would appear accurate. It is also worthy to acknowledge at this stage that the measured Q factor values will have some contribution from the antennas used in the measurement (irrespective of efficiency).

A very recent communication in [8] discussed this point and concluded that an assessment of the chamber time constant to determine the chamber Q, instead of the direct frequency domain measurement of (2.39) could diminish the contribution of the antennas involved, leaving just the effect of the chamber alone.

2.7 Statistical Forms

The statistical forms of RC measured data are very important. As previously stated, in an operational environment, a typical mobile terminal will seldom ‘see’ a base station. Therefore, the communication link between terminal and base station is maintained in a NLOS type of propagation environment most amount of the time. The NLOS propagation environment in mobile communications is well known to exhibit Rayleigh fading properties [23], and it is this that we would like to be able to replicate. The RC has been shown to

emulate similar statistical properties as found in the NLOS urban and indoor environment; this is how it is appropriate for use, and attempts to provide a realistic characterisation of terminals in this type of environment.

The RC statistical forms have received much treatment over the years. Kostas and Boverie examined the forms back in 1991 [24], and concluded that each of the three measured components of the electric field (voltage) manifest themselves as being Rayleigh distributed (which is the same as the Chi squared distribution with six degrees of freedom). From there they concluded that the power density is exponentially distributed [24].

From [14] it is further stated that as long as the LOS is absent and enough planes waves exist, the in-phase and quadrature components of the received complex signal are normally distributed (complex gaussian), and the phase is uniformly distributed over 2π . However, it should be noted that if any remote LOS path were to exist, then the statistical distributions, specifically the magnitudes, will be altered (see section 2.8).

The purpose of this sub-section is to briefly discuss and examine the theoretical statistical forms in the University of Liverpool RC, to visually assess how the chamber complies with the ideal NLOS theoretical forms. This sub-section is further divided into six separate sections to discuss the method of analysis and to individually represent the magnitude, complex signal, power and phase information (respectively) in a NLOS scenario. Concluding remarks and recommendations on the method of analysis are presented in section 2.7.6.

The statistical forms issued herewith have all been configured with a non-line of sight path between source and receiver, based upon practical measurements in the University of Liverpool RC. The measurement details for these tests are portrayed in Table III.

Table III: Statistical forms measurement details

Parameter	Description
Source antenna	Vivaldi
Receive antenna	Log periodic (HL223)
Frequencies (MHz)	100 - 1000
Number of frequency data points	801
Stirring sequences	1 degree mechanical stirring Polarisation stirring
Vector Network Analyser (VNA)	Anritsu 37369A
Source power (dBm)	-7
Chamber loading	None

2.7.1 Statistical Methods of Analysis

Two primary methods that can be chosen as characterisation techniques to visually represent the statistical forms of the measured data are the cumulative distribution function (cdf) and the probability density function (pdf). These two aspects can be theoretically and mathematically defined as follows:

Since a probability cannot be negative, all probability density functions must be positive or zero [25].

$$f(g) \geq 0 \quad (2.41)$$

The probability density functions are not always continuous or even finite; however, since the random variable g must lie between $-\infty$ and ∞ , the relationship in (2.42) must hold [25].

$$\int_{-\infty}^{\infty} f(g) dg = 1 \quad (2.42)$$

From the above definitions, we can assess the cumulative distribution function properties as the probability P that a random variable G lies between a and b as an integral over f in the form of (2.43).

$$P(a < G \leq b) = \int_a^b f(g) dg \quad (2.43)$$

Thus the cumulative distribution function must exhibit the following:

1. $F(g)$ is a non-decreasing function of g
2. $F(-\infty) = 0$
3. $F(\infty) = 1$

2.7.2 Statistical Distribution of Measured Magnitudes

As stated previously, the ideal form of any magnitudes obtained in a NLOS scenario manifest themselves as being statistically Rayleigh distributed. The following plots depict the cdf and pdf forms of practically measured magnitudes against a theoretical Rayleigh form as a means of comparison. However, for brevity, only plots relating to measured data at 600 MHz and 800 MHz are presented (chosen arbitrarily where the frequency is high enough for the cavity to be considered electrically large). The theoretical Rayleigh distributions have been defined in (2.44) and (2.45) according to [26].

For the cdf:

$$F(x) = (1 - e^{(-x^2/2\sigma^2)}), x \in [0, \infty] \quad (2.44)$$

and for the pdf:

$$f(x) = \frac{x}{\sigma^2} e^{-x^2/2\sigma^2}, x \geq 0 \quad (2.45)$$

where σ = distribution shape parameter.

- All plots issued herewith are presented *as a visual means only*; no significance of the quality of the statistical fit is implied with the depiction of any plots.

Figs. 2.14 and 2.15 portray the cdfs of the measured magnitudes against a theoretical Rayleigh distribution at 600 MHz and 800 MHz respectively.

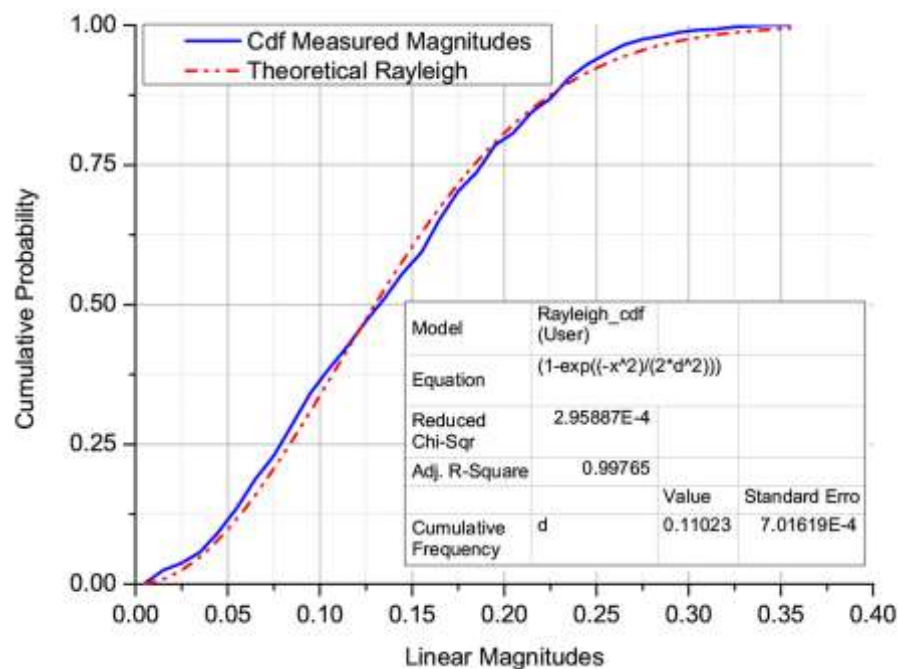


Fig. 2.14: Cdf of measured magnitudes Vs theoretical Rayleigh distribution at 600 MHz

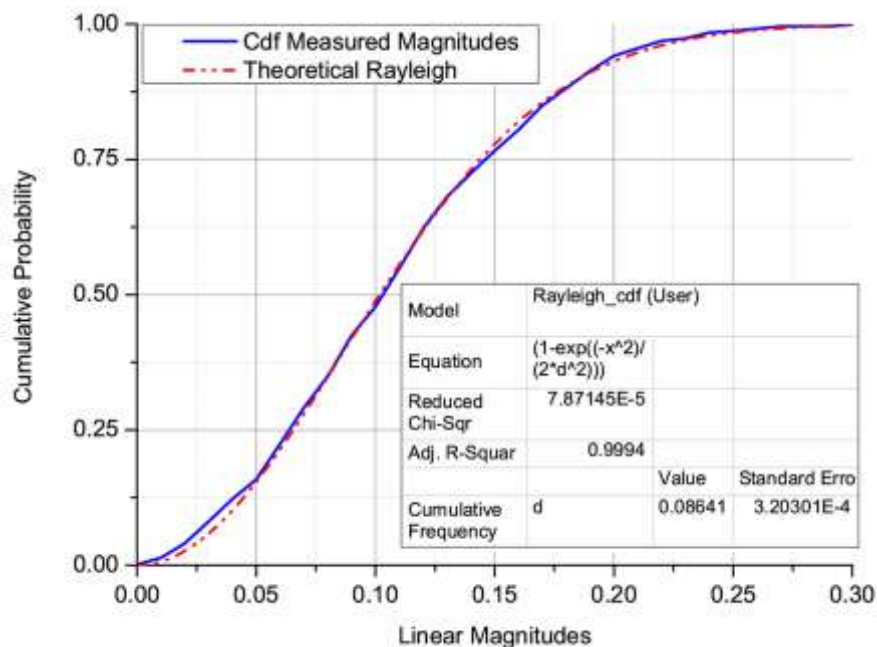


Fig. 2.15: Cdf of measured magnitudes Vs theoretical Rayleigh distribution at 800 MHz

The pdfs can be viewed in Figs. 2.16 and 2.17 at 600 MHz and 800 MHz respectively.

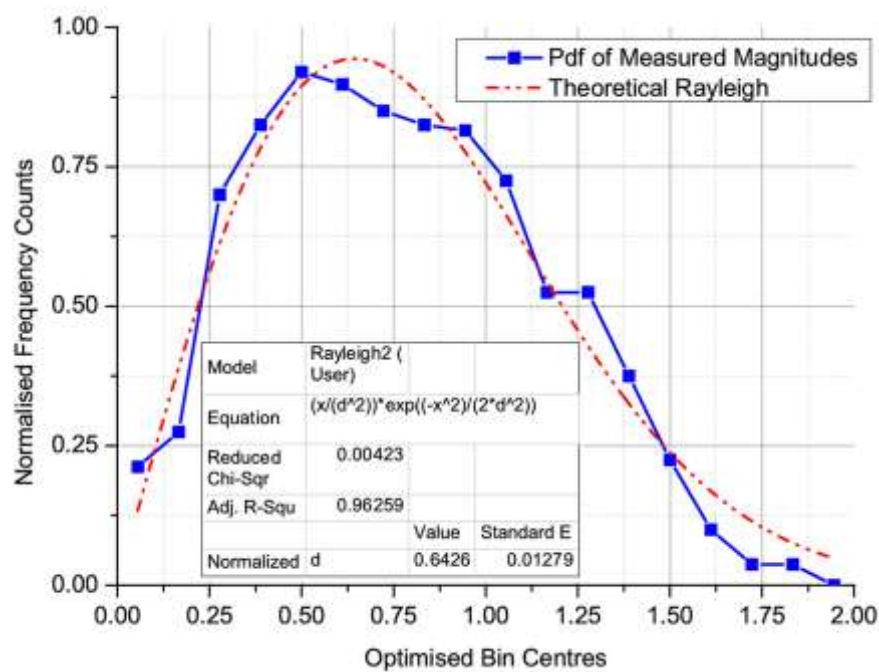


Fig. 2.16: Pdf of measured magnitudes Vs theoretical Rayleigh distribution at 600 MHz

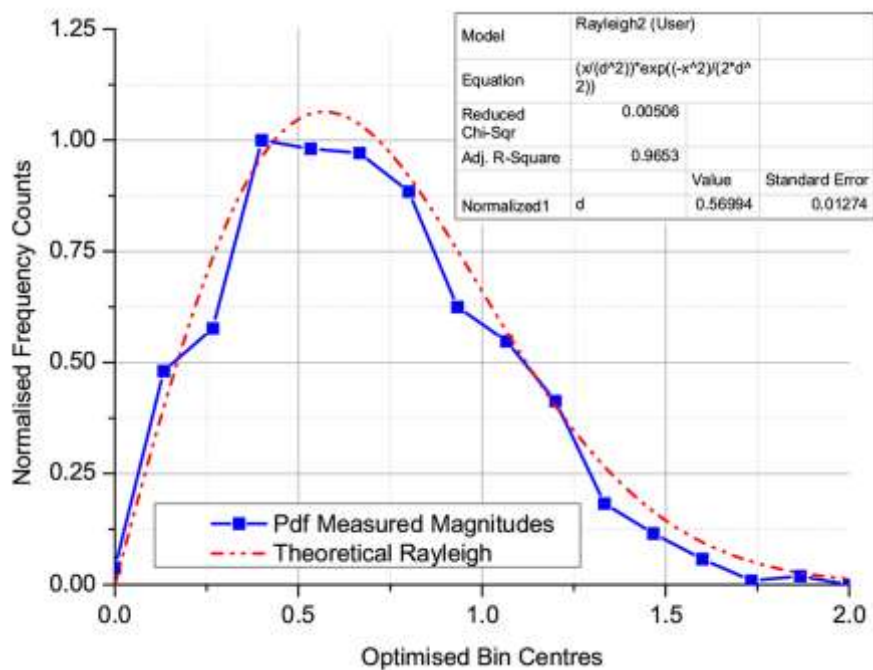


Fig. 2.17: Pdf of measured magnitudes Vs theoretical Rayleigh distribution at 800 MHz

2.7.3 Statistical Distribution of Complex Samples

As stated previously, the complex forms of any measured data (assuming NLOS), should manifest themselves as being normally distributed (complex gaussian). The following plots depict the cdf and pdf forms against their ideal forms as a means of visualisation; again, no significance of the quality of the statistical fit is to be implied. The theoretical normal distributions have been defined in (2.46) and (2.47) according to [26].

For the cdf:

$$F(x) = \frac{1}{2} \left[1 + \operatorname{erf}\left(\frac{x-\mu}{\sigma\sqrt{2}}\right) \right], x \in \mathfrak{R} \quad (2.46)$$

where: $\operatorname{erf}(x) = \frac{2}{\sqrt{\pi}} \int_0^x e^{-t^2} dt$ and is defined as the error function, μ = mean and σ^2 in this

(normal) distribution will represent the variance.

For the pdf:

$$f(x) = \frac{1}{\sigma\sqrt{2\pi}} e^{-(x-\mu)^2/2\sigma^2}, x \in \mathfrak{R} \quad (2.47)$$

where: μ = mean and σ^2 in this (normal) distribution will represent the variance.

Figs. 2.18 and 2.19 depict the cdfs of the measured complex data at 600 MHz and 800 MHz respectively against their theoretical forms.

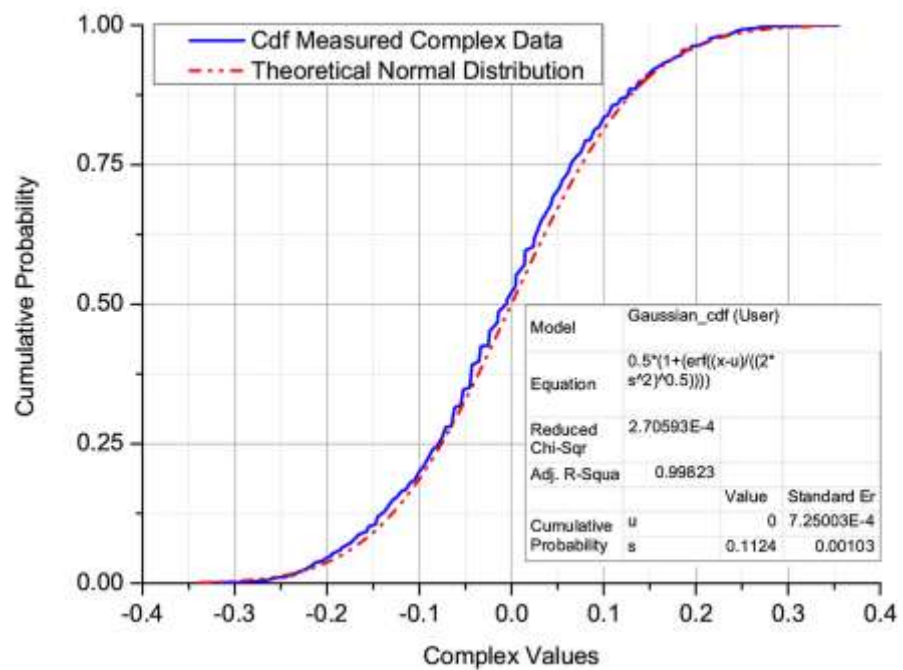


Fig. 2.18: Cdf of measured complex samples Vs theoretical Normal distribution at 600 MHz

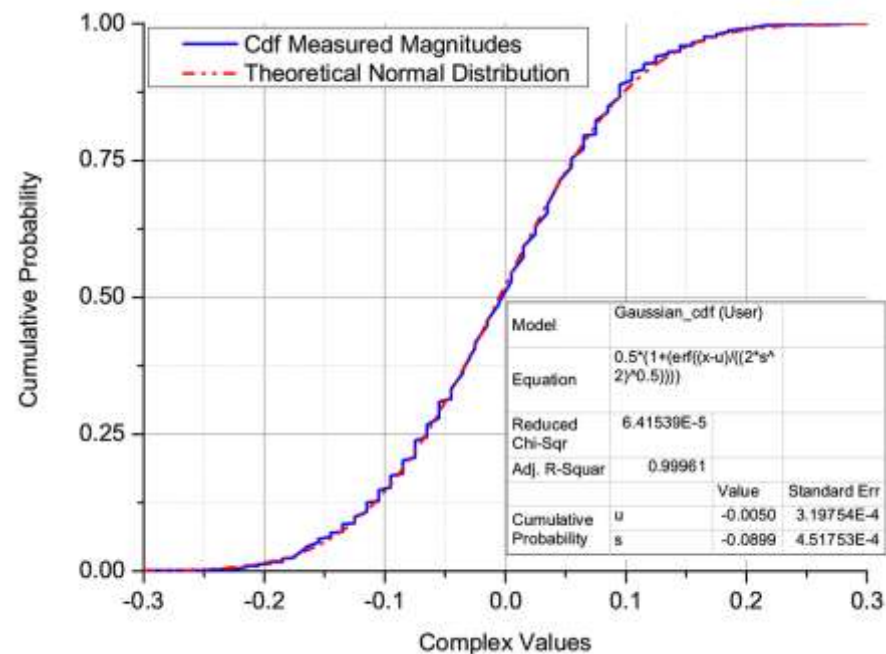


Fig. 2.19: Cdf of measured complex samples Vs theoretical Normal distribution at 800 MHz

The pdf forms of the measured complex samples at 600 MHz and 800 MHz can be viewed in Figs. 2.20 and 2.21 respectively.

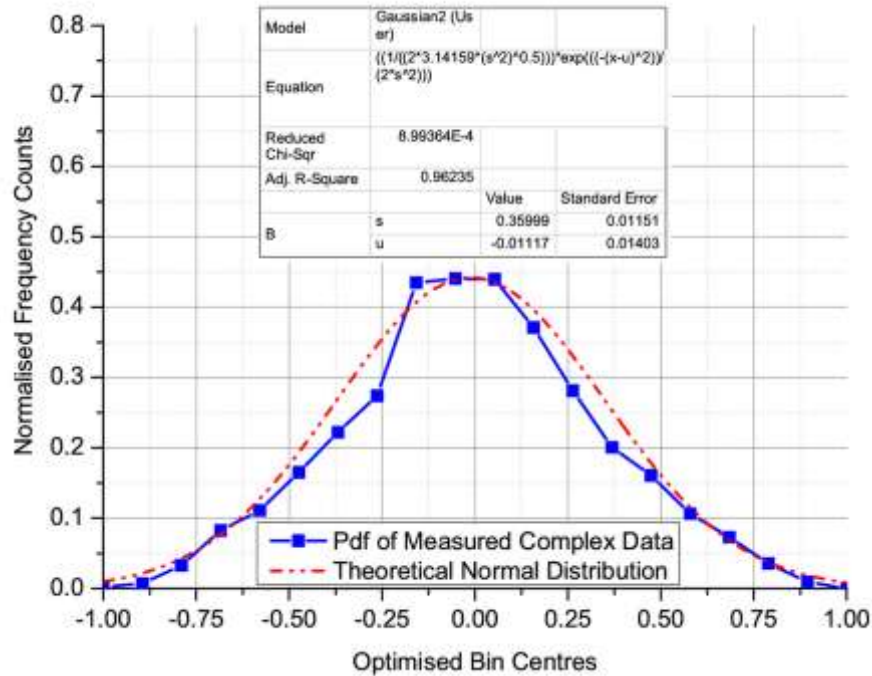


Fig. 2.20: Pdf of measured complex samples Vs theoretical Normal distribution at 600 MHz

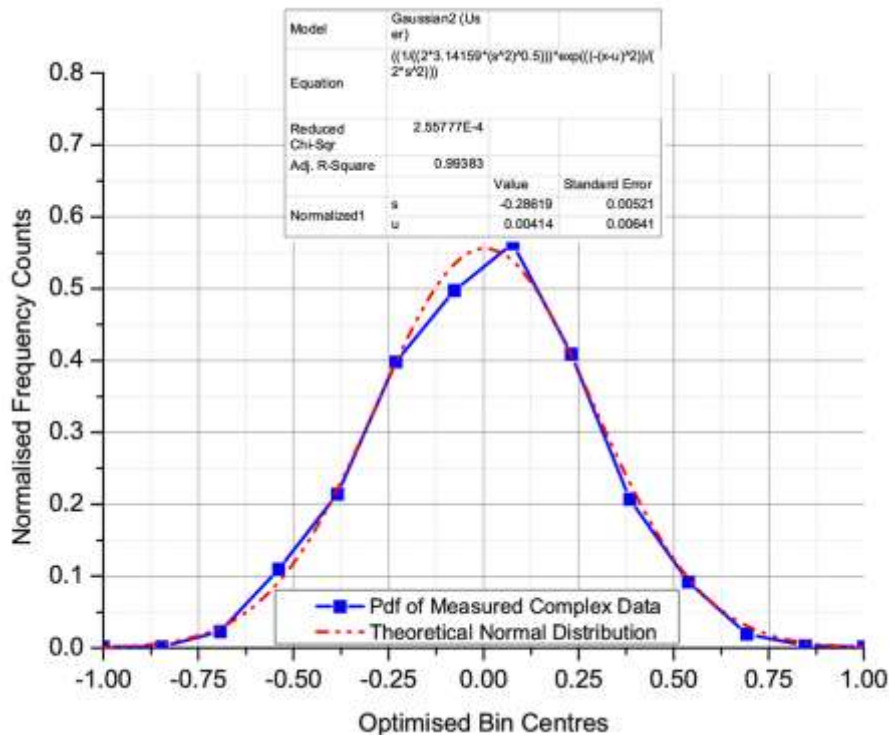


Fig. 2.21: Pdf of measured complex samples Vs theoretical Normal distribution at 800 MHz

2.7.4 Statistical Distribution of Measured Power

Again, as stated previously, the ideal statistical form of any power samples obtained in a NLOS scenario should ideally be exponentially distributed. This sub-section discloses the measured obtained power samples against the ideal theoretical cdf and pdf forms. These ideal forms have been defined according to [26]:

For the cdf:

$$F(x; \lambda) = \begin{cases} 1 - e^{-\lambda x}, & x \geq 0 \\ 0, & x < 0 \end{cases} \quad (2.48)$$

where: λ = distribution rate parameter.

For the pdf:

$$f(x; \lambda) = \begin{cases} \lambda e^{-\lambda x}, & x \geq 0 \\ 0, & x < 0 \end{cases} \quad (2.49)$$

Figs. 2.22 and 2.23 depict the cdfs of the measured power at 600 MHz and 800 MHz respectively against their theoretical forms.

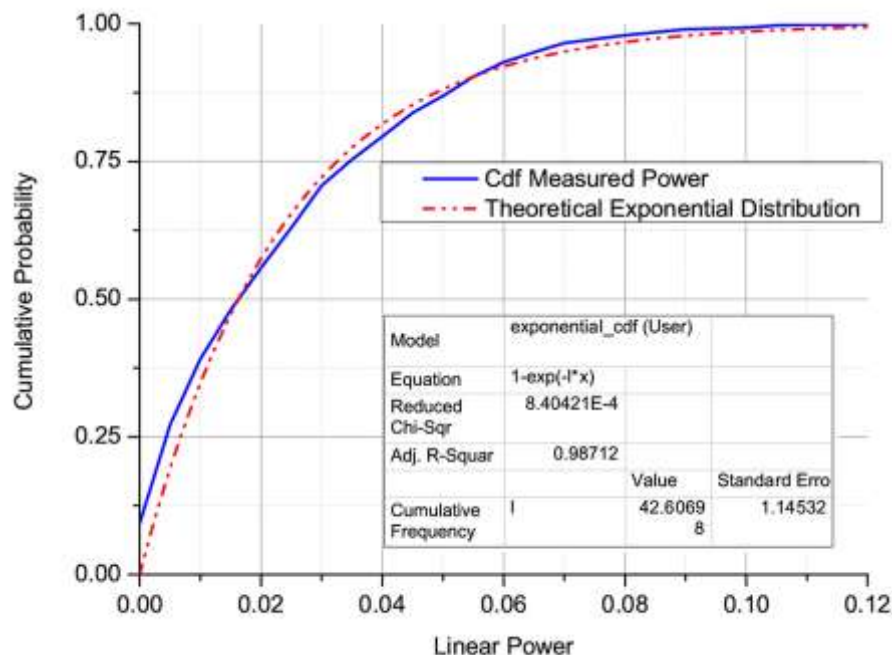


Fig. 2.22: Cdf of measured power Vs theoretical Exponential at 600 MHz

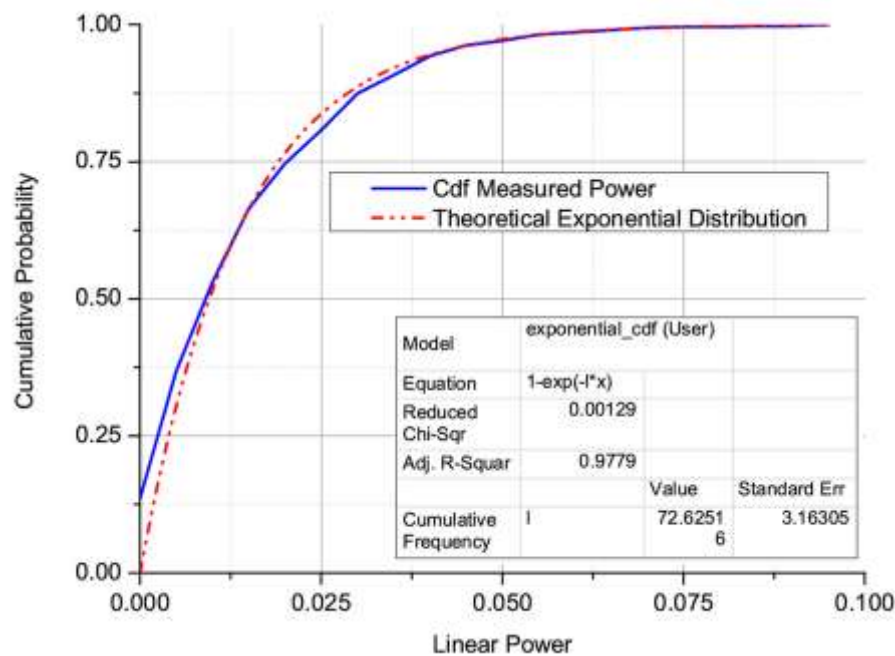


Fig. 2.23: Cdf of measured power Vs theoretical Exponential at 800 MHz

The pdf forms of the measured power at 600 MHz and 800 MHz can be viewed in Figs. 2.24 and 2.25 respectively.

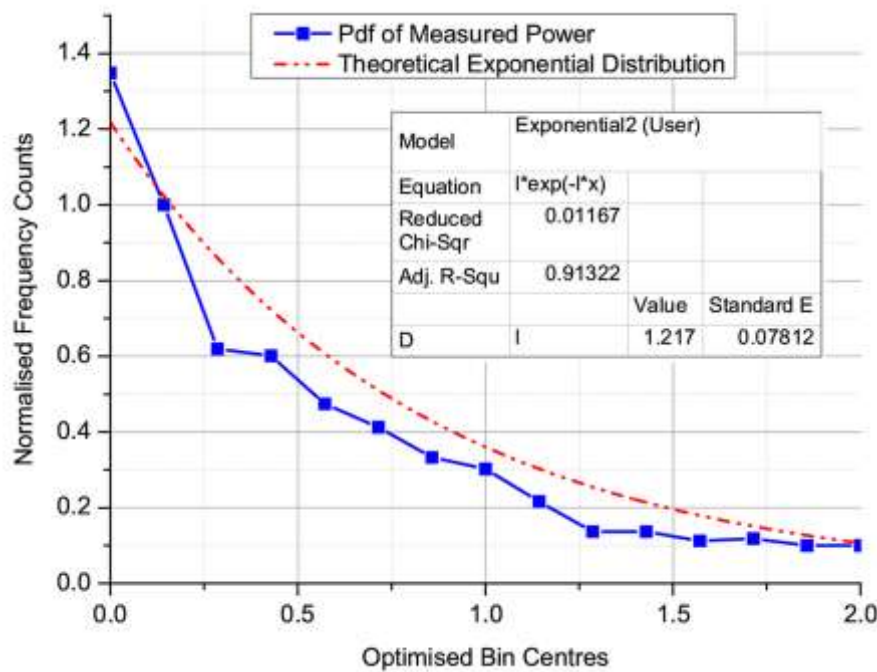


Fig. 2.24: Pdf of measured power Vs theoretical Exponential at 600 MHz

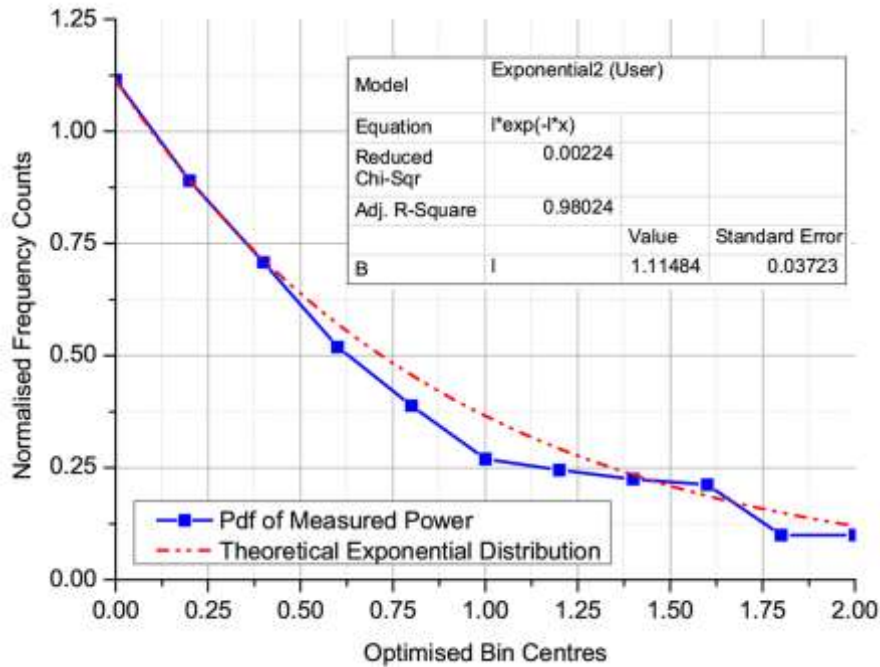


Fig. 2.25: Pdf of measured power Vs theoretical Exponential at 800 MHz

2.7.5 Statistical Distribution of Measured Phase

The phase information obtained from a NLOS scenario should be uniformly distributed. This section tests the uniformity of the measured phase information against their ideal theoretical forms. The theoretical cdf and pdf have been defined as follows [26]:

For the cdf:

$$F(x) = \begin{cases} 0, & x \leq a \\ \frac{x-a}{b-a}, & a < x \leq b \\ 1, & x \geq b \end{cases} \quad (2.50)$$

For the pdf:

$$f(x) = \begin{cases} \frac{1}{b-a}, & a < x < b \\ 0, & otherwise \end{cases} \quad (2.51)$$

The cdfs for the measured phase at 600 MHz and 800 MHz can be viewed in Figs. 2.26 and 2.27 respectively.

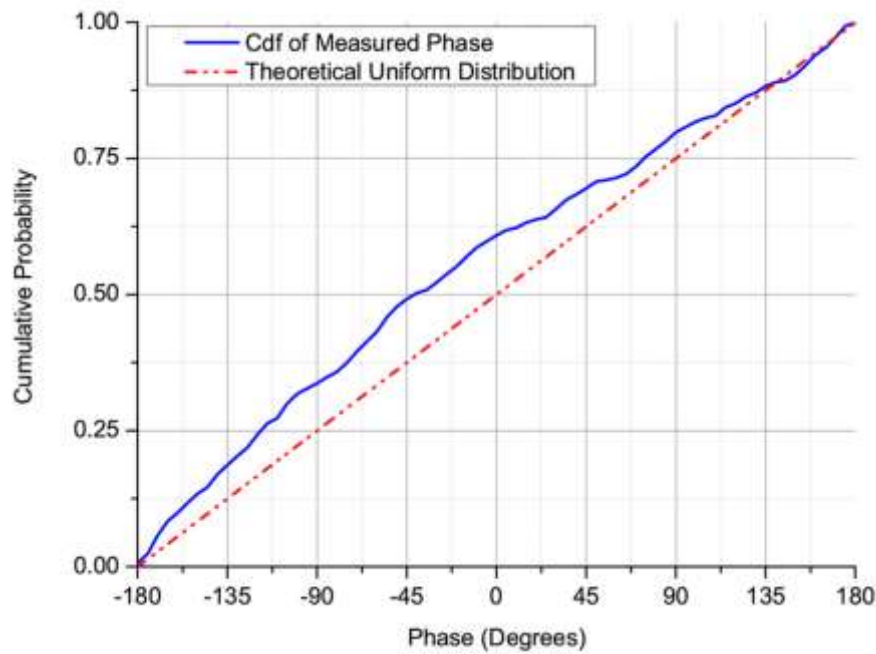


Fig. 2.26: Cdf of measured phase Vs theoretical Uniform at 600 MHz

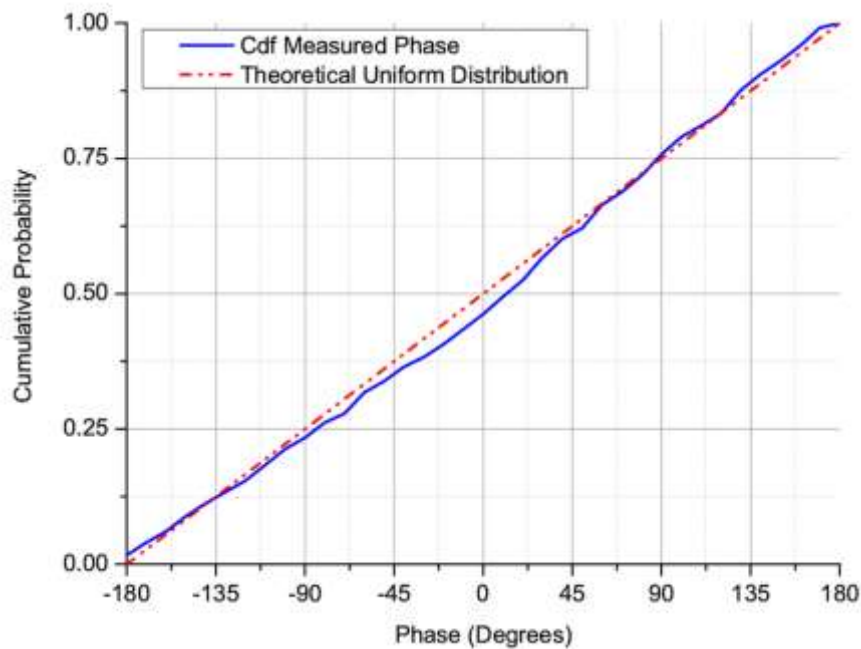


Fig. 2.27: Cdf of measured phase Vs theoretical Uniform at 800 MHz

The pdf forms of the measured phase at 600 MHz and 800 MHz can be viewed in Figs. 2.28 and 2.29 respectively. In each of the two plots the measured pdf has been offset slightly so its form can be clearly seen in comparison to the theoretical distribution.

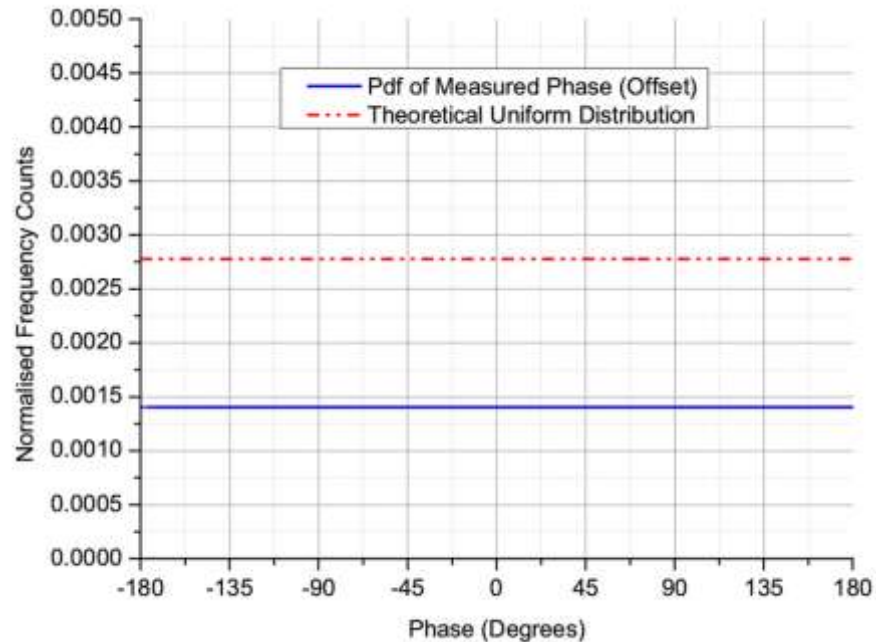


Fig. 2.28: Pdf of measured phase Vs theoretical Uniform at 600 MHz

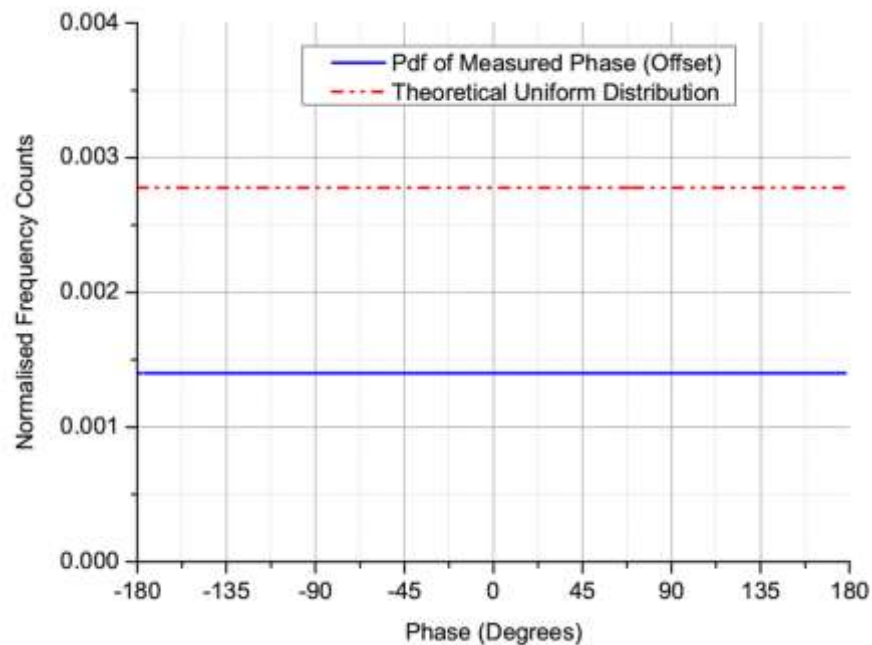


Fig. 2.29: Pdf of measured phase Vs theoretical Uniform at 800 MHz

2.7.6 Concluding Remarks and Recommendations

Assessing the measured and theoretical forms depicted in Figs. 2.14 to 2.29, one could be tempted to conclude that the trends between the measured and theoretical trends are very close, and be thus convinced that the measured data does correspond to the idealised forms. However, on the use of such graphical evidence alone, one must attach little weight to that evidence. Placing sole reliance on coefficient of determination analysis through curve fitting alone in determining statistical significance could be considered questionable as inferred on page 37.

The reason why such evidence could be considered questionable is because it fails to take into account the following recommended points:

- 1) The definition and testing of a null hypothesis
- 2) The assignment of a confidence interval in testing the null hypothesis
- 3) The acceptance and rejection of the null hypothesis based on (1) and (2)
- 4) The probability of a given result upon accepting or rejecting the null hypothesis
- 5) A comparison to other methods / results

In our case, points (1) to (5) must also be performed as a function of frequency, which as a consequence, does render the graphical techniques extremely time consuming. Statistical methods do exist however that attempt to satisfy the constraints highlighted above, and are aimed at deriving more confident outcomes.

One such technique is the ‘Kolmogorov Smirnov’ (KS) test [27]. This test, in a one sample format, is only valid for continuous cdfs and seeks to test the distribution of unknown samples against a hypothesised continuous distribution. When performed with tools such as Matlab, it will allow for the specification of a null hypothesis and the assignment of confidence intervals, it will also provide results concerning the acceptance or rejection of a null hypothesis and the probability in accepting or rejecting that null hypothesis. The downside to the method is that the hypothesised distribution must be fully specified, which is not always convenient to do given that any standard deviations, mean values and any other associated parameter concerned with the distribution are liable to change with changing frequency.

One technique that seeks to relax the requirements of the Kolmogorov-Smirnov test was developed by Lilliefors in 1967 and 1969 [28, 29]. The Lilliefors test compares the same test statistic as the Kolmogorov-Smirnov test, but relaxes the constraints on completely

specifying the hypothesised continuous distribution. When employed with Matlab, this statistical test allows for the testing of both normal and exponential distributions and could provide more of a reliable benchmark of statistical significance than the one sample KS test and curve fitting methods alone; such a test and methodology is therefore recommended. When it comes to the measured magnitudes in an RC, such a statistical test is not necessarily needed; there is a simpler and more straightforward procedure that can be applied: The Rician K factor.

2.8 Line of Sight (LOS) Elements

Statistically, if any line of sight path exists in a reverberation chamber, the Rayleigh distribution will be altered. The elements of multipath (stirred power) and any line of sight path (unstirred power) together will manifest itself as being Rician distributed if the unstirred power becomes dominant.

A definition of unstirred and stirred power can be stated as [30]:

“Unstirred power is the power that is coupled directly from a transmitting antenna to an antenna under test that undergoes minimal reflection or interaction with any mode stirrer”.

“Stirred power results from power radiating from a transmitting antenna that fully interacts with a mode stirrer. This also includes significant reflections from the chamber walls that interact with the paddle”.

A thorough discussion was presented in [30] which showed how the RC could be used to emulate a Rician environment if desired - this could prove advantageous where measurements in different statistical environments are concerned (for example, mobile phone antennas near to a base station).

However, for the majority of antenna terminal measurements in a reverberation chamber, the minimisation of any unstirred power and the promotion of a Rayleigh environment is of crucial importance for reasons previously discussed. Further, for measured quantities such as radiation and total efficiency, it has been shown that any unstirred power can represent a serious source of measurement uncertainty [31]. For these types of measurements therefore, unstirred elements must be crucially minimised.

The format of any unstirred multipath propagation in the RC has become better known as a Rician K factor. A full proof relating to the derivation of this quantity can be found in [30]; however, it will be briefly summarised as follows.

Any transmission measurement in a reverberation chamber essentially initiates a measured transfer function in the chamber, comprising of the chamber's physical and statistical properties. This measured transfer function ($|S_{21}|$) or ($|S_{12}|$), assuming the use of S - Parameters and depending on the measurement set up, can be stated to represent the sum of two components [30]: a direct component (d) and a component which constitutes the stirred energy in a chamber (s).

$$|S_{21}| = S_{21d} + S_{21s} \quad (2.52)$$

where: S_{21d} = the direct component and S_{21s} = the stirred component. If no stirred component exists (i.e. pure line of sight environment) then only a direct component will exist, such as what is present in an anechoic environment.

As the statistical investigation on the complex data yielded; under ideal reverberation chamber conditions (pure NLOS scenario), the complex transmission measured data should be normally distributed with a zero mean and identical variance.

$$\langle S_{21s} \rangle = 0 \quad (2.53)$$

where: $\langle \rangle$ signify the average of the said scattering parameters, and:

$$\text{var}[\text{Re}(S_{21s})] = \text{var}[\text{Im}(S_{21s})] = \langle [\text{Re}(S_{21s})]^2 \rangle = \langle [\text{Im}(S_{21s})]^2 \rangle = \sigma_R^2 \quad (2.54)$$

where: σ_R is essentially the standard deviation. The direct component (S_{21d}) on the other hand has a zero variance and a non-zero mean:

$$\text{var}[\text{Re}(S_{21d})] = \text{var}[\text{Im}(S_{21d})] = \langle [\text{Re}(S_{21d})]^2 \rangle = \langle [\text{Im}(S_{21d})]^2 \rangle = 0 \quad (2.55)$$

From (2.54) and (2.55), the variance of the real and imaginary components of S_{21} can be given as [30]:

$$\text{var}[\text{Re}(S_{21})] = \text{var}[\text{Im}(S_{21})] = \langle [\text{Re}(S_{21})]^2 \rangle = \langle [\text{Im}(S_{21})]^2 \rangle = \sigma_R^2 \quad (2.56)$$

Alternatively:

$$2\sigma_R^2 = \left\langle |S_{21} - \langle S_{21} \rangle|^2 \right\rangle \quad (2.57)$$

The mean value of S_{21} is related to the direct component as:

$$d_R = \langle |S_{21}| \rangle \quad (2.58)$$

Thus the Rician K factor (ratio of unstirred to stirred power) can be expressed fully as [30]:

$$K = \frac{d_R^2}{2\sigma_R^2} = \frac{\langle |S_{21}| \rangle^2}{\left\langle |S_{21} - \langle S_{21} \rangle|^2 \right\rangle} \quad (2.59)$$

The following figures depict results for the Rician K factor as a function of frequency in the University of Liverpool RC, calculated from (2.59). For frequencies up to and including 1000 MHz, Table III again details the measurement parameters used in the investigation, with the measurement set-up being shown in Fig. 2.30. The results presented in this subsection are representative of what can be termed the ‘average Rican K factor’, which is an average of the K factor in (2.59), measured for two transmit polarisations (used in polarisation stirring). The results presented have also been frequency stirred by 25 MHz to improve the readability.

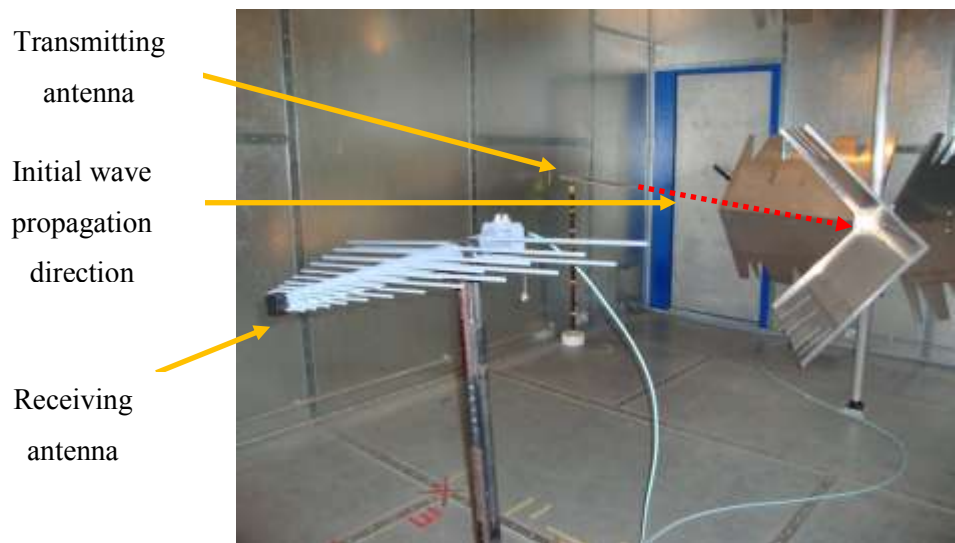


**Fig. 2.30: Rician K Factor measurement set-up
(100 MHz - 1000 MHz)**

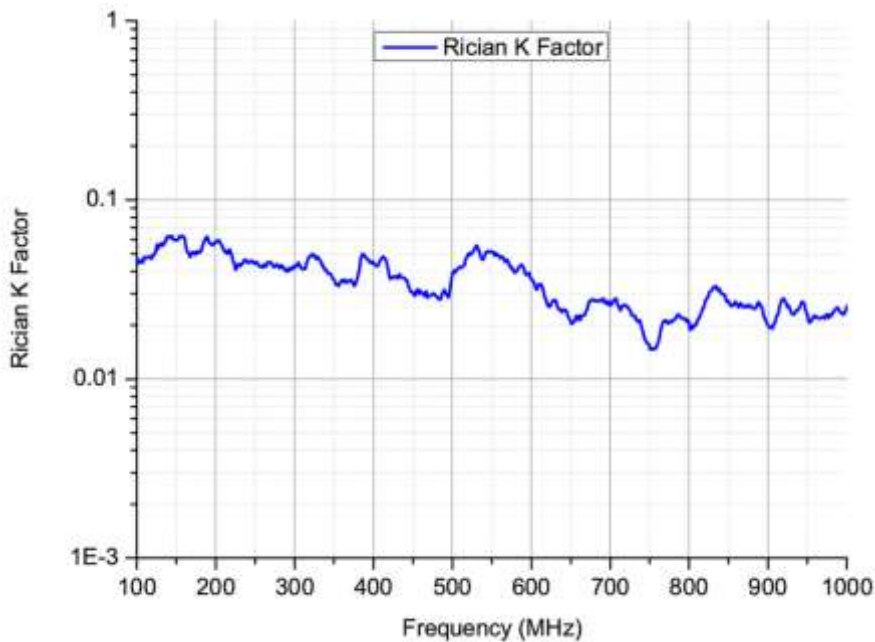


Fig. 2.31: Rician K Factor from 100 MHz to 1000 MHz

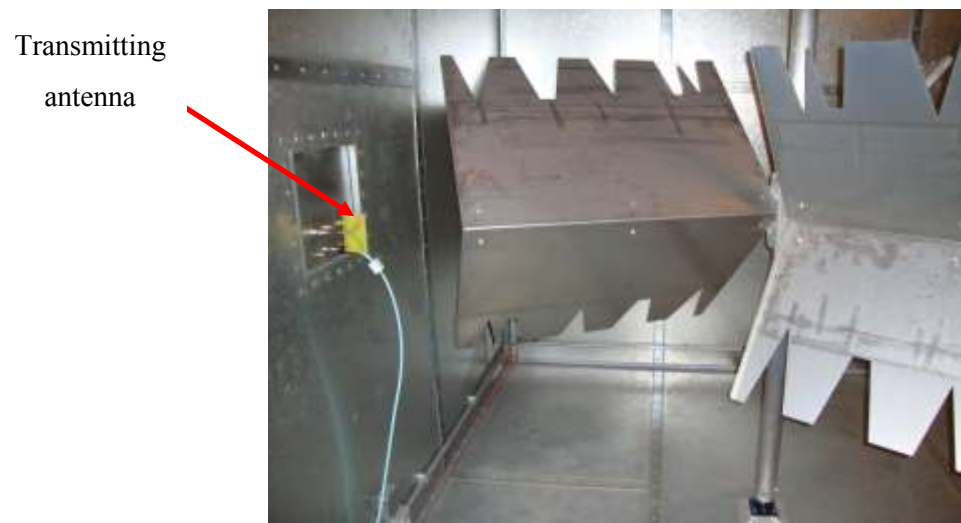
From Fig. 2.31 it can be seen that the stirred power in the chamber is dominant as the measured K factor value is much less than 1. Fig. 2.31 proves that any LOS path is very small and as a result it can be confirmed that the statistical form of the magnitudes will tend towards a Rayleigh distribution as opposed to a Rician distribution (ideal Rayleigh distribution: $K \rightarrow 0$). Furthermore, the scattered nature of the power will help to yield the ideal forms of angle of arrival as discussed in section 2.4. The result also confirms that the placement of the transmitting and receiving antenna in Fig. 2.30 does not give rise to any significant proportion of direct power being received. Nevertheless, a different placement of transmitting antenna should be tested to see if the K factor is affected. Furthermore, an omnidirectional antenna should also be tested on the receiving side in addition to the directional antenna type in Fig. 2.30 to see the overall effect on the K factor.

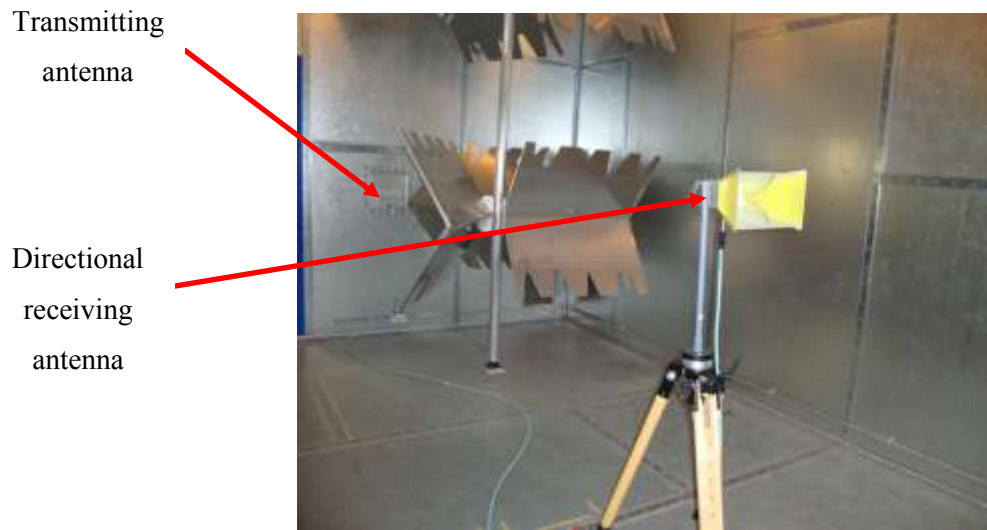
Table IV details the measurement parameters for this parallel investigation.

Table IV: Measurement parameters for K factor parallel investigation

Parameter	Description
Frequencies (MHz)	1000 - 6000
Frequency data points	1601
Transmitting antenna	Small (homemade) Vivaldi
Receiving antenna (directional)	Rohde & Schwarz dual ridge horn (HF 906)
Receiving antenna (omni-directional)	Small (homemade) Monopole
Chamber loading	None
Source power (dBm)	-7
Stirring sequences	1 degree mechanical stirring Polarisation stirring 25 MHz frequency stirring

Fig. 2.32 illustrates the different placement of the transmitting antenna and Fig. 2.33 depicts the typical measurement set-up.

**Fig. 2.32: Rician K Factor measurement set-up****(1000 MHz - 6000 MHz)**



**Fig. 2.33: Rician K Factor measurement set-up
(1000 MHz - 6000 MHz)**

The small Vivaldi (transmitting) antenna is seen in Fig. 2.32 to be located on a fixed rigid cable right behind the mechanical stirring paddles. The question now is: Will this result in a significantly different K factor?

The K factor results for the directive receiver (pictured in Fig. 2.33) and the omni-directional receiver are presented together in Fig. 2.34.

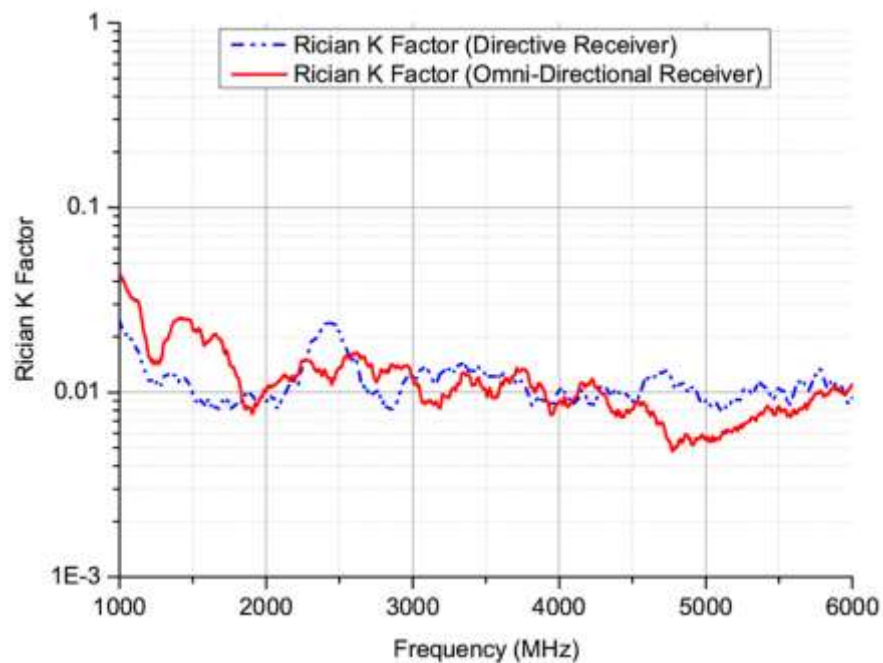


Fig. 2.34: Rician K Factor from 1000 MHz to 6000 MHz

From Fig. 2.34 it can be seen that the different placement of antenna has no significant effect on the proportion of unstirred power; the chamber performs equally well. Further, it can also been seen that irrespective of the receiver type (directional or omni-directional), the chamber also performs consistently well - no significant proportion of direct power is evident. Figs. 2.31 and 2.34 therefore prove that a rich isotropic Rayleigh scattering environment exists in the chamber across a wide frequency range.

We can further test this point with the issue of scatter plots in Figs. 2.35 and 2.36, where it can be seen that the scatter plots are consistent with the K factor results of Fig. 2.34.

At this stage it should be noted that antennas in the chamber can be pointed towards each other if a Rician statistical environment is desired. In this situation, the K factor becomes proportional to the polarisation and directivities of the antennas involved and also the separation distance between them [30]. K factors of 10 and greater have been experimentally confirmed in [30].

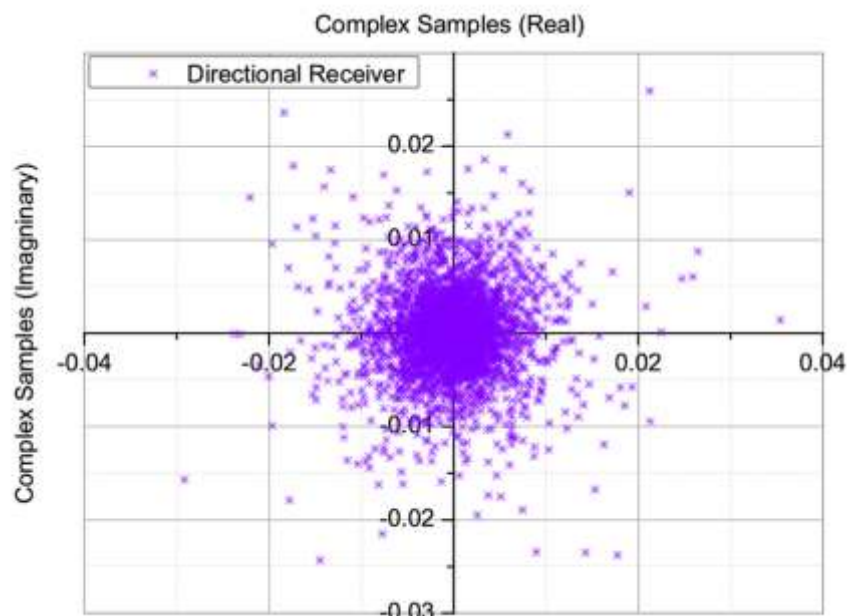


Fig. 2.35: Scatter plot from directional receiver 1000 MHz to 6000 MHz

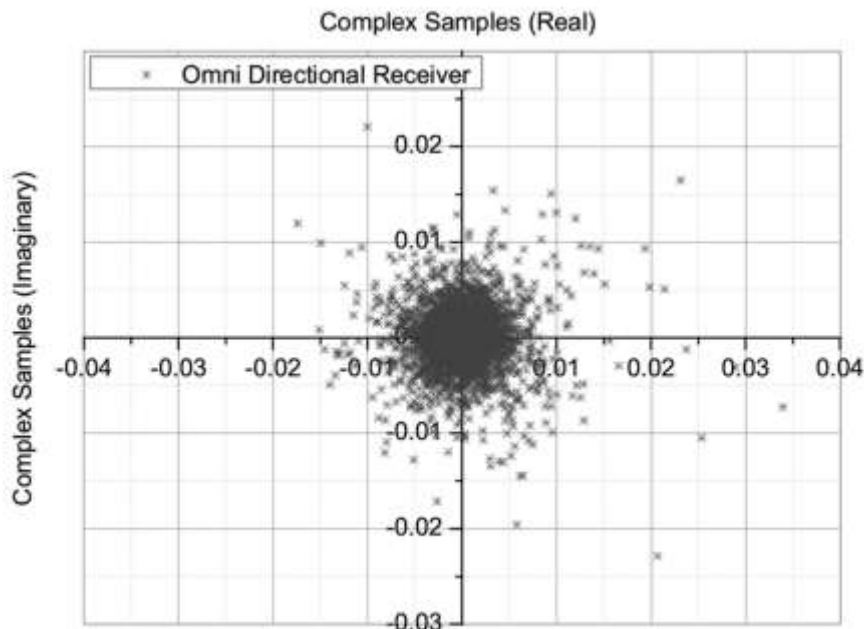


Fig. 2.36: Scatter plot from omni-directional receiver 1000 MHz to 6000 MHz

Figs. 2.31, 2.34, 2.35 and 2.36 further validate that the chamber would appear more than suitable for performing antenna measurements; a subject that forms the focus of the next chapter.

2.9 References

- [1] R. F. Harrington, *Time-harmonic electromagnetic fields*. New York,: McGraw-Hill, 1961.
- [2] C. A. Balanis, *Advanced engineering electromagnetics*: John Wiley & Sons, 1989.
- [3] J. D. Jackson, *Classical electrodynamics*, 3rd ed.: John Wiley & Sons, 1999.
- [4] J. D. Kraus, *Electromagnetics*, 4th Edition ed.: McGraw Hill, 1991.
- [5] D. A. Hill, *Electromagnetic fields in cavities: Deterministic and statistical theories*: John Wiley & Sons, 2009.
- [6] Y. Huang, "The investigation of chambers for electromagnetic systems," D Phil Thesis, Department of Engineering Science, University of Oxford, 1993.
- [7] Y. Huang, "Private communication," S. J. Boyes, Ed., ed. University of Liverpool: University of Liverpool, 2012.
- [8] C. L. Holloway, H. A. Shah, R. J. Pirkle, W. F. Young, D. A. Hill, and J. Ladbury, "Reverberation Chamber Techniques for Determining the Radiation and Total Efficiency of Antennas," *Antennas and Propagation, IEEE Transactions on*, vol. 60, pp. 1758-1770, 2012.

- [9] D. A. Hill, "Boundary fields in reverberation chambers," *Electromagnetic Compatibility, IEEE Transactions on*, vol. 47, pp. 281-290, 2005.
- [10] P. S. Kildal and C. Carlsson, "Detection of a polarization imbalance in reverberation chambers and how to remove it by polarization stirring when measuring antenna efficiencies," *Microwave and Optical Technology Letters*, vol. 34, pp. 145-149, 2002.
- [11] P. S. Kildal, X. Chen, C. Orlenius, M. Franzen, and C. S. L. Patane, "Characterization of Reverberation Chambers for OTA Measurements of Wireless Devices: Physical Formulations of Channel Matrix and New Uncertainty Formula," *Antennas and Propagation, IEEE Transactions on*, vol. 60, pp. 3875-3891, 2012.
- [12] K. Rosengren, P.-S. Kildal, C. Carlsson, and J. Carlsson, "Characterization of antennas for mobile and wireless terminals in reverberation chambers: Improved accuracy by platform stirring," *Microwave and Optical Technology Letters*, vol. 30, pp. 391-397, 2001.
- [13] K. Rosengren and P. S. Kildal, "Study of distributions of modes and plane waves in reverberation chambers for the characterization of antennas in a multipath environment," *Microwave and Optical Technology Letters*, vol. 30, pp. 386-391, 2001.
- [14] P. S. Kildal, *Foundations of antennas: A unified approach*: Studentlitteratur, 2000.
- [15] S. J. Boyes, Y. Huang, and N. Khiabani, "Assessment of UWB antenna efficiency repeatability using reverberation chambers," in *Ultra-Wideband (ICUWB), 2010 IEEE International Conference on*, 2010, pp. 1-4.
- [16] "BS EN 61000-4-21:2011 Electromagnetic compatibility (EMC). Testing and measurement techniques. Reverberation chamber test methods," ed, 2011.
- [17] X. Chen and P. S. Kildal, "Theoretical derivation and measurements of the relationship between coherence bandwidth and RMS delay spread in reverberation chamber," in *Antennas and Propagation, 2009. EuCAP 2009. 3rd European Conference on*, 2009, pp. 2687-2690.
- [18] X. Chen, P. S. Kildal, and L. Sz-Hau, "Estimation of Average Rician K-Factor and Average Mode Bandwidth in Loaded Reverberation Chamber," *Antennas and Wireless Propagation Letters, IEEE*, vol. 10, pp. 1437-1440, 2011.
- [19] P. Corona, G. Latmiral, and E. Paolini, "Performance and Analysis of a Reverberating Enclosure with Variable Geometry," *Electromagnetic Compatibility, IEEE Transactions on*, vol. EMC-22, pp. 2-5, 1980.
- [20] D. A. Hill, M. T. Ma, A. R. Ondrejka, B. F. Riddle, M. L. Crawford, and R. T. Johnk, "Aperture excitation of electrically large, lossy cavities," *Electromagnetic Compatibility, IEEE Transactions on*, vol. 36, pp. 169-178, 1994.
- [21] U. Carlberg, P. S. Kildal, A. Wolfgang, O. Sotoudeh, and C. Orlenius, "Calculated and measured absorption cross sections of lossy objects in reverberation chamber," *Electromagnetic Compatibility, IEEE Transactions on*, vol. 46, pp. 146-154, 2004.
- [22] P. S. Kildal, C. Orlenius, J. Carlsson, U. Carlberg, K. Karlsson, and M. Franzen, "Designing reverberation chambers for measurements of small antennas and wireless terminals: Accuracy, frequency resolution, lowest frequency of operation, loading and shielding of chamber," in *Antennas and Propagation, 2006. EuCAP 2006. First European Conference on*, 2006, pp. 1-6.

- [23] W. Jakes, C, *Microwave mobile communications*. Wiley-IEEE Press John Wiley & Sons, 1974.
- [24] J. G. Kostas and B. Boverie, "Statistical model for a mode-stirred chamber," *Electromagnetic Compatibility, IEEE Transactions on*, vol. 33, pp. 366-370, 1991.
- [25] D. A. Hill, *Electromagnetic Fields in Cavities: Deterministic and Statistical Theories*: John Wiley & Sons, 2009.
- [26] L. C. Andrews, R. L., Phillips,, *Mathematical Techniques for Engineers and Scientists* vol. PM118: SPIE Press Monograph 2003.
- [27] F. J. Massey, "The Kolmogorov-Smirnov test for goodness of fit," *Journal of the American Statistical Association*, vol. 46, pp. 68-78, 1951.
- [28] H. W. Lilliefors, "On the Kolmogorov-Smirnov test for normality with mean and variance unknown," *Journal of the American Statistical Association*, vol. 62, pp. 399-402, 1967.
- [29] H. W. Lilliefors, "On the Kolmogorov-Smirnov test for the exponential distribution with mean unknown," *Journal of the American Statistical Association*, vol. 64, pp. 387-389, 1969.
- [30] C. L. Holloway, D. A. Hill, J. M. Ladbury, P. F. Wilson, G. Koepke, and J. Coder, "On the Use of Reverberation Chambers to Simulate a Rician Radio Environment for the Testing of Wireless Devices," *Antennas and Propagation, IEEE Transactions on*, vol. 54, pp. 3167-3177, 2006.
- [31] P. S. Kildal, S. H. Lai, and X. M. Chen, "Direct Coupling as a Residual Error Contribution During OTA Measurements of Wireless Devices in Reverberation Chamber," *2009 IEEE Antennas and Propagation Society International Symposium and Usnc/Ursi National Radio Science Meeting, Vols 1-6*, pp. 1428-1431, 2009.

Chapter 3: Textile Antenna Efficiency Performance

3.1 Introduction

A growing interest is evident concerning body centric wireless communication technology, aimed at providing solutions for a wide range of applications from the medical / healthcare industries, the consumer electronic industries, wearable technology for the fashion industry and the military sector to name but a few. A crucial component in the body centric wireless communication ‘chain’ concerns the antenna device itself; the antenna should be ergonomically suitable for integration onto a human body. Furthermore, the antenna should not be obtrusive, it should be able to maintain flexibility, exhibit minimal degradation in terms of bandwidth, reflection coefficient and efficiency performance, and be manufactured in a low cost manner. To satisfy this broad criterion, the textile antenna has been developed and continues to receive ever growing attention [1-9].

When communicating wirelessly in the proximity of a human body, the propagation channel is dependent upon the body condition, the human activity being performed, the antenna position, the immediate surrounding environment and any interaction between the human body and the antenna [10-12]. Therefore, the radio propagation channel in this (on-body) scenario directly includes the body effect and is not usually stationary. In this thesis, the main parameter of interest concerns the radiation and total radiation efficiency performance of some newly designed textile antennas. This work results from a collaboration between two parties; the textile antennas have been developed by P. J. Soh and G. A. E. Vandenbosch [3, 4], while the contribution from this author concerns all the practical measurements for the antennas validation and any supporting evidence.

The RC measurement facility was chosen for this investigation partly because of the statistically emulated environment it can offer, but also it was felt that it can offer a more robust / less uncertain measurement solution to the problem of measuring textile antenna efficiencies when acquired in conjunction with a human being. To explain further, it is inevitable that some human movements will be present during any measurement procedures due to breathing etc. This could prove problematic in other facilities, but in the RC environment they could be tolerated as any movements would add to the randomness of the field inside the chamber which can be viewed positively. A further benefit exists with the RC in the fact that it is potentially relatively quicker and easier to start the measurement process.

To the best of this author's knowledge, only one experiment concerning antenna radiation efficiency analysis measured on live human beings in an RC exists; see [13]. The conclusions drawn from this piece of work indicated that RC results obtained with human test subjects was sufficiently representative of results acquired in anechoic chambers and also measured against tissue phantoms - this potentially validates the live human approach against phantoms often used in the field, and benchmarks the RC facility against alternative measurement facilities.

The antennas used in the study from [13] consisted of four low profile microstrip patch antennas constructed on dielectric substrates and a quarter wavelength monopole antenna, with the results indicating that the type of antenna plays a more dependent role in determining the overall efficiency performance, as opposed to the characteristics of different human subjects. Further study is required from [13] however; there is a lack of information specifically concerning the performance of antennas specifically designed for on-body communications (i.e. the textile antenna), particularly so in the on-body role. An assessment of movement related bending effects on antenna performance should also be provided as well as the effect of different body locations and proximity distances from the human on the antennas performance.

There are few more deficiencies in knowledge that also require rectifying. No detailed measurement procedures in the RC exist, no information concerning the statistical effects of different human subjects on RC measurements exists and very limited information concerning the repeatability of such measurements exists. Furthermore, definite uncertainty deductions are also required so that absolute confidence can be placed in antenna performance results when acquired on human beings. All these former points constitute new knowledge within this subject area.

The organisation of this chapter is as follows. The chapter will be sub-divided into two separate entities to assess the performance of two distinct types of textile antenna; one operational in the Industrial Scientific and Medical (ISM) 2.45 GHz band, the second designed to offer a dual band characteristic at 2.45 GHz and 5.2 GHz. Each entity will firstly define all measurement procedures before assessing the antenna performance in free space conditions and on-body. The purpose of the free space investigation is to establish a performance benchmark such that the expected degradation in performance can be charted accurately. In addition, the frequency de-tuning performance of all antennas will be presented for completeness.

Where appropriate, theoretical and simulated evidence are provided to establish increased confidence in any derived results. A concise repeatability investigation and a comprehensive uncertainty assessment are also provided at the end of this chapter to benchmark the accuracy of all results presented.

3.2 Definitions: Antenna Efficiency

For the quantity of antenna radiation efficiency, the IEEE standard definition is referred to [14]:

“Ratio of total radiated power to net power accepted by the antenna at its terminals”.

Mathematically, when acquired using an RC, Eq. (3.1) applies [15].

$$\eta_{RAD} = \left\{ \frac{\langle |S_{21AUT}|^2 \rangle}{\langle |S_{21REF}|^2 \rangle} \times \frac{\left(1 - (|S_{22REF}|)^2\right)}{\left(1 - (|S_{22AUT}|)^2\right)} \right\} \times \eta_{REF} \quad (3.1)$$

where: $\langle \rangle$ = average of the scattering parameters, $| |$ = absolute value, S_{21} = transmission coefficient, S_{22} = reflection coefficient, AUT = antenna under test, REF = reference antenna and η_{REF} = known reference efficiency. In this thesis the reflection coefficient quantities are not signified as being an ensemble average, this is because it was chosen to acquire these parameters in an anechoic chamber. This selection was made with respect to the following points:

- 1) The reflection coefficient parameters could be obtained in a faster time frame as the automated software for the RC only allows for one parameter at a time.
- 2) Since the equation for the efficiency calculation requires a free space equivalent reflection coefficient - it is not incorrect by any means to establish this in an anechoic chamber.

It should be noted that the reflection coefficient quantity can be measured using an RC [16], and as such the reflection coefficient terms in (Eq. 3.1) should be indicated being from an ensemble average.

For the quantity of total radiation efficiency, the IEEE standard definition of terms is again referred to:

“The ratio of total radiated power to the power incident on the antenna port”.

Mathematically, this is a product of the radiation efficiency and mismatch efficiency of an antenna as depicted in Eq. (3.2).

$$\eta_{TOTAL} = \eta_{RAD} \times \left(1 - (|S_{22AUT}|)^2\right) \quad (3.2)$$

Again, assuming that the reflection coefficient terms are acquired in an anechoic chamber.

3.3 Definitions: Single Band Textile Antennas

As stated previously, this author’s contribution to the work centres solely on the validation on the antennas performance; it is therefore beyond the scope of this thesis to present any detailed optimisation and design analysis for the textile antennas. Hence, in this section the antennas will only be introduced and briefly described. For further information please see [4].

The single band textile antennas in this study are based on a Planar Inverted F Antenna (PIFA) topology. They are constructed using a 6 mm thick felt fabric with (respective) relative permittivity and loss tangent parameters of ($\epsilon_r = 1.43$, $\tan \delta = 0.025$) at 2.45 GHz [4]. The felt fabric substrate is sandwiched between a slotted radiator at the top and a small ground plane underneath, with two different conductive textile materials being subject to investigation [17, 18].

- 1) Copper textile (plain woven and coated, 0.08 mm thick, $\sigma = 2.5 \times 10^6$ S/m at 2.45 GHz).
- 2) ShieldIt™ conductive fabric (0.17 mm thick, $\sigma = 1.18 \times 10^5$ S/m at 2.45 GHz).

The profile and dimensions of each respective antenna can be viewed in Figs. 3.1 and 3.2.

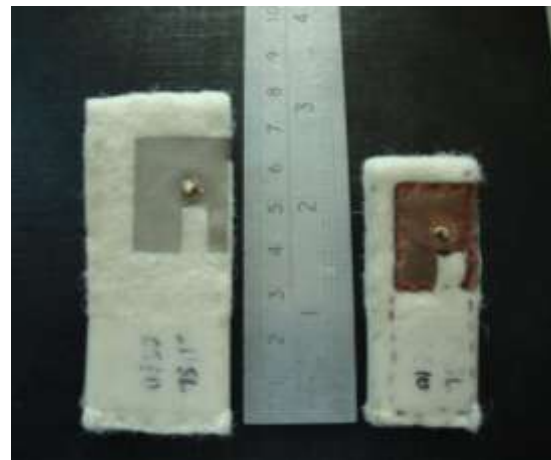


Fig. 3.1: Single band textile antenna radiating elements, ShieldIt radiating element (left) and Copper radiating element (right)

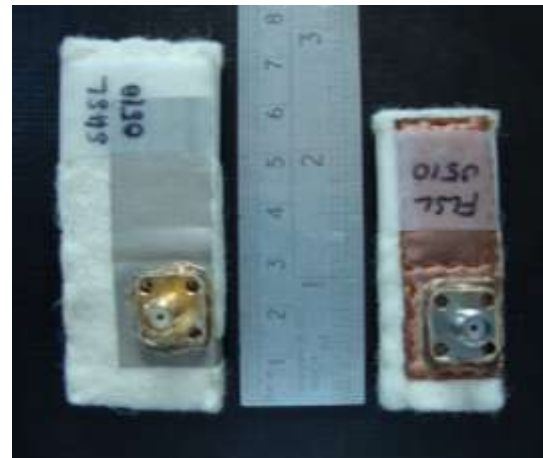


Fig. 3.2: Single band textile antenna ground planes, ShieldIt ground plane (left) and Copper ground plane (right)

3.4 Measurement Procedures

The measurement investigation was carried out using the RC at the University of Liverpool. As stated previously, the chamber has dimensions of width = 3.6 m, height = 4 m and length = 5.8 m. For the efficiency deduction, the chamber required an initial reference measurement for calibration purposes. This calibration was performed using a dual ridge horn antenna (Satimo Model: SH2000), the antenna being selected as its unidirectional pattern characteristics was similar to that of the AUT. In this investigation a frequency range of 2000 MHz - 3500 MHz was selected using 801 frequency data points. The number of data

points was selected to ensure that an adequate number of modes would be excited in the chamber throughout the measurement range.

In the free space efficiency measurement, the calibration needed to be performed with just the AUT's located inside the chamber. The requirement for having all antennas inside the chamber at all times is that the chamber Q factor (and thus the subsequent chamber losses) has to be constant from the reference to the AUT measurement to ensure accuracy. If the chamber Q factor was allowed to vary from the reference to AUT measurement, this would have a consequence of varying the level of received power in (Eq. 3.1) and as such would represent a serious form of measurement uncertainty.

For the on-body efficiency measurement, the human 'loading' had to be present in the chamber throughout the calibration phase. This requirement is for the same reason as explained above, but also because the human body was expected to significantly 'load' the chamber, and was thus surmised to be the dominant contributor to any loss mechanisms that exist inside the chamber (more so than for example, wall losses, losses from aperture leakage and losses in any antenna). The stirring sequences used for both the free space and on-body measurements, encompassing the reference and AUT measurements in both scenarios, comprised the following parameters as detailed in Table V.

Table V: Measurement parameters for textile antenna efficiency investigation

Parameter	Description
Stirring sequences	5 degree mechanical stirring Polarisation stirring 5 x Position stirring 20 MHz frequency stirring
Total number of measured samples per frequency point	710
Frequencies (MHz)	2000 - 3500
Number of frequency data points	801
Source power (dBm)	+ 13

From Table V, the stirring sequences were selected for four primary reasons:

- 1) A large amount of samples (with a given percentage being sufficiently uncorrelated) are required in order to resolve the efficiency quantity accurately.
- 2) When it came to the measurements on the human subject, it meant that the human did not have to spend prolonged amounts of time in the chamber to complete each measured sequence. Hence, the subject could take regular breaks if need be.
- 3) The exact same number and the manner of the stirring techniques for both free space and on-body measurements meant that an accurate comparison could be formed to benchmark performance.
- 4) The 20 MHz frequency stirring value (averaged over 11 frequency points) was selected such that it was far less than the bandwidth of the antennas to minimise the reduction in frequency resolution (configured to be 4% of the absolute bandwidths of the antennas).

During any measurements it is always desired practice to terminate any antennas not undergoing measurement with impedance matched loads - this ensures that all antennas inside the chamber are in a balanced condition. For the free space measurements, the AUT was mounted using a dummy cable on a separate platform and terminated in an impedance matched load. This is subsequently transferred for the reference antenna when the AUT is measured.

For the on-body reference measurements, the AUT was fixed to the human subjects' chest via the same dummy cable and terminated in the same impedance matched condition. For the on-body AUT measurements, the reference antenna remained on a separate platform in a matched terminated condition. Throughout the on-body measurements, the contents of the human subjects' pockets was always emptied (no coins, mobile phone etc) such that the loading to the chamber would be as constant and consistent as possible. In this, any varying factor that could potentially introduce a source of uncertainty, and that could be removed, was removed to attempt to yield the most consistent and accurate results possible.

The measurement set-up for the on-body reference measurements can be viewed in Fig. 3.3.



Fig. 3.3: On-body reference measurement set-up

The distance between the consecutive position locations marked out in Fig. 3.3 was configured such that each location was larger than the correlation distance (about $\frac{1}{2}$ wavelength) to create independent samples - in this, the distances selected were 0.8 m apart. Furthermore, a prescribed distance was placed between the human subject and the reference antenna at all times to avoid coupling between the two, as shown in Fig. 3.3.

3.5 Measurement Investigation

In this sub-section, a separate discussion will be presented concerning different on-body locations and proximity distances in turn, and the results for both antennas will be presented side by side for ease of comparison. Where appropriate, the measurement results will be issued alongside simulated evidence obtained from CST Microwave Studio (based on the finite integration technique) to depict the accuracy of the measured trends. The simulation efficiency results have been obtained by the gain/directivity method.

The layout is configured to be able to compare the radiation and total radiation efficiency values of each AUT on different body locations with each other and also with respect to their free space efficiency values. By this, the assessment of which antenna yields the highest efficiency on body and in what location is sought, but also the difference in the overall efficiency is charted to assess what degradation occurs when the textile antennas are located on-body in specific locations and proximity distances.

This sub-section begins with the establishment of the free space performance of the textile antennas.

3.5.1 Free Space Performance

With respect to the measurement procedures in section 3.4 and the measurement parameters in Table V, Figs. 3.4, 3.5 and 3.6 depict the free space performance of the copper based textile and Figs. 3.7, 3.8 and 3.9 depict the shieldIt based textile.

Before the results are issued, from herewith the antennas will be referred to by their manufactured names: FLSL 0510 = **copper based textile**, SHSL 0510 = **shieldIt based textile**.

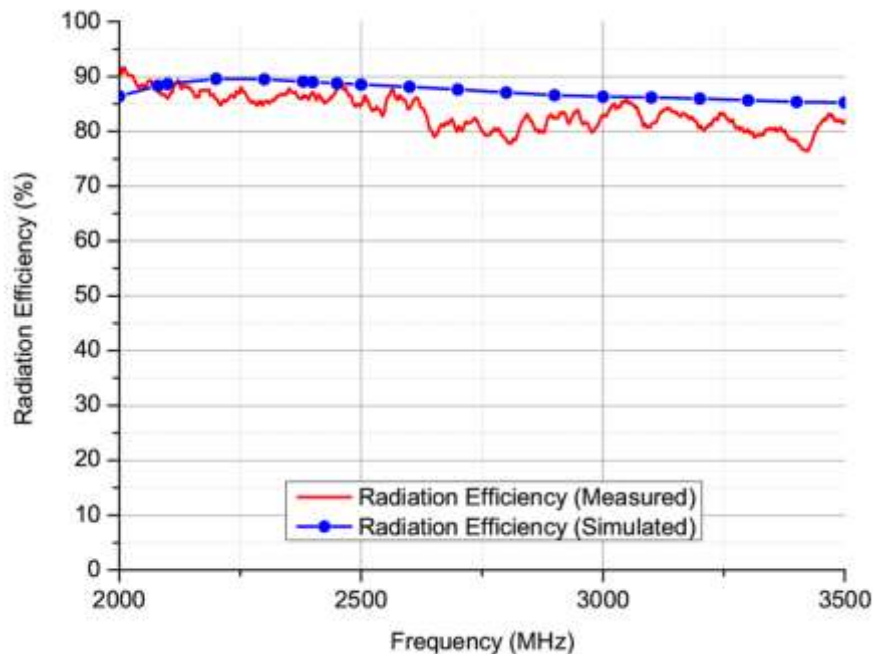


Fig. 3.4: FLSL 0510 free space measured and simulated radiation efficiency (%)

From Fig. 3.4 we see that a very good agreement is obtained from both measurement and simulation. In free space, the copper based textile antenna is seen to be highly efficient.

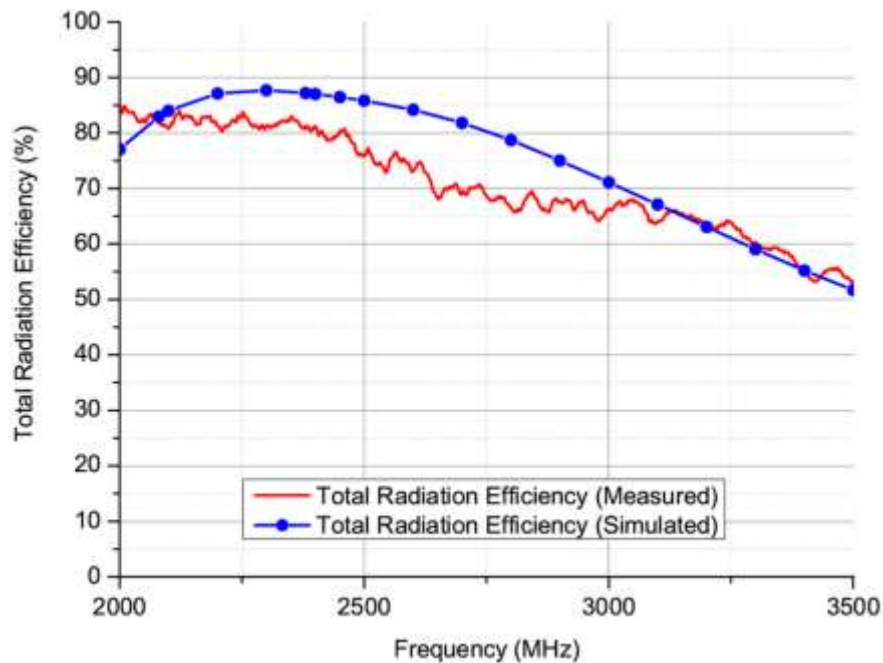


Fig. 3.5: FLSL 0510 free space measured and simulated total radiation efficiency (%)

From Fig. 3.5 we see a good agreement at the start and end of the frequency range but less so in the mid-range. The discrepancy between the measured and simulated cases can be attributed to differences between the measured and simulated reflection coefficients as shown in Fig. 3.6, and *not* the efficiency measurement.

The discrepancy in the reflection coefficients has resulted from slight differences in the fabricated dimensions between the simulated model and physical design, and also the presence of the SMA connector in the physical design.

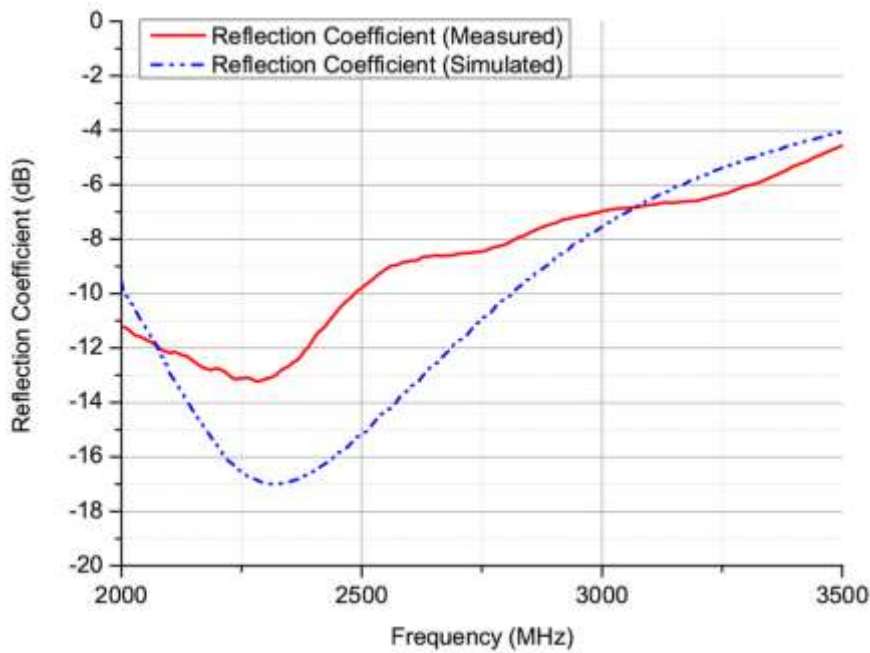


Fig. 3.6: FLSL 0510 free space measured and simulated reflection coefficients (dB)

Irrespective of the discrepancy between measured and simulated reflection coefficients, the practical antenna is seen to be sufficiently impedance matched at its desired 2450 MHz centre frequency. Moving on, we can assess the free space radiation efficiency performance of the ShieldIt based material in Fig. 3.7.

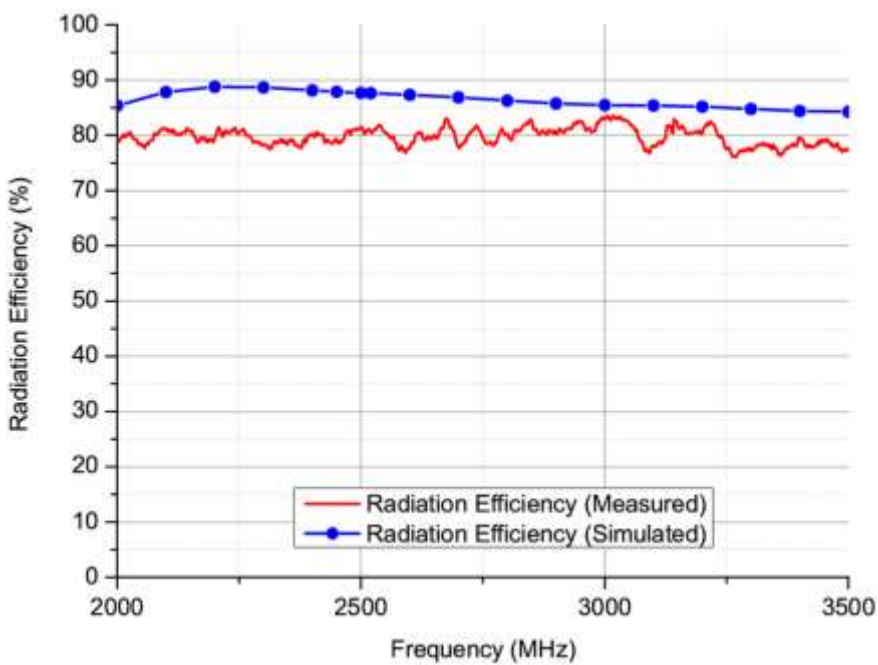


Fig. 3.7: SHSL 0510 free space measured and simulated radiation efficiency (%)

From Fig. 3.7 we see relatively high levels of radiation efficiency are evident for the ShieldIt based textile material, but comparing with Fig. 3.4 (copper based textile) they are 8% - 10% lower, particularly over the first 500 MHz. These results conform completely to expectations, since the higher conductivity material is expected to yield higher levels of radiation efficiency.

Moving on, the total radiation efficiency performance of the ShieldIt based textile can be viewed in Fig. 3.8.

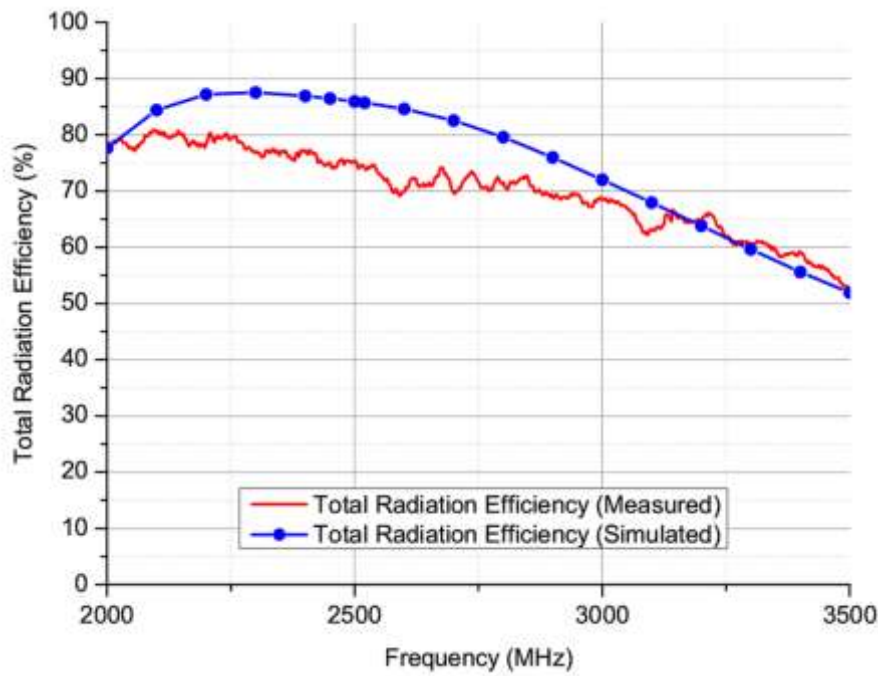


Fig. 3.8: SHSL 0510 free space measured and simulated total radiation efficiency (%)

From Fig. 3.8 we again see a good agreement between measurement and simulation at the beginning and end of the frequency band, but a discrepancy is also present in the mid-frequency range. This can be explained again by differences between the measured and simulated reflection coefficients, as Fig. 3.9 proves.

Nevertheless, from Fig. 3.9 we see that the ShieldIt based textile antenna is sufficiently well impedance matched over the desired band.

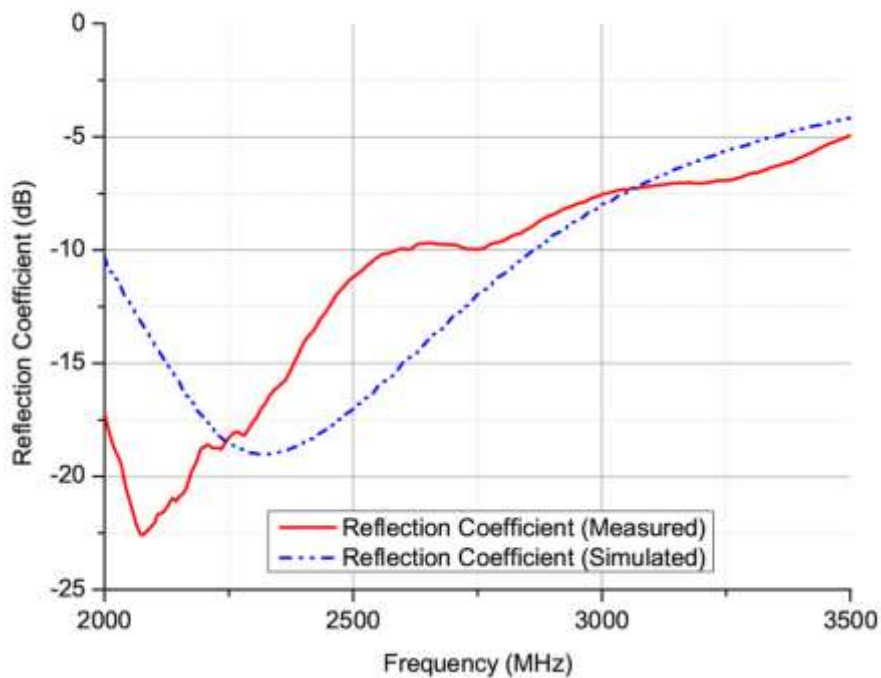


Fig. 3.9: SHSL 0510 free space measured and simulated reflection coefficients (dB)

In conclusion we find that both antennas are highly efficient and sufficiently impedance matched over the frequency band of interest. In free space we can conclude that the copper based textile antenna with the higher conductivity exhibits a higher radiation and total radiation efficiency as compared to the lower conductivity ShieldIt material.

3.5.2 On-Body Chest (0 mm) Performance

As previously stated, for the on-body efficiency assessment, different on-body locations will be investigated but also different proximity distances from the human subject. It is important at this stage to justify prior to the investigation why the proximity distances have been selected. Two distinct proximity distances have been selected throughout this investigation; at 0 mm (touching) from the human subject, and at 20 mm from the human subject. The purpose of these selections is to depict a kind of ‘envelope’ that will show the magnitude of the on-body efficiency from strong (expected) body coupling to reduced body coupling to chart the performance.

It should be acknowledged that when antennas are worn on clothing, movements in the body will cause the differences between the human subject and the antenna to vary, such that a definite separation will not always be evident (i.e. at 5 mm, 10 mm etc). The distances

presented in this case have also been chosen to determine the efficiency at two extreme distances applicable across distinct domains (consumer and emergency services/military applications in this case).

Fig. 3.10 portrays the measurement set-up used in this investigation.



Fig. 3.10: Chest (0 mm) measurement set-up

In this investigation the antenna was located on the centre of the human subjects' chest, 1.38 m from the floor. The 0 mm dimension in this case does not mean that the antenna was physically touching the human subjects' skin; rather, the human subject was wearing a woollen jumper 1.5 mm thick (constant throughout all experiments) and it was this which the antenna was placed against. The antenna element was not physically strapped to the human by any means - standard Velcro straps were used to fix the attached cable to the human being which was sufficient to hold the antenna to the chest of the subject. Throughout the measurement sequences this aspect was rigorously checked and at no time did the antenna shift location.

In Fig. 3.10, the human subject faces the back wall with the antenna on his chest. The simple aim here is not to face the transmitting antenna which is located behind the human subject (off shot). The antenna orientation in Fig. 3.10 (normal to the chest) was chosen because of the location of the SMA connector in the physical design, meaning that it was easier to secure the antenna in position at the 0 mm proximity distance in the manner shown. The radiation efficiency results for FLSL 0510 (copper based textile antenna) are disclosed in Fig. 3.11. Three separate and independent measurements have been completed for this antenna in this scenario to provide an indication as to the measurement repeatability on-

body. A comparison with the free space measured radiation efficiency is also presented so that the degradation in radiation efficiency can be easily assessed.

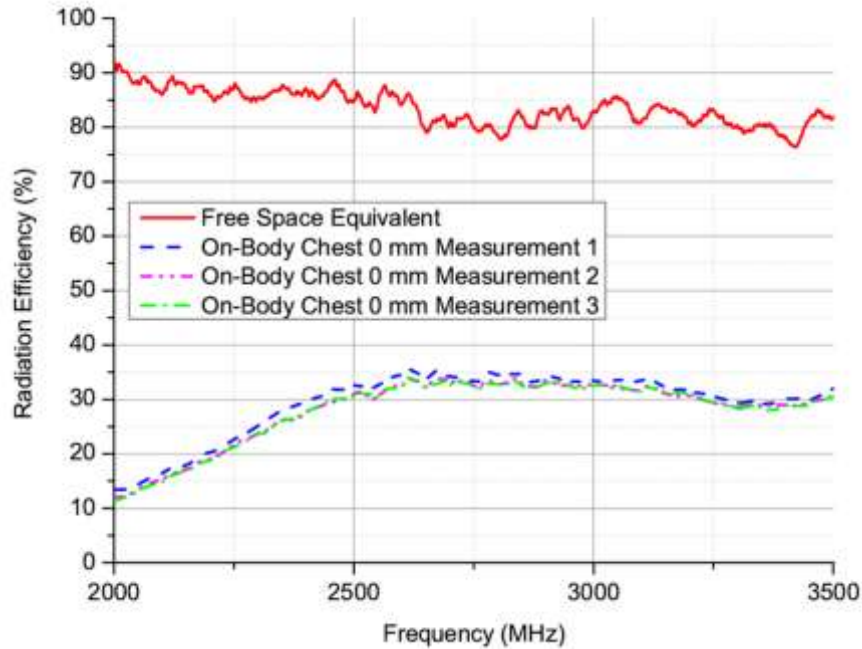


Fig. 3.11: FLSL 0510 free space and on-body chest (0 mm) radiation efficiency (%)

From Fig. 3.11 it can be seen that the effect of the body at the 0 mm placement distance is severe, and the levels of radiation efficiency are degraded considerably. At the start of the measured band (2000 MHz) this is as much as 78.15%. The levels of on-body radiation efficiency are also seen to rise, particularly over the first 600 MHz measured band; this is believed attributed to reductions in coupling between the human body and the antenna element (remembering the antenna is not physically touching the human skin). Thus, as frequency begins to rise, the inter element (human body and antenna) spacing is also increasing.

The repeatability in the on-body efficiency measurements using the aforementioned procedures is also seen to be excellent. A maximum difference of 2% is found between the three independent measured runs in this case. This result proves that consistent and reliable results can be acquired with the use of human beings if correct and consistent procedures are followed. The on-body total radiation efficiency results for FLSL 0510 can be found in Fig. 3.12, three independent measured runs are also depicted to chart the measurement repeatability.

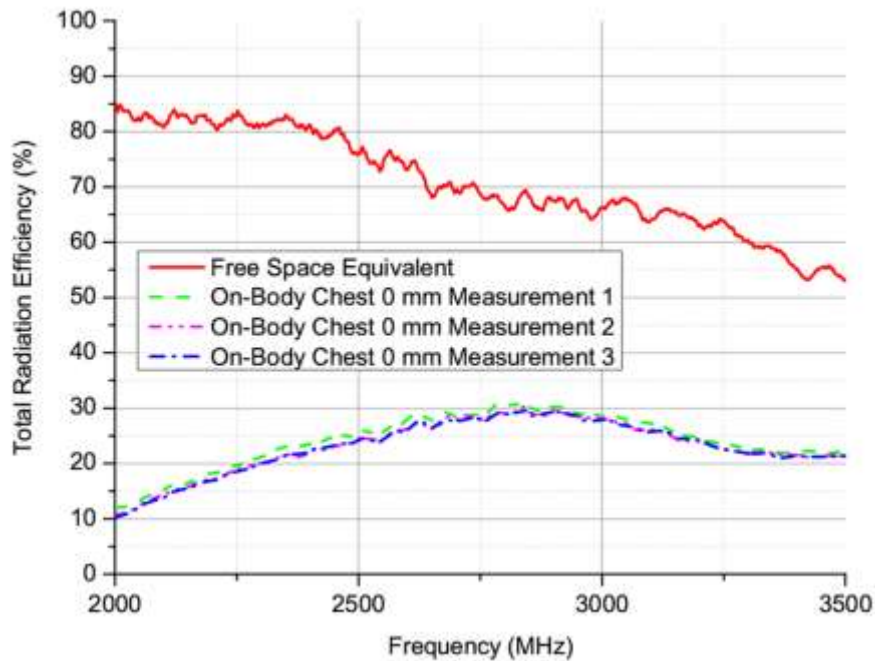


Fig. 3.12: FLSL 0510 free space and on-body chest (0 mm) total radiation efficiency (%)

Again, severe deficiencies in performance are evident. At the start of the measured band there is a 72.65% drop in measured performance. Similar trends as to the radiation efficiency are witnessed and the repeatability levels are still in the order of 2% between each of the three measured runs undertaken.

Questions might arise with respect to the antennas on-body orientation (from Fig. 3.10), particularly as the antenna is mounted normal to the chest instead of being parallel; an investigation was undertaken with a different on-body orientation. The purpose for this investigation is because in a worn application, it is well known that the antenna orientation can change due to the users' movements. Therefore, even when a wearable antenna is designed specifically to be radiating along the body or away from the body, neither of these orientations will exist consistently at all times.

Therefore, a need exists for two distinct evaluations, one radiating along the body (normal to the chest) and one radiating away from the body (parallel to the chest). Moreover, fixing the antenna in an on-body role beats the purpose of having a wearable antenna which can offer the flexibility and comfort that conventional (metallic) type antennas cannot.

The measurement set-up for the different orientation measurement can be viewed in Fig. 3.13.



Fig. 3.13: (0 mm) measurement set-up for alternative orientation

This investigation utilised the exact same measurement parameters and procedures as previously discussed to ensure that an accurate comparison could be formed. The on-body antenna location was configured such that the cable was mounted and secured under the arm, enabling the antenna radiating patch to be away from the human body. The exact same (0 mm) proximity distance was also maintained. Fig. 3.14 illustrates the measurement results from this investigation and the results are directly compared alongside the previous normal orientation.

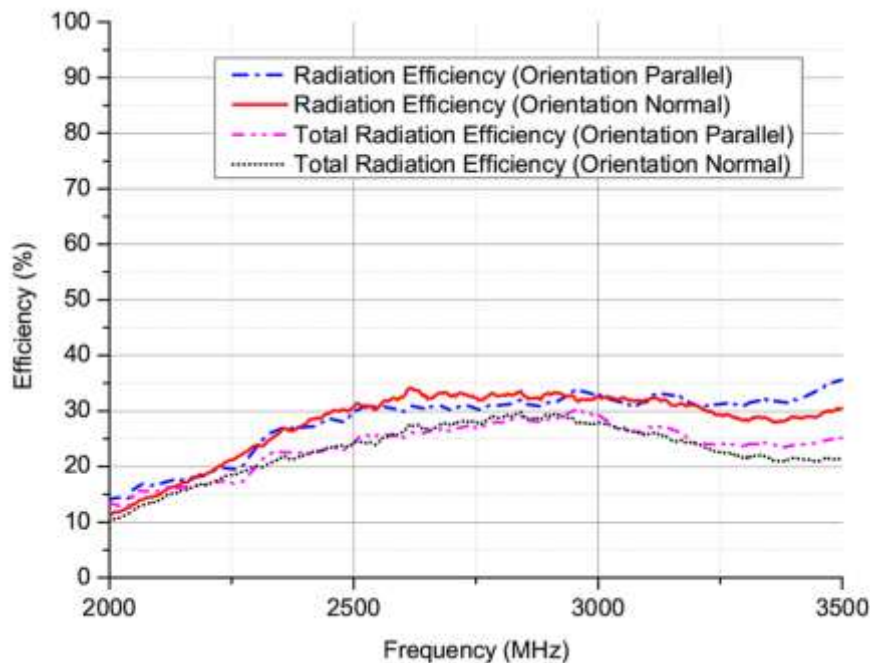


Fig. 3.14: (0 mm) measurement results for parallel and normal on-body orientations

From Fig. 3.14 it can be seen that irrespective of the antennas on-body orientation, the deduced radiation and total radiation efficiency results are very close indeed; the difference at the largest point is in the order of 4%. The result proves that in this particular case it does not matter too much what the orientation is (i.e. the results are valid irrespective of the orientation). The question now is: Why is this so?

- 1) In a LOS environment, the on-body orientation will be crucial because of the radiation pattern characteristics with respect to how the antenna is orientated on-body. In the LOS scenario, such an agreement (as in Fig. 3.14) is not necessarily expected. In the NLOS environment however, as proved back in chapter 2, there is a uniform distribution of plane wave angle of arrivals, meaning that the probability of the wave coming from every conceivable direction will be equal. The existence of this environment can therefore serve to mitigate the effect of the antennas radiation pattern with respect to the on-body orientation. A similar argument to this was put forward in [19].
- 2) Another contributing factor concerns the size of the ground plane. If a large ground plane size was to exist, then such an agreement is again not expected - that is, a more pronounced difference is envisaged as the on-body antenna pattern characteristics would be more strongly influenced by the larger ground plane.

The parallel measured results from Fig. 3.14 were acquired on a different human subject as compared to the normal measured results; therefore it can be concluded that any results measured at the 0 mm proximity distance are comparable irrespective of the on-body antennas orientation (within reason), and secondly that the measured results are reproducible and representative of different human subjects. From herewith, all results measured at the 0 mm proximity distance have used the normal antenna orientation (as in Fig. 3.10) due to the ease of this set-up.

As previously stated, all measured reflection coefficients were acquired using an anechoic chamber. The on-body locations for the RC measurements were measured and marked, such that for the anechoic chamber measurements, the antennas were placed in exactly the same position to ensure that accuracy ensued. Fig. 3.15 details the typical measurement set-up and Fig. 3.16 depicts the on-body reflection coefficient performance.

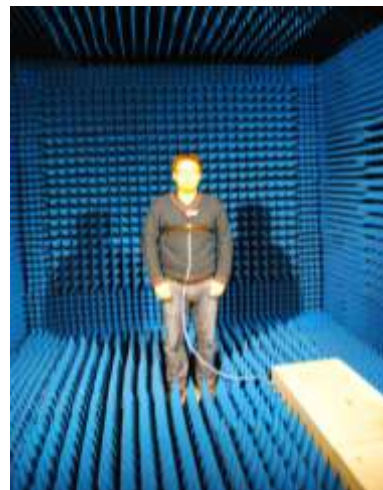


Fig. 3.15: Measurement set-up for on-body reflection coefficients

As seen in Fig. 3.15, the exact same Velcro straps have been employed and the antenna is fixed in the exact same manner as the RC measurements.

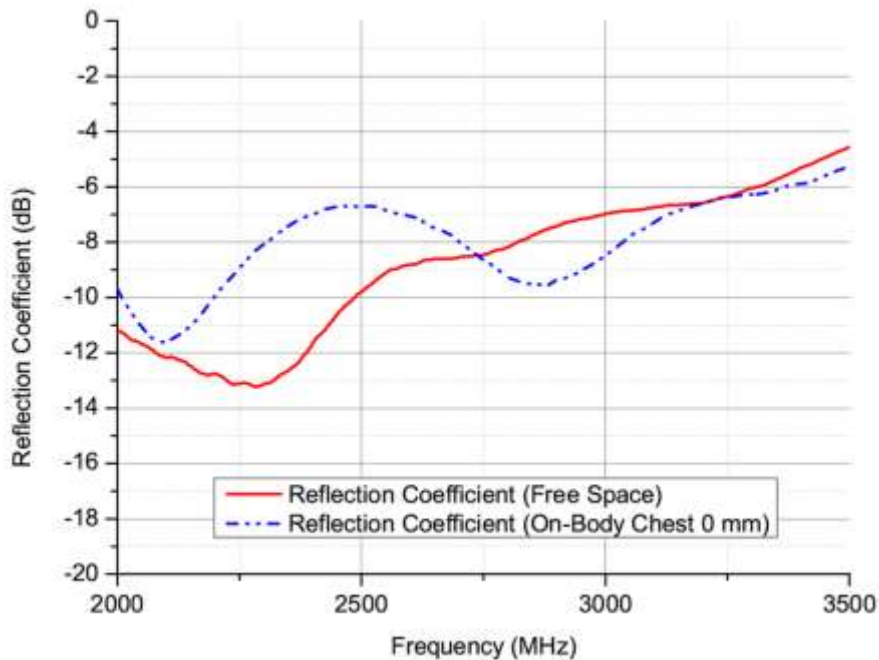


Fig. 3.16: FLSL 0510 free space and chest (0 mm) measured reflection coefficients (dB)

From Fig. 3.16, in addition to the severely degraded efficiency performance, the antenna is also seen to exhibit a degree of de-tuning. At 2.45 GHz the mismatch efficiency measured on the chest is 78% as compared to the earlier depicted free space value of 91%.

We can now assess the performance of the lower conductivity material textile antenna (SHSL 0510), and compare against the higher conductivity copper based textile antenna (FLSL 0510) to see if any difference in performance is evident. Figs. 3.17 and 3.18 depict the on-body efficiency and reflection coefficient performance respectively.

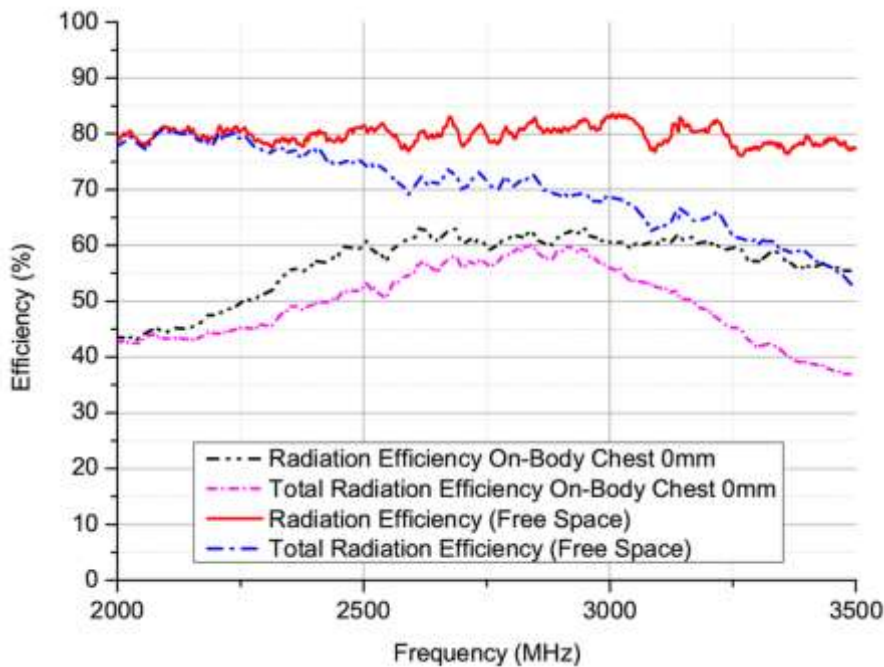


Fig. 3.17: SHSL 0510 free space and on-body chest (0 mm) efficiencies (%)

Comparing Figs. 3.11 and 3.12 with Fig. 3.17 we find that the antenna constructed with the ShieldIt type material is lossier in free space conditions than the higher conductivity copper based textile. As previously established, this is completely in-line with expectations. However, when the on-body efficiencies are compared, we find that the lower conductivity (lossier free space) antenna is grossly more efficient than its copper based counterpart. The difference between the performances of the two textile antennas on-body (chest 0 mm) yields up to 30% for the radiation efficiency and 25% for the total radiation efficiency.

Therefore, when assessing the efficiency degradation on-body, the ShieldIt material in this case has by far the superior performance. An assessment of the reflection coefficient performance on-body for SHSL 0510 is pictured in Fig. 3.18.

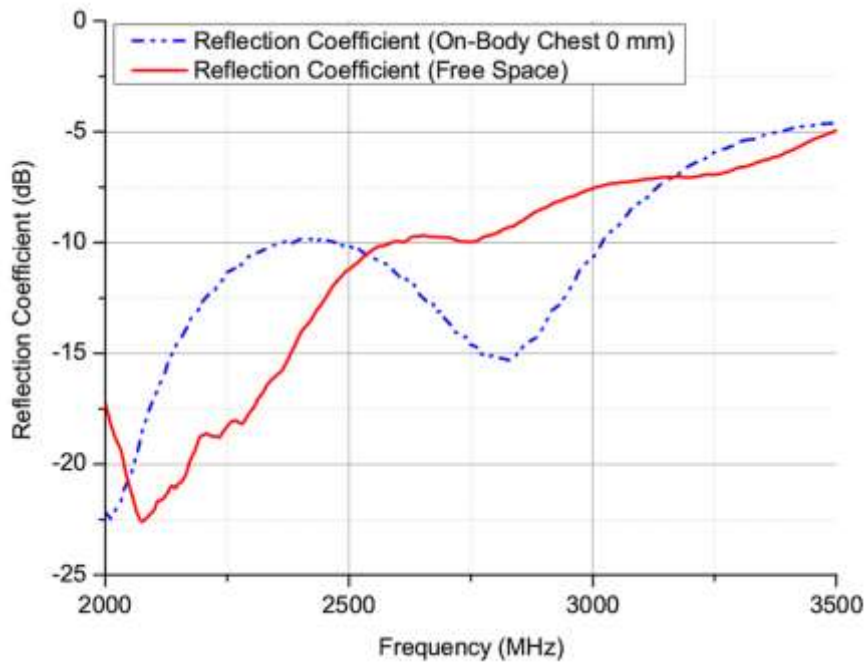


Fig. 3.18: SHSL 0510 free space and chest (0 mm) measured reflection coefficients (dB)

From Fig. 3.18 it can be seen that evidence of de-tuning also exists but it is not as severe as for the higher conductivity (copper based) textile antenna. Comparing the mismatch efficiencies of the two textile antennas at 0 mm we find that the ShieldIt textile material exhibits a value of 90% as opposed to the 78% witnessed from the copper textile material. About the designed centre frequency, the ShieldIt textile antenna remains well matched.

3.5.3 Bent Elbow (0 mm) Performance

This investigation looks to assess the antennas performance under a bent condition. The purpose of this investigation is to demonstrate what can happen to the antennas performance if it becomes stressed and unnecessarily flexed due to human movements.

The on-body location area used to perform this experiment was chosen to be the elbow. This location was selected as opposed to the knee for example, because the antenna could not be located so close to a metallic boundary (i.e. the floor), for field uniformity purposes as detailed back in chapter 2.

In this experiment the antenna had to be secured with the standard Velcro ties owing to the loading placed on the antenna through bending. The bending radius (measured from the

centre of the elbow to the edge of the elbow) was 55 mm. The antenna element selected to perform this test was the copper based textile (FLSL 0510), and was located 1.2 m from the chamber floor. The human subjects arm was fixed in place by a Velcro tie which was strapped around the arm and the shoulder; this was sufficient to hold the arm in place and prevent any unnecessary movement. The RC measurement set-up can be viewed in Fig. 3.19 and the radiation efficiency, total radiation efficiency and reflection coefficient performance in this measurement scenario can be viewed in Fig. 3.20.



Fig. 3.19: Measurement set-up for bent elbow investigation

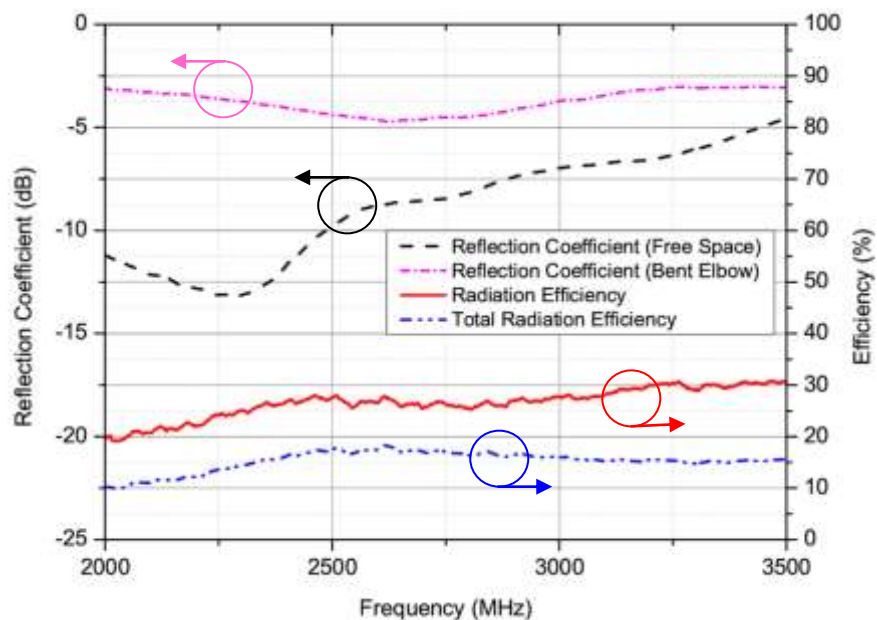


Fig. 3.20: FLSL 0510 bent elbow reflection coefficients (dB) and efficiencies (%)

Comparing with the FLSL 0510 chest (0 mm) measurement results from Fig. 3.11, the radiation efficiency results at 2 GHz would appear to be slightly higher in the bent configuration; this is believed to be due to the absence of major human organs near to the antenna. Throughout the mid and upper frequency range the radiation efficiency values are comparable. However, the main effect here concerns the total radiation efficiency. The levels are 12% to 15% lower than the 0 mm chest values from Fig. 3.12 owing to the severe de-tuning in the magnitude of the reflection coefficient; rendering the mismatch efficiency in the bent configuration at 62% as compared to 78% on the chest at 0 mm and 91% in free space.

It is worth acknowledging that the antenna was stressed for a considerable period of time, more so than for example if it was employed in a real on-body scenario. However, in a real scenario, if the antenna was in a location on the body that was liable to bend, then at any instantaneous point in time the antenna could severely de-tune and this could have consequences on the communication link. The conclusion drawn from this investigation is that severely loading the antenna under a bent configuration is *not* good practice, and on the evidence of the results seen in Fig. 3.20, should be avoided when an on-body location is to be chosen.

In respect of these conclusions, this experiment was not repeated.

3.5.4 On-Body Back (0 mm) Performance

This investigation looks to assess if any fundamental differences in performance are witnessed at different on-body locations. Any differences, if revealed, would not necessarily be a result of differing pattern characteristics with respect to different on-body locations within the RC environment; rather, a difference in coupling levels between the human body and the antenna as a function of body location.

The option selected for this investigation was the human subjects' back. The reason for this selection was to situate the antenna away from the main human organs and not in a scenario where it was likely bend severely. The RC measurement set-up can be viewed in Fig. 3.21, the efficiency and reflection coefficient results for FLSL 0510 can be found in Figs. 3.22. The results for SHSL 0510 are presented in Fig. 3.23. The exact same measurement procedures previously discussed have also been adopted in this investigation.



Fig. 3.21: Measurement set-up for the back (0 mm) investigation

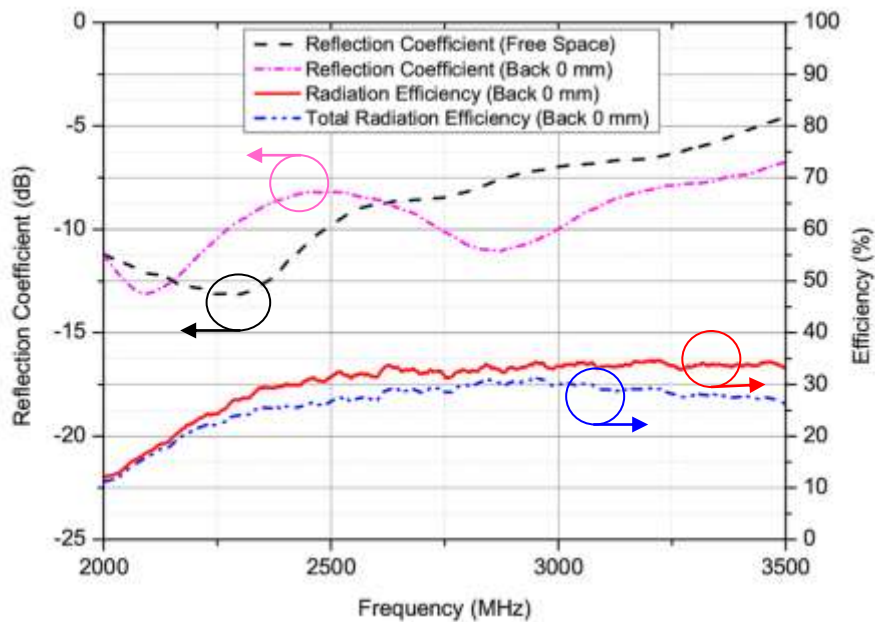


Fig. 3.22: FLSL 0510 back (0 mm) reflection coefficients (dB) and efficiencies (%)

Comparing the radiation efficiency performance of FLSL 0510 on the back at 0 mm to that of the chest at 0 mm (Fig. 3.14) it is found that the results on the back are generally comparable in nature. There is an increase of 5% towards the end of the measured band however. The results for the total radiation efficiency are generally comparable in nature with the chest (0 mm) values, although they are slightly higher by a few percent.

There is also frequency de-tuning evident with the antenna at this on-body location. At the centre frequency, the mismatch efficiency on the back is recorded as 85% as opposed to the 78% witnessed on the chest and 91% measured under free space conditions. From the

evidence witnessed it can be concluded that no wholesale differences in performance are apparent from the change in on-body location.

Assessing the ShieldIt material on the back at 0 mm, the results are presented in Fig. 3.23. Please note the slight shift in scale on the right hand y axis.

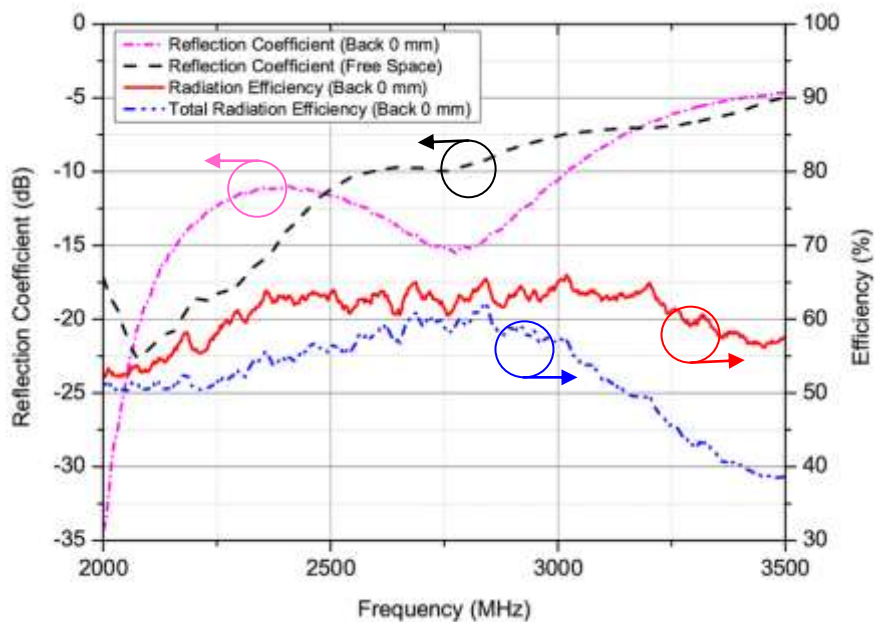


Fig. 3.23: SHSL 0510 back (0 mm) reflection coefficients (dB) and efficiencies (%)

From Fig. 3.23 it can be seen that again the lower conductivity ShieldIt based material has superior performance on-body as compared to the higher conductivity copper textile. The radiation efficiency and total radiation efficiency results for SHSL 0510 on the back are again comparable with the levels witnessed on the chest (at 0 mm).

Comparing the magnitude of the reflection coefficient obtained on the chest (0 mm) and in free space, we find that on the back no negative de-tuning is evident whatsoever in this on-body location.

The results in Fig. 3.23 re-enforce the results obtained in Fig. 3.17 (chest 0 mm), in so much that any measurement anomaly or error can be ruled out - in different on-body scenarios the lossier free space antenna continues to outperform the higher free space antenna (copper textile), both in terms of efficiency and reflection coefficient performance.

3.5.5 On-Body Chest (20 mm) Performance

In the previous investigations we have established the following:

- 1) A lossier antenna in free space grossly outperforms a higher free space efficient antenna when placed on-body.
- 2) The radiation efficiency values obtained in the RC environment for each respective antenna are within a few percent of the values obtained at different on-body locations.
- 3) The total radiation efficiency values are subject to variations at different on-body locations due to the added dependence of this quantity with the on-body reflection coefficient performance of the antenna.

The next investigation looks to assess the effect of having different spacing between the antenna and the human body - i.e. if the inter element spacing were to be slightly increased, what difference in the magnitude of radiation and total radiation efficiency could be obtained?

The theoretical rationale guiding this investigation is considered to be a function of (expected) decreased coupling between the antenna and the human subject; noting that the medium that is coupling to the antenna (i.e. the human being) will present a loss (sometimes significant) if the antenna is close enough.

As previously stated, the 20 mm proximity distance was chosen to complete the ‘envelope’ from strong expected coupling (very close to the body) to reduced coupling (slightly away from the body), maintaining a distance that can still be applicable in an on-body scenario. The practical application for such a 20 mm distance from the body can be realised for emergency service workers who may have antennas attached to their overcoats, and/or military service personnel who could have antennas attached to protective clothing worn in combat.

In this investigation the antenna was placed 1.38 m from the floor and situated from the human subjects’ chest. To achieve and maintain the 20 mm prescribed distance from the body, the antenna was attached via a 90 degree ‘elbow’ connector. Fig. 3.24 details the measurement set-up for this investigation.



Fig. 3.24: Measurement set-up for the chest (20 mm) investigation

From Fig. 3.24 it can be seen that with the presence of the elbow connector, the antenna is orientated parallel with the body. Consistent with the previous on-body investigations, Velcro straps have again been used to fix the cable to the human subject to prevent any movements, and the exact same measurement procedures have again been employed.

Fig. 3.25 details the on-body efficiency and reflection coefficient performance of the copper textile antenna (FLSL 0510).

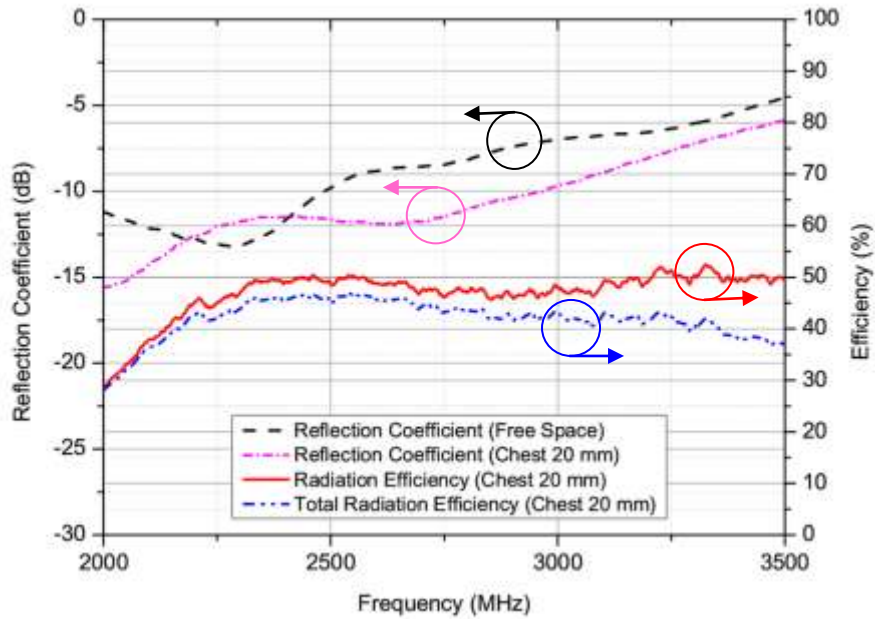


Fig. 3.25: FLSL 0510 chest (20 mm) reflection coefficients (dB) and efficiencies (%)

Comparing Figs. 3.14, 3.22 and 3.25, that is on the chest at 0 mm, on the back at 0 mm and on the chest at 20 mm, it can be clearly seen that the radiation and total radiation efficiency values are at a higher level at 20 mm than previously deduced. A 20% to 30% increase in the radiation efficiency is apparent in this case and a 15% to 19% increase in the total radiation efficiency. Furthermore, the radiation efficiency levels in Fig. 3.25 are also seen to rise with increasing frequency which provides confidence to believe that the coupling theory can explain this trend.

It is also revealed that the added distance from the human subject has reduced the loading effects on the antenna sufficiently enough such that no negative de-tuning is apparent in the on-body reflection coefficient. The performance of SHSL 0510 at the 20 mm proximity distance can be viewed in Fig. 3.26. Please note again the slight shift in the right hand y axis.

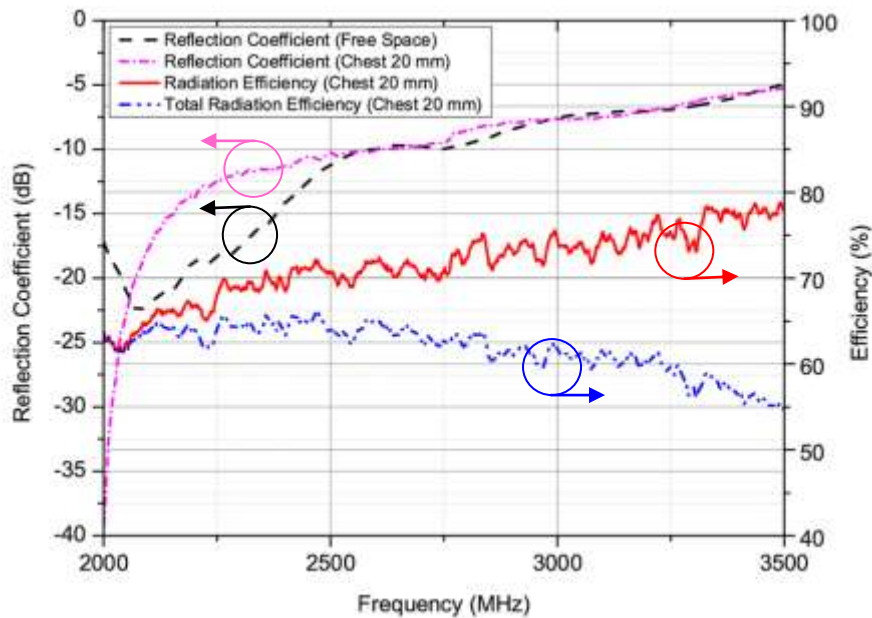


Fig. 3.26: SHSL 0510 chest (20 mm) reflection coefficients (dB) and efficiencies (%)

Comparing Figs. 3.17, 3.23 and 3.26, that is on the chest at 0 mm, on the back at 0 mm and on the chest at 20 mm, it is again evident that the added proximity distance mitigates the detrimental effect of the human body. This trend can be explained again by the reduced coupling between the antenna and human body due to the added (electrical) distance between both elements. Further, by assessing the magnitude of the radiation efficiency at 20 mm, it can be seen that the antenna towards the end of the measured range has decoupled itself from the human body to such an extent, the on-body radiation efficiency levels approach the levels evident in free space.

This fact could prove useful when antennas with multi band operational frequencies are used (progressively higher frequencies), such that the higher frequency bands suffer less of a radiation efficiency degradation due to antenna / body coupling - particularly so when located 20 mm off the body as seen here. If we assess the effect on the measured reflection coefficient, we find that again no negative de-tuning has taken place at all at the 20 mm distance using this antenna - the antenna is operational over a similar bandwidth as free space. It is proved therefore that certain antennas can be placed in a (relatively) close proximity to the human body in an operational role, and suffer only minor detrimental performance effects.

3.6 Theoretical & Simulated Evidence

Drawing conclusions from section 3.5, it is clearly proved that the antenna constructed from the lower conductivity, thicker textile material (ShieldIt - SHSL 0510) outperforms the thinner, higher conductivity copper textile antenna (FLSL 0510) when placed in various locations and proximity distances of the human body, in terms of both the efficiency and the frequency de-tuning levels. This result is in stark contrast to the free space (efficiency) case and counter-intuitive to what we would normally expect. The question therefore is: Why is this the case?

It is stated in [20] that demands placed upon antennas with small ground planes, when placed near the proximity of a human body, can result in an interaction with the reactive near fields of the antenna and cause a loss. The reason here for the difference in the magnitude of efficiency between the two antennas is due to the fact that the lower conductivity (thicker) textile material has given rise to lower electric fields in the body as more power has been lost in this antenna itself for the same input power. This fact is understood to have had the effect of causing lower losses in the human body as opposed to the higher conductivity (copper) textile material [21].

To help reinforce this statement and provide evidence that this theory can explain the trends, two simulated models have been adopted using CST Microwave Studio. The models have been mounted (at 1.5 mm to reflect the woollen jumper worn in practice) onto a structure whose material parameters have been chosen to emulate muscle at 2.45 GHz ($\sigma = 1.773 \text{ S/m}$ and $\epsilon_r = 52.668$ [22]). Fig. 3.27 depicts the simulated radiated power and radiation efficiency from the two models, showing clearly that the copper based textile

antenna (FLSL) radiates less power into free space than the SHSL counterpart. Further, by definition, it is also seen to be less efficient when placed in conjunction with the simulated lossy structure. Fig. 3.28 depicts the simulated electric field magnitudes inside the emulated muscle structure at a depth of 10 mm. A clear difference is shown between the two antenna models which reinforces the theory that explains this trend.

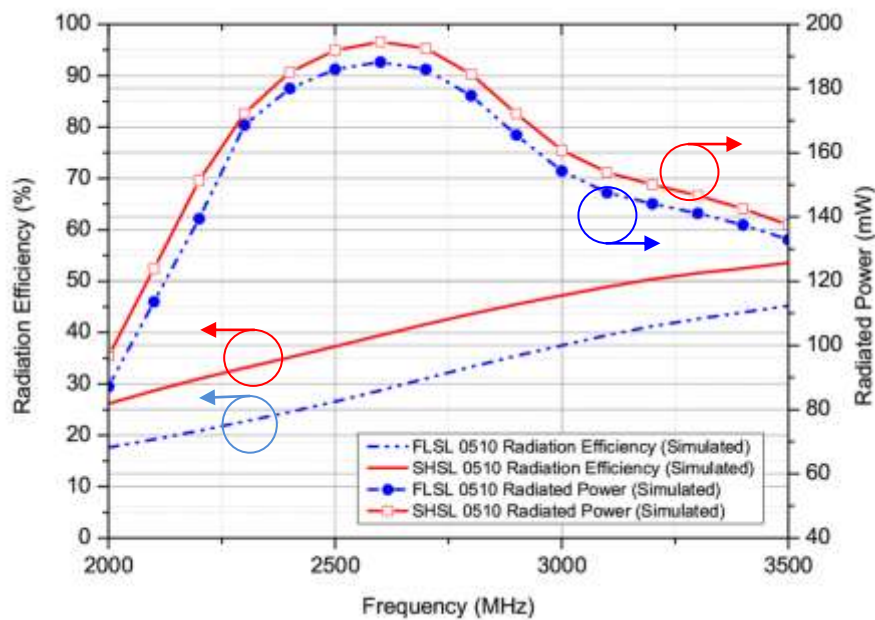


Fig. 3.27: Simulated radiation efficiency and radiated power on muscle emulated material

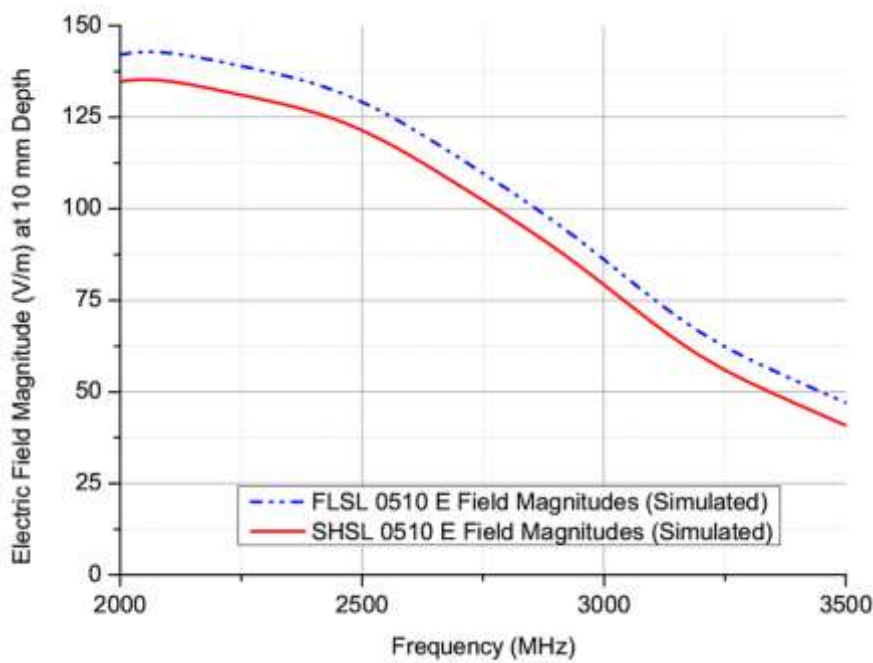


Fig. 3.28: Simulated electric field magnitude at 10 mm depth inside muscle emulated material

3.7 Summary

Briefly summarising the results so far, it has been shown that for the case of small sized textile antennas, crucially with small ground planes, a higher conductive textile material is seen to be more efficient in free space conditions, but grossly less efficient when operating in proximity to the human body. Conversely, a small sized textile antenna that is lossier in free space conditions is proved to be superior when operational on-body.

The results in the section 3.5 represent previously unknown knowledge and this is one of the contributions to new knowledge that this thesis yields. In this, it is proved that if small sized textile antennas with small ground planes are to be employed on body, then a lower conductivity, thicker textile material would be the better choice.

It has also been shown bending the textile antenna whilst on-body can have profound consequences. Although the textile antenna is proposed and flexible enough to allow for this action, severely stressing the antenna can result in serious frequency de-tuning which can impact negatively on the communications link.

Finally, it has been shown that a 20 mm proximity distance from the human body is sufficient in some cases to virtually eradicate any detrimental effects of the human body on the antennas performance. For the ShieldIt textile in this study, at the end of the measured band (3.5 GHz), it had de-coupled itself completely from the human body with only a 20 mm separation. This physical distance represents an electrical separation of slightly less than $\lambda/4$.

3.8 Definitions: Dual Band Textile Antennas

With all the aforementioned information established, the motivation and purpose for the rest of this chapter is to test the validity of this new found information on larger sized textile antennas to see if the relation holds. The expectation for these larger sized devices is that a higher conductivity material should yield greater efficiencies in both free space and on-body as compared to a lower conductivity textile material.

The dual-band textile antennas are constructed using a 6 mm thick felt substrate which is sandwiched between a triangular Sierpinski radiator at the top and a ground plane at the bottom. A shorting wall (W_s) is centred at the top-edge of the antenna, while power is being

fed to the radiator by a 50Ω SMA connector from its ground plane. The two antennas are designed to operate with centre frequencies of 2.45 GHz and 5.2 GHz respectively, with a view to cater for various future 802.15 wireless standards. Similar to the previous (single band) investigation, this work again results from a collaboration between two parties; the textile antennas have been developed by P. J. Soh and G. A. E. Vandenbosch [3, 23], while this authors contribution again concerns all the practical measurements for the antennas verification and any supporting evidence required.

Therefore, it is beyond the scope of this thesis to present detailed optimisation and design analysis for the antennas under test, please refer to [23] for further information. The topology of both dual band textile antennas is constant but two different conductive materials are again subject to investigation.

- 1) Copper tape (0.035 mm thick with adhesive backing, $\sigma = 5.88 \times 10^7$ S/m at 2.45 GHz).
- 2) ShieldIt™ (woven polyester coated with copper and nickel, 0.17 mm thick, $\sigma = 1.18 \times 10^5$ S/m at 2.45 GHz).

The dimensions of the optimised antenna from [23] are $f_v = 9$ mm, $f_H = 8.5$ mm, $D = 24$ mm, $G_L = 44$ mm, and $R_W = 34$ mm. The antennas' schematic can be viewed in Figs. 3.29 and 3.30.

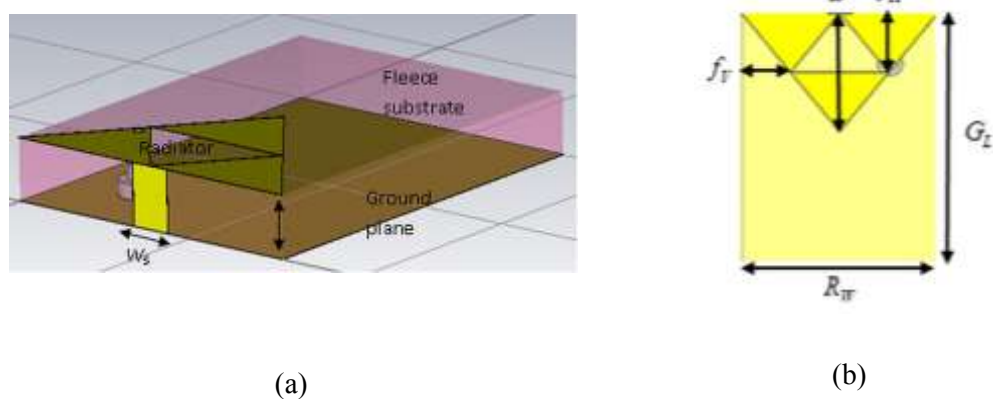


Fig. 3.29: Dual band textile antenna (a) schematic and (b) optimised dimensions

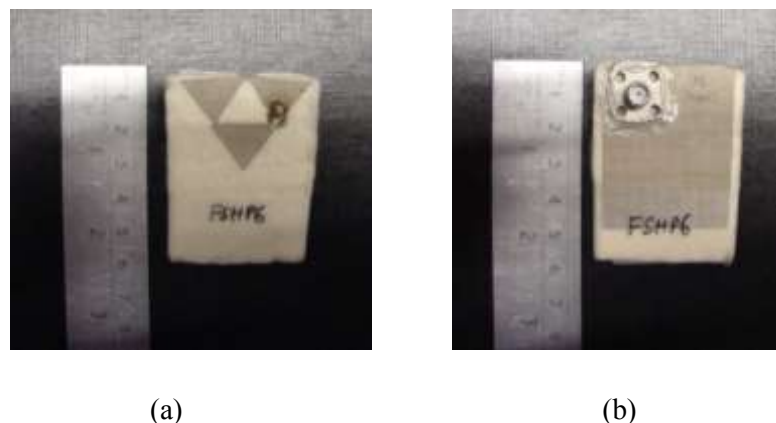


Fig. 3.30: Dual band textile antenna (a) Sierpinski radiator and (b) ground plane

3.9 Measurement Procedures

This investigation utilised the exact same measurement procedures as detailed back in section 3.4; therefore, to avoid repetition they will not be stated again in this section. In terms of the parameters of the dual band textile antenna measurements, a few changes were needed to reflect the antennas working range; these are detailed in Table VI.

Table VI: Measurement parameters for dual band textile antenna efficiency investigation

Parameter	Description
Stirring sequences	5 degree mechanical stirring Polarisation stirring 5 x Position stirring 100 MHz frequency stirring
Total number of measured samples per frequency point	710
Frequencies (MHz)	2000 - 7000
Number of frequency data points	1601
Source power (dBm)	+ 13

With respect to Table VI, the number of frequency data points has been increased to provide an adequate number of excited modes throughout the larger measurement range. The amount of frequency stirring has also been slightly increased with respect to this range also. Taking into account the dual range of impedance matched frequencies only (ignoring the ranges outside), this value still only corresponds to approximately 10% of the antennas total bandwidth to minimise the reduction in frequency resolution of the measured data.

3.10 Measurement Investigation

In this sub-section, similar to the single band investigation, a separate discussion will be presented concerning different on-body locations and proximity distances in turn, and the results for both antennas will be presented side by side for ease of comparison. Where appropriate, the measurement results will also be issued alongside simulated evidence obtained from CST Microwave Studio to depict the accuracy of the measured trends. The layout is configured in the same manner as the single band investigation to assess which antenna yields the highest efficiencies and minimal de-tuning on body.

This sub-section begins with the establishment of the free space performance of the dual band textile antennas.

3.10.1 Free Space Performance

With respect to the measurement procedures detailed in sections 3.4 and 3.9, Figs. 3.31 and 3.32 depict the free space performance of the copper tape based textile antenna and Figs. 3.33 and 3.34 depict the shieldIt based textile.

Before the results are issued, from herewith the antennas will be referred to by their manufactured names: FCTP3 = **copper tape based textile antenna**, FSHP6 = **shieldIt based textile**.

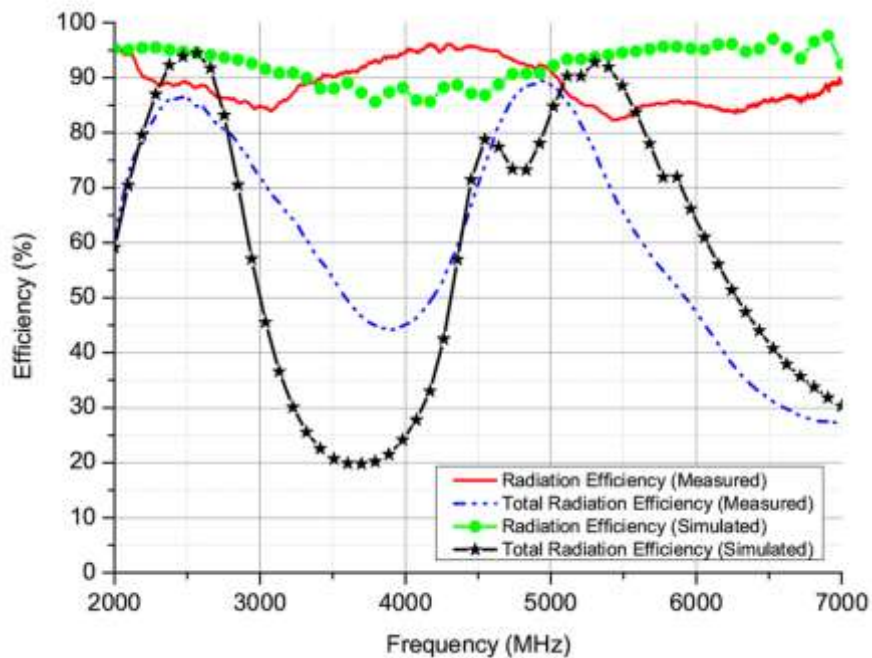


Fig. 3.31: FCTP3 free space measured and simulated efficiencies (%)

From Fig. 3.31 it can be seen that the copper tape based (higher material conductivity) textile antenna is highly efficient in free space conditions. A reasonable agreement is obtained with the simulated assessment. The total radiation efficiency is in good agreement, but the peak in the higher band is seen to be offset when comparing the measured and simulated results. This is a direct result of differences between the measured and simulated radiation efficiency and also the reflection coefficients as Fig. 3.32 suggests.

The differences between the measured and simulated reflection coefficients can be attributed to slight differences in the dimensions between the simulated model and the physical design, and furthermore, the presence of the SMA connector in the physical design can also have an effect.

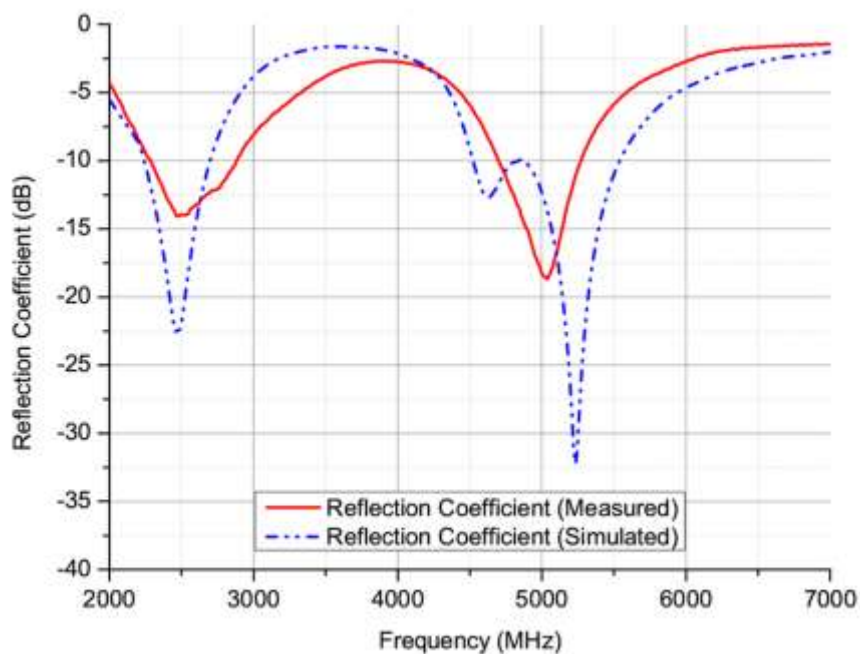


Fig. 3.32: FCTP3 free space measured and simulated reflection coefficients (dB)

The free space performance of the ShieldIt material can now be charted in Figs. 3.33 and 3.34.

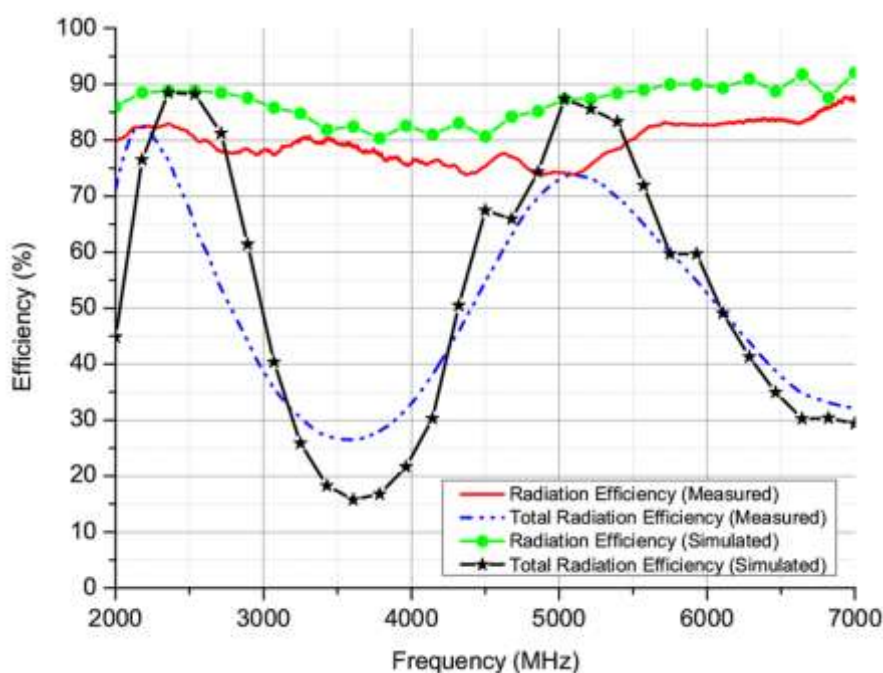


Fig. 3.33: FSHP6 free space measured and simulated efficiencies (%)

Comparing Figs. 3.31 and 3.33 we find that the higher conductivity copper tape material yields higher efficiencies in free space conditions. Differences in the lower frequency band are in the order of 10%. It can be seen that a good agreement is obtained with the simulation results, with the measured trends tracking the simulated values well. Differences in the total radiation efficiency are witnessed in the lower band this time - this results from a frequency shift in the measured and simulated reflection coefficients as proved by Fig. 3.34.

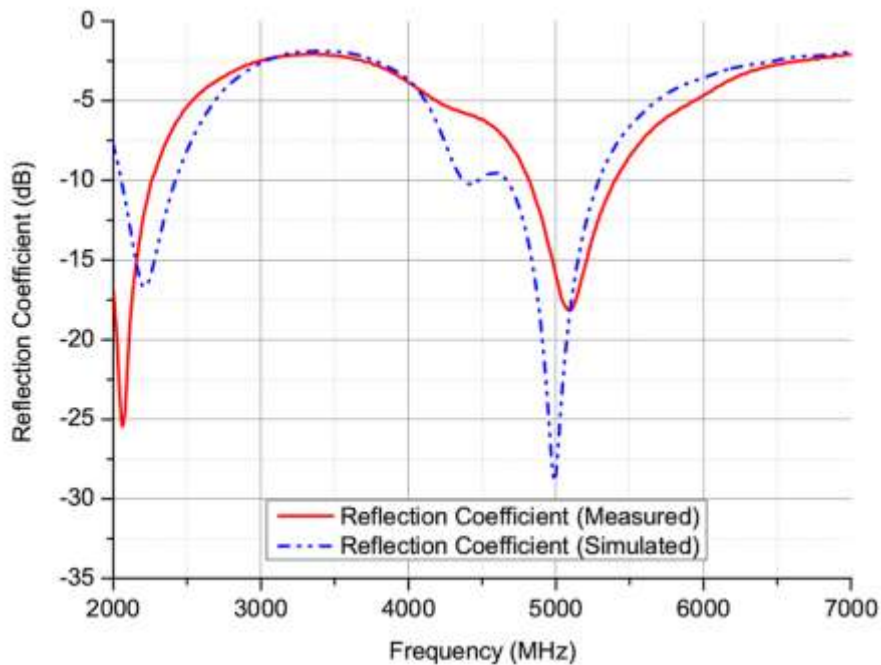


Fig. 3.34: FSHP6 free space measured and simulated reflection coefficients (dB)

3.10.2 On-Body Chest (0 mm) Performance

The on-body experiment for the dual band textile antennas used the exact same measurement set-up and procedures as the previous single band textile antenna investigation (section 3.5.2). Therefore, to avoid repetition, the procedures will not be issued again. Figs. 3.35 and 3.36 detail the on-body performance of the copper tape based antennas (FCTP3), while Figs. 3.37 and 3.38 detail the performance of the ShieldIt textile antenna.

In each figure the on-body results will be issued alongside the free space values so that any performance degradation on-body can be easily assessed.

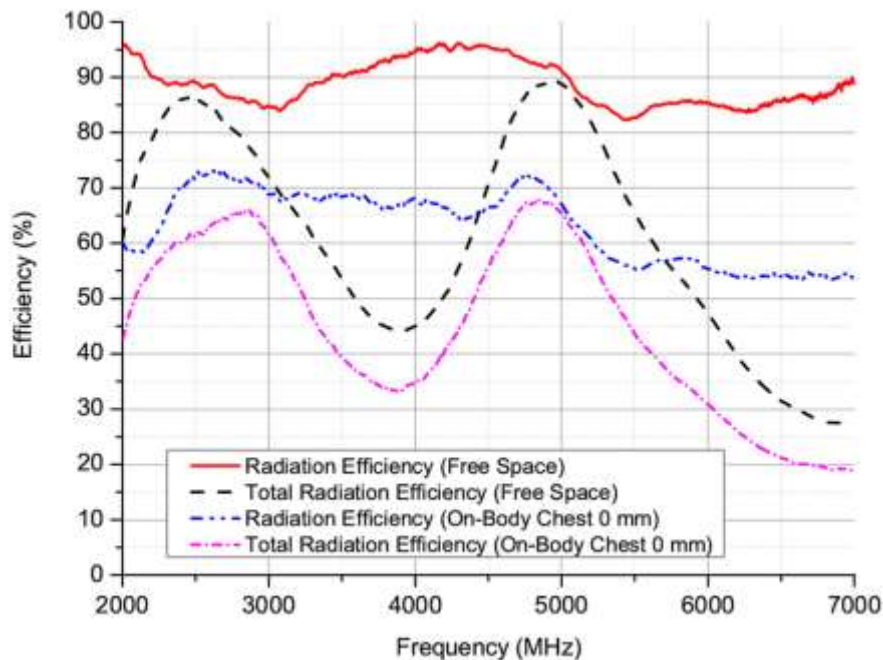


Fig. 3.35: FCTP3 free space and on-body chest (0 mm) efficiencies (%)

From Fig. 3.35 we see a relatively high level of radiation efficiency at the chest location on-body. The radiation efficiency has degraded only 17% in the lower (2.45 GHz) band and 20% in the upper band around 5 GHz. Similar values are also evident concerning the total radiation efficiency. This result is quite remarkable since at the 0 mm proximity distance the results would represent a ‘worse case’ scenario (i.e. the largest loss is expected).

Looking at the profile of the lower band total radiation efficiency, it would appear slightly distorted - this suggests evidence of detuning which is apparent from Fig. 3.36.

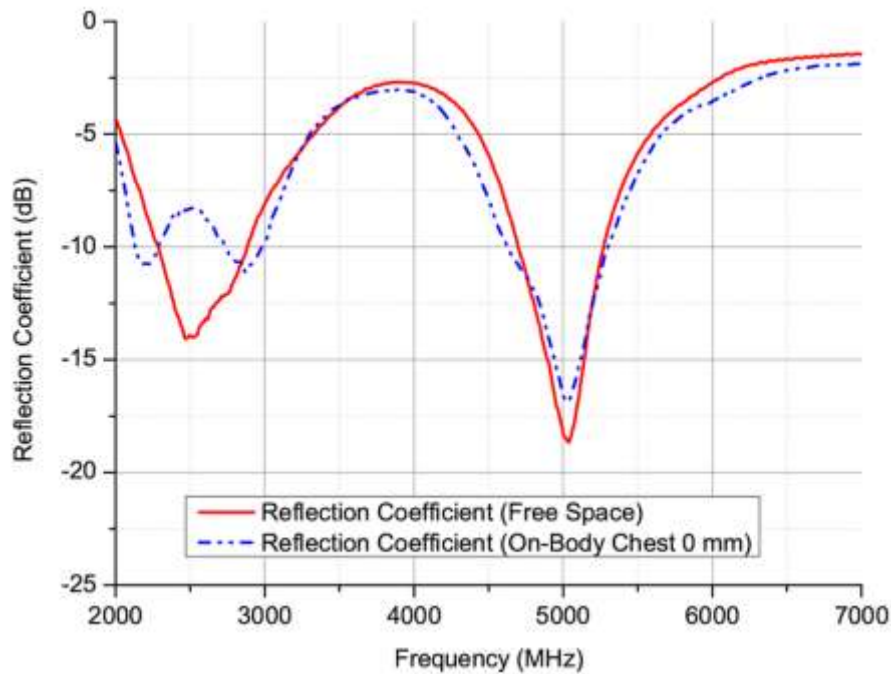


Fig. 3.36: FCTP3 free space and on-body chest (0 mm) reflection coefficients (dB)

We can now assess the ShieldIt antenna (FSHP6) at this location on-body to see how it compares.

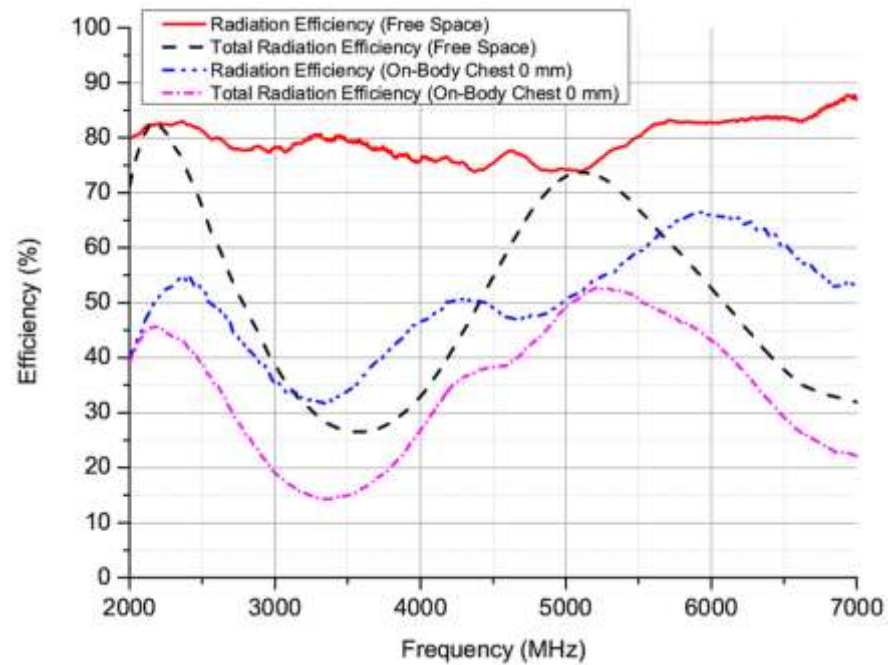


Fig. 3.37: FSHP6 free space and on-body chest (0 mm) efficiencies (%)

Comparing Figs. 3.35 and 3.37 we find that for the larger sized dual band antennas, the higher conductivity material is seen to yield higher efficiencies in both free space and on-body, which conforms completely to expectations this time around.

In terms of the radiation efficiency, the copper tape material (FCTP3) is 17% more efficient on-body than the shieldIt material in the lower band and 18.5% more efficient in the higher band (with respect to where the FCTP3 antenna is impedance matched). Furthermore, with the larger dimension sized antennas, the extreme degradation in performance as the single band (FLSL 0510) antenna is not evident - the efficiencies measured on-body are more or less reasonable.

One trend that requires comment concerns the high frequency on-body performance of FCTP3. Comparing the on-body trends in Figs. 3.35 and 3.37 we see the high frequency performance of the copper tape based antenna degrading sharply, whilst the ShieldIt material has a gradual upwards trend.

The reason for the degraded copper tape performance is believed to be due to peeling and deformation of the edges of the Sierpinski radiator. This is understood to have affected the high frequency radiation characteristics of this antenna, as at higher frequencies the surface current on the antenna will seek to find clusters comparable in size in order to radiate efficiently [24]. Further, it should be noted that a period of six months separated the free space and on-body measurements for this antenna; which can explain the trend witnessed at higher frequencies on-body as opposed to free space.

Fig. 3.38 compares the measured free space and chest (0 mm) reflection coefficient performance of the ShieldIt textile material (FSHP6), where it can be seen that slight detuning is again evident in the lower band - similar to the copper tape based textile antenna. The higher frequency band is again seen not to suffer from any adverse effects from the human body - it remains perfectly impedance matched.

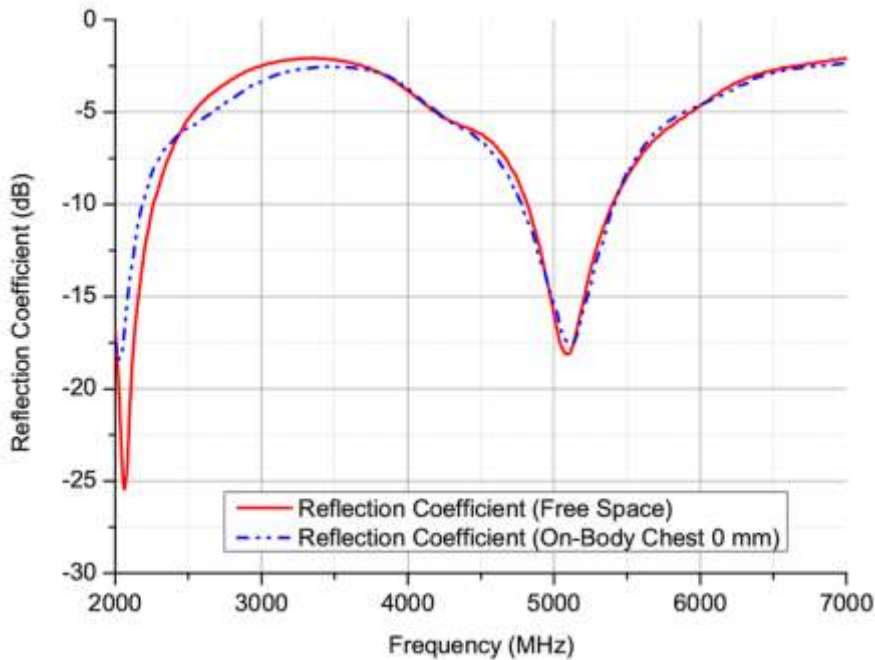


Fig. 3.38: FSHP6 free space and on-body chest (0 mm) reflection coefficients (dB)

3.10.3 On-Body Back (0 mm) Performance

The purpose of this investigation is to firstly investigate whether the larger ground plane sized antennas are sensitive to different locations on-body, and secondly to analyse the repeatability in the measurements over a larger frequency range and at a different on-body location. The measurement set-up for this investigation was configured exactly the same as for the single band investigation back in section 3.5.4; the measurement procedures also remained consistent as previously described.

The efficiency performance and measurement repeatability of FCTP3 on the back at 0 mm is pictured in Fig. 3.39, and the on-body measured reflection coefficient is depicted in Fig. 3.40.

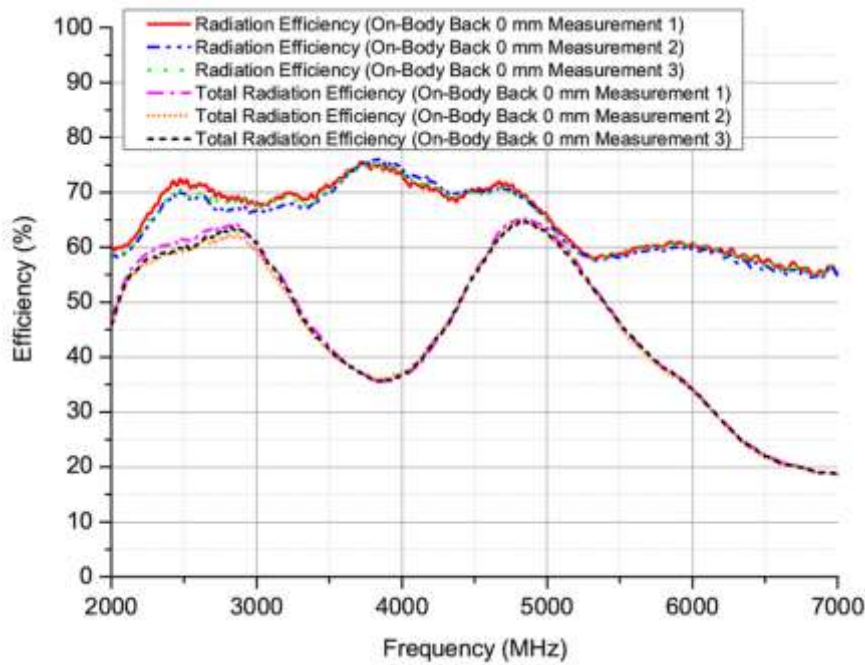


Fig. 3.39: FCTP3 on-body back (0 mm) efficiencies (%) and measurement repeatability

From Fig. 3.39 it can be seen that consistent results are again evident - the repeatability between three separate independent measurements is in the order of 2% at the maximum. It is conclusively proved therefore that with the adoption of the correct measurement procedures (as detailed in this chapter), statistically repeatable and consistent results can be obtained with measurements on real human beings in the RC, irrespective of antenna type, on-body location or different frequency ranges.

The repeatability provides confidence that any measurement undertaken using the procedures detailed in this chapter is correct, as no wild fluctuations or anomalies are seen to be present. Fig. 3.40 details the reflection coefficient of FCTP3 on the back at 0 mm.

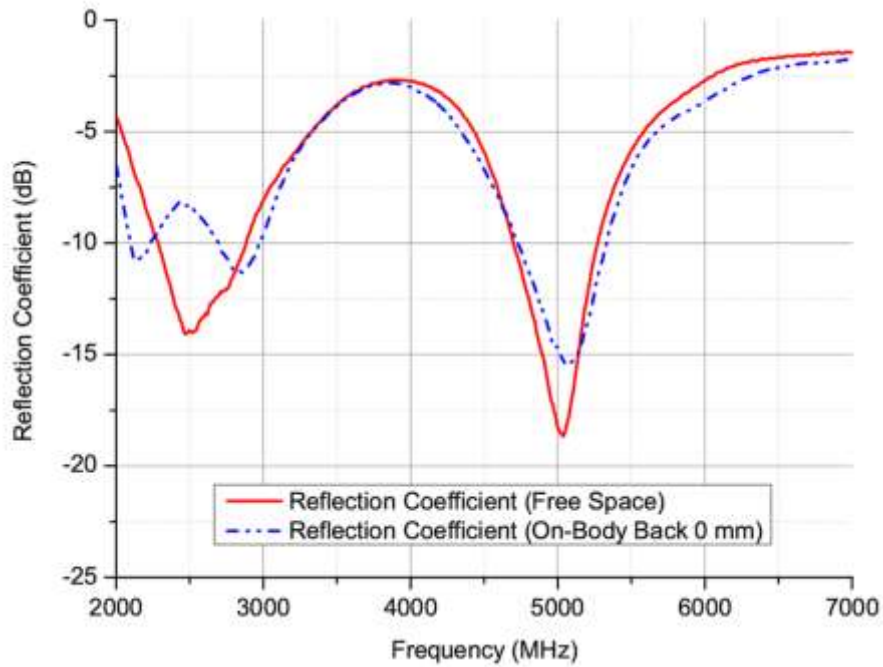


Fig. 3.40: FCTP3 free space and on-body back (0 mm) reflection coefficients (dB)

From Fig. 3.40 we see that de-tuning is evident in lower band only, the higher frequency band remains perfectly impedance matched. The reasons for the de-tuning in the lower band only can be attributed to coupling between the human being and the antenna, and also partly because of the ground plane. To elaborate further, at smaller wavelengths the ground plane should be more effective because of its increased electrical size; hence this is believed responsible here for the evidence witnessed in the lower band only [25].

Fig. 3.41 portrays the on-body performance of FSHP6 at the back location.

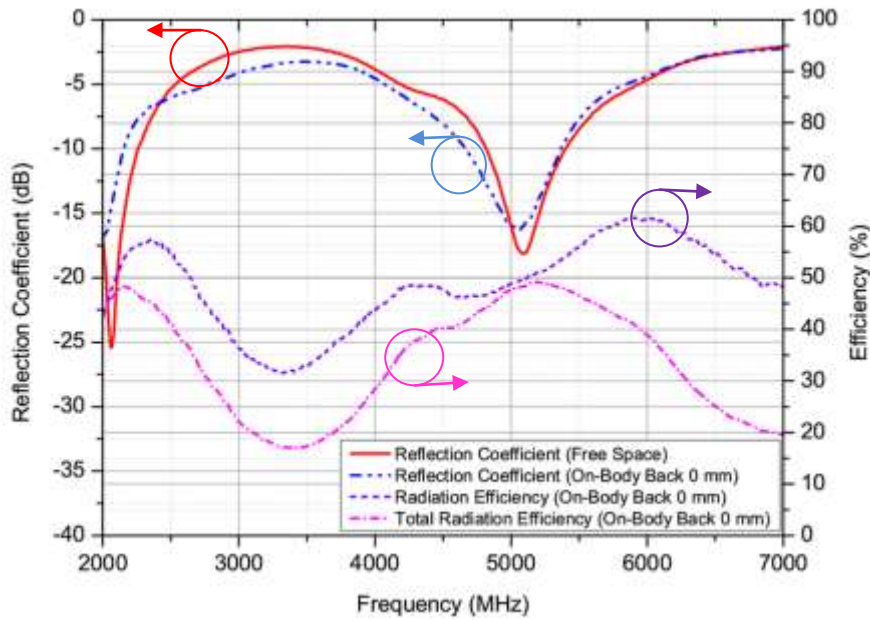


Fig. 3.41: FSHP6 on-body back (0 mm) reflection coefficients (dB) and efficiencies (%)

Comparing Figs. 3.37 and 3.41 (FSHP6 chest 0 mm and back 0 mm respectively) it can be seen that the on-body efficiency results are generally comparable - no discernable difference is witnessed in this case. The lower band reflection coefficient again shows evidence of de-tuning - the frequency shift is seen to be in the order of 90 MHz downwards, rendering the impedance match at 2.45 GHz to be -6.2 dB. Nevertheless, the antenna is not seen to be impedance matched in free space to begin with due to slight differences between the dimensions of the initial simulated design and the manufactured prototype.

The upper band is again seen to be perfectly matched; no de-tuning is evident in this range.

3.11 Theoretical & Simulated Evidence

Drawing conclusions from section 3.10, it is clearly proved that this time, the antenna constructed from the higher conductivity, thinner material (copper tape - FCTP3) outperforms the thicker, lower conductivity ShieldIt textile antenna (FSHP6) in free space and when placed in various locations of the human body. This result conforms completely to expectations this time around. Nevertheless, in this section we seek to provide further evidence that support the measurement conclusions. Similar to section 3.6, the dual band antennas have been mounted (at 1.5 mm) onto a structure whose material parameters have been chosen to emulate muscle at 2.45 GHz ($\sigma = 1.773 \text{ S/m}$ and $\epsilon_r = 52.668$ [22]). Fig.

3.42 depicts the simulated radiation and total radiation efficiency from the two models, showing clearly that the simulated copper tape based textile antenna (FCTP3) agrees with the measurement findings perfectly, in the sense that it exhibits enhanced levels of efficiency in conjunction with the lossy structure.

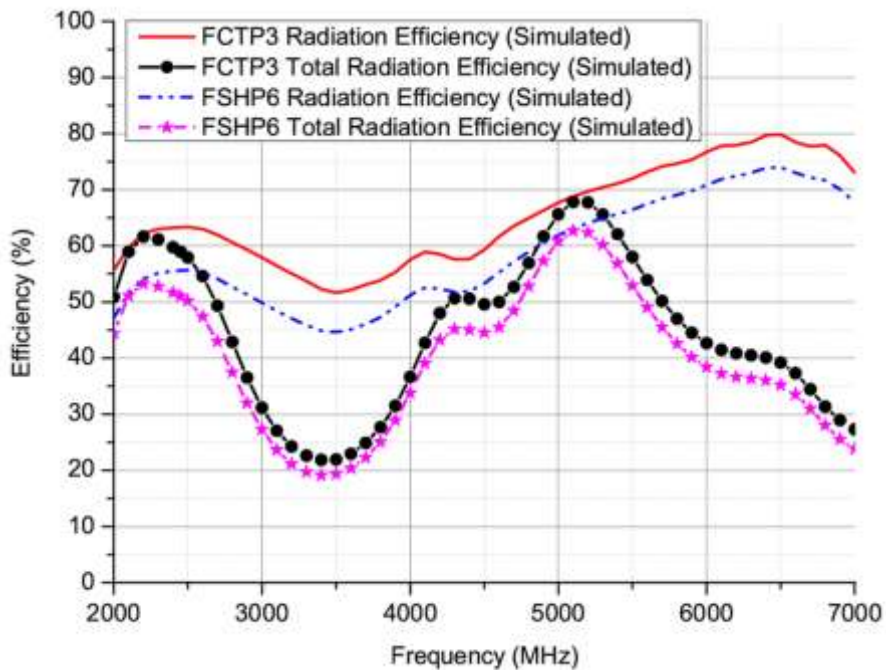


Fig. 3.42: Simulated radiation and total radiation efficiencies on muscle emulated material

3.12 Measurement Uncertainties

For the measurement uncertainties the following aspects are considered. Firstly, it is known from [26] that direct coupling can be a major source of uncertainty during Over the Air (OTA) measurements in the RC; therefore, the direct coupling (expressed as the Rician K factor as detailed in section 2.8) should be as small as possible.

Models were presented in [26] that equate the total standard deviation in the average power transfer function to be comprised of the non line of sight number of independent samples (σ_{NLOS}), the line of sight number of independent samples (σ_{LOS}) and the Rician K factor as detailed in Equation (3.3).

$$\sigma = \sqrt{\frac{(\sigma_{NLOS})^2 + (K_{av})^2 (\sigma_{LOS})^2}{\sqrt{1 + (K_{av})^2}}} \quad (3.3)$$

where: (K_{av}) is the average Rician K factor, comprising the samples obtained from the different stirring mechanisms used throughout the measurements as detailed in Tables V and VI. The standard deviation in dB scale can be presented as an average of $(1+\sigma)$ and $(1-\sigma)$ [27], and is detailed in (3.4).

$$\sigma_{dB} = \frac{10 \{ \log_{10}(1+\sigma) - \log_{10}(1-\sigma) \}}{2} = 5 \log_{10} \left(\frac{(1+\sigma)}{(1-\sigma)} \right) \quad (3.4)$$

To calculate the non line of sight number of independent samples, the autocorrelation function was employed as defined in [28]. After which, [29] was referred to and repeated in terms of the total number of measurement samples used throughout this investigation (710 samples per frequency point), to obtain the correct critical value for use in the autocorrelation calculation at a 99% confidence interval; thus the $1/e = 0.37$ criterion was *not* used in this investigation. The full procedure of how the non line of sight number of independent samples is calculated is detailed in Appendix A1.

The line of sight number of independent samples can be calculated by (3.5) after consultation with [21].

$$\sigma_{LOS} = N_{PL} \times N_{ANTENNA_IND} \quad (3.5)$$

where: N_{PL} = number of position locations = 5, and $N_{ANTENNA_IND}$ = number of independent transmitting antenna locations = 1.

Before any standard deviations are issued, it is important to assess the statistics of the measurement on the different on-body locations used throughout the investigation. Any difference in the measured statistics at different on-body locations could result in a different uncertainty which is unacceptable. Figs. 3.43 and 3.44 detail the measured Rician K factor at different on-body locations for the single band and dual band antennas respectively. A result taken from the free space textile antenna measurements (i.e. no human presence) is also provided to depict the magnitude of the human ‘loading’ to the chamber.

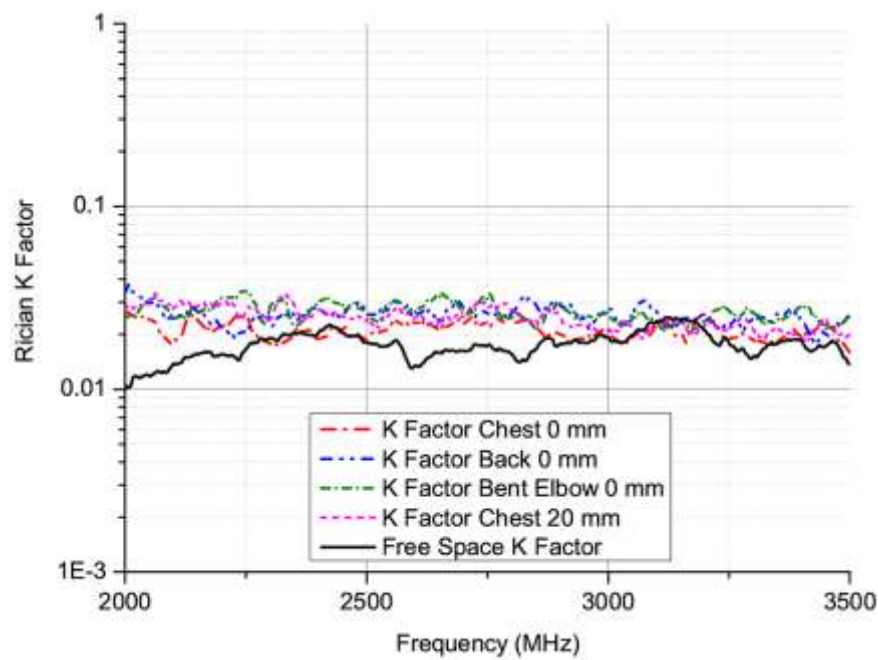


Fig. 3.43: Measured Rician K factor in free space and at different on-body locations for single band antennas

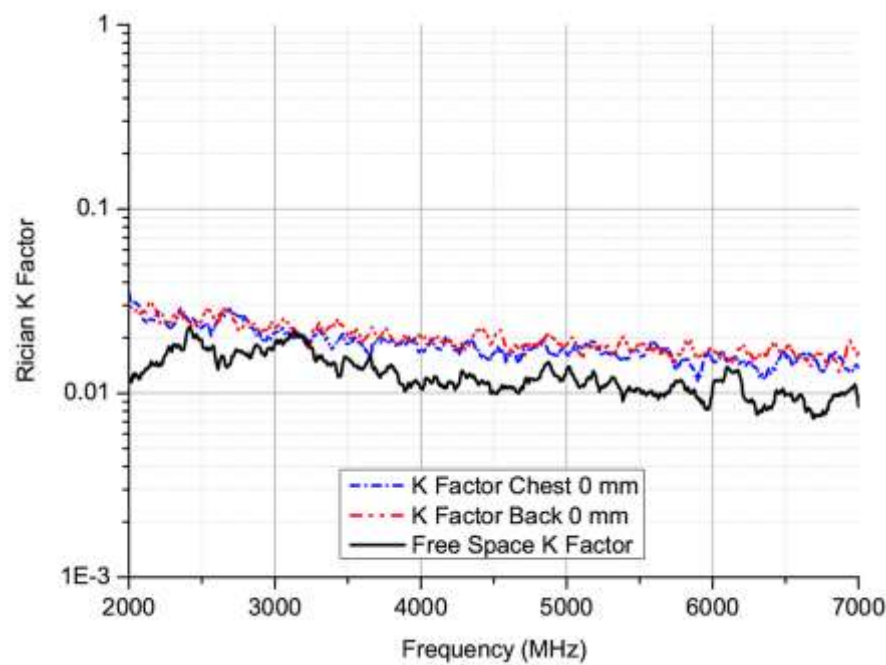


Fig. 3.44: Measured Rician K factor in free space and at different on-body locations for dual band antennas

Figs. 3.43 and 3.44 shows that a slight increase in the proportion of direct power is evident in the on-body measurements from the free space equivalent (no human presence), but this

increase is not seen to be large as to expect a significant rise in the measurement uncertainty resulting from this quantity.

Figs. 3.43 and 3.44 also prove that the measured statistical environment is consistent from one body location to another. No major fluctuations are present which means that similar uncertainty levels are to be expected irrespective of different on-body locations. With respect to different human subjects, Fig. 3.45 depicts the effect on the proportion of direct power in the chamber. Two male and one female subject was used with heights ranging from 1.74 m to 1.8 m and weights ranging from 70.5 kg to 81.3 kg, each subject wearing different clothing. Fig. 3.45 shows that the statistics are comparable irrespective of the human being proving that a consistent platform in the chamber is realised from one human being to the next.

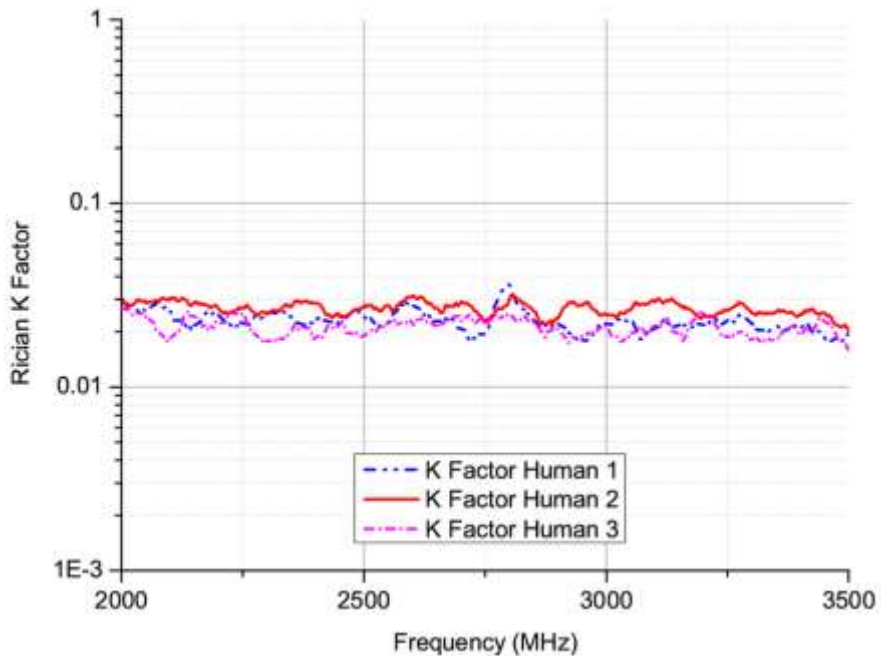


Fig. 3.45: Measured Rician K factor for different human subjects

The final standard deviations can now be issued. Fig. 3.46 depicts the standard deviations in linear and dB scale for the single band antennas as a function of different on-body locations, where it can be seen that a very low overall uncertainty exists (in the order of 0.22dB for all the different locations tested). The uncertainty is also seen to be comparable irrespective of the on-body location chosen, which proves that any different on-body locations or any slight movements that may have occurred in the measurements do not affect the measurement repeatability and/or accuracy.

Fig. 3.47 depicts the dual band measurement uncertainty and proves that similar low uncertainties are present with the larger sized antennas at higher frequencies. The results here further re-enforce that the measurement procedures are thus accurate and correct.

- Please note that the scales in the graphs below *do not* represent a direct conversion from linear to dB and vice-versa. The graphs have been scaled such that both information sets are clearly visible.

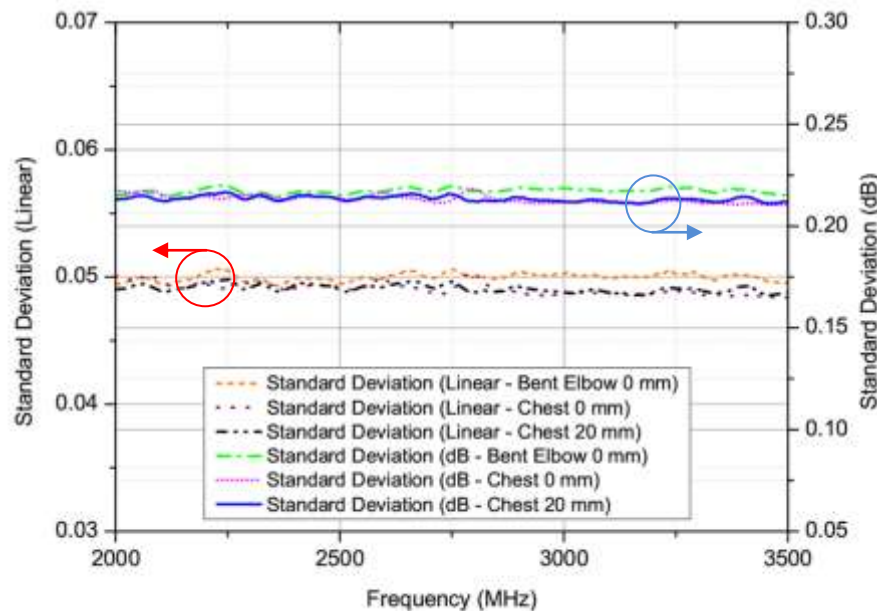


Fig. 3.46: Measurement uncertainties (linear and dB) for single band investigation

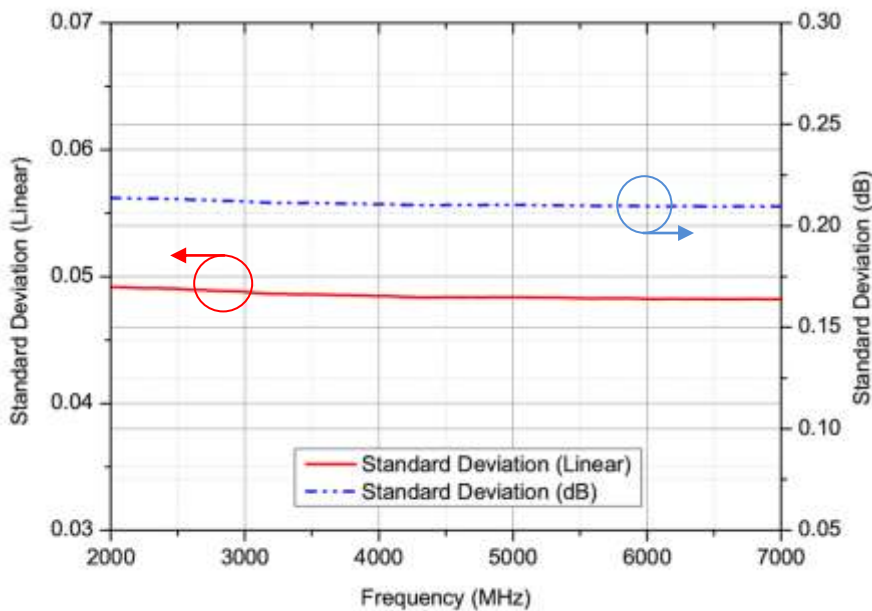


Fig. 3.47: Measurement uncertainties (linear and dB) for dual band investigation

3.13 Conclusion

This chapter has shown that efficiency measurements performed using textile antennas on live human beings can be performed in an accurate and controlled manner, with the repeatability being as close as 2%. The magnitude of on-body losses experienced by a given textile antenna with a small ground plane is seen in this case to be a function of the material properties of that antenna - a higher conductivity, thinner (copper based) textile material which is more efficient in free space is seen to perform worse when placed on body as compared to a lower conductivity and lossier free space textile antenna with the same overall design topology. This is proved to be due to the fact that the lower conductivity material based antenna has given rise to lower electric fields in the body as more power has been lost in the antenna itself for the same input power. This is a remarkable result from this study, constituting new knowledge which can have a profound impact on the material choice for these small sized antennas, in the sense that a higher conductivity material would appear not always to be the best option when operating in close proximity to a human being.

The magnitude of efficiency losses on body has been experimentally shown to be mitigated somewhat by a variation in the distance from the body - a small 20 mm distance from the body (for antenna SHSL) in this case was sufficient to show that a reduction in radiation efficiency can be eliminated by up to 22%. For the single band (SHSL) antenna, at higher frequencies the 20 mm (off) body result approached the radiation efficiency value in free space.

From the experiment that looked to assess the effect of loading the antenna via bending, one can conclude that this aspect is not good practice - the antenna was severely loaded for a considerable period of time (more so than for example if placed on a body part that relaxed the antenna from time to time), and thus the de-tuning performance was seen to be severe in this scenario. From the results seen here this condition cannot be recommended.

For the dual band antennas, the investigation has determined that the higher conductivity based material provides a more resilient operation on-body in terms of its efficiency performance. The results also show this aspect is valid both in free space and on-body operational roles which in this case is entirely expected. This facet is different from the single band study, thus it can be surmised that in addition to the conductivity of the textile material, the ground plane size of the antenna is also a crucial design parameter.

Two facets have presented themselves in the dual band study. Firstly, the ShieldIt material selection had a tendency to frequency de-tune in the lower band of operation. In this case it manifested itself as a frequency shift of 90 MHz. Therefore, any future designs using the shieldIt material that aim to operate on-body should aim to compensate for this de-tuning in the lower band by designing the initial centre frequency with the body in mind to account for the frequency shift. Potentially, another option remains here to increase the distance between the antenna and human subject where we expect reduced coupling. For the copper based antenna, obtaining an enhanced impedance match in the initial design would solve the problem in the lower band.

Secondly, although both measurement and simulated results showed the higher conductivity material used in this study to perform better (in terms of efficiency at the dual band frequencies), the fabricational construction of the copper tape material should be improved for a more robust design. The adhesive backing used for the copper tape construction has a tendency to degrade over time meaning that the edges of the Sierpinski gasket began to peel and deform - this is believed to have affected the practical high frequency efficiency performance of the antenna. A more robust method might be to use a copper based textile and stitch this to the fleece substrate instead. On the whole however, the investigation has confirmed the textile antenna is a strong candidate for use in the on-body role. With regards to the measurement practices and facility, the methods utilised have yielded an accurate and repeatable series of results; this validates the RC's use for this type of measurement. Repeatability in the dual band measurement results is also seen to be in the order of 2% at the maximum and the uncertainty in the order of 0.2 dB, which proves that any (inevitable) subtle human movements have not affected the accuracy.

It has also been proved that the statistical measurement environment is consistent irrespective of different on-body locations or different human subjects. This is a useful fact, proving the suitability of the RC facility.

3.14 References

- [1] P. Salonen, L. Sydanheimo, M. Keskilammi, and M. Kivikoski, "A small planar inverted-F antenna for wearable applications," in *Wearable Computers, 1999. Digest of Papers. The Third International Symposium on*, 1999, pp. 95-100.
- [2] P. Salonen, M. Keskilammi, J. Rantanen, and L. Sydanheimo, "A novel Bluetooth antenna on flexible substrate for smart clothing," in *Systems, Man, and Cybernetics, 2001 IEEE International Conference on*, 2001, pp. 789-794 vol.2.

- [3] P. J. Soh, G. A. E. Vandenbosch, S. L. Ooi, and M. R. N. Husna, "Wearable dual-band Sierpinski fractal PIFA using conductive fabric," *Electronics Letters*, vol. 47, p. 365, 2011.
- [4] P. J. Soh, G. A. E. Vandenbosch, O. Soo Liam, and N. H. M. Rais, "Design of a Broadband All-Textile Slotted PIFA," *Antennas and Propagation, IEEE Transactions on*, vol. 60, pp. 379-384, 2012.
- [5] M. Klemm and G. Troester, "Textile UWB Antennas for Wireless Body Area Networks," *Antennas and Propagation, IEEE Transactions on*, vol. 54, pp. 3192-3197, 2006.
- [6] W. Zheyu, Z. Lanlin, D. Psychoudakis, and J. L. Volakis, "GSM and Wi-Fi textile antenna for high data rate communications," in *Antennas and Propagation Society International Symposium (APSURSI), 2012 IEEE*, 2012, pp. 1-2.
- [7] J. Lilja, P. Salonen, T. Kaija, and P. De Maagt, "Design and Manufacturing of Robust Textile Antennas for Harsh Environments," *Antennas and Propagation, IEEE Transactions on*, vol. 60, pp. 4130-4140, 2012.
- [8] M. Hirvonen, C. Bohme, D. Severac, and M. Maman, "On-Body Propagation Performance With Textile Antennas at 867 MHz," *Antennas and Propagation, IEEE Transactions on*, vol. 61, pp. 2195-2199, 2013.
- [9] Q. Bai and R. J. Langley, "Effect of bending and crumpling on textile antennas," in *Antennas and Propagation for Body-Centric Wireless Communications, 2009 2nd IET Seminar on*, 2009, pp. 1-4.
- [10] Z. H. Hu, Y. I. Nechayev, P. S. Hall, C. C. Constantinou, and H. Yang, "Measurements and Statistical Analysis of On-Body Channel Fading at 2.45 GHz," *Antennas and Wireless Propagation Letters, IEEE*, vol. 6, pp. 612-615, 2007.
- [11] D. B. Smith, L. W. Hanlen, J. Zhang, D. Miniutti, D. Rodda, and B. Gilbert, "First- and second-order statistical characterizations of the dynamic body area propagation channel of various bandwidths," *annals of telecommunications - annales des télécommunications*, vol. 66, pp. 187-203, 2010.
- [12] K. Minseok and J. I. Takada, "Statistical Model for 4.5-GHz Narrowband On-Body Propagation Channel With Specific Actions," *Antennas and Wireless Propagation Letters, IEEE*, vol. 8, pp. 1250-1254, 2009.
- [13] G. A. Conway, W. G. Scanlon, C. Orlenius, and C. Walker, "In situ measurement of UHF wearable antenna radiation efficiency using a reverberation chamber," *Antennas and Wireless Propagation Letters, IEEE*, vol. 7, pp. 271-274, 2008.
- [14] "IEEE Standard Definitions of Terms for Antennas," *IEEE Std 145-1993*, p. i, 1993.
- [15] G. Le Fur, C. Lemoine, P. Besnier, and A. Sharaiha, "Performances of UWB Wheeler Cap and Reverberation Chamber to Carry Out Efficiency Measurements of Narrowband Antennas," *Antennas and Wireless Propagation Letters, IEEE*, vol. 8, pp. 332-335, 2009.
- [16] X. Chen, P. S. Kildal, "Accuracy of antenna input reflection coefficient and mismatch factor measured in reverberation chamber," in *Antennas and Propagation, 2009. EuCAP 2009. 3rd European Conference on*, 2009, pp. 2678-2681.
- [17] L. Juha and P. Salonen, "On the modeling of conductive textile materials for SoftWearAntennas," in *Antennas and Propagation Society International Symposium, 2009. APSURSI '09. IEEE*, 2009, pp. 1-4.
- [18] www.lessemf.com/fabric.html, ed, 1996-2013.

- [19] W. G. Scanlon and N. E. Evans, "Numerical analysis of bodyworn UHF antenna systems," *Electronics & Communication Engineering Journal*, vol. 13, pp. 53-64, 2001.
- [20] P. S. Hall, H. Yang, Y. I. Nechayev, A. Alomalny, C. C. Constantinou, C. Parini, *et al.*, "Antennas and Propagation for On-Body Communication Systems," *Antennas and Propagation Magazine, IEEE*, vol. 49, pp. 41-58, 2007.
- [21] S. J. Boyes, P. J. Soh, Y. Huang, G. A. E. Vandenbosch, and N. Khiabani, "Measurement and Performance of Textile Antenna Efficiency on a Human Body in a Reverberation Chamber," *Antennas and Propagation, IEEE Transactions on*, vol. PP, pp. 1-1, 2012.
- [22] P. S. Hall and H. Yang, *Antennas and Propagation for Body-centric Wireless Communications*, 2nd ed.: Artech House, 2012.
- [23] P. J. Soh, S. J. Boyes, G. A. E. Vandenbosch, Y. Huang, and S. L. Ooi, "On-body characterization of dual-band all-textile pifa," *Progress In Electromagnetics Research B*, vol. 129, pp. 517-539, 2012.
- [24] C. Puente-Baliarda, J. Romeu, R. Pous, and A. Cardama, "On the behavior of the Sierpinski multiband fractal antenna," *Antennas and Propagation, IEEE Transactions on*, vol. 46, pp. 517-524, 1998.
- [25] S. J. Boyes, P. J. Soh, Y. Huang, G. A. E. Vandenbosch, and N. Khiabani, "On-body performance of dual-band textile antennas," *Microwaves, Antennas & Propagation, IET*, vol. 6, pp. 1696-1703, 2012.
- [26] P. S. Kildal, S. H. Lai, and X. M. Chen, "Direct Coupling as a Residual Error Contribution During OTA Measurements of Wireless Devices in Reverberation Chamber," *2009 IEEE Antennas and Propagation Society International Symposium and Usnc/Ursi National Radio Science Meeting, Vols 1-6*, pp. 1428-1431, 2009.
- [27] P. S. Kildal, X. Chen, C. Orlenius, M. Franzen, and C. S. L. Patane, "Characterization of Reverberation Chambers for OTA Measurements of Wireless Devices: Physical Formulations of Channel Matrix and New Uncertainty Formula," *Antennas and Propagation, IEEE Transactions on*, vol. 60, pp. 3875-3891, 2012.
- [28] "BS EN 61000-4-21:2011 Electromagnetic compatibility (EMC). Testing and measurement techniques. Reverberation chamber test methods," ed, 2011.
- [29] H. G. Krauthäuser, T. Winzerling, J. Nitsch, N. Eulig, and A. Enders, "Statistical interpretation of autocorrelation coefficients for fields in mode-stiffed chambers," *EMC 2005: IEEE International Symposium on Electromagnetic Compatibility, Vols 1-3, Proceedings*, pp. 550-555, 2005.

Chapter 4: Multi-Port & Array Antennas

4.1 Introduction

Antenna arrays have many different performance parameters which can be applied as an indicative measure of the merits in a given design. Traditionally, the performance of such arrays has always been characterised in the anechoic chamber (AC) or free space in conjunction with the much sought after radiation pattern characteristics of a given device. However, over the past few years the RC has emerged as a promising candidate for the measurement of multi-port antenna parameters [1, 2]. In these prior published works, the measurement techniques have considered the ‘embedded element’ - that is, one element excited while all other elements are terminated in impedance matched loads.

For Multiple Input Multiple Output (MIMO) characterisation, the embedded element approach is desired because access is required to characterise each individual measured ‘channel’ in turn. The essential requirement for MIMO antennas is that diverse reception must be provided - i.e. the different ports on one single device must be capable of receiving different signals; which implies that the signals at different ports must be sufficiently uncorrelated from one another. This way, when employed in a MIMO system (which consists of several transmitters and receivers), the antenna can provide for a high data rate / high capacity, and when the different signals are combined according to given diversity techniques, they are able to combat fading in multipath propagation environment [3, 4].

Antenna diversity can be realised in various ways. Depending on the environment and the interference that is expected, designers usually have a choice of which scheme to apply. The most common techniques include spatial, polarisation and pattern diversity. Spatial diversity is performed with multiple antennas, usually having the same characteristics, which are physically separated by space. Depending on the environment, sometimes a distance in the order of half wavelength is sufficient [2].

Spatial diversity can become impractical however when designing multiple antennas on small devices such as mobile telephones and laptops as the space available is limited. The addition of multiple feeds in close proximity to one another will inevitably result in high mutual coupling and increased correlation so other techniques are needed. It is well known that the PIFA is widely employed in mobile and portable applications due to its simple design, lightweight construction and desirable radiation pattern [5], there is a motivation and need to use the PIFA topology to develop new diversity antennas having two or more feeds.

For multiport arrays that are not designed for MIMO applications, a distinction should perhaps be created, as in their practical operation they are typically used in an “all excited” manner. Typically, this “all excited” scenario could be active in nature; that is, an array of elements excited individually by separate generators [6]. However, this active nature could be complicated to analyse and would deter from the convenient nature of measurements in the RC that use standard network analysers. Thus, from a measurement perspective, a concession can be made to treat the analysis of multi-port arrays via a “passive” approach instead; that is, a single excitation source exciting all the array elements through a series of power dividers [6]. This would retain the favourable nature of using standard network analysers but would begin to encompass the “all excited”, realistic nature of the array’s operation.

Another benefit to this approach is that the radiation efficiency measurement of the entire array; important because the radiation efficiency performance of such arrays is liable to be affected by mutual coupling, can be effectively treated in a manner similar to a single port antenna - this can simplify the measurement procedures and can also serve to reduce the overall measurement time. In this case, the radiation efficiency is also an important parameter to assess because it provides an indication as to the sensitivity of the array (defined as the ratio of effective area to the noise temperature), which is also a crucial parameter in radio astronomy applications.

An approach of this kind can be found within literature, see [7]. One of the problems discussed in [7] with this type of measurement is that a power loss will be evident from any power divider that is external to any physical array. Therefore, this power loss requires quantifying and “de-embedding” from the array to accurately deduce the array’s performance alone; this forms the focus of this investigation and the method of de-embedding employed is what differs from [7]. In this thesis, a new direct method of de-embedding the power divider by a new modified version of the standard single port efficiency equation is presented, which can simplify the de-embedding process.

This chapter begins with the discussion on the dual feed PIFAs in the following sub-section.

4.2 Definitions: Single Element Dual Feed PIFAs

The single element dual feed PIFA was developed at Liverpool in 2010 by H. T. Chattha [8]. The motivation for the antenna development was to create a small sized MIMO/diversity antenna based on the popular PIFA topology that could be successfully employed into a handset device. Initially however, the antennas were only developed theoretically and numerically with limited practical results. The motivation therefore was fully characterise and demonstrate the practical merits of the new designs. This work results from a collaboration between two parties; the antennas theoretical and numerical development was performed by H. T. Chattha, while the contribution from this author concerns the practical manufacture and all measurements, the measurement processing and any supporting evidence acquired for this thesis. It is beyond the scope of this thesis to present any detailed optimisation analysis and design guidelines for the antennas - please refer to [8] for further information. In this section therefore, the antennas will only be briefly described.

The single element dual feed PIFAs under investigation consist of two separate cases - one where the feeds are aligned parallel to each other (co-polarised feeds); the other has the feeds aligned perpendicular to each other (cross-polarised feeds). For both antennas, the copper radiating top plate has dimensions width = 40 mm and length = 20 mm and ground plane dimensions of width = 40 mm and length = 100 mm. The dielectric material used between the rectangular ground plane and the feeds is FR4, which has a thickness of 1.5 mm and a relative permittivity ($\epsilon_r = 4.4$). The height of the top plate from the FR4 substrate is 10 mm.

Fig. 4.1 and 4.2 depicts the topology of the two antennas under investigation in this study.

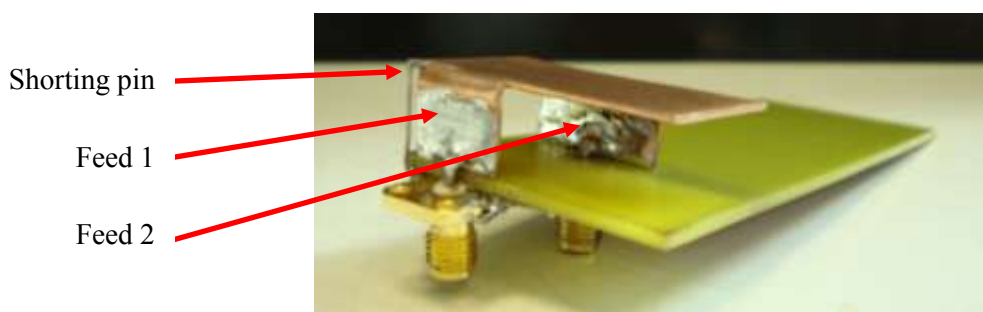


Fig. 4.1: Dual feed PIFA with co-polarised feeds

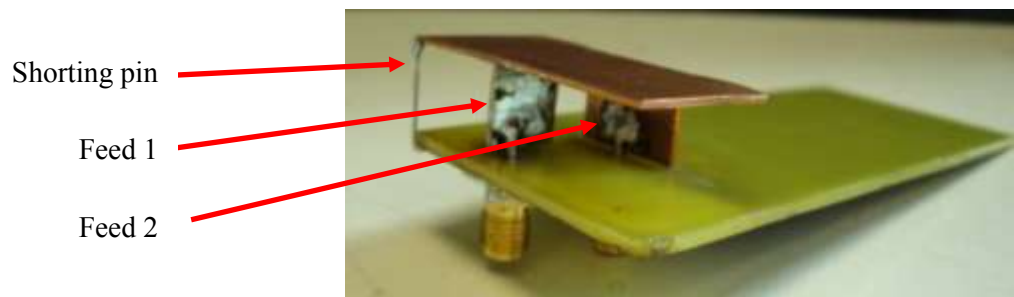


Fig. 4.2: Dual feed PIFA with cross-polarised feeds

The antennas are designed to operate in the 2.45 GHz Bluetooth / WLAN band as a diversity/ MIMO antenna. The electrical separation between the two feeds evident in Figs. 4.1 and 4.2 is 0.17λ at 2.45 GHz.

The isolation between the two closely spaced feeds is provided in this case by etching away a portion of the ground plane between the feeds. In this, it aims to provide a barrier to current flow by means of an antiresonant LC circuit in between the two ports to allow for an increase in isolation. The etching technique is depicted in Fig. 4.3 while the approximate equivalent circuit and current distributions that support the technique can be viewed in [5].



Fig. 4.3: Etching technique to provide isolation between the two feeds

There are other examples in literature to accomplish the isolation of closely spaced feeds; for example, by the insertion of a suspended line between a PIFAs feeding or shorting points [9], or via the use of de-coupling networks [10, 11].

Although prior work has been performed characterising antennas with spatial diversity [12, 13], the novelty of the designs and this work is that the antennas are configured only to provide pattern diversity (co-polarised feeds) and pattern and polarisation diversity (cross-polarised feeds). A brief summary of these techniques can be presented as follows.

Pattern or angle diversity involves multi-port antennas that are configured to produce beams pointing in slightly different directions. This technique is able to provide diversity as it has been stated that the scattered signals associated with these (different) directions resulting from a multipath propagation environment are uncorrelated [14].

Polarisation diversity advocates that multiple feeds on a single device be configured with different polarisations. This technique is clever in the sense that the different (orthogonal) polarisations can serve to minimise the space requirements on a device as it capitalises on the fact that the field orthogonality suffices to de-correlate any signals [14]. Other diversity schemes do exist such as frequency and time diversity. A further in-depth discussion on all the diversity schemes can be found in [14].

With respect to the radiation pattern characteristics of the devices, Figs. 4.4 and 4.5 portray the three dimensional pattern (diversity) for the co-polarised and cross-polarised feeding networks respectively. It can be seen that (pattern) diversity is achieved due to the fact that feed 1 mainly uses the top plate as the its radiating element whereas the feed 2 is using the top plate and the ground plane as the radiating elements [5]. Hence, the radiation patterns produced by the two feeds are different and the diversity is aimed to be achieved through these differing patterns.

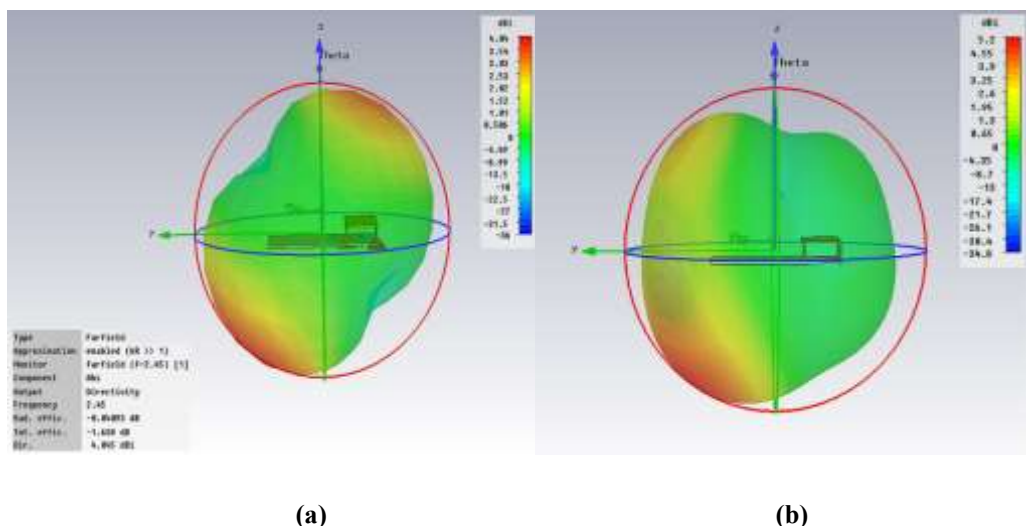


Fig. 4.4: 3D simulated radiation patterns for co-polarised PIFA: (a) Port 1 and (b) Port 2

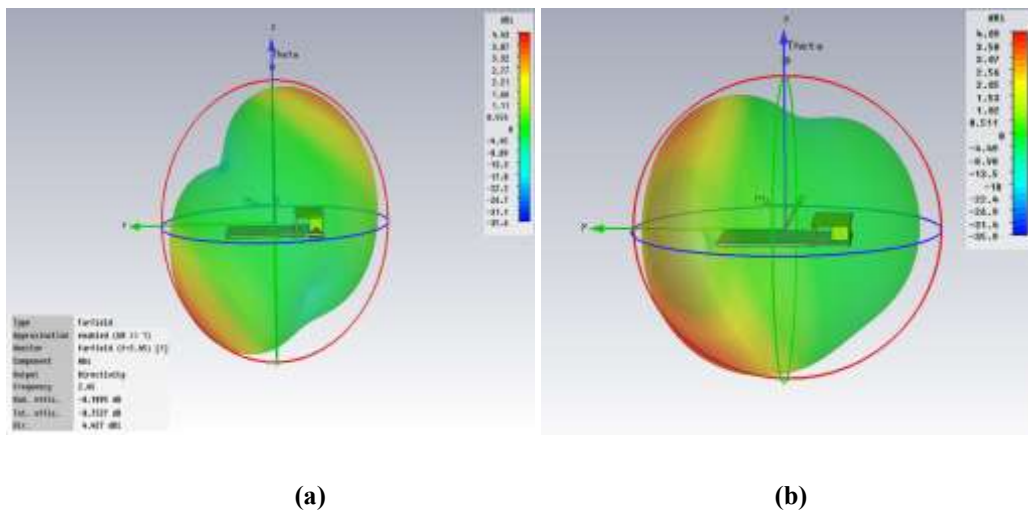


Fig. 4.5: 3D simulated radiation patterns for cross-polarised PIFA: (a) Port 1 and (b) Port 2

4.3 Measurement Parameters

In this thesis, the following performance indicators are sought:

1. Diversity gain
2. Correlation levels
3. Channel capacity
4. Embedded element efficiencies

Performance indicators (1) to (3) in this thesis have been acquired using the RC and their measurement parameters are indicated below. Point (4) has been acquired using an anechoic chamber and will be discussed separately in section 4.7.

With respect to the RC measurements, Table VII details the parameters used in this investigation.

Table VII: Measurement parameters for MIMO investigation

Parameter	Description
Frequency (MHz)	2000 - 3000
Stirring sequences	1 degree mechanical stirring Polarisation Stirring 12.5 MHz frequency stirring
Number of frequency data points	801
Source power (dBm)	-7
Reference antenna	Satimo SH2000
Transmitting antenna	Rohde & Schwarz HF 906
Miscellaneous	MIMO antenna port not being measured terminated in 50 ohm. Any other antenna not being measured (e.g. reference) left inside the chamber and terminated in 50 ohm.

From Table VII, the stirring sequences have been selected to allow for a relatively large amount of data to acquire the performance indicators accurately. The number of frequency data points has been selected to excite a sufficient number of modes throughout the measurement range.

With regards to the miscellaneous row, the requirement for terminating any unused feeds on the MIMO antenna with 50 ohm is to keep the MIMO antenna in a balanced condition throughout, and to prevent any differences occurring in the mismatch from either feed if they were left open circuit [15].

As previously discussed, the requirement for having all antennas inside the chamber at the same time is to ensure that the chamber Q factor is constant from the reference measurement to the MIMO antenna measurement to ensure accuracy.

4.4 Diversity Gain from Cdfs

Before any results are issued, a few definitions are warranted. In the simplest terms, the diversity gain can be expressed as the improvement in the signal to noise ratio (SNR) at the output of a diversity combiner compared to the input of the diversity antenna at a given (usually 1%) cumulative probability level [16]. A more precise definition is possible based upon the type of diversity gain one is interested in [17]:

1. **Apparent diversity gain:** difference between the power levels in dB scale at a given cumulative probability level between the cdf of a combined signal and the cdf of a signal at the antenna port with the strongest average signal level.
2. **Effective diversity gain:** difference between the power levels in dB scale at a given cumulative probability level between the cdf of a combined signal and the cdf of a signal at the port of an ideal single antenna corresponding to 100% radiation efficiency when measured in the same environment.
3. **Actual diversity gain:** difference between the power levels in dB scale at a given cumulative probability level between the cdf of a combined signal and the cdf of a signal at the port of an existing practical single antenna that is to be replaced by the diversity antenna when measured at the same location and in the same environment.

In this thesis, we are interested in the apparent diversity gain only. With regards to the diversity combination techniques, many different schemes have been devised to exploit the (ideal) uncorrelated fading exhibited by separate isolated antenna elements.

In this work, the selection combining (SC) technique has been applied with respect to all diversity gain results that are issued; the reason for this selection is simply because from a signal processing and hardware perspective, it is perhaps one the easiest methods of all to apply [14]. The basic premise of SC will be outlined below; however, the fundamental principles of the other existing combination techniques can be found in [14].

Fig. 4.6 illustrates the principle of selection combining.

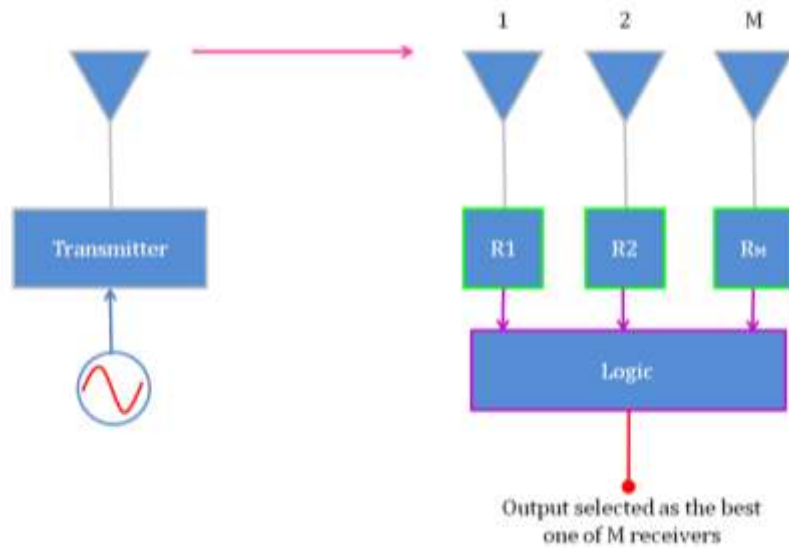


Fig. 4.6: Principle of selection combining

As Fig. 4.6 aims to illustrate, the signal with the highest SNR is simply selected. This is one example of how multipath fading can be overcome - that is, if a signal received by one antenna suffers from fading, anyone of the other antennas should receive a signal with a larger power (providing they are sufficiently uncorrelated), and the largest signal among all receivers is thus selected.

It is possible to calculate the diversity gain from both cdfs and the measured correlation between two or more antenna feeds in the RC. In this sub-section, the cdf approach will receive treatment first.

To begin with, a transfer function from the reference antenna is established as detailed in Equation (4.1). The purpose of this measurement is to ‘calibrate’ the attenuation in the chamber.

$$TF_{REF} = \frac{\langle |S_{21REF}|^2 \rangle}{\left(1 - (|S_{11TX}|)^2\right)\left(1 - (|S_{22REF}|)^2\right)} \quad (4.1)$$

where: $|S_{11TX}|$ = reflection coefficient of the transmitting antenna and $|S_{22REF}|$ = reflection coefficient of the reference antenna. Please note that similar to chapter 3, the reflection coefficient quantities are acquired in an anechoic chamber. The reference transfer function should then be corrected for its known radiation efficiency (η_{REF}) as in (4.2).

$$P_{REF} = \frac{TF_{REF}}{\eta_{REF}} \quad (4.2)$$

Once completed, the reference antenna should be substituted for the MIMO antenna. The transmission coefficient is then measured between the transmitting antenna and both feeds of the antenna (in turn), ensuring that the feed not undergoing measurement is terminated in a matched load (50 ohms in this case). The resulting channel samples ($S_{1\times 2}$); that is, one transmitting and two separate receive channels (Single Input Multiple Output: SIMO), are a function of frequency and the stirring parameters as detailed in Table VII.

It is necessary to then normalise the measured channel samples with respect to the square root of the pre-defined reference power level. The square root is needed because the measured channel samples ($S_{1\times 2}$) are a function of voltage (measured transmission coefficient S-parameters), and the normalisation takes into account the path loss in the chamber, defined by the reference transfer function and the known radiation efficiency in (4.2). Thus, the resulting channel matrix ($H_{1\times 2}$) can be formed by [18].

$$H_{1\times 2} = \frac{S_{1\times 2}}{\sqrt{P_{REF}}} \quad (4.3)$$

Once the channel matrix is formed, the cumulative probability can be calculated by equations (4.4) and (4.5), and is graphed against the relative received power, calculated by equations (4.6) - (4.8).

For the cumulative probabilities, calculate the sum for each respective channel (i):

$$sum_i = \sum_{n=1}^N H_{1\times i} \quad (4.4)$$

where: $i = 1, 2$ and $N = 718$. After which, the cumulative probability ($Cumprob$) can be deduced from:

$$Cumprob_i = \frac{Cumsum_i}{sum_i} \quad (4.5)$$

where: $Cumsum$ represents the cumulative sum.

For the relative received power, the channel matrix (voltage) value for each respective branch is squared:

$$H_{sq_i} = (H_{1xi})^2 \quad (4.6)$$

The time average is then found from (4.7).

$$T_{AV_i} = \frac{1}{N} \sum_{n=1}^N H_{sq_i} \quad (4.7)$$

Each power sample is then normalised to the time average and converted to dB scale by (4.8).

$$P_i(\text{dB}) = 10 \log_{10} \left(\frac{H_{sq_i}}{T_{AV_i}} \right) \quad (4.8)$$

Figs. 4.7 and 4.8 represent the measured apparent diversity gain from cdfs for the co-polarised PIFA and cross polarised PIFA respectively.

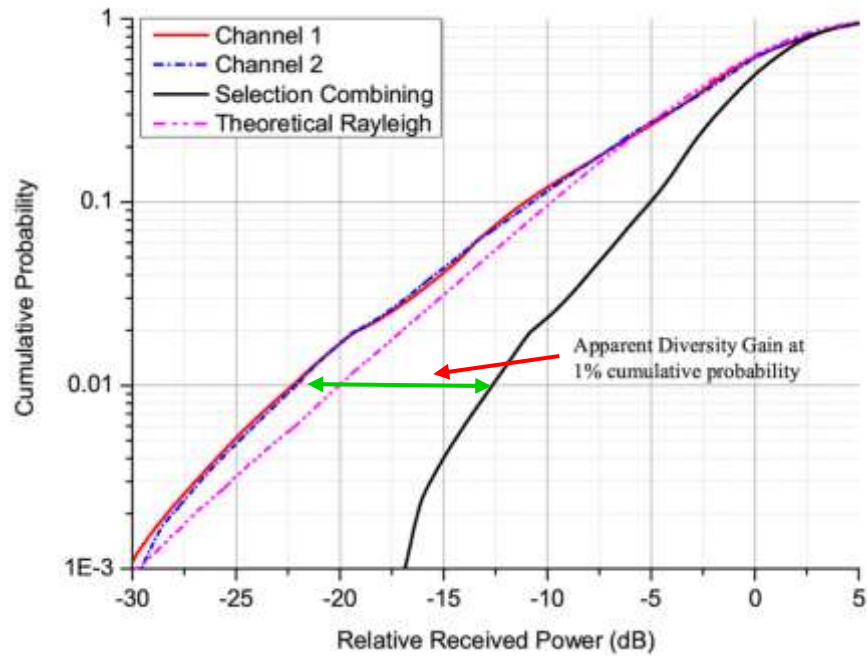


Fig. 4.7: Diversity gain from cdf for co-polarised PIFA

From Fig. 4.7 it can be seen that a high level of apparent diversity gain is evident from the co-polarised design. The power level of the strongest branch at the 1% cumulative probability level (Channel 2) is recorded as -22.104 dB, with the power level of the selection combined level being measured at -12.66 dB. This provides a diversity gain of 9.44 dB.

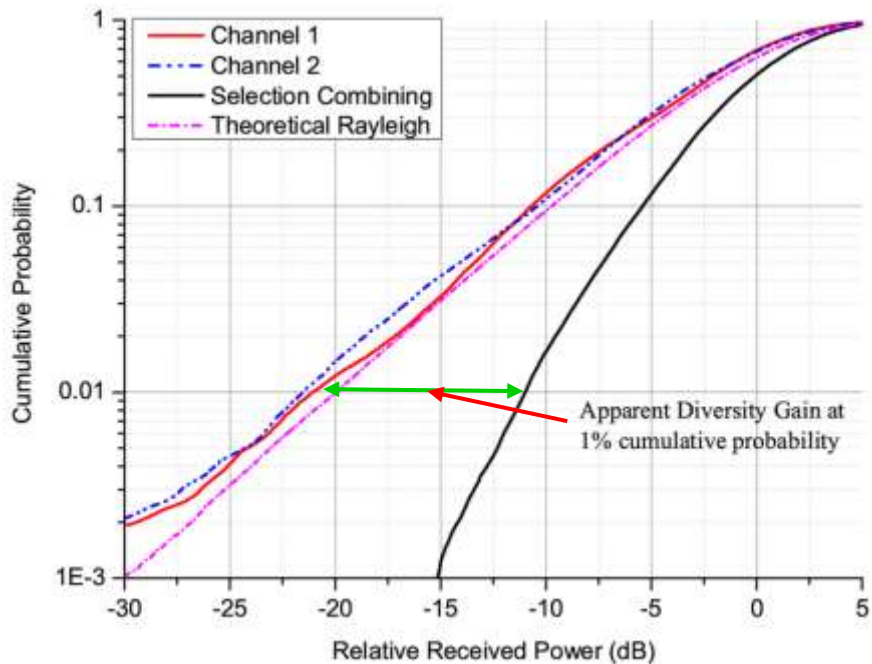


Fig. 4.8: Diversity gain from cdf for cross-polarised PIFA

From Fig. 4.8 it can be seen that a high level of apparent diversity gain is obtained for the cross-polarised design. The power level of the strongest branch at the 1% cumulative probability level (Channel 1) is recorded as -21.086 dB, with the power level of the selection combined level being measured at -10.991 dB. This provides a diversity gain of 10.095 dB; very close to the theoretical two port selection combining maximum of 10.2 dB in this case.

Both channel branches for both co-polarised and cross-polarised designs are seen to follow the theoretical Rayleigh cdf curve well which would suggest that the samples are inherently Rayleigh distributed. However, they are slightly offset to the left of the Rayleigh curves which is due to the fact that the respective branch efficiencies are less than 100% [2]. The theoretical Rayleigh curve here signifies the performance of an ideal lossless (and hypothetical) antenna with 100% efficiency.

So far the evidence would suggest that the antennas perform well, and the isolation technique employed would appear successful in eliminating any detrimental performance effects.

However, we seek further evidence to verify the antennas operational quality and to substantiate the measured levels of diversity gain witnessed.

4.5 Diversity Gain from Correlation

Although the diversity gain can be easily predicted from the measured and calculated cdfs, a degree of information is lost here as all the measured samples for each channel across the entire frequency range have been utilised in order to define the cdfs accurately. In many instances, it could be important to know how the diversity gain varies as a function of frequency. To achieve this, the correlation between measured samples from both the antenna feeds can be measured and calculated as a function of frequency, and the diversity gain thus obtained.

It is well known that the complex correlation coefficient (ρ) can be measured and calculated from the far field embedded element pattern acquired in an anechoic chamber [17]:

$$\rho = \frac{\int \int_{4\pi} G_1(\theta, \varphi) \cdot G_2^*(\theta, \varphi) d\Omega}{\int \int_{4\pi} G_1(\theta, \varphi) \cdot G_1^*(\theta, \varphi) d\Omega \int \int_{4\pi} G_2(\theta, \varphi) \cdot G_2^*(\theta, \varphi) d\Omega} \quad (4.9)$$

where: $G_1(\theta, \varphi)$ and $G_2(\theta, \varphi)$ are the embedded far field functions of ports 1 and 2 respectively - i.e. the far field function when all the other elements are present and terminated in impedance matched loads, and $(^*)$ represents the complex conjugate. It is also possible to express the same complex correlation in terms of S-parameters measured at the antenna ports [17]:

$$\rho = \frac{S_{11}^* S_{12} + S_{21}^* S_{22}}{\left[1 - (|S_{11}|^2 + |S_{12}|^2)\right] \times \left[1 - (|S_{21}|^2 + |S_{22}|^2)\right]} \quad (4.10)$$

Where the square of the complex correlation in (4.10) is equal to the envelope correlation. The form of (4.10) is only valid for lossless antennas; hence it will not be employed here. Using the same RC measured data as in section 4.4, the correlation between both antenna feeds can be found from the measured voltage samples ($S_{1\times 2}$) by use of (4.11) after consultation with [19].

$$\rho = \frac{S_{xy}}{S_x S_y} \quad (4.11)$$

where: x represents the samples obtained for feed 1 in this case and y represents the samples obtained for feed 2. Also:

$$S_{xy} = \frac{1}{N-1} \sum_{j=1}^N (x_j - \bar{x})(y_j - \bar{y}) \quad (4.12)$$

where: $\bar{x} = \frac{1}{N} \sum_{j=1}^N x_j$ and $\bar{y} = \frac{1}{N} \sum_{j=1}^N y_j$

$$S_x^2 = \frac{1}{N-1} \sum_{j=1}^N (x_j - \bar{x})^2 \quad (4.13)$$

And:

$$S_y^2 = \frac{1}{N-1} \sum_{j=1}^N (y_j - \bar{y})^2 \quad (4.14)$$

Figs. 4.9 and 4.10 detail the measured and simulated correlation as a function of frequency for the co-polarised and cross-polarised PIFA respectively. The simulated correlation values have been acquired in CST Microwave Studio from the optimised antenna models developed in [8]. The correlation (and the subsequent diversity gain) values have been calculated from the 3D far field embedded patterns (Eq. 4.9) and *not* from simulated S parameters (Eq. 4.10) for reasons previously explained.

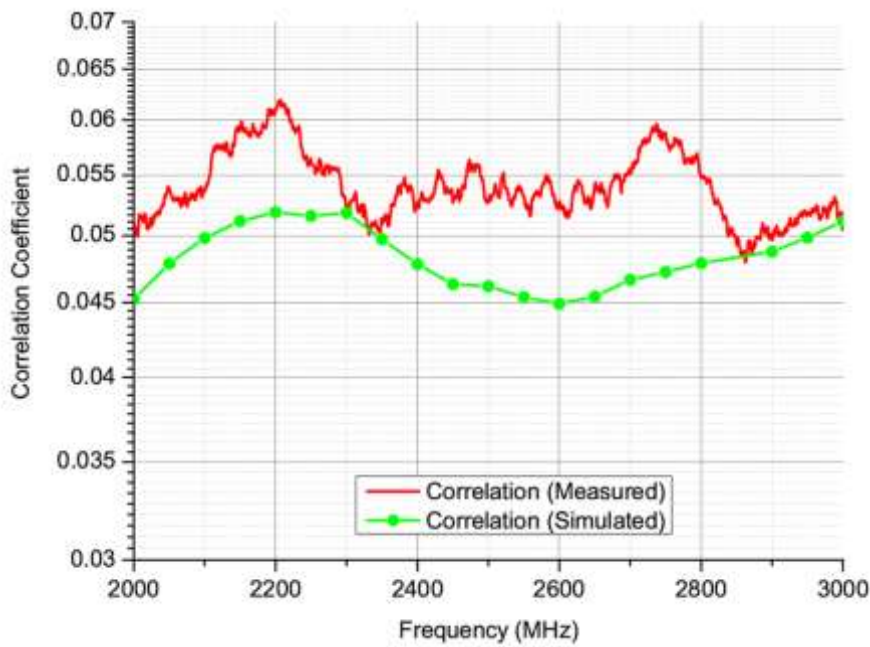


Fig. 4.9: Measured and simulated correlation for co-polarised PIFA

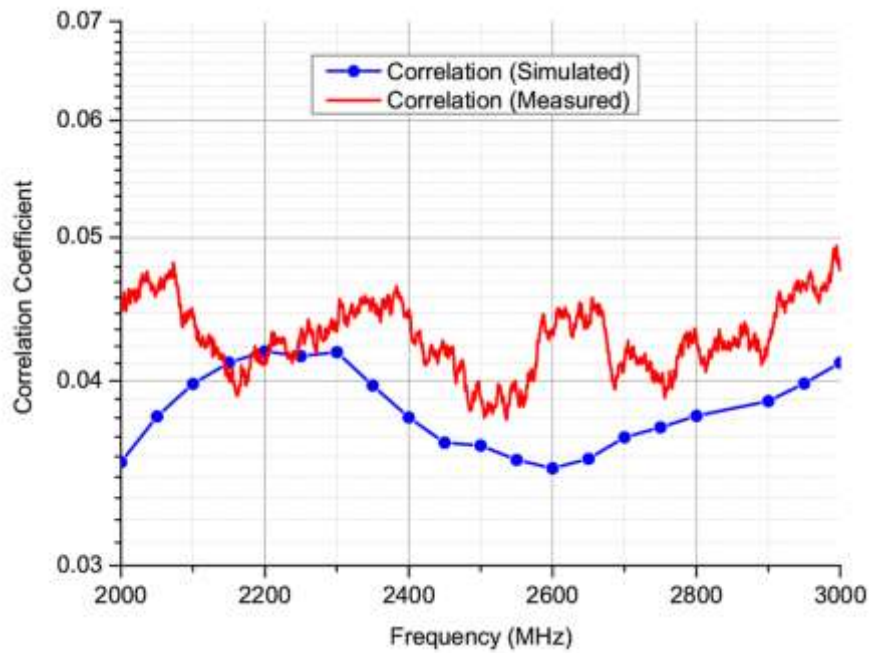


Fig. 4.10: Measured and simulated correlation for cross-polarised PIFA

From Figs. 4.9 and 4.10 it can be seen that the correlation levels, measured from voltage samples obtained at both antenna ports, are very low indeed. Both figures prove that the respective feeds for both the co-polarised and cross-polarised designs are well isolated from

one another, and as such, the respective voltage samples obtained at either port are substantially different. The agreement with simulated values is also seen to be very good; generally, differences in the order of 0.01 are witnessed.

The low values of measured correlation in Figs. 4.9 and 4.10 potentially validate the diversity gain results obtained from the cdfs, as a low correlation between the antenna ports can give rise to a high level of diversity gain as we can see next.

Mathematically, the standard definition for diversity gain (DG), estimated from the complex correlation goes as [1].

$$DG = 10\sqrt{1 - |\rho|^2} \quad (4.15)$$

where: $\sqrt{1 - |\rho|^2}$ is the approximate expression for the correlation efficiency - i.e. the reduction in diversity gain due to the correlation between the two antenna feeds. Assuming (two port) selection combining techniques, it is possible to revise (Eq. 4.15) to [20]:

$$DG = 10.48\sqrt{1 - |\rho|^2} \quad (4.16)$$

where: the 10.48 in (Eq. 4.16) is quickly proved as follows:

$$\begin{aligned} 0.01 &= 1 - e^{-SNR} \Rightarrow SNR = -\ln(0.99) = 0.01 = -20dB \\ 0.01 &= 1 - (e^{-SNR})^2 \Rightarrow SNR = -\ln(1 - \sqrt{0.01}) = 0.105 = -9.8dB \end{aligned} \left. \right\} 10.2dB = 10.48 \quad (4.17)$$

Figs. 4.11 and 4.12 detail the measured and simulated diversity gains, calculated from the correlation using (4.16), for the co-polarised and cross-polarised designs respectively.

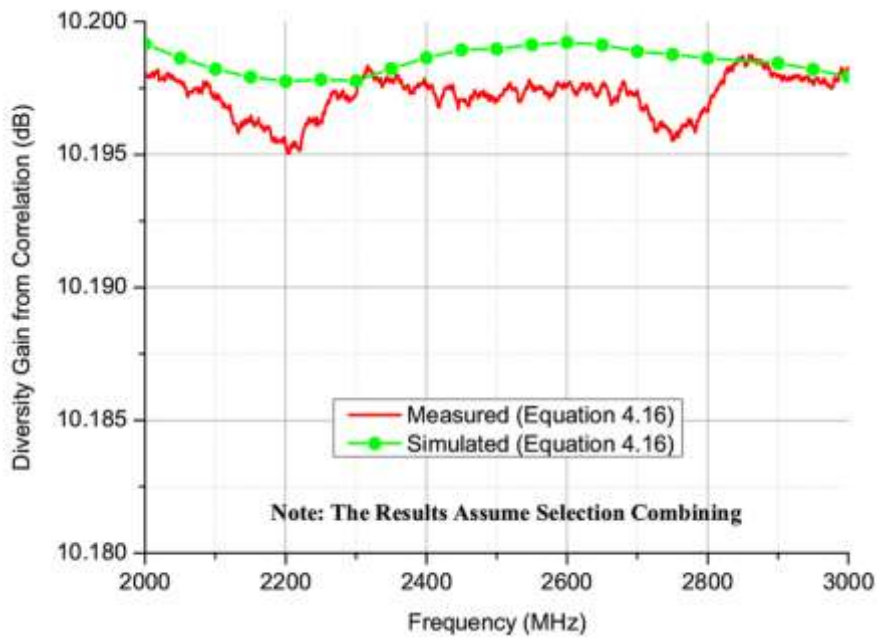


Fig. 4.11: Measured and simulated diversity gain from correlation for co-polarised PIFA

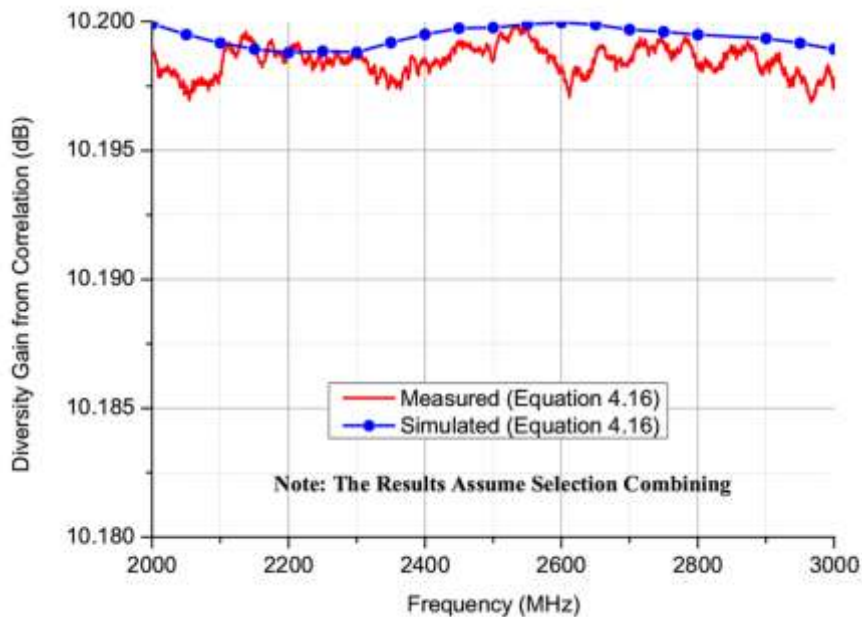


Fig. 4.12: Measured and simulated diversity gain from correlation for cross-polarised PIFA

From Figs. 4.11 and 4.12 we see that very high levels of diversity gain are witnessed due to the very low correlation levels between both feeds on each respective antenna. The (average) difference in diversity gain between the cdf deduced and the correlation deduced results for the co-polarised design is 0.76 dB, while for the cross-polarised design the difference is 0.103 dB. This proves that from either method (cdf or correlation deduced), the results are

generally comparable to one another. Further, the results from the correlation analysis substantiate the accuracy in the cdf measurement results, proving its appropriateness and correctness. To conclude this sub-section, it is proved therefore that small antennas with closely spaced feeds that cannot employ spatial diversity can perform successfully in a MIMO operational role.

4.6 Channel Capacity

The channel capacity is a measure of how many bits per second can be transmitted through a radio channel per Hz - a quantity which can also be referred to as the spectral efficiency [1]. By the use of the same normalised channel samples from the diversity gain measurement (Eq. 4.3), and assuming that the receiver has perfect channel state information, the channel capacity can be deduced from the measured channel matrices by [18]:

$$C = \left\langle \log_2 \left\{ \det \left(I_{1 \times 2} + \frac{SNR}{N_{TX}} (H_{1 \times 2}) \left(H_{1 \times 2}^T \right) \right) \right\} \right\rangle \quad (4.18)$$

where: I = identity matrix, N_{TX} = number of transmitting antennas = 1, and $(^T)$ signifies the complex conjugate transpose. The average notation in (4.18) is required because the channel capacity and signal to noise ratio (SNR) are subject to fading with time in the RC. Hence, the capacity needs to be averaged over the statistical distribution in the channel [17].

Fig. 4.13 details the measured 1×2 (SIMO) channel capacity for the co-polarised and cross-polarised designs. In Fig. 4.13, the measured result is compared against a maximum theoretical capacity that assumes that the two receive ports are completely uncorrelated. The maximum theoretical capacity for a parallel 1×2 (SIMO) channel can be calculated from [17]:

$$C_{1 \times 2} = \log_2 (1 + SNR_{TX1_RX1} + SNR_{TX1_RX2}) \quad (4.19)$$

From Fig. 4.13 it can be seen that the two designs yield a high level of capacity owing to the low correlation levels. The cross-polarised design is seen to exhibit slightly higher levels of capacity - this can be attributed to the slightly reduced correlation levels between the two antenna ports as proved in Figs. 4.9 and 4.10.

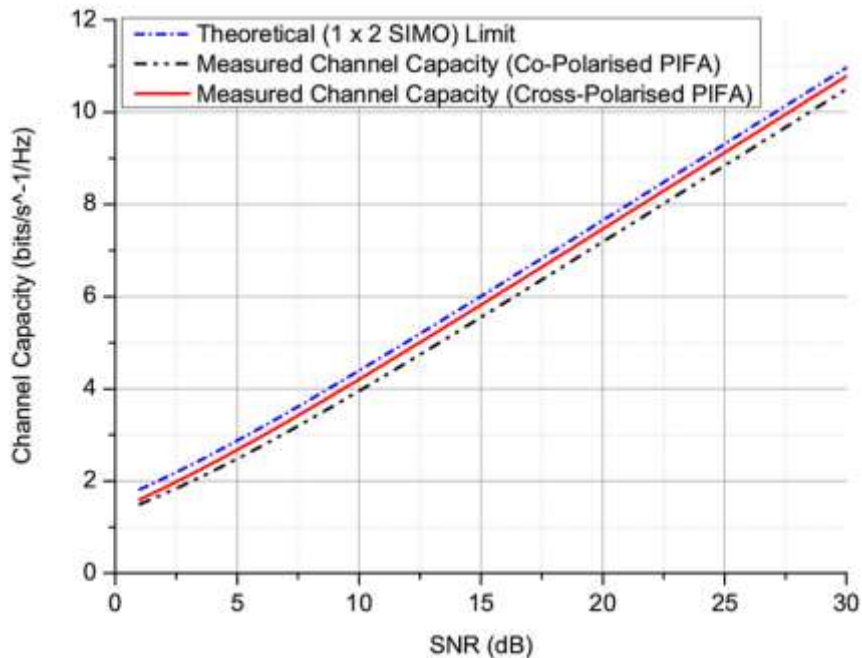


Fig. 4.13: Measured and theoretical channel capacity as a function of SNR

In [18], a discussion was presented concerning the accuracy of the channel capacity model in (4.18) - referred to as the ‘full correlation model’ against an alternative channel format referred to as the ‘Kronecker model’. The difference between the two formats is in the construction of the channel matrix - the Kronecker model relies on the use of a covariance matrix format which differs slightly from the adopted procedures used throughout this thesis. In [18] it was shown that the models predicted the same capacity level; however, when using a small RC, the capacity could be overestimated using both models at high SNR’s and for more than three receive elements.

It was concluded that the subsequent reason for the overestimation was that the measured channel samples did not satisfy Multivariate Normality (MVN) - i.e. the measured channel samples were not jointly normally distributed, contravening the single antenna normal statistical model as discussed back in chapter 2.

In appendix A2, the normality of the two receive channels is put to the test to provide confidence in the estimation of the channel capacity for both designs in Fig. 4.13.

4.7 Embedded Element Efficiency

The embedded element efficiency - that is, the efficiency of the MIMO antenna when one port is excited and the unused ports are terminated in impedance matched loads, can be expressed and treated simply by the use of S-Parameters.

The quantities derived here are based upon the *total embedded radiation efficiency* - i.e. mismatch factors due to imperfect impedance matching are included. It is stated in [17] that if the diversity antenna is constructed from materials with small ohmic losses, then the major contributions towards the total radiation efficiency are from the reflections on the excited port and the absorption of power in the impedance matched terminations.

The difference between the power that is accepted by the excited port (P_{ACC}) and the absorption in the impedance matched ports equates to the total radiated power (P_{RAD}). From [17], which assumed the use of a two port network model, the power dissipated on the impedance matched port (assumed as port 2) can be expressed as:

$$\eta_{ABS} = \frac{P_{RAD}}{P_{ACC}} = \frac{1 - |S_{11}|^2 - |S_{12}|^2}{1 - |S_{11}|^2} \quad (4.20)$$

The power accepted by the excitation port (assumed as port 1) can be stated as [17]:

$$\eta_{MISMATCH} = 1 - |S_{11}|^2 \quad (4.21)$$

Thus the total embedded element efficiency is expressed as [17]:

$$\eta_{TOT_EMBED} = \eta_{ABS} \times \eta_{MISMATCH} = 1 - |S_{11}|^2 - |S_{12}|^2 \quad (4.22)$$

From (4.22), using the assumption that the ohmic losses in the construction materials are small and excitation port is well impedance matched, the dominant contribution towards the efficiency is from the mutual coupling between the antenna ports. That is, the higher the mutual coupling, the more power will be dissipated in the loads of the other antenna ports and the lower the resultant efficiency will be. It is also stated from [17] that the mutual coupling term represents a fundamental limitation in conventional antenna arrays - that is if the inter-element spacing is small (typically < 0.5 wavelengths), the mutual coupling can offer a severe reduction in efficiency [21].

An additional efficiency factor should be present in (4.22) if the ohmic losses are to be considered. In the results to follow, the assumption that the ohmic losses are small has been applied. It is felt that this is a reasonable assumption to make in this case, since the antennas are constructed from high quality copper having a large material conductivity ($\approx 5.7 \times 10^7$ S/m at 2.45 GHz). Figs. 4.14 and 4.15 detail the measured and simulated S-parameters for the co-polarised and cross-polarised design respectively, while Figs. 4.16 and 4.17 detail the measured and simulated embedded element efficiencies.

All measured parameters herewith were acquired in an anechoic chamber - the same justification presented in section 3.2 on page 64 applies. All unused ports in the measurements have been terminated in impedance matched loads (50 ohms in this case).

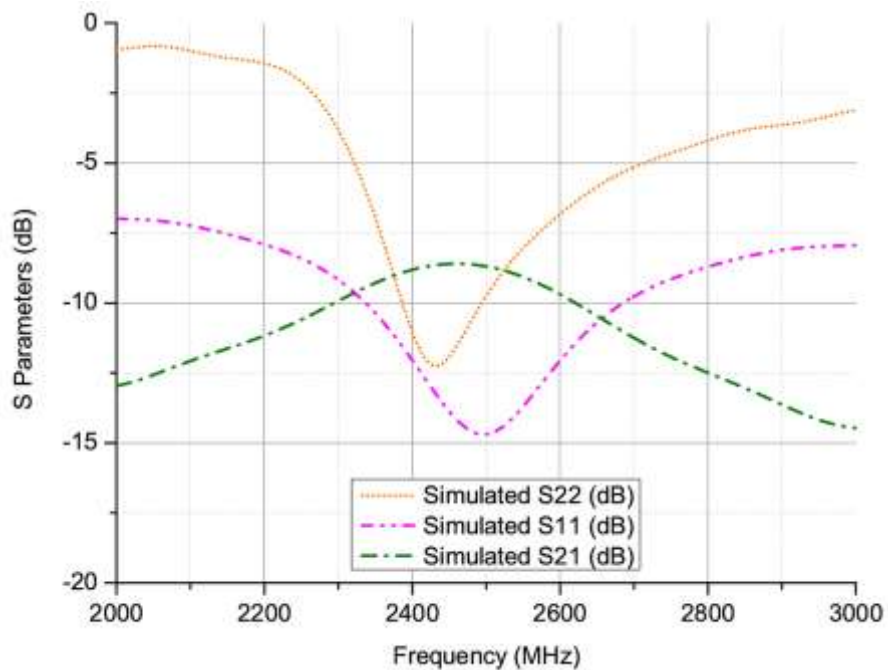


Fig. 4.14(a): Simulated S-Parameters for co-polarised PIFA

From the measured S-Parameters (Fig. 4.14 b) for the co-polarised design it can be seen that the antenna is reasonably well isolated ($S_{21} \approx -10$ dB) at the desired centre frequency. As we have already seen, this is sufficient for the measured correlation between both feed ports to be acceptably low. Both antenna ports are also seen to be well impedance matched at the desired centre frequency, meaning that the proportion of power lost due to impedance mismatch about the centre frequency should be relatively small.

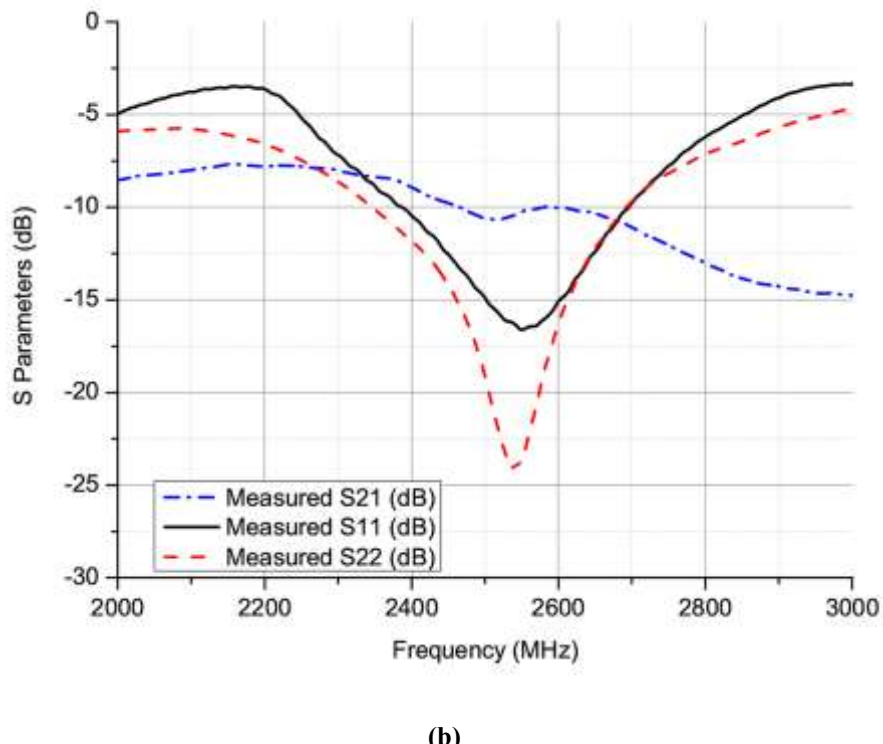


Fig. 4.14(b): Measured S-Parameters for co-polarised PIFA

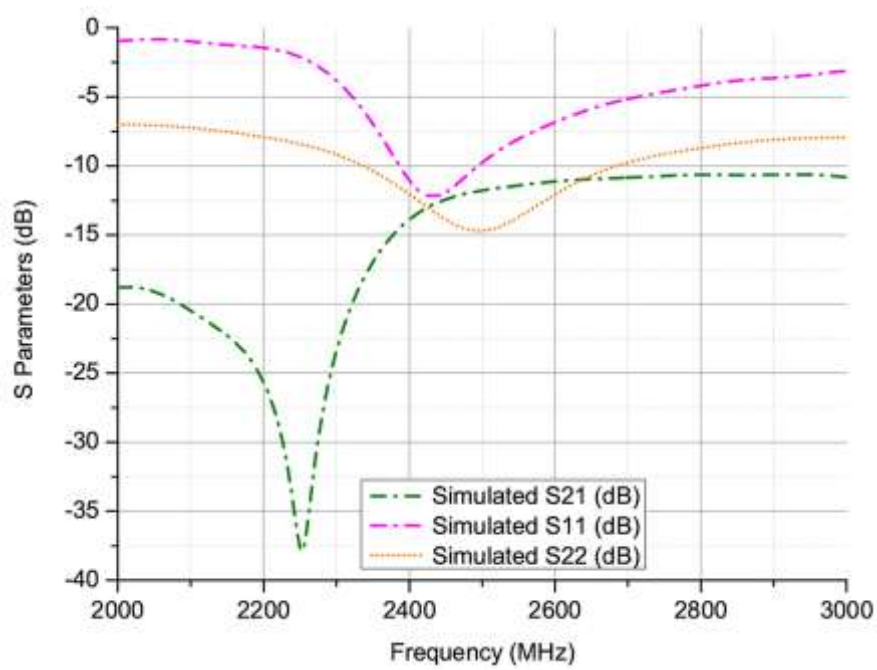


Fig. 4.15(a): Simulated S-Parameters for cross-polarised PIFA

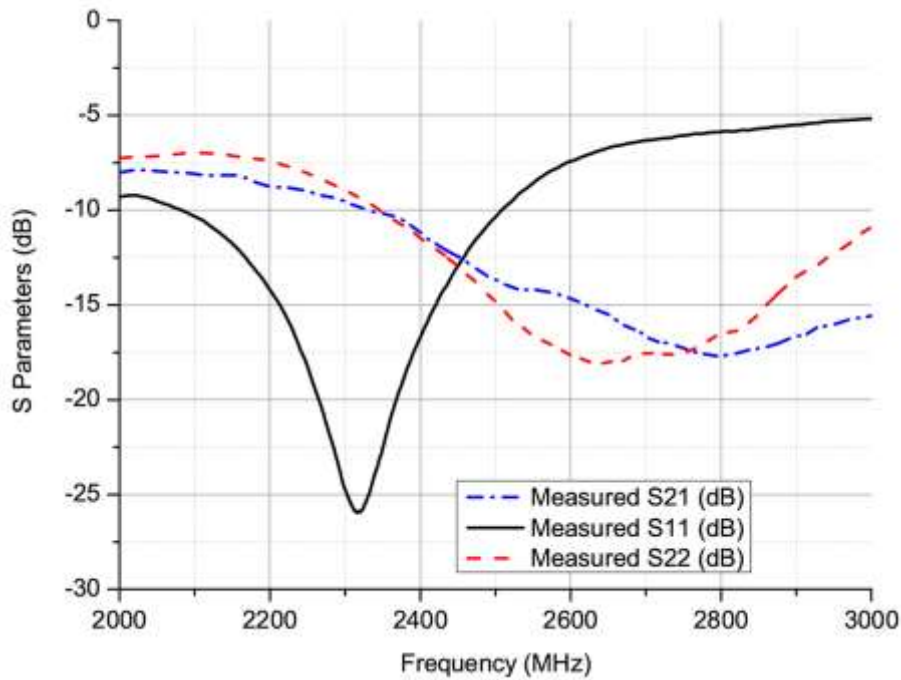


Fig. 4.15(b): Measured S-Parameters for cross-polarised PIFA

From the measured S-Parameters (Fig. 4.15 b) for the cross-polarised design it can be seen that the antenna is slightly better isolated ($S_{21} \approx -12.5$ dB) at the desired centre frequency than the co-polarised design (Fig. 4.14 b). Measured data for port 1 is seen to be slightly offset from the centre frequency which can be attributed to slight differences in dimensions between the simulated and manufactured design - this is because the practical cross polarised design was manufactured in three separate pieces and the placement of the orthogonal feed was not exact enough. Nevertheless, at the centre frequency it is still well impedance matched. On the whole, both designs are more than acceptable for operation.

The measured and simulated total embedded element efficiency (including matching losses) for the co-polarised design can be viewed in Fig. 4.16. Please note that the graph has been constrained about the centre frequency to more clearly depict the measurement and simulation comparison at the antennas desired working range.

From Fig. 4.16 it can be seen that the co-polarised antenna yields a high level of efficiency - the measured levels at the peak are at 91%. The agreement with the simulated assessment is very good at the peak values - away from the peak value; the simulated assessment for port 1 is much higher than the measured data over the first 200 MHz. This is due to the greater impedance matching in this range from the simulated design. Conversely, the simulated

assessment for port 2 is a lot lower than the measured data owing to the worse impedance match in this range.

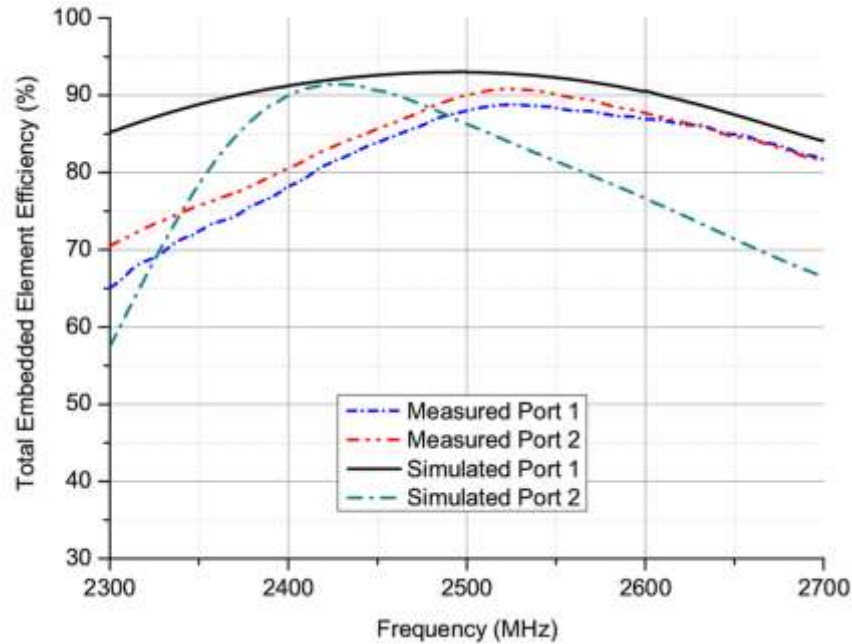


Fig. 4.16: Measured and simulated total embedded element efficiency for co-polarised PIFA

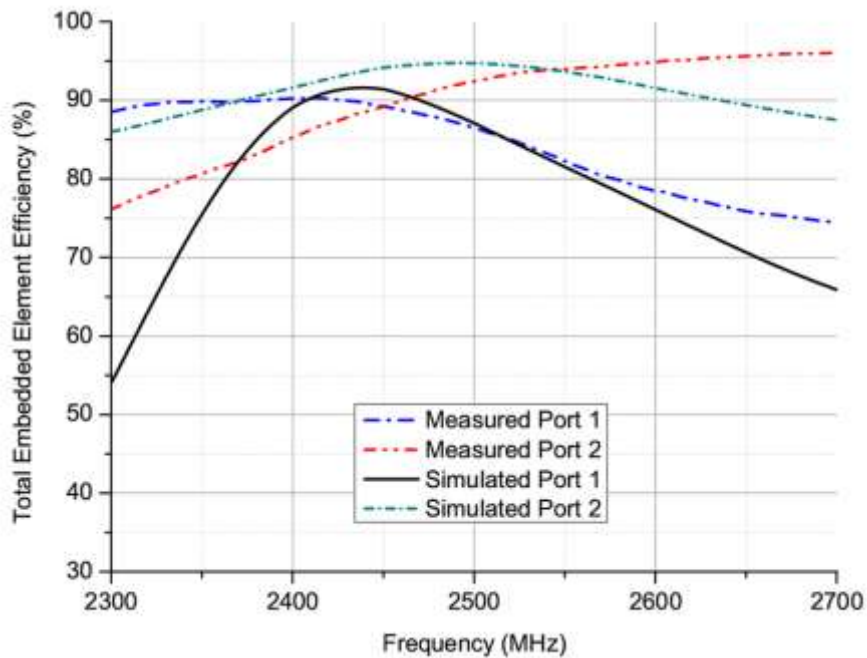


Fig. 4.17: Measured and simulated total embedded element efficiency for cross-polarised PIFA

From Fig. 4.17 it can be seen that the cross-polarised antenna also yields a high level of efficiency - the measured levels at the peak for branch 1 is 90%, and 96% for branch 2. The agreement with the simulated assessment is very good around the centre frequency - away from this the simulated assessment for port 1 is much lower than the measured data over the first 100 MHz. This is due to the greater impedance matching in this range from the measured design. Conversely, the simulated assessment for port 2 is a lot higher than the measured data owing to the better impedance match in this range; on the whole though the agreement is reasonable. To improve this agreement the manufacturing strategy needs to be more precise than what was originally conducted.

4.8 Summary of Dual Feed PIFA

In in-depth conclusion will be presented at the end of this chapter but it is felt prudent to briefly summarise thus far. Two new and novel single element dual feed PIAs have been disclosed and their MIMO performance fully characterised practically. The antennas, despite having two very closely spaced feeds (designed compact in size), are seen to suffer from no detrimental performance effects - thus it can be concluded that the etching isolation technique is very successful in this case.

Also, through the provision of pattern diversity (co-polarised design) and pattern and polarisation diversity (cross-polarised design), the designs allow for substantially different channels to be formed on the one device. This fact is proved and validated by high levels of measured diversity gain - from both cdf and correlation. The measured correlation assessment also serves to underline the isolated nature of the two feeds on the single device. The channel capacity and total embedded element efficiency is also practically measured proving that the designs provide a near maximum level of spectral efficiency and suffer from minimal losses (considered about the centre frequency, inclusive of mismatch power losses).

The compact nature and size of the designs coupled with the excellent practically validated performance mean that the antennas are strong candidates to be employed within a handset or other mobile device.

With regards to the measurements, it has been proved that a high level of accuracy exists, which justifies and validates the parameter selections made, the measurement procedures and all the processing involved. As a means of a multipath emulator, the RC is proved here to be an ideal tool for the characterisation of MIMO performance.

4.9 Definitions: Conventional Array Antenna

As previously stated, for multiport arrays that are not designed for MIMO applications, a distinction should perhaps be created, as in their practical operation they are typically used in an “all excited” manner - that is, we are not necessarily interested in separate ‘embedded’ channels. The rest of this chapter is devoted to the efficiency characterisation of larger sized (conventional) antenna arrays designed for radio astronomy applications.

In this chapter, a new equation is developed to characterise the efficiency performance of conventional arrays, taking into account the realistic “all excited” nature of the arrays’ practical operation. This sub-section is concerned with an introduction of the antenna array under test. Again, this work results from a collaboration between two parties; the antenna array (denoted the Octagonal Ring Antenna or ORA for short), was developed by A. K. Brown and Y. Zhang at the University of Manchester [22]. Therefore, in this sub-section it will only be briefly described.

The antenna under test in this study is a five-element compact dual polarised aperture array prototype based on an octagonal ring configuration as proposed in [22]. The basic design premise of the array has been formed from the conceptual theory of current sheet arrays (CSA) introduced by Wheeler [23]. Thus, the design aims to make use of, instead of reducing the mutual coupling between the array elements. The reason why the coupling is required in the design strategy is because in order to keep the radiation pattern side lobes under control, the array must be operated in a region where the electrical separation between elements is small; hence the mutual coupling is high. This also necessitates why the array must be used in an ‘all-excited’ manner.

The spacing between successive elements in the prototype is configured in a triangulated manner with the horizontal distances set at 112 mm between each consecutive feed and vertical feedlines of 55 mm in length. Each antenna element includes an integrated stripline transition which was known to introduce some loss. However due to its integrated nature this was treated as part of the antenna.

The desired operational frequencies of the prototype are from 400 MHz to 1400 MHz in which the aforementioned coupling effects are used to obtain a good level of impedance matching throughout the entire range. The overall dimensions of the array are width = 540 mm, height = 215 mm and the depth of the array from the front to the metallic ground at the back is 105 mm.

The front and side view of the array prototype can be viewed in Figs. 4.18 (a) and (b) respectively.

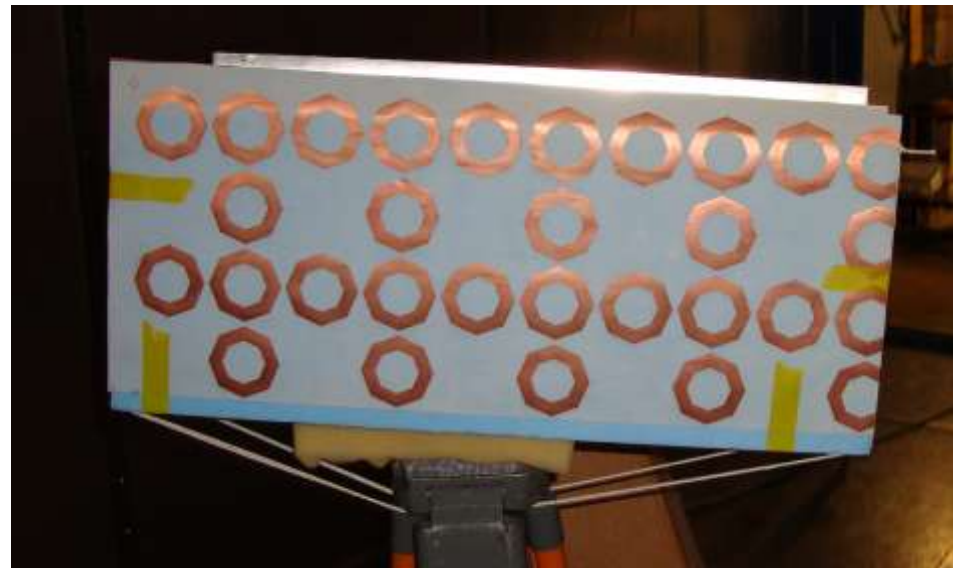


Fig. 4.18 (a): Front view of five element ORA prototype



Fig. 4.18 (b): Side view of five element ORA prototype

4.10 Measurement Parameters

The measurement parameters and procedures will be split into two sections; one to detail the all-excited efficiency measurements in the RC, the other details the power loss deduction of the power dividers that were employed for this study.

4.10.1 RC ‘All-Excited’ Measurement Parameters

The stirring sequences were configured to encompass 1° mechanical stirring intervals and polarisation stirring. A total of 718 measurement samples thus existed per frequency point. The measured frequency ranges in this instance were selected from 400 MHz to 1000 MHz owing to the upper frequency limit of the power divider employed. A total of 801 frequency data points was utilised to ensure a sufficiently large number of modes would be excited in the chamber throughout the measurement range. As consistent with standard efficiency measurement procedures in the RC, a reference measurement first took place for calibration purposes; a log periodic antenna (Rohde & Schwarz HL223) was used having known performance values (> 90%). The transmitting antenna was a homemade Vivaldi antenna working from 400 MHz to 2 GHz. The set-up used in the all-excited array measurement is depicted in Figs. 4.19 (a) and (b).

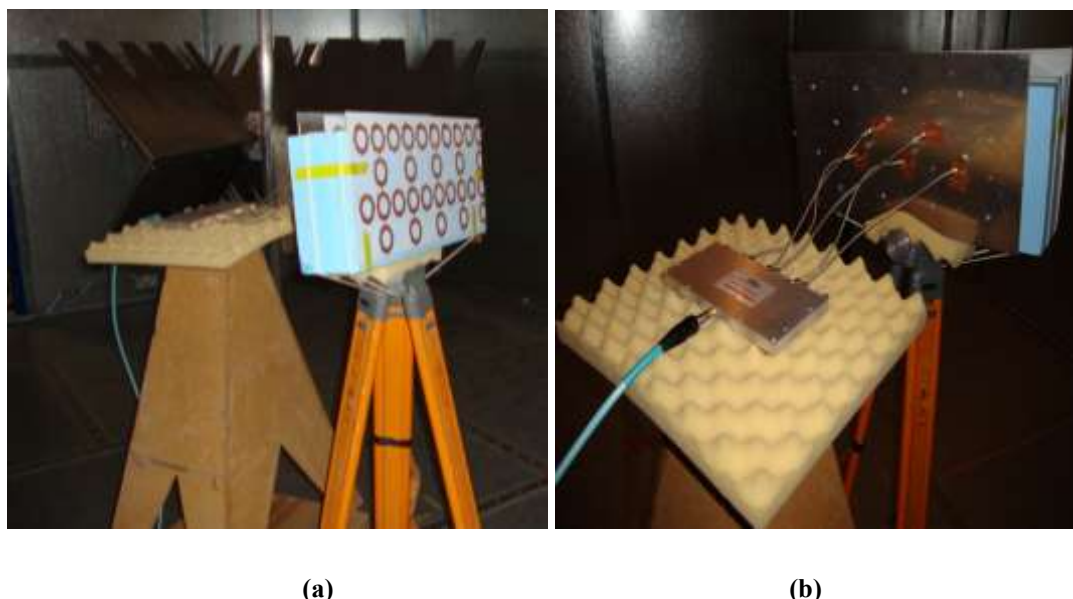


Fig. 4.19: Measurement set-up: (a) Array mounting and (b) power divider connections

4.10.2 Power Divider Measurement Procedures

For the determination of the power divider loss values, an open air test site was selected. An 8:1 power divider (Mini Circuits model no. ZC8PD1-10-S+) with a voltage standing wave ratio (VSWR) < 1.21 from 300 MHz to 1 GHz was employed in this study. The power divider had rigid coaxial cables connected from the output ports of which five in total were used to connect to the array feeds with equal weights. This left three ports on the power divider obviously unused; hence throughout all measured sequences these ports were terminated in impedance matched loads (50 ohm in this case). Fig. 4.20 depicts the measurement set-up to determine the power divider loss.

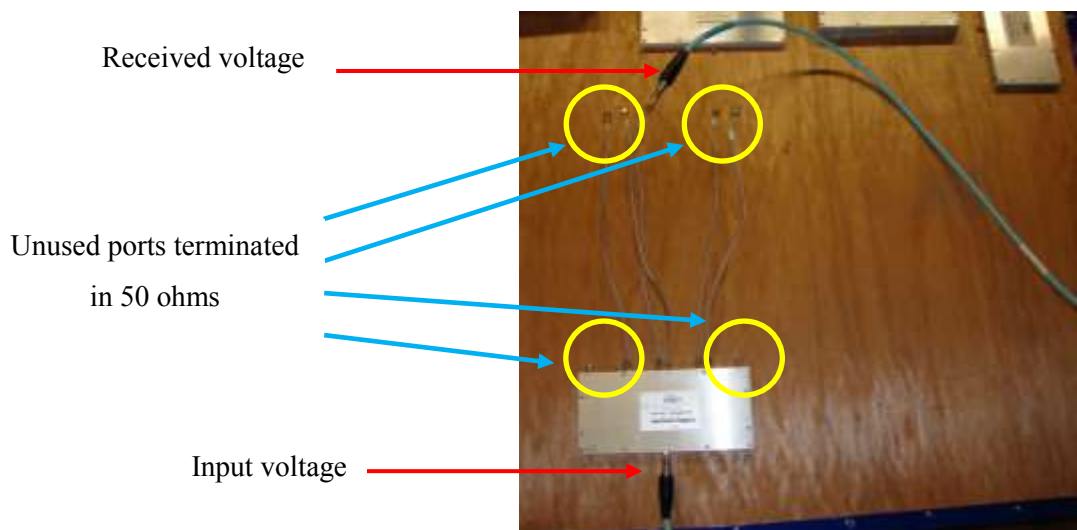


Fig. 4.20: Power divider measurement

To deduce the loss of the power divider accurately, the same impedance matched loads on the unused ports needed to remain in place during the loss deduction measurement to ensure the power dissipated by the divider would be consistent.

To determine the power loss, S-Parameters were employed in conjunction with a VNA. All outputs bar one were terminated in impedance matched loads and the transmission coefficient $|S_{21}|$ was measured between the common input and one output as a function of frequency. This gave rise to five separate transmission coefficient measurements; one for each output port, and a total insertion loss (T_L) was defined according to (4.23).

$$T_L (dB) = 10 \log_{10} \left\{ \sum_{m=2}^6 |S_{m,1}|^2 \right\} \quad (4.23)$$

where: $|S_{m,1}| = \frac{V_{R,m}}{V_T}$, for $m = 2, 3, 4, 5, 6$ respectively.

4.11 Deduction of New Equation

As previously stated, the presence of the power divider will present a power loss that is external to the physical array under test. In this section, the direct de-embedding technique is developed that is used in this study to account for the loss and calculate the array's efficiency in one.

In standard single port efficiency measurements (Eq. 3.1), assuming that the transmitting antenna (excited from port 1 in this case) is well impedance matched, the power transfer function for the reference and antenna under test at the receiving side can be determined by the well known power ratio (P) in (4.24).

$$P = \frac{\langle |S_{21}|^2 \rangle}{\left(1 - \langle |S_{22}|^2 \rangle\right)} \quad (4.24)$$

where: the reflection coefficient parameter in (4.24) is assumed to be measured in an anechoic chamber, $\langle \rangle$ = average of the scattering parameters and the term $\left(1 - \langle |S_{22}|^2 \rangle\right)$ is applied to effectively normalise the averaged power transmission coefficient by a factor of what power is reflected from the terminal due to impedance mismatch.

Clearly, the inclusion of the power divider will offer a further power loss in addition to (4.24) before the cable on the receiving side (Fig. 4.19 (b)). Therefore, a further normalisation factor is simply introduced to account for the loss which has nothing to do with the array. Hence, when the array is introduced, the normalisation factor in (4.24) effectively becomes (4.25).

$$\left(1 - \langle |S_{22}|^2 \rangle\right) \times (PD_{Loss}) \quad (4.25)$$

where: (PD_{Loss}) is the linear form of (T_L) from (4.23). The complete unknown radiation efficiency for the antenna array (η_{RAD}) with the power divider then becomes as (4.26) - (4.29) using the same adopted terminology.

$$P_{REF} = \frac{\langle |S_{21REF}|^2 \rangle}{\left(1 - \langle |S_{22REF}|^2 \rangle\right)^2} \quad (4.26)$$

$$P_{ARRAY} = \frac{\langle |S_{21ARRAY}|^2 \rangle}{\left(1 - \langle |S_{22ARRAY}|^2 \rangle\right) \times (PD_{Loss})} \quad (4.27)$$

$$\eta_{RAD} = \left\{ \frac{P_{ARRAY}}{P_{REF}} \right\} \times \eta_{REF} \quad (4.28)$$

$$\eta_{RAD} = \left\{ \frac{\langle |S_{21ARRAY}|^2 \rangle}{\langle |S_{21REF}|^2 \rangle} \times \frac{\left(1 - \langle |S_{22REF}|^2 \rangle\right)}{\left(1 - \langle |S_{22ARRAY}|^2 \rangle\right) \times (PD_{Loss})} \right\} \times \eta_{REF} \quad (4.29)$$

The total radiation efficiency of the array can be calculated from (4.30).

$$\eta_{TOTAL} = \eta_{RAD} \times \left(1 - \langle |S_{22ARRAY}|^2 \rangle\right) \quad (4.30)$$

where: *ARRAY* and *REF* stand for the array and reference antennas respectively and η_{REF} signifies the known reference efficiency. Consistent with the prior investigations in this thesis, the reflection coefficient parameters have been acquired in an anechoic chamber hence the omission of the ensemble average. Further, the reflection coefficient parameter for the antenna array should be acquired in conjunction with the power divider - the mutual coupling levels on the antenna will differ from an embedded scenario to the all-excited scenario, because the power loss between successive embedded elements will not be the same throughout each excitation, owing to the differing distances between the embedded element and the single excitation location.

In this case, the difference in mutual coupling levels meant that in an embedded scenario, the mutual coupling levels were much reduced and the array could not be properly impedance matched over the entire frequency band (this was confirmed practically). Hence, to obtain the desired impedance matching, the coupling levels had to be strong which the all-excited scenario provided.

4.12 Measurement Results

In this sub-section the results will be split into two separate sections for the power divider loss and the radiation efficiency performance of the array.

4.12.1 Power Divider Measurement Results

With respect to section 4.10.2, Figs. 4.21 and 4.22 detail the individually measured transmission coefficients for the five feeds of the power divider, and the combined total insertion loss (Eq. 4.23) in both linear and dB scales respectively.

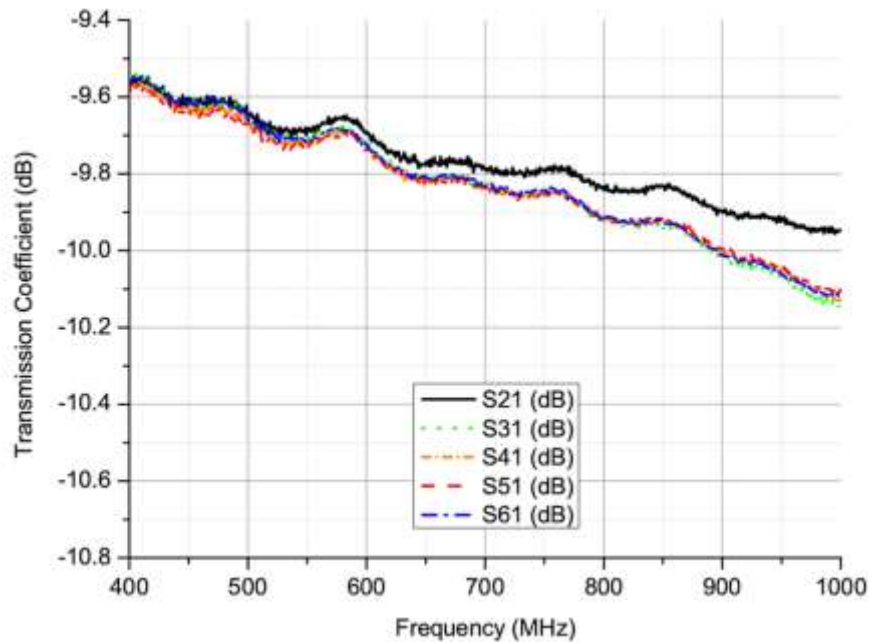


Fig. 4.21: Power divider transmission coefficients Vs frequency

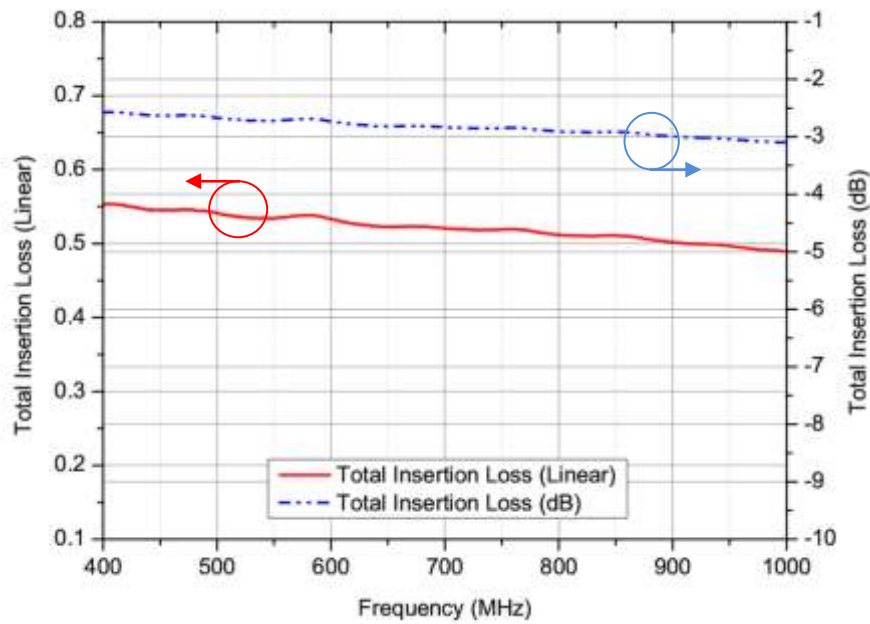


Fig. 4.22: Power divider total insertion loss Vs frequency

From Fig. 4.22, the linear values depicted are the values used in (Eq. 4.29) to ‘de-embed’ the power divider and thus deduce the array’s efficiency.

4.12.2 Antenna Array Measurement Results

We can now proceed to disclose the antenna array’s reflection coefficient and efficiency performance (Figs. 4.23 and 4.24 respectively).

From Fig. 4.23 it can be seen that when the antenna is operational in conjunction with the power (i.e. an all excited mode of operation) an excellent impedance match is obtained across the working frequency band. The designers’ concept of making use of mutual coupling in this regard is seen to be fully validated.

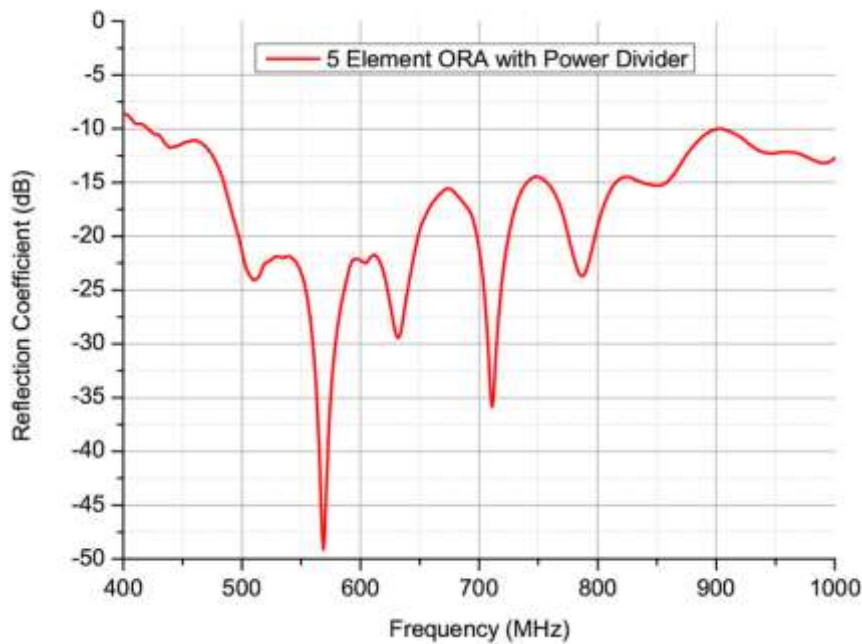


Fig. 4.23: Measured reflection coefficient (dB) with power divider

From Fig. 4.24 the efficiency quantities have been plotted with and without the ‘de-embedding’ performed to re-enforce the necessity of this operation.

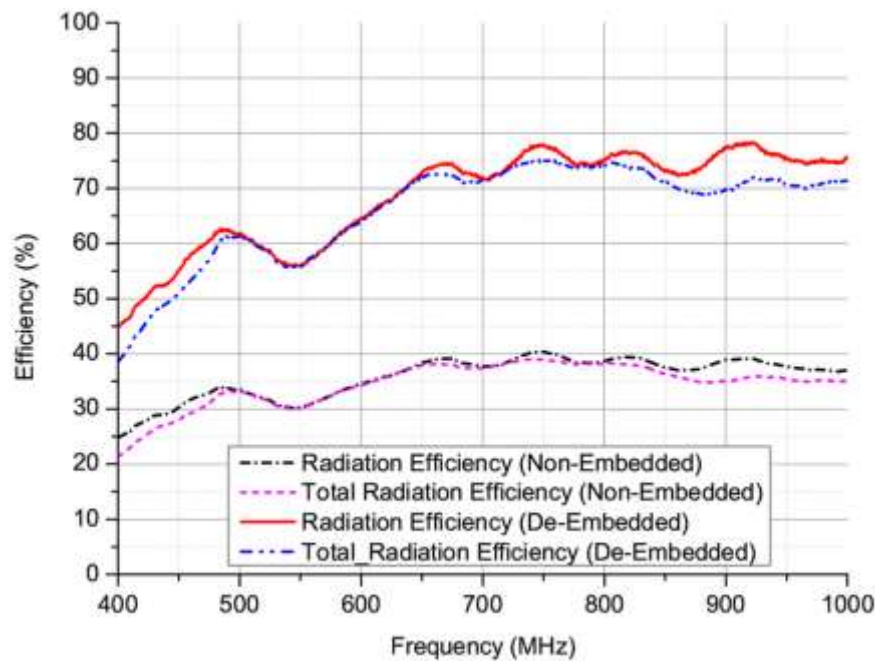


Fig. 4.24: Measured array efficiencies with and without de-embedding

From Fig. 4.24 it can be seen that the effect of not de-embedding the power divider is significant. The de-embedding technique developed in this thesis is direct and

straightforward to implement, and the passive ‘all-excited’ measurement can characterise the efficiency of the complete array in a timely manner.

The trend of the efficiency results, particularly over the first 300 MHz band, suggests that the mutual coupling is having a diminishing effect on the magnitude of the efficiency; which, since (electrically) the inter-element spacing is increasing for a decreasing wavelength, is in-line completely with expectations.

No simulated assessment is provided against the measurement results in Fig. 4.24 with respect to the following two points.

1. The mutual coupling in the simulated assessment, unless it can be specifically configured, would be based upon an ‘embedded element’ approach; which, as previously discussed, would under-estimate the strength of the mutual coupling in the antenna array as opposed to the all-excited scenario. The net effect of this would be twofold: (a) the impedance matching characteristics will differ (from all-excited to embedded scenario), and (b) because the mutual coupling levels can be lower, a larger radiation efficiency value can be predicted than what necessarily exists in practice.
2. The simulated assessment should also be performed with a large structure in order to obtain a reasonable approximation to the coupling levels in the array. Computationally speaking, this can be challenging. It has been stated that in this case, an existing simulated smaller section of the array is not big enough to obtain an accurate representation of the overall coupling, and any subsequent efficiency results could be questionable [24].

We can proceed therefore to directly assess the uncertainty in the array measurements to establish confidence in the derived results.

4.13 Measurement Uncertainty

The uncertainty models used for RC measurements have already been defined; the Rician K factor back in section 2.8, and the standard deviation in section 3.12 (Eqns. 3.3 and 3.4). Therefore, to avoid repetition they will not be issued again here. Fig. 4.25 details the Rician K factor and standard deviations inherent in the array measurements.

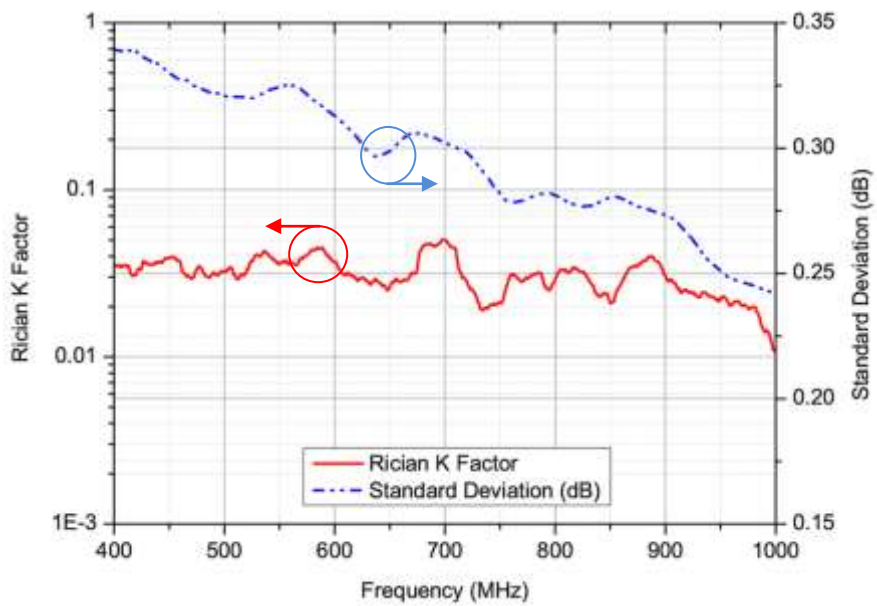


Fig. 4.25: All excited array measurement uncertainty

From Fig. 4.25 it can be seen that the uncertainty inherent in the measured approach is low. The Rician K factor proves that no direct proportion of power is evident in the measurement scenario and the standard deviations justify that the measurement procedures and parameters selected.

4.14 Conclusions

This chapter has charted a distinction between multiport antennas designed for MIMO applications and conventional antenna arrays that are not. For the MIMO applications, two new and novel single element dual feed PIFAs have been fully characterised and validated practically. These antennas, despite having very closely spaced feeds and not relying on spatial diversity techniques, are seen not to suffer from any detrimental performance effects - a high level of diversity gain is provided (close to the theoretical maximums, the measured correlation between the feeds is very low, a high level of channel capacity (spectral efficiency) is evident and about the centre working frequencies, the antennas are highly efficient. All measurement results provided have been benchmarked with simulated and/or theoretical results with excellent agreements obtained. This fact proves the correctness and appropriateness of all procedures and parameters selected for the measurement campaigns.

The theoretical strategy and idea for the antennas is thus proved to be successful, and because the antennas are small and compact in size, it is believed they can be useful in more practical and commercial applications than larger sized designs which rely upon spatial diversity.

For the conventional antenna arrays, a new equation has been developed which allows for the technique of de-embedding externally used power dividers and the calculation of the arrays' efficiency in one. It has been proved that this new developed technique is simple, easy to implement and accurate. This technique paves the way for further array characterisations in the RC, as the overall measurement techniques here have the potential to be faster, simpler and less uncertain than if other measurement facilities were to be employed.

Other than the de-embedding of power dividers connected to antenna arrays, the new equation could also find use in other measurements within the RC; for example, single port antennas connected to baluns - provided of course the balun loss can be characterised by the S-Parameter method as shown.

4.15 References

- [1] K. Rosengren, P. S. Kildal, "Radiation efficiency, correlation, diversity gain and capacity of a six-monopole antenna array for a MIMO system: theory, simulation and measurement in reverberation chamber," *Microwaves, Antennas and Propagation, IEE Proceedings*, vol. 152, pp. 7-16, 2005.
- [2] P. S. Kildal, K. Rosengren, "Correlation and capacity of MIMO systems and mutual coupling, radiation efficiency, and diversity gain of their antennas, Simulations and measurements in a reverberation chamber," *IEEE Communications Magazine*, vol. 42, pp. 104-112, Dec 2004.
- [3] R. G. Vaughan and J. B. Andersen, "Antenna diversity in mobile communications," *Vehicular Technology, IEEE Transactions on*, vol. 36, pp. 149-172, 1987.
- [4] P. Mattheijssen, M. H. A. J. Herben, G. Dolmans, and L. Leyten, "Antenna-pattern diversity versus space diversity for use at handhelds," *Vehicular Technology, IEEE Transactions on*, vol. 53, pp. 1035-1042, 2004.
- [5] H. T. Chattha, Y. Huang, S. J. Boyes, and X. Zhu, "Polarization and Pattern Diversity-Based Dual-Feed Planar Inverted-F Antenna," *IEEE Transactions on Antennas and Propagation*, vol. 60, pp. 1532-1539, Mar 2012.
- [6] B. H. Allen, *Ultra-wideband : antennas and propagation for communications, radar and imaging / edited by Benjamin Hugh Allen ... [et al.]*: Chichester : John Wiley & Sons, 2007., 2007.

- [7] M. V. Ivashina, M. N. M. Kehn, P. S. Kildal, and R. Maaskant, "Decoupling Efficiency of a Wideband Vivaldi Focal Plane Array Feeding a Reflector Antenna," *IEEE Transactions on Antennas and Propagation*, vol. 57, pp. 373-382, Feb 2009.
- [8] H. T. Chattha, "Planar Inverted F Antennas for Wireless Communications," PhD Thesis, Dept. Electrical Engineering & Electronics, The University of Liverpool, U.K., 2010.
- [9] A. Diallo, C. Luxey, P. Le Thuc, R. Staraj, and G. Kossiavas, "Study and Reduction of the Mutual Coupling Between Two Mobile Phone PIFAs Operating in the DCS1800 and UMTS Bands," *Antennas and Propagation, IEEE Transactions on*, vol. 54, pp. 3063-3074, 2006.
- [10] A. C. K. Mak, C. R. Rowell, and R. D. Murch, "Isolation Enhancement Between Two Closely Packed Antennas," *Antennas and Propagation, IEEE Transactions on*, vol. 56, pp. 3411-3419, 2008.
- [11] C. Shin-Chang, W. Yu-Shin, and C. Shyh-Jong, "A Decoupling Technique for Increasing the Port Isolation Between Two Strongly Coupled Antennas," *Antennas and Propagation, IEEE Transactions on*, vol. 56, pp. 3650-3658, 2008.
- [12] A. Diallo, P. Le Thuc, R. Starajf, G. Kossiavas, M. Franzen, P. S. Kildal, "Evaluation of the performances of several four-antenna systems in a reverberation chamber," *In. Proc. EuCap 2007*, 2007.
- [13] X. Chen, Y. Gao, C. Parini, Y. Zhinong, , "Study of a dual-element PIFA array for MIMO terminals," in *Antennas and Propagation Society International Symposium 2006, IEEE*, 2006, pp. 309-312.
- [14] W. Jakes, C, *Microwave mobile communications*. Wiley-IEEE Press John Wiley & Sons, 1974.
- [15] P. S. Kildal, K. Rosengren, J. Byun, and J. Lee, "Definition of effective diversity gain and how to measure it in a reverberation chamber," *Microwave and Optical Technology Letters*, vol. 34, pp. 56-59, 2002.
- [16] P. S. Kildal and K. Rosengren, "Electromagnetic analysis of effective and apparent diversity gain of two parallel dipoles," *Antennas and Wireless Propagation Letters, IEEE*, vol. 2, pp. 9-13, 2003.
- [17] P. S. Kildal, *Foundations of antennas: A unified approach*: Studentlitteratur, 2000.
- [18] X. Chen, "Spatial correlation and ergodic capacity of MIMO channel in reverberation chamber," *International Journal of Antennas and Propagation*, vol. 2012, pp. 1-7, 2012.
- [19] E. Kreyszig, *Advanced Engineering Mathematics*, 8th ed.: John Wiley & Sons, 1999.
- [20] J. Yang, S. Pivnenko, T. Laitinen, J. Carlsson, and X. Chen, "Measurements of diversity gain and radiation efficiency of the Eleven antenna by using different measurement techniques," in *Antennas and Propagation (EuCAP), 2010 Proceedings of the Fourth European Conference on*, 2010, pp. 1-5.
- [21] P. Hannan, "The element-gain paradox for a phased-array antenna," *Antennas and Propagation, IEEE Transactions on*, vol. 12, pp. 423-433, 1964.
- [22] Y. W. Zhang and A. K. Brown, "Octagonal Ring Antenna for a Compact Dual-Polarized Aperture Array," *IEEE Transactions on Antennas and Propagation*, vol. 59, pp. 3927-3932, Oct 2011.

- [23] H. A. Wheeler, "Simple Relations Derived from a Phased-Array Antenna Made of an Infinite Current Sheet," *IEEE Transactions on Antennas and Propagation*, vol. Ap13, pp. 506-&, 1965.
- [24] A. K. Brown, "Novel Broadband Antenna Arrays," ed. LAPC 2012: IET.tv, 2012.

Chapter 5: Improved Mechanical Stirrer Designs

5.1 Introduction

As we have already established, the field distribution in a ‘un-empty’ cavity, outside of the source area, is the superposition of all TE and TM excited cavity modes. Theoretically, it has also been shown that the fields are formed in the chamber as a result of standing waves that have a sine and cosine dependence. Further, we have also established that ‘Mechanical Stirring’ is one of the key tools that are used in reverberation chambers to render this field distribution statistically homogeneous and isotropic on average, and thus make the environment suitable for antenna measurements.

In any given RC, it is widely acknowledged that the chambers’ performance will improve with increasing frequency. The reasons for this:

1. For an increase in frequency there is an increasing amount of modes - governed approximately by Weyl’s law, giving the amount of modes available proportional to the third power of frequency and the chamber volume.
2. Different modes are needed to be excited in order to promote a sufficient change in the field distribution.

In addition to (1) and (2), it can also be argued that the performance in the chamber is also a result of the mechanical stirring paddles or plates being electrically large enough to interact with and adequately ‘stir’ the modes (that is, the paddles can change the boundary conditions sufficiently such that it causes the resonant frequencies of the modes to shift).

Conversely, towards lower frequencies in a given chamber, fewer modes exist - in terms of the frequency domain spectrum, the individual mode resonant frequencies are spaced further apart making it more difficult to excite and stir different modes. We can also argue again that at larger wavelengths, the electrical size of the paddles becomes smaller thus diminishing their ability to adequately interact with and stir the modes.

In terms of the frequency domain spectrum, Fig. 5.1 illustrates the modal deficiencies at lower frequencies in the University of Liverpool RC. Each vertical line represents a mode.

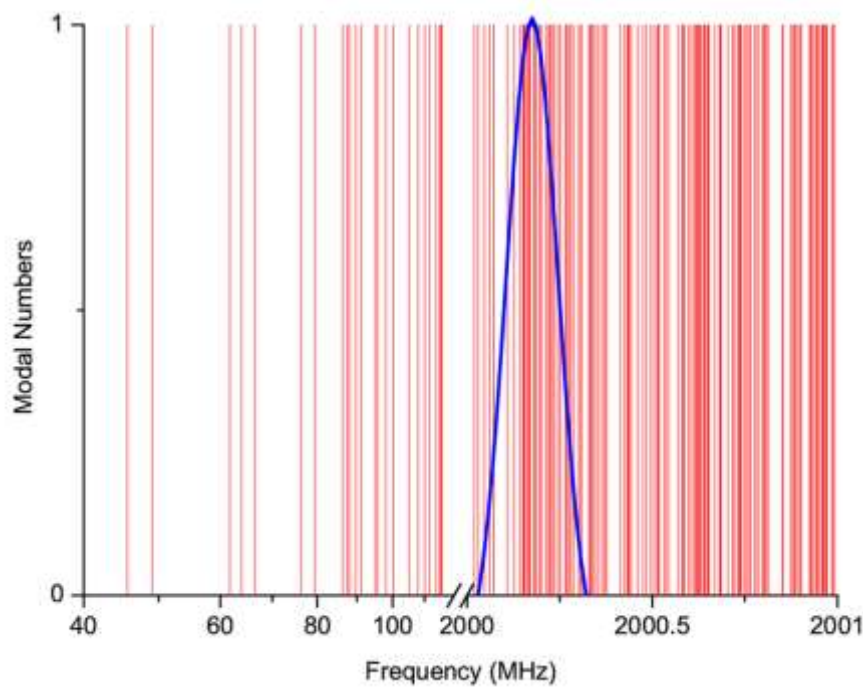


Fig. 5.1: Modal density in low and high frequency domain

As Fig. 5.1 shows, towards lower frequencies it will become more difficult to excite different modes and promote a sufficient change in the field distribution. The blue curve from Fig. 5.1 serves to illustrate the ‘average mode bandwidth’ which is defined as: ‘*The bandwidth over which the excited power in a particular cavity mode with resonance frequency f_0 is larger than half the excited power at f_0* ’. Despite the narrow width it potentially proves that many modes can still be excited at high frequencies.

Upon accepting the prior rationale, the question therefore is: What can one do about this at lower frequency?

In terms of the modal structure, one could be tempted to severely load the chamber to broaden the average mode bandwidth. This would indeed serve to excite more modes; however, having too large an average mode bandwidth will mean that the mechanical stirring process will struggle to sufficiently change the modal structure enough to excite different modes about the large modal bandwidth. The consequence of this is that the field distributions would not sufficiently change and a large standard deviation in any measurements would ensue. In addition, by loading the chamber with large amounts of anechoic absorber (for example), this would dampen the angle of arrival of plane waves from given directions resulting in an increase in the proportion of direct power in the chamber (increased Rician K factor). Neither of these consequences is desirable.

One option could be to just simply increase the size of the chamber such that at a desired frequency of operation there are plenty of available modes. This is true, but the chamber would always face the same problem as the frequency went lower.

In terms of the mechanical stirring paddles themselves, researchers have looked into the issue of design. As previously stated, the stirrer should be electrically large at the operating frequency [1]. Furthermore, since very large stirrer designs are liable to occupy precious space inside the chamber, two or more stirrers are often used in practice to provide equivalent or better performance [2].

Practically, the effect of the stirrer angle, height and width (aspect ratio) was studied in [3] as a function of chamber Q factor, field uniformity, number of excited modes and stirrer efficiency (number of independent samples). It was concluded that multiple stirrers performed best, and a 90 degree plate angle coupled with a minimum 80 cm height in conjunction with the use of 1λ reflectors were offered as optimised dimensions in that case.

Wellander, Lunden and Backstrom undertook an experimental and mathematical modelling investigation in [4]. It was concluded here that the efficiency in which the stirrer operates can be greatly improved by increasing its diameter. However, increasing a stirrer's physical diameter will result in that stirrer occupying more area inside the chamber, and consequently the working volume in the chamber will be decreased. This is not desired so as an alternative, it was stated that the stirrers could be re-designed by varying the aspect ratios to occupy less volume [4].

Arnaut presented a mathematical formulation in [5] based upon the effect of size, orientation and eccentricity of mode stirrers. It was found that for a sufficiently large radius of rotation (sufficiently large diameter); the eccentricity of a stirrers design had a greater effect on the stirrers' performance than the effect of the aspect ratio or relative orientation. This conclusion agreed with Clegg's earlier research in [6] who proposed a randomised plate stirrer based upon the work of a genetic algorithm in conjunction with a transmission line matrix (TLM) software; with the TLM approach also proposed in [7].

Reviewing the aforementioned published works, the one common aspect that they all have in common (excluding [1] and [2]) is that the stirrer designs have all been founded upon the use of solid metallic plates - i.e. the physical design of the paddles has been overlooked. This formulates the gap in knowledge where this new research is issued to address and improve upon.

The motivation in this thesis is to improve performance in the chamber down towards lower modal densities (in a broadband manner) where the performance is degraded, by the validation of new paddle designs.

The organisation of this chapter is as follows:

Section 5.2 will discuss the design methodology and explain the theoretical principles about what is specifically proposed in this research. Section 5.3 details the complete numerical analysis used in this study to formulate a new and novel design. Section 5.4 presents comments concerning the practical validation on the chambers' performance and section 5.5 and 5.6 detail all practical measurements undertaken to validate the new designs in this study. A conclusion is present in section 5.7 to review all findings.

5.2 Design Methodology

With regards to the paddle structure, the design methodology proposes the creation of various cuts across the paddle structure as opposed to leaving the paddles as solid metallic sheets. Fig. 5.2 (a) and (b) illustrates this concept.

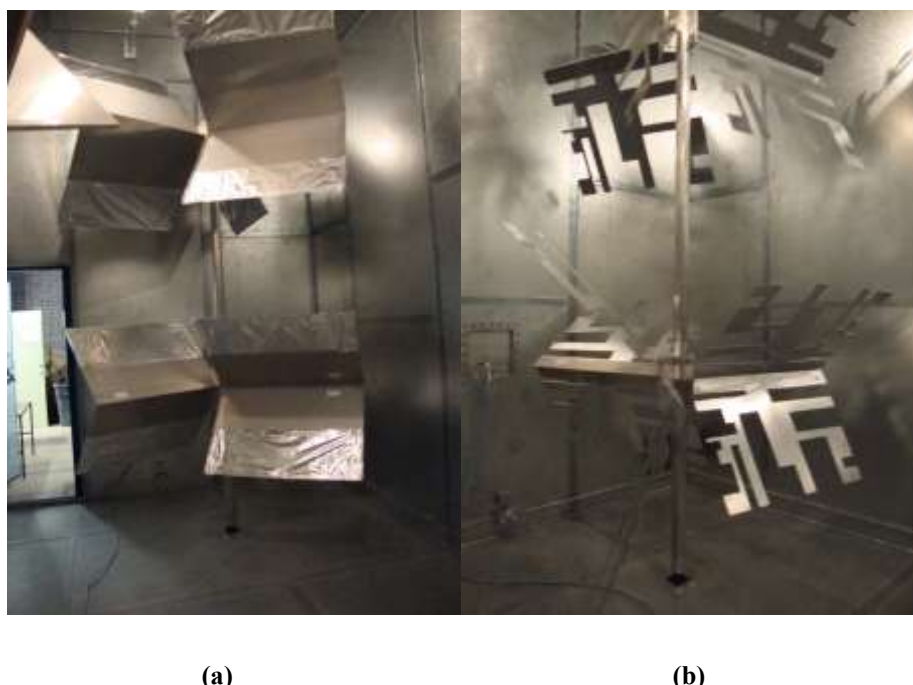


Fig. 5.2: Stirrer design concepts: (a) Standard (solid) paddles and (b) cuts made on paddle structure

With reference to Figs. 5.2 (a) and (b), the question now is: What theory would support such a modification?

The theory supporting such a modification is based on the concept of meanderline theory. As established in the introduction section (5.1), it is accepted that increasing the diameter of a stirrer will improve the stirrers' performance at lower frequencies. From the meanderline theory, it is well known that this technique can enable the lowering of the resonant capability of an antenna structure without increasing its overall physical size [8].

Therefore, in this case, the paddle structure is to be treated in a similar manner as an antenna (i.e. a frequency selective surface). The meanderline principle has been adopted as a means of increasing the electrical size of the structure while leaving the physical dimensions of the paddle the same. Hence, the cuts on the paddle are designed to increase the current path length on the plates, with the current being induced whenever a plane wave comes into contact.

The induced current is stated to be at maximum when the stirrer is resonant [7]; this is why the resonant capability of the paddle is aimed to be driven lower. With a longer current path length, the stirrer can be resonant at lower frequencies. If the stirrer has lower resonant capabilities, it has the potential to interact with and 'stir' modes at lower frequencies where standard paddles will not perform that well.

Another motivation with regards to the design concerns the statement of eccentricity in [5]. The eccentricity is formed in this case as a result of all the varying cuts on the paddle with different sizes. Hence as this structure rotates, the various cuts and shapes will provide for an extreme eccentric volume of rotation which is aimed at improving performance.

More questions are probably prevalent now:

1. How has such a design come about?
2. What evidence exists to suggest this approach works and is better performing?

These two points will be conclusively addressed in section 5.3. Beforehand, a few comments on the numerical method of analysis are warranted.

The design methodology has been performed using an Eigenanalysis in conjunction with a given physical stirrer design. Since it is well known (and has been proved in this thesis) that the field distribution in a given cavity can be written in terms of cavity modes [9], and a shift

in the resonant frequency of a mode implies a change in the field distribution [7], then the following can be applied.

The proposed Eigenanalysis technique in this thesis is based upon the use of a spherical cavity. It is accepted that spherical cavities do not necessarily make good reverberation chambers owing to the presence of multiple degenerate modes, but the spherical cavity approach does has advantages in this case:

- It can save time and computational resources as the stirrer paddles do not need to be rotated because the cavity is entirely symmetrical.
- Rectangular cavities would require the paddles to be rotated and any results obtained would be a function of the number of stirrer increments.
- All designs in this thesis are assessed under the same conditions.

Therefore, one should:

1. Obtain the eigenfrequencies in a empty cavity (λf_{empty})
2. Introduce each subsequent design into the cavity and calculate how the modes are permuted (λf_{loaded}).
3. Calculate the eigenfrequency shifts ($\Delta \lambda f$) according to (5.1).

$$\Delta \lambda f = |\lambda f_{empty} - \lambda f_{loaded}| \quad (5.1)$$

Simply, the design that permutes the eigenfrequencies by the greatest amount is the optimum choice. This is consistent with [7] who postulated that the key mechanism behind an effective stirrer lies in its ability to shift the eigenfrequencies.

5.3 Numerical Analysis

The numerical analysis has been performed using CST Microwave studio. Fig. 5.3 serves to illustrate the typical set-up in the software.

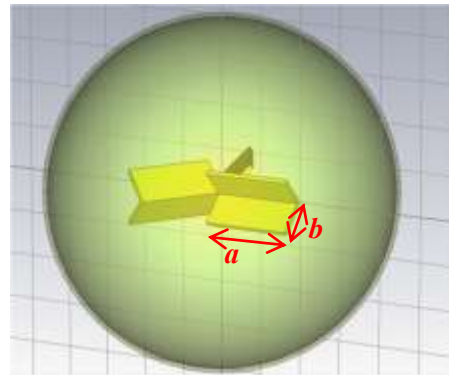


Fig. 5.3: Numerical set-up showing standard paddles

From Fig. 5.3, the internal volume of the cavity has been chosen as 2.144 m^3 . This selection was made as a trade-off between the total number of modes available in the cavity and the overall computational time and resources that are required in order to yield a solution. Three plates are seen to be co-joined about the centre of the spherical cavity - this has been configured to be as close to the physical reality as possible (see set-up in Fig. 5.2). The dimensions of the numerical plates have been configured as width (a) = 0.4 m and (b) height = 0.35 m. The reason for this selection is because the aspect ratio (b/a) = 0.875 is equal to the aspect ratio of one of the paddle sets in the real physical chamber. Hence, the numerical set-up is again based as much as possible on physical reality. The simulated cavity is constructed from aluminium 1 cm thick and the material filling the cavity is air (free space). The boundary conditions selected for the numerical investigation was selected as $E = 0$; that is, the field converges to zero at the cavity walls. The reason for this selection is that this is the typical boundary condition that is implied in the real physical chamber.

The numerical investigation used the AKS (Advanced Krylov Subspace) technique available in CST Microwave Studio. The reason for this selection is that only a certain amount of lower order modes were desired in the investigation to chart how the eigenmodes are permuted at lower modal densities. It is known that the AKS method in CST Microwave Studio uses a special polynomial filter to suppress the higher order modes; in practice this meant that a number of modal solutions could potentially be inaccurate towards the cut-off point of this filter. It was empirically determined therefore that although only 200 modes were desired in this investigation, 250 modes were selected to be calculated and 50 of those modal solutions were effectively discarded in order to avoid this inaccuracy.

The convergence accuracy of the modal solutions was configured to be accurate to 10^{-6} . The reason for this selection was simply to allow for an accurate enough solution within a time frame that potentially was not obtrusive. The meshing was selected as a ‘hexahedral’ type

and the automatic PBA (Perfect Boundary Approximation) was selected to allow for a good approximation of the structure within the mesh.

In terms of the total lengths of the meanderline cuts, it is proposed here to make this length proportional to the wavelength of where the first three overlapping modes occur. In the simulation, this corresponds to $0.986 \text{ m} = 304 \text{ MHz}$; when scaled up to the real physical design this translates to $2.6 \text{ m} = 115 \text{ MHz}$ - i.e. significantly larger than the original paddle dimensions (width = 1 m and heights = 0.58 m to 0.9 m) in order to lower the resonant capability.

The reason for this selection is as follows:

1. The wavelength selected for the real physical design corresponds to a frequency where at least one mode per MHz (mode density) exists. A lower frequency was not chosen because the modal structure would simply be too sparse.
2. The length of the cuts at this range provided a degree of flexibility with regards to how the cuts could be structured. Longer length cuts would inhibit this flexibility somewhat.
3. A higher frequency wasn't selected as the bound on the resonant capability of the paddle structure was envisaged to be pushed to the maximum that could possibly be achieved.

5.3.1 Effect of the Number of Cuts

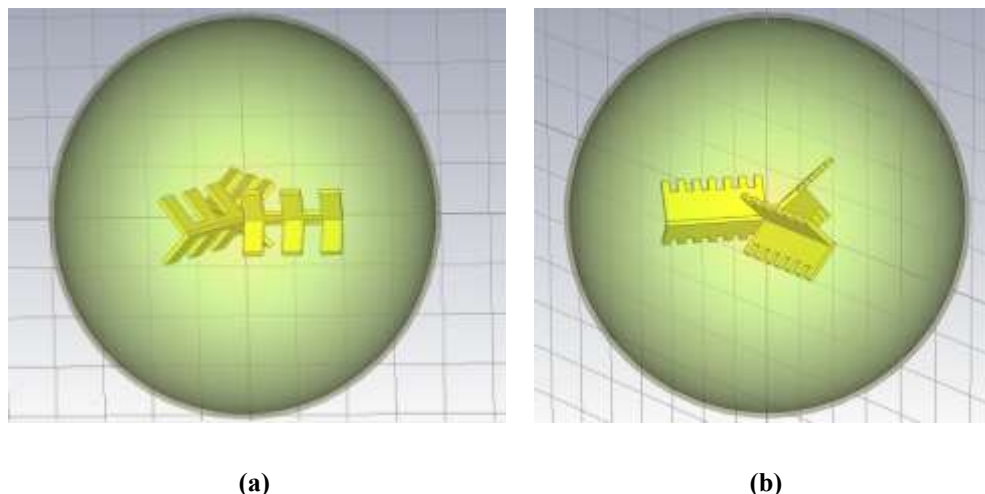
As previous, the overall question guiding the investigation is what is the optimum design?

As a first step, the total number of cuts on the paddle is numerically investigated. Table VIII details the parameters used in this investigation.

Table VIII: Parameters for investigation on number of cuts

Parameter	Description
Simulation set-up	Rectangular cuts 90 degree plate angle Cuts all periodic in nature Paddles all the same dimension

Fig. 5.4 (a) and (b) provides a visual representation of the numerical models in this investigation and Fig. 5.5 details the numerical eigenshifts result.

**Fig. 5.4: Numerical Investigation on Number of Cuts: (a) 2 Cuts and (b) 6 Cuts**

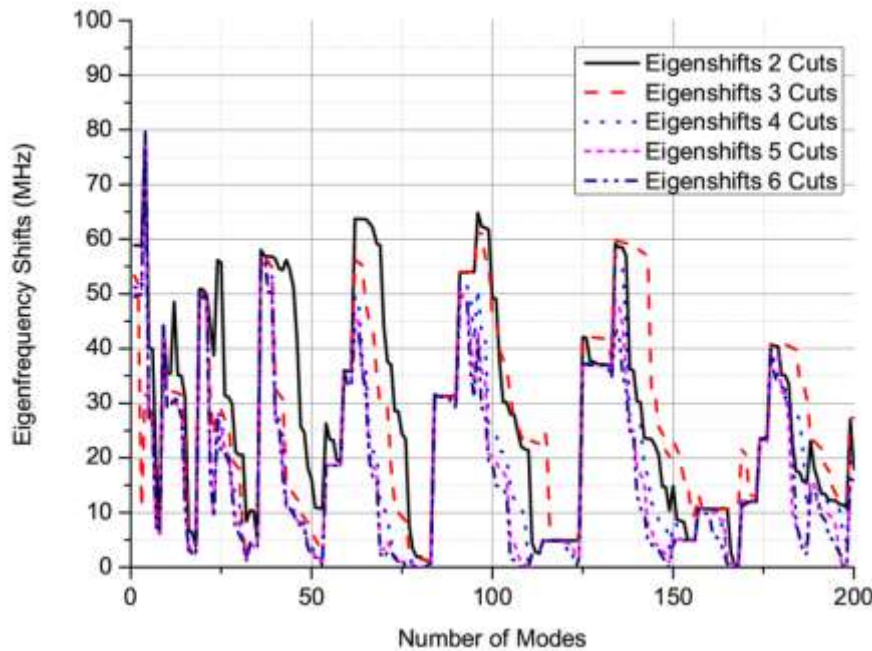


Fig. 5.5: Eigenfrequency Shifts (MHz) Vs Number of Cuts

From Fig. 5.5 it can be seen that in this case, a lower number of cuts performs better than a larger number. Computationally speaking, this result was also advantageous as it took fewer resources to yield a solution for a lower number of cuts. Although there are areas where the eigenfrequencies of the modes are significantly shifted from their original (empty cavity) resonant frequencies, there are also areas where little or no eigenfrequency shifts are present. In practice, a broadband response would be advantageous instead of isolated frequencies.

5.3.2 Effect of the Periodicity of the Cuts

As a second step, the effect of periodicity of the cuts is investigated; that is, should the cuts be periodic or non-periodic in nature? The length, width and non symmetrical design are looked at here. What this investigation is trying to establish is the effect of the frequency response with respect to the nature of the designs. Each specific dimension of cut is considered to be a half wavelength multiple of the frequency (see Table IX) in which to enhance. Table IX details the investigation parameters.

Table IX: Parameters for periodicity investigation

Parameter	Description
Simulation set-up	Rectangular cuts 90 degree plate angle Varied length of cuts only 3 x ($\lambda/2$) cuts chosen: 1) 0.37 m = 405 MHz 2) 0.24 m = 625 MHz 3) 0.177 m = 847.46 MHz Paddles all the same dimension Mirror image design

Fig. 5.6 details the numerical set-up for this investigation and Fig. 5.7 depicts the eigenfrequency shift results.

**Fig. 5.6: Non-periodic investigation 1, varying just length of cuts**

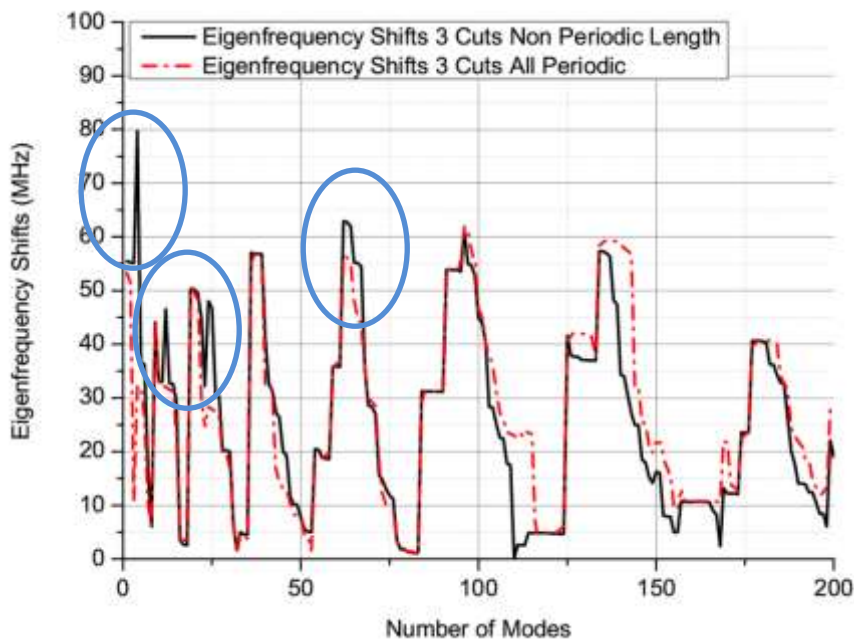


Fig. 5.7: Eigenfrequency Shifts (MHz) varying just length of cuts Vs number of modes

From Fig. 5.7 it can be seen that specific enhancements are provided with the varying lengths of cuts as opposed to having all the cuts made periodically. However, the design is still not sufficient as there is not a desired broadband response.

For the next step, both the length and width of the cut was varied to assess the overall response. Table IX again details the main parameters, although the dimensional size of the cuts was varied slightly to reflect the changing circumstances. 3 x ($\lambda/2$) cuts chosen: (1) 0.39m = 384 MHz, (2) 0.26 m = 576.92 MHz and (3) 0.177 m = 750 MHz

Fig. 5.8 portrays the numerical set-up while the eigenfrequency shift results can be seen in Fig. 5.9.

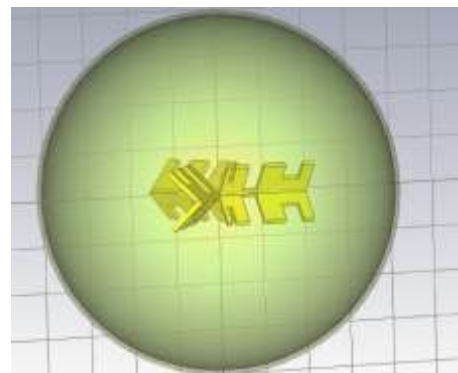


Fig. 5.8: Non-periodic investigation 2, varying both length and width of cuts

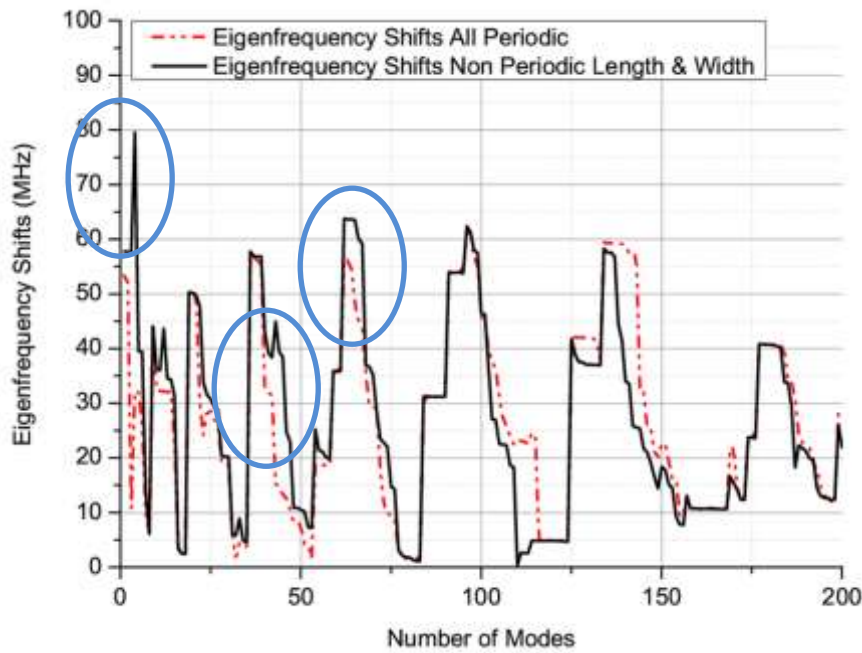


Fig. 5.9: Eigenfrequency Shifts (MHz) varying both length and width of cuts Vs number of modes

From Fig. 5.9, the response is seen to be receptive to the changing lengths and widths of the cuts to a certain extent; however, the design is still not broadband, and performance here is not satisfactory.

As a fourth step, the design was also varied such that the top and bottom of the plate sections were not a mirror image. The same parameters as in Fig. 5.8 were applied. The results showed a marginal difference to those depicted in Fig. 5.9, so for brevity they will be omitted here. In practice however, it is desired not to have rotational symmetry [5].

Therefore, retaining the varying length, width and non-mirrored design strategy, the shape of the cuts was investigated next.

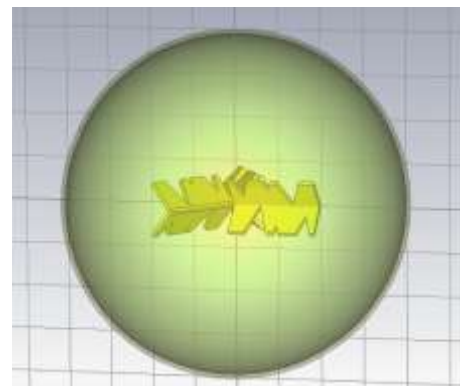
5.3.3 Effect of the Shape of the Cuts

Three different meanderline shapes are to be compared in this section; the rectangular shape which has already been disclosed, a triangular meanderline and a normal mode helical shape. This investigation begins by considering a triangular meanderline structure. Table X details the numerical parameters.

Table X: Parameters for effect of cut shape investigation 1

Parameter	Description
Simulation set-up	Triangular cuts 90 degree plate angle Varied length of cuts Cut angles periodic (40 degrees) $3 \times (\lambda/2)$ cuts chosen: 1) $0.3236 \text{ m} = 463.5 \text{ MHz}$ 2) $0.206 \text{ m} = 728.15 \text{ MHz}$ 3) $0.08 \text{ m} = 1875 \text{ MHz}$ Paddles all the same dimension Design not mirror image

Fig. 5.10 details the numerical model, while the eigenfrequency shifts can be viewed in Fig. 5.11.

**Fig. 5.10: Effect of cut shape investigation 1; Triangular meanderline**

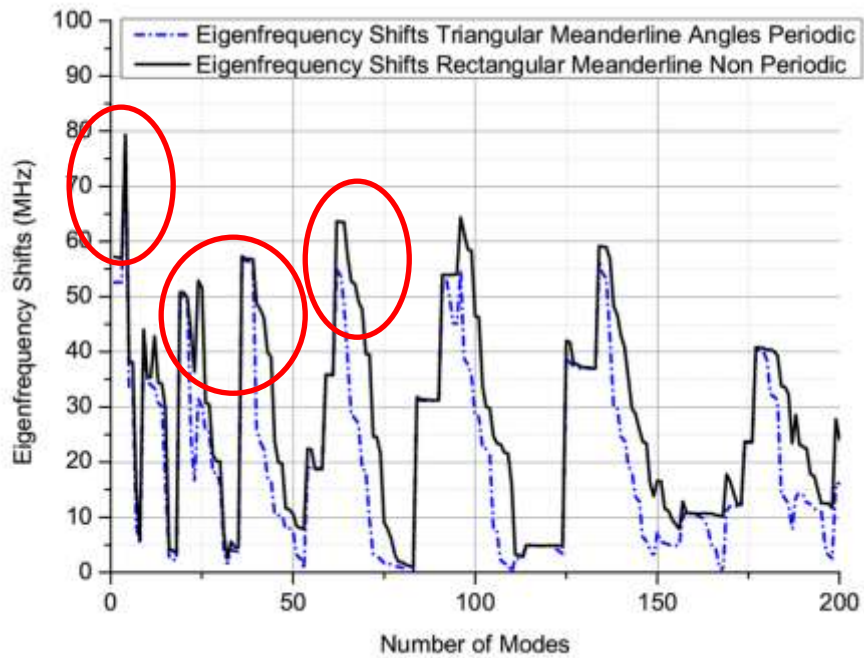


Fig. 5.11: Eigenfrequency Shifts (MHz) for rectangular and triangular meanderline shapes Vs number of modes

From Fig. 5.11 it can be seen that the rectangular meanderline exhibits a lower resonant capability and a better frequency response. The effect of varying the triangular cut angles was also investigated and was found to offer no significant improvement to the results seen in Fig. 5.11.

So far, the investigation has determined that the rectangular meanderline has a lower resonant capability than the triangular meanderline - a fact also validated in [8] for wire monopole antennas, and that the overall frequency response can be improved for varying lengths and widths of cuts. The results seen so far however are still problematic in the sense that the improvements are only narrowband in nature; a broadband response is desired.

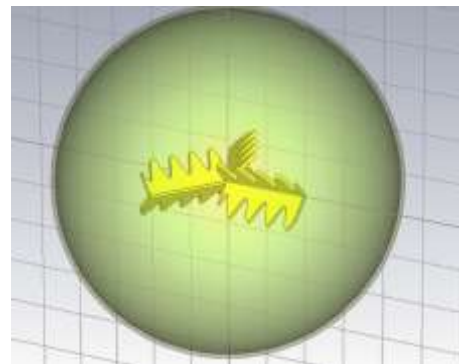
Furthermore, from a manufacturing perspective, the rectangular (straight edge) cuts would be an easier proposition to create than varying angles and lengths of triangular cuts. Therefore, the decision was taken not to pursue the triangular meanderline theme further.

The next investigation looked at a normal mode helical design to assess the performance of such a meanderline shape. Table XI details the numerical parameters.

Table XI: Parameters for effect of cut shape investigation 2

Parameter	Description
Simulation set-up	Normal mode helix cut 90 degree plate angle Same length of cuts: Period = 0.2465 m = 608 MHz Paddles all the same dimension Design not mirror image

Fig. 5.12 details the numerical set-up while the eigenfrequency shift results can be viewed in Fig. 5.13.

**Fig. 5.12: Effect of cut shape investigation 2; Helical meanderline**

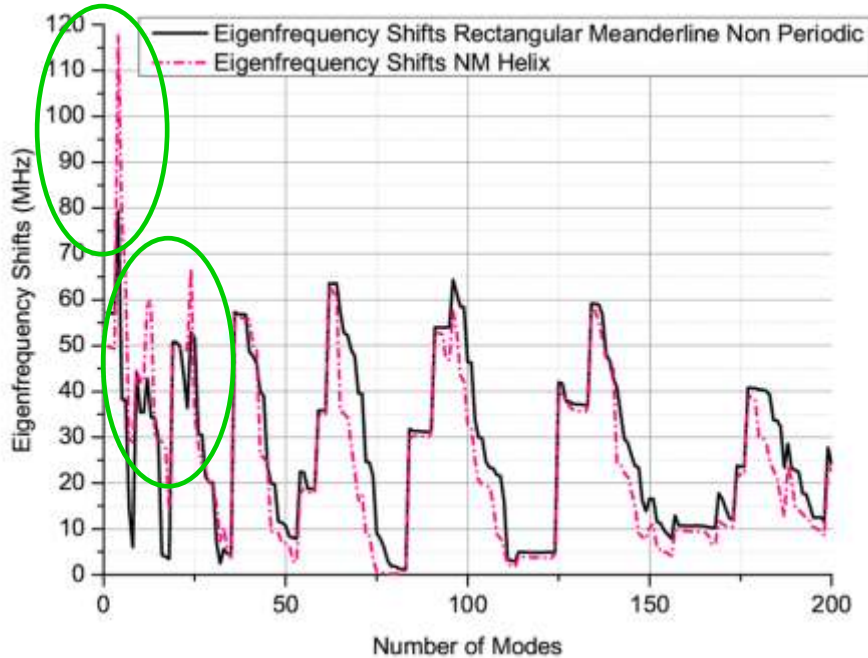


Fig. 5.13: Eigenfrequency Shifts (MHz) for rectangular and helical meanderline shapes Vs number of modes

From Fig. 5.13 it is shown that the helix type structure has greatly enhanced the resonant capabilities at lower modal numbers - in this range it is by far superior to the rectangular meanderline shaped cuts. However, the design is not broadband as the periodicity of the cuts is the same. To make the structure broadband, it is envisaged having many different $\lambda/2$ sized individual cuts on the paddle structure, such that in a given range, there is a cut comparable or nearly comparable in size in order for the paddle to interact with a plane wave efficiently. Please see Appendix A3 for evidence to support this statement.

With the helix shaped cuts, the flexibility of this design strategy was questioned; meaning that given the shape of the design, it was envisaged that difficulties would result in trying to fit many different sized cuts onto one paddle structure. Furthermore, the shape would be more complex to manufacture than straight edge cuts.

Therefore, although the helix shape structure showed a degree of promise, the decision was taken to drop the helix meanderline for the aforementioned reasons. Furthermore, complicated Koch fractal type shapes were also disregarded due to their complex nature of design and difficulties envisaged in manufacture.

5.3.4 Complex Nature of the Cuts

With the decision taken not to pursue the triangular and helical meanderline shaped structures any further, the rectangular meanderline came back into thought.

Since the design strategy looks to having many different $\lambda/2$ sized cuts on the paddle to offer a broadband characteristic, the straight edge cuts would offer a degree of flexibility in structuring all these different cuts onto one paddle structure.

This investigation therefore looked into the complex nature of rectangular meanderline cuts on the paddle structure; specifically, should the cuts be made in both a vertical and horizontal plane? The guiding theory supporting this move is as follows:

1. As previously stated, the more cuts available on the paddle is envisaged to offer a broadband characteristic - the vertical plane would be needed to fit all these cuts on the paddle.
2. Although the existing chamber has two principle sets of mechanical stirring paddles for vertical and horizontally polarised waves, when the chamber is employed for measurements, the transmitting antenna is typically directed straight at the vertically mounted stirrer paddles as seen in Fig. 5.14.

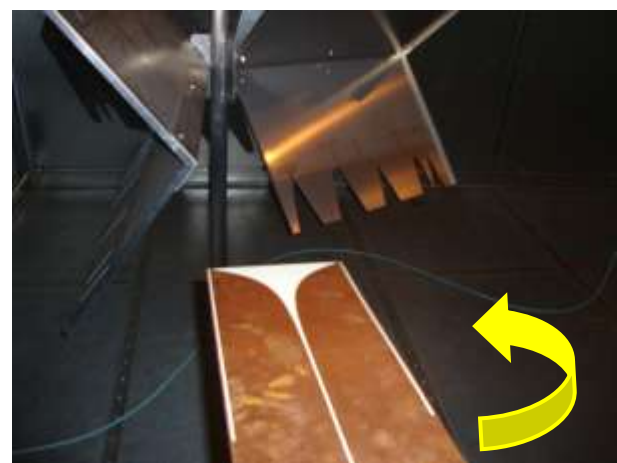


Fig. 5.14: Transmitting antenna location

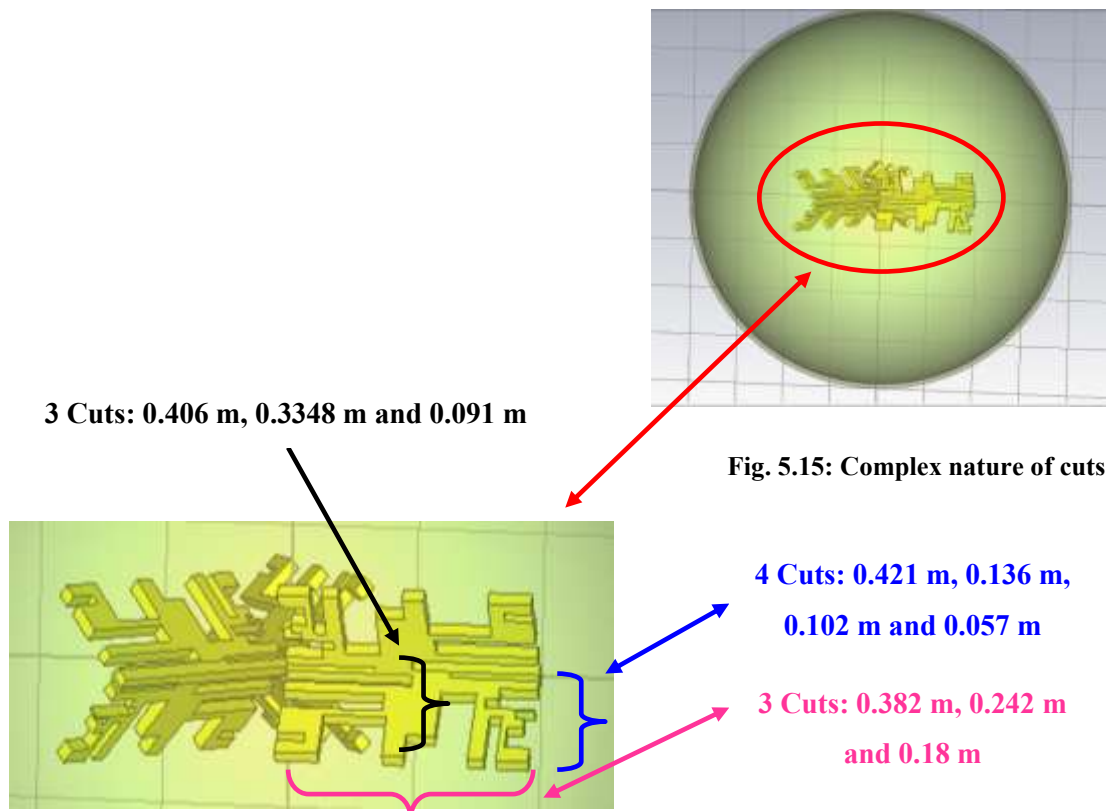
As discussed and detailed throughout this thesis, polarisation stirring is always employed which directs the transmitting antenna in two orthogonal orientations directly at these paddles in the manner shown above. Therefore, cuts in both a vertical and horizontal plane on the paddle structure could theoretically serve both of these transmitting polarisations.

With respect to the theoretical rationale in section 5.3.4, Table XII details the numerical parameters for this investigation.

Table XII: Parameters for the complex nature of cuts

Parameter	Description
Simulation set-up	Rectangular meanderline design 90 degree plate angle $10 \times \lambda/2$ cuts all different dimensions Paddles all the same dimension Design not mirror image Completely non-periodic

Figs. 5.15 and 5.16 depict the complex numerical model.



With respect to Fig. 5.16, the selections in the dimensions of cuts have been specifically made to provide a resonant capability in the rectangular designs where before there wasn't any. The selections are made simply to span a varying range of wavelengths, and the nature of how the cuts are orientated was made simply to be able to fit all cuts onto the metallic plate. Fig. 5.17 portrays the numerical results for the complex design as compared with the (original) non periodic rectangular meanderline with only 3 varying cuts.

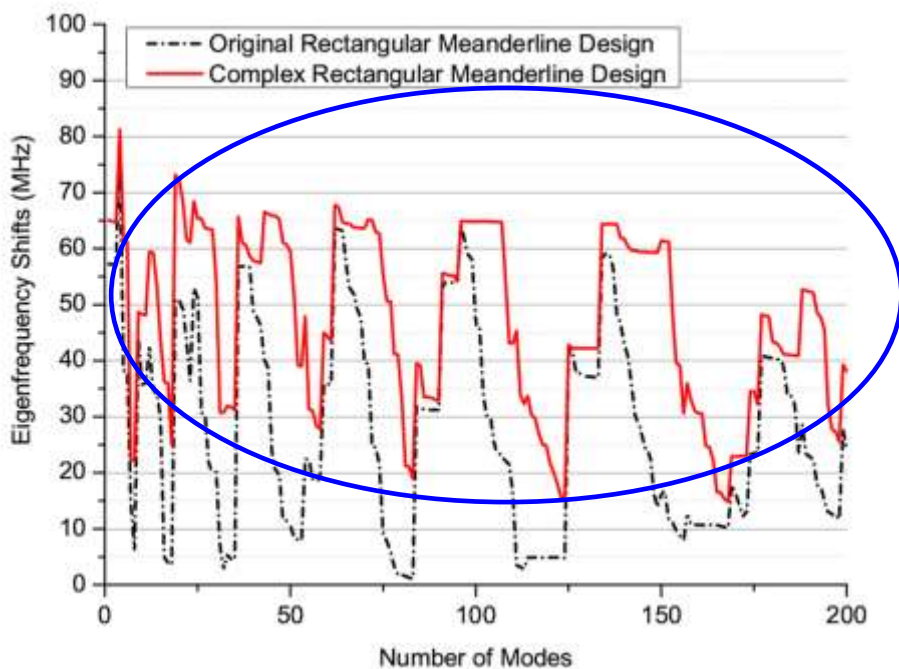


Fig. 5.17: Eigenfrequency Shifts (MHz) for complex and original rectangular meanderline

From Fig. 5.17, it can be seen that the complex nature of the design coupled with the use of varying specific length cuts grossly outperforms the simple natured (original) design. The complex design here has a broadband frequency response that is desired. The numerical results issued in Fig. 5.17 provided confidence to re-enforce the theory of specific $\lambda/2$ cuts, and provides evidence to assert that highly irregular shaped mechanical stirring paddles can perform better in terms of their mode stirring performance.

Comparing the complex design to standard paddles with no cuts at all as shown in Fig. 5.18, we see the enhanced performance of the complex design strategy.

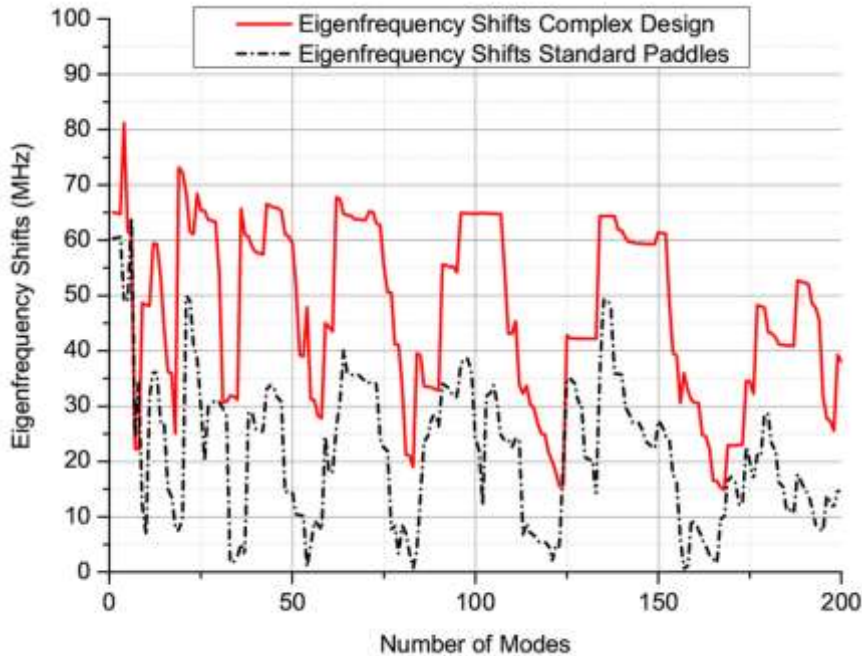


Fig. 5.18: Eigenfrequency Shifts (MHz) for complex and standard (no cuts) paddles

With confidence established in the theoretical idea, can we do even better?

5.3.5 Variation in the Paddle Dimensions

Briefly referring back to the earlier statement concerning eccentricity and to the rationale presented in [5], and also to the effect of having rotational symmetry in [7], it has been known for a long time that rotational symmetry within an electrically large design and a concentric mode of operation would serve to reduce randomness. Hence, in a reverberation chamber, when rotational patterns are repeated, no additional stirring is gained [7].

To be theoretically precise, the effect of a stirrers scattering / diffusion performance should not be taken in isolation from the details and vicinity of its cavity boundary [5]. Hence, it has been stated that a small and simple stirrer inside a highly complex corrugated cavity might produce a statistically more uniform field distribution than a large complex stirrer inside a cavity with simple smooth walls [5].

In this case, since the walls of our chamber, and indeed the vast majority of chambers, are rectangular and smooth / metallic in nature, the statement concerning the rotational symmetry and eccentricity is applied.

In this investigation therefore, the dimensions of each of the three numerical paddle sets are varied in an attempt to assess the effect of employing no rotational symmetry and an extreme eccentric design.

Two separate investigations are presented:

1. One of the paddle dimensions retains its original dimensions; the other two paddle sets are scaled 1.25 and 1.5 times in height only.
2. One of the paddle dimensions retains its original dimensions; the other two paddle sets are scaled 1.5 and 1.75 times in height only.

Table XIII details the selections made in this regard, while Fig. 5.19 depicts the typical numerical model.

Table XIII: Parameters for the variation in paddle dimensions

Parameter	Description
Simulation set-up	Rectangular meanderline design 90 degree plate angle $10 \times \lambda/2$ cuts all different dimensions Design not mirror image Completely non-periodic 1 x paddle original size 1 x paddle scaled 1.25 and 1.5 times in height 1 x paddle scaled 1.5 times and 1.75 times in height

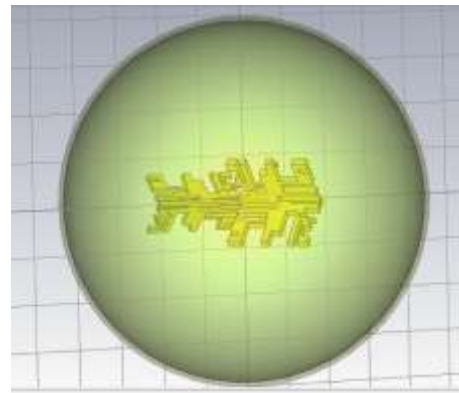


Fig. 5.19: Complex cuts with differing paddle heights

Fig. 5.20 displays the numerical result comparing the effect of changing the paddle dimensions for the complex design.

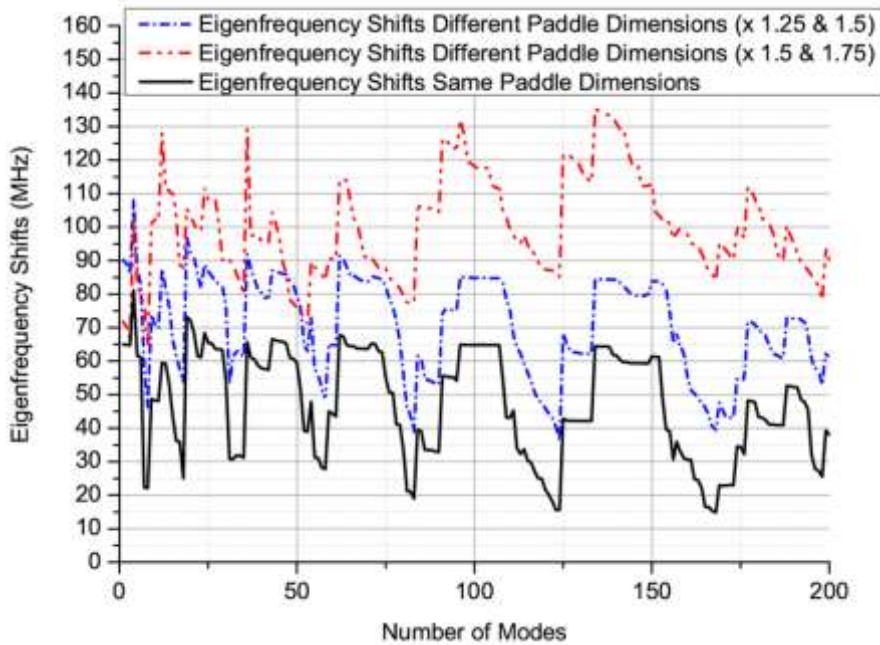


Fig. 5.20: Eigenfrequency Shifts (MHz) for complex paddles with different dimensions

From Fig. 5.20, we see that as the electrical size of the paddles increase, this better serves to permute the modes in the cavity. In addition, because each of the paddle sets is different in dimension, the cuts made on those paddles are also scaled accordingly - this means that a wider broadband nature can be provided for as there are more different sized cuts on the entire paddle structure.

In practice there are dimensional constraints that must be adhered to. When scaling the designs up to full size in the real physical chamber, the 1.5 and 1.75 increases in height

would be prohibitive as the paddles would catch on the walls of the chamber given the proximity of where the paddles are situated. However, the 1.25 and 1.5 increases in height can be allowed, so the results here serve to illustrate what will be taken into practice.

5.4 Comments on Practical Validation

Conventionally, when assessing the performance of a given chamber, one would typically refer to the relevant standards [10] and follow the guidelines issued to determine the chambers' performance by deducing the electromagnetic field uniformity. Typically, the standards advocate:

1. Measuring the maximum electric (E) field value at 8 different chamber locations for three different cartesian orientations of the field (x , y and z).
2. Use logarithmic spaced frequency points.
3. Number of measurement samples (stirrer steps) proposed = 12 (minimum).
4. Calculate the chamber performance by assessing the standard deviation in the maximum electric field values - for each x , y and z orientation and when all the orientations are combined.

This procedure is *not* going to be followed in this study for the following reasons.

1. The electric field values may or may not be accurate if an antenna is employed as the receiver as opposed to a specific electric field probe. This is because a large metallic antenna would be expected to disturb the local electric field in where it was situated, creating uncertainties in the maximum magnitudes of the measured E field.
2. For antenna measurements, unlike some EMC measurements, we do *not* use just maximum values; we use all values in which to form an average - why then characterise the chamber performance using just maximum values?
3. Throughout this thesis it has been seen that very accurate measurement results have been obtained using over 700 measurement samples per antenna with a variety of stirring mechanisms. The 12 sample minimum not taking into account multiple stirring mechanisms is simply not an accurate enough reflection on the chambers' true performance.

Assessing current literature, it can be seen that other researchers [4, 11-14] are now choosing not to implicitly follow the standards doctrine and / or have expressed doubts concerning their overall applicability. The standards approach therefore could be considered to be an approximation as to the true chamber performance for antenna measurements, and in this study greater certainty is sought.

Therefore, the procedures to characterise the chamber performance will be changed. The assessment of using a standard deviation from different measurement locations in the chamber will be retained, but crucially the standard deviation will be calculated as the deviation in the average power transfer function at different measurement locations in the chamber - using all measured samples, instead of just the (minimum of) 12 maximum electric field values [11].

Furthermore, looking at the accepted theory from chapter 2 and the uncertainty models used for antenna measurements (Eqs. 3.3 and 3.4 on page 108), the following three parameters will also be assessed:

1. The non line of sight number of independent samples as a function of frequency.
2. The measured polarisation imbalance that exists as a function of frequency.
3. The proportion of direct power (Rician K Factor) as a function of frequency.

The standard deviation and points (1) - (3) above form all of the accepted components that can contribute to the uncertainty in antenna measurements. By this, these procedures should provide more of a reliable and accurate indicator of chamber performance than the BS EN 61000-4-21 standards decree.

5.5 Measurement Parameters for Validation

Table XIV details the parameters for the practical investigation. With respect to the parameters detailed, the six receiver locations has been selected as a trade-off between the measurement accuracy and the overall measurement time needed to complete each measured sequence. Also, since each receiver location should be separated by at approximately $\lambda/2$ so that each location is independent (uncorrelated); at lower frequency this meant that any additional receiver locations could not be included as they would be too closely spaced.

The number of measurement samples has been chosen simply to give a similar number to what has been performed in prior investigations in this thesis, such that a separate method here can compare to the theoretical uncertainty model to further validate the accuracy of the chamber and all procedures.

Table XIV: Parameters for the practical investigation

Parameter	Description
Frequency (MHz)	100 - 1000
Number of frequency data points	801
Number of independent receiver locations	6
Stirring sequences	3 degree mechanical stirring Polarisation stirring 18 MHz frequency stirring
Receive antenna orientations	3 (x , y and z orientation)
Total number of measured samples per receiver location (for all orientations)	714
Miscellaneous	Source power = -7 dBm RX antenna = Log Periodic (HL 223) TX antenna = Homemade Vivaldi Chamber loading (when used) = 4 pieces of anechoic absorber, 2 each in the back 2 corners of chamber Full 2 port calibration performed

5.6 Measurement Results

This section will be sub-divided into two separate sections to assess the unloaded and loaded chamber performance separately. In each section a direct comparison will be made from standard stirrer paddles (no cuts at all) to the new stirrer designs to assess any improvement in practical performance.

The new stirrer designs from the numerical model have simply been scaled up in size to match the dimensions of the original stirrer paddles in the chamber - no changes whatsoever in the overall dimensions has been made between the respective stirrer sets so that the effect of the meanderline cuts alone can be conclusively charted.

Please note that for the concept validation, only the vertically mounted stirrer paddles have been subject to modification. The paddles designed for horizontally polarised waves have remained as solid plates with no modifications whatsoever.

For the vertically mounted paddles, six separate paddles exist each with different height dimensions. For completeness these are listed in Table XV.

Table XV: Paddle dimensions

Parameter	Description
Paddle set 1 (height x width in metres)	0.71 x 1
Paddle set 2 (height x width in metres)	0.85 x 1
Paddle set 3 (height x width in metres)	0.9 x 1
Paddle set 4 (height x width in metres)	0.67 x 1
Paddle set 5 (height x width in metres)	0.77 x 1
Paddle set 6 (height x width in metres)	0.62 x 1

5.6.1 Standard Vs New Designs: Unloaded Chamber

With respect to Table XIV, the first measurement assessment concerns the standard deviations. As previously stated, this is the standard deviation in the average power transfer function from six different receiver locations in the chamber.

The specific receiver locations (constant throughout) are detailed as follows:

1. Pos 1 = 1.15 m from left wall, 1.1 m back from stirrers
2. Pos 2 = 1.15 m from right wall, 1.1 m back from stirrers
3. Pos 3 = 1.15 m from left wall, 1 m back from Pos1
4. Pos 4 = 1.15 m from right wall, 1 m back from Pos2
5. Pos 5 = 1.15 m from left wall, 1.1 m from back wall
6. Pos 6 = 1.15 m from right wall, 1.1 m from back wall

Fig. 5.21 shows the typical set-up in the measurements, depicting the new stirrer designs and the receive antenna in position 1, orientated in the x direction.



Fig. 5.21: Standard deviation measurement set-up

The average power transfer function (P) was deduced from (Eq. 5.2) for each receive antenna orientation (j) and at each specific location (i) using 3 degree mechanical stirring and polarisation stirring. Thus:

$$P_{i-j} = \frac{\langle |S_{21}|^2 \rangle}{(1 - |S_{11}|^2)(1 - |S_{22}|^2)} \quad (5.2)$$

where: $i = 1, 2, 3, 4, 5, 6$ and $j = 1, 2, 3$. Hence, at the end of the measurement sequences, 18 separate average power transfer function measurements existed per frequency point. An average was then formed, comprising all $N = 18$ measurements:

$$P_{AV} = \frac{1}{N} \sum P_{i,j} \quad (5.3)$$

where this average should represent a good estimation of the true expected value [11].

The standard deviation (σ) was then calculated using (5.4).

$$\sigma = \sqrt{\frac{\sum_{i=1}^6 \sum_{j=1}^3 \{(P_{i,j}) - (P_{AV})\}^2}{N}} \quad (5.4)$$

In this case $N = 18$ instead of $N-1$ has been applied because the entire dataset population (population standard deviation) has been used in the calculations [15] - i.e. every single measurement value as opposed to just the selected maximums (sample standard deviation) in [10]. Finally, the standard deviation in dB scale is expressed relative to the mean and deduced using (5.5).

$$\sigma(dB) = 10 \log_{10} \left\{ \frac{\sigma + (P_{AV})}{(P_{AV})} \right\} \quad (5.5)$$

Fig. 5.22 details the measured standard deviation comparison between the standard paddles (no cuts) and the new modified paddles as a function of frequency in the unloaded chamber. It can be seen that up to approximately 380 MHz the new stirrer design outperforms the conventional (solid plate) paddle design. In the 100 MHz to 200 MHz range, the improvement in performance is seen to be in the order of 0.5 dB, which beyond 200 MHz decreases to around 0.15 dB.

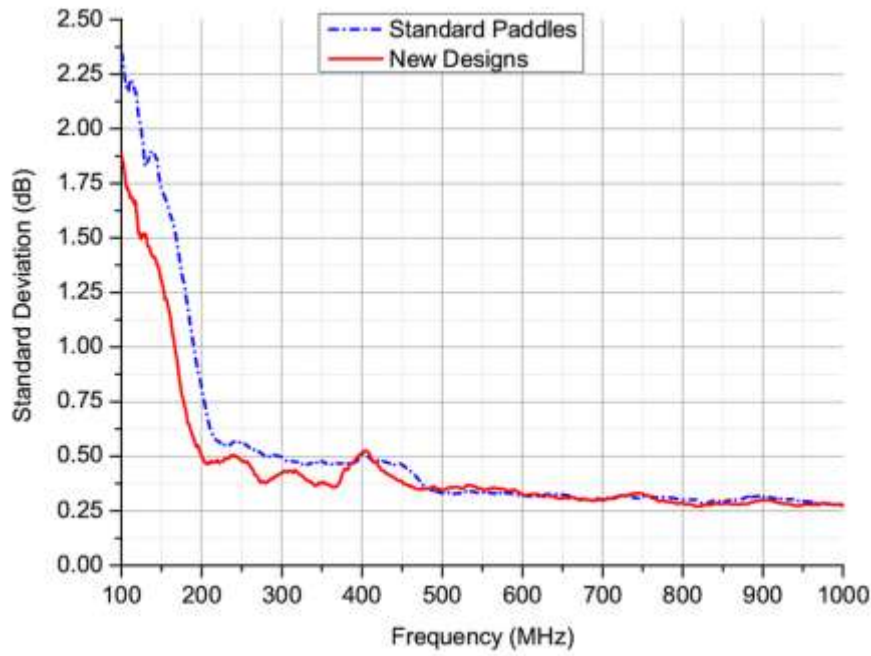


Fig. 5.22: Standard deviation comparison in unloaded chamber

Towards higher frequencies the performance of both paddle sets is seen to be comparable, proving that up to 1000 MHz, the cuts on the new paddle do not seem to have affected the high frequency performance of the chamber.

Furthermore, given the measurement results from Fig. 5.22, the agreement in terms of the measured standard deviation performance and that calculated by the theoretical uncertainty formula for antenna measurements (from Chapters 3 and 4) is seen to be very good. This serves to prove two points:

1. The theoretical uncertainty formula is useful and accurate.
2. The measurement rationale, measurement procedures and all subsequent processing in this chapter would appear to be valid and correct upon inspection.

The results seen so far would appear to practically validate the theoretical concept; however three more performance indicators need to be compared in order to derive more confidence in the performance merits of the new designs.

The polarisation imbalance can be detailed as follows after consultation with [11].

Considering just the x orientated measurements, a power transfer function can be established from the mechanical stirring and polarisation stirring schemes to yield (5.6).

$$P_{i,x} = \frac{\langle |S_{21,x}|^2 \rangle}{(1 - |S_{11}|^2)(1 - |S_{22}|^2)} \quad (5.6)$$

where: $i = 1, 2, 3, \dots, 6$.

An average level can then be formed from the x orientations according to (5.7).

$$P_{AV_x} = \frac{1}{6} \sum P_{i,x} \quad (5.7)$$

Similarly, for the y and z orientations, similar averages can be formed as (5.8) and (5.9) by using y and z orientated measurement data in the form of (5.6).

$$P_{AV_y} = \frac{1}{6} \sum P_{i,y} \quad (5.8)$$

$$P_{AV_z} = \frac{1}{6} \sum P_{i,z} \quad (5.9)$$

A total polarisation reference level can then be defined as [11]:

$$P_{POL_REF} = \frac{1}{3} \sum P_{AV_x,y,z} \quad (5.10)$$

The polarisation imbalance for the x , y and z orientations can then be expressed as (5.11).

$$\frac{P_{AV_x}}{P_{POL_REF}}, \frac{P_{AV_y}}{P_{POL_REF}}, \frac{P_{AV_z}}{P_{POL_REF}} \quad (5.11)$$

Fig. 5.23 and 5.24 depict the measured polarisation imbalance in dB scale as a function of frequency between the standard paddles and the new paddle design.

A polarisation imbalance is stated to result from both unstirred direct power and a modal excitation error in the chamber [11]. The latter is stated to appear as a result of the chamber and the mechanical stirrers being too regularly shaped, causing the TE and TM modes not to mix when stirred [11]. Hence, it is important to minimise this effect such that the amount received power in the chamber does not depend upon an antennas orientation.

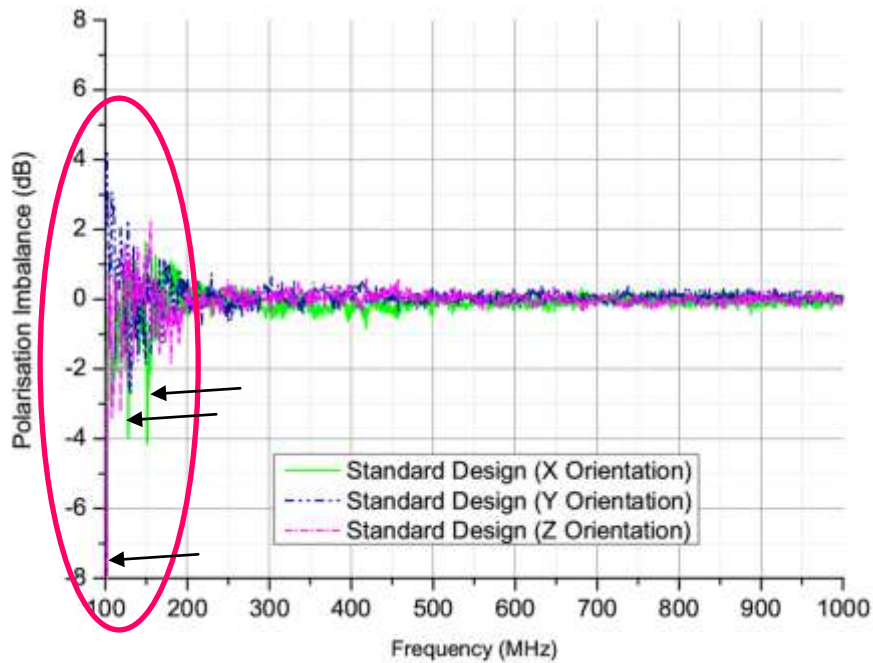


Fig. 5.23: Polarisation Imbalance (dB) for standard paddles

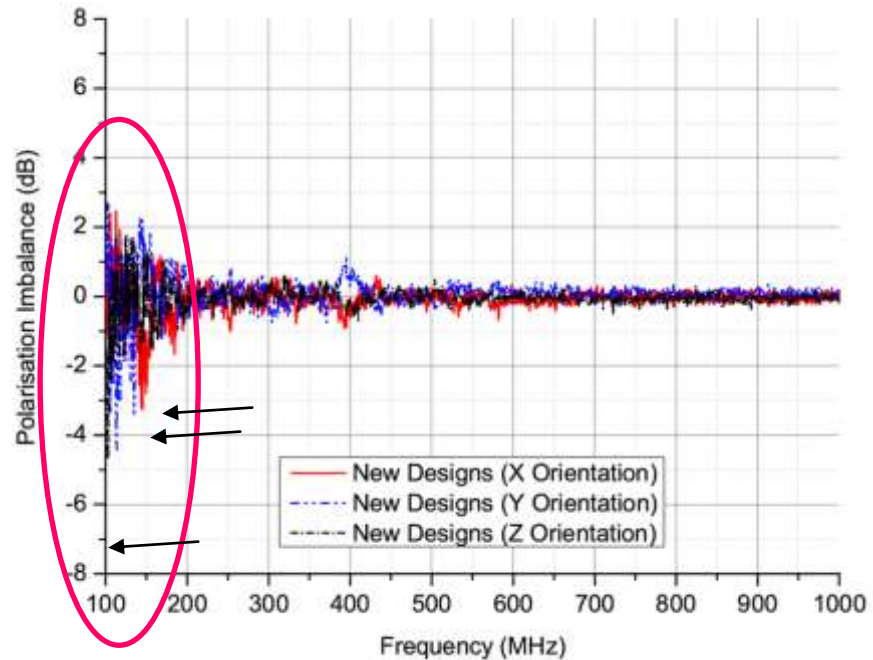


Fig. 5.24: Polarisation Imbalance (dB) for new designs

Comparing Figs. 5.23 and 5.24 it can be seen that there is an improvement in performance from the new designs in the 100 MHz - 200 MHz range. In the z orientation there is a 4dB improvement witnessed in some cases, and 1 - 1.5dB improvements are witnessed for the x and y orientations. In the lower frequency regions (< 200 MHz), a relatively high imbalance

was expected due to the sparseness in the overall number of modes available. However, it can be seen that due to the extreme irregular nature of the cuts that are configured to be resonant in this lower frequency region, in particular in the two principle planes, has served to minimise the polarisation discrepancy. At higher frequencies it can be seen that both standard and new designs perform perfectly - no imbalance is present.

The strange peak that is evident within the new designs at 400 MHz is believed to be due to an anomaly in the resonant performance of the cuts from the new paddle sets at this frequency - it is also present where the standard deviations are concerned (Fig. 5.22). Recommendations in the conclusion (section 5.7) are provided as a means of rectifying this, although in general the concept should be further investigated to mitigate this effect.

The Rician K factor performance of the standard and new designs is detailed next in Fig. 5.25. Please refer back to Chapter 2 page 49 for the derivation of this quantity.

Please note that a separate measurement sequence has been undertaken for the deduction of this and the following quantity. In this, 1 degree mechanical stirring, polarisation stirring and 1 x receiver location has been applied. The antenna has also been orientated in the z direction. All other parameters in Table XIV apply.

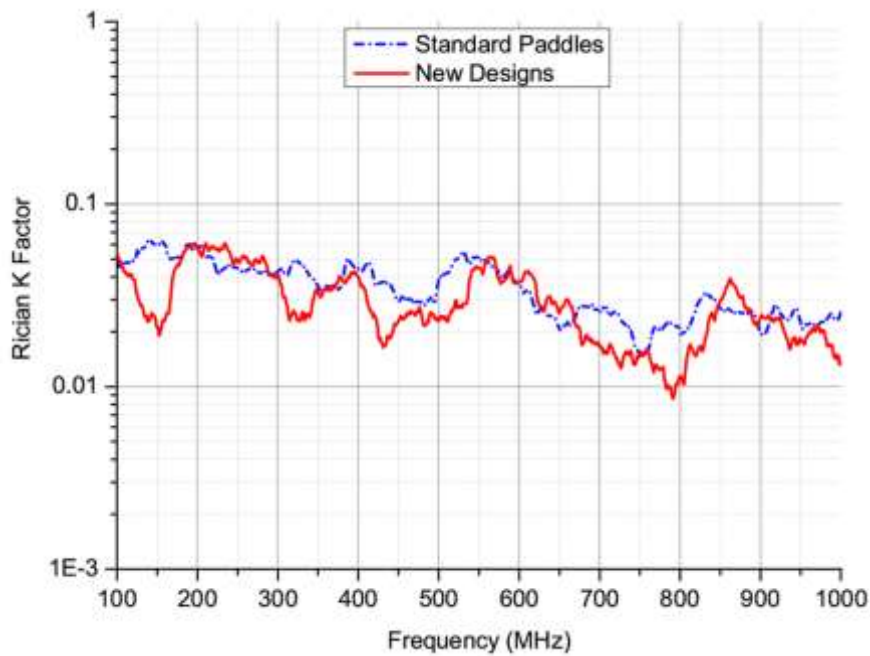


Fig. 5.25: Rician K Factor comparison in unloaded chamber

From Fig. 5.25 it can be seen that generally, there is a lower proportion of direct power being registered at the receiver. Particularly, at lower measured frequencies, there is a marked

difference. This is believed attributed to the added resonant capability of the new stirrer designs, in the fact that there are specific length cuts on the paddle that promote this resonant behaviour. Further evidence to support this statement can be found in Appendix A3 where the current distributions on the stirrer paddles are analysed.

For the non-line of sight number of independent samples, the full procedure is detailed in Appendix A1. To avoid repetition, it will not be repeated here. Using the 1 degree mechanical stirred, polarisation stirred and 1 x receiver location acquired data; Fig. 5.26 details the comparison between the standard and new designs, for each measured transmitting polarisation.

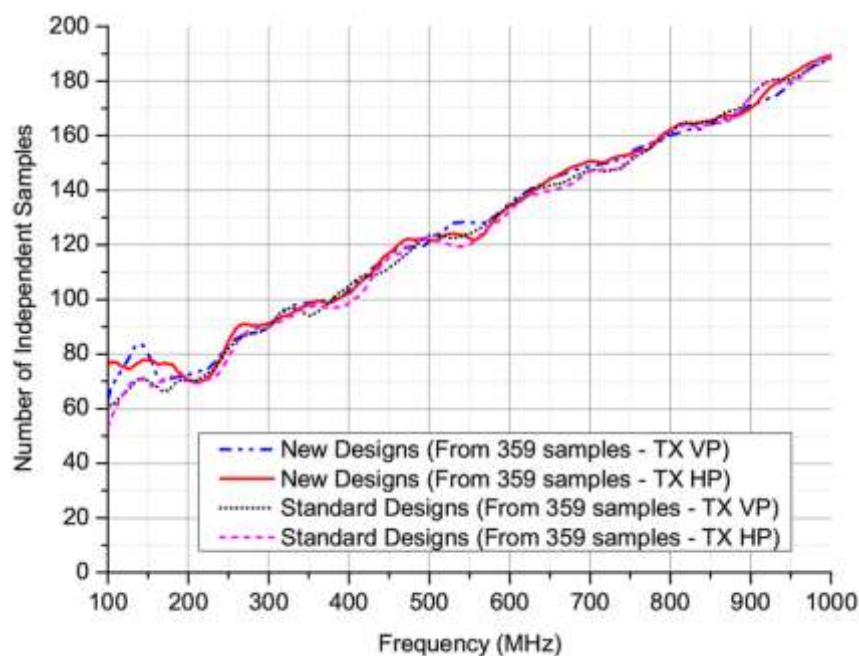


Fig. 5.26: Number of Independent samples comparison in unloaded chamber

From Fig. 5.26 it can be seen that in the 100 MHz - 200 MHz range there is an improvement in the overall number of samples that can be considered independent (sufficiently uncorrelated) with the new designs. This improvement is seen to be registered for both transmitting polarisations which would suggest that the cuts on the paddle in orthogonal planes have had a positive effect in stirring both polarised waves.

Beyond 200 MHz, in a region where the original paddle dimensions can generally be considered to be electrically large, performance is seen to be more or less comparable, although in areas the new designs appear to be better performing.

To conclude this sub-section, four different performance benchmarks have been applied to assess the performance merits of the new designs as compared to a standard design of paddle. The four separate benchmarks have all confirmed improved performance for the new designs in the lower modal region which serves to provide confidence that the design strategy does indeed work and does improve the chamber performance. For antenna measurements down at this lower modal region, quantities could be acquired with less uncertainty; and where the standard deviations are concerned, using less measurement samples (and less time) to yield the same overall performance levels.

The final sub-section of this thesis repeats all the aforementioned results but in a loaded chamber. The purpose of assessing this is because during some measurements (for example, large array antennas with the chamber loaded with power dividers, stands, boxes etc), the chamber can be presented with significant loading. The chamber should always be characterised in both scenarios to provide a complete picture of its true performance.

5.6.2 Standard Vs New Designs: Loaded Chamber

In this section all the aforementioned measurement parameters and details still apply. The only factor that has changed is that the chamber is loaded with 4 large pieces of anechoic absorber, two each in the back two corners of the chamber to simulate the ‘loading’.

The standard deviation comparison in the loaded scenario is detailed in Fig. 5.27.

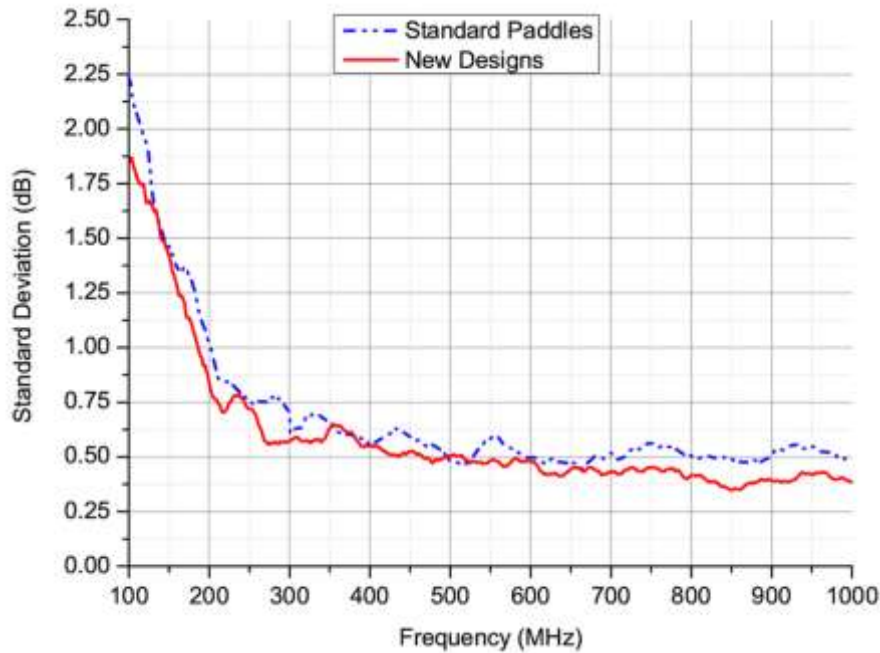


Fig. 5.27: Standard deviation comparison in loaded chamber

From Fig. 5.27 it is immediately apparent the effect that the loading has had on chamber performance; the standard deviations in this case are typically 0.25 dB higher. Towards higher frequencies this difference becomes slightly lower - typically in the order of 0.15 dB. The subsequent reason for the increase in the standard deviation with the loading is because the pieces of anechoic absorber can serve to dampen given resonant modes depending on where in the chamber that loading is situated [9]. If a given resonant mode is damped, this will have a consequence on the nature of the field distribution in the chamber as some of the electric field peaks can be suppressed. At given stirrer increments therefore, this can cause the field value not to vary significantly which in turn can result in a larger deviation inherent from different receiver antenna locations as seen.

In this loaded scenario it can be seen that the new paddle still outperforms the standard design. At higher frequencies this time the standard deviation for the new paddles shows better performance than the standard design which is believed to be due to the nature of the resonant cuts in two principle planes that has managed to stir both the TE and TM modes more efficiently about the larger average mode bandwidth.

The polarisation imbalance can be displayed as in Figs. 5.28 and 5.29. On the whole, when comparing Figs. 5.28 and 5.29, it can be seen that the new stirrer designs again outperform the standard design. From Fig. 5.28 it can be seen that a polarisation imbalance for the standard design in the z orientation is prevalent all the way out to 1000 MHz - this coincides

with the larger standard deviations inherent from Fig. 5.27. This is again believed to be due to the nature of the resonant cuts in two principle planes that has managed to stir both the TE and TM modes more efficiently about the larger average mode bandwidth.

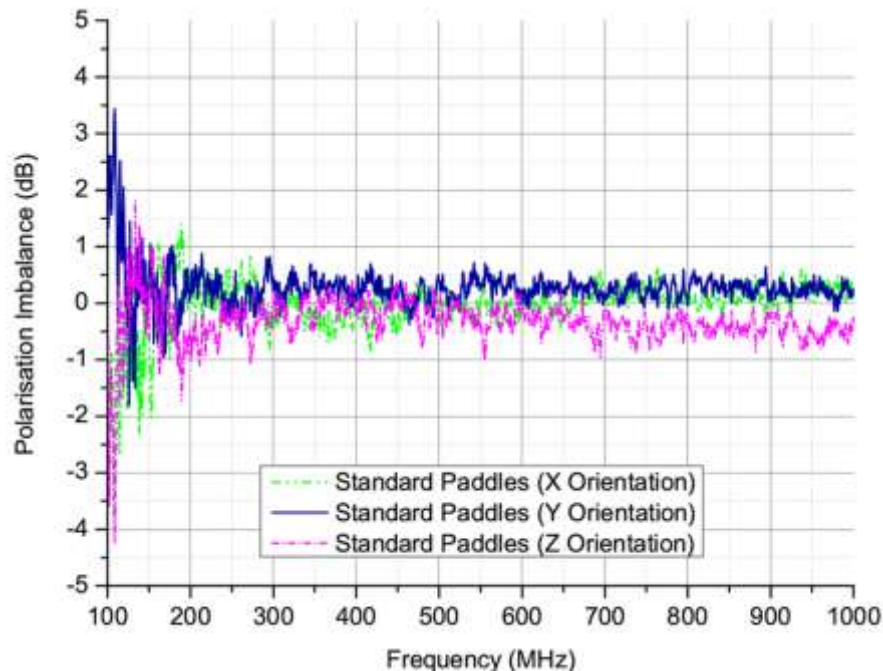


Fig. 5.28: Polarisation Imbalance (dB) for standard paddles

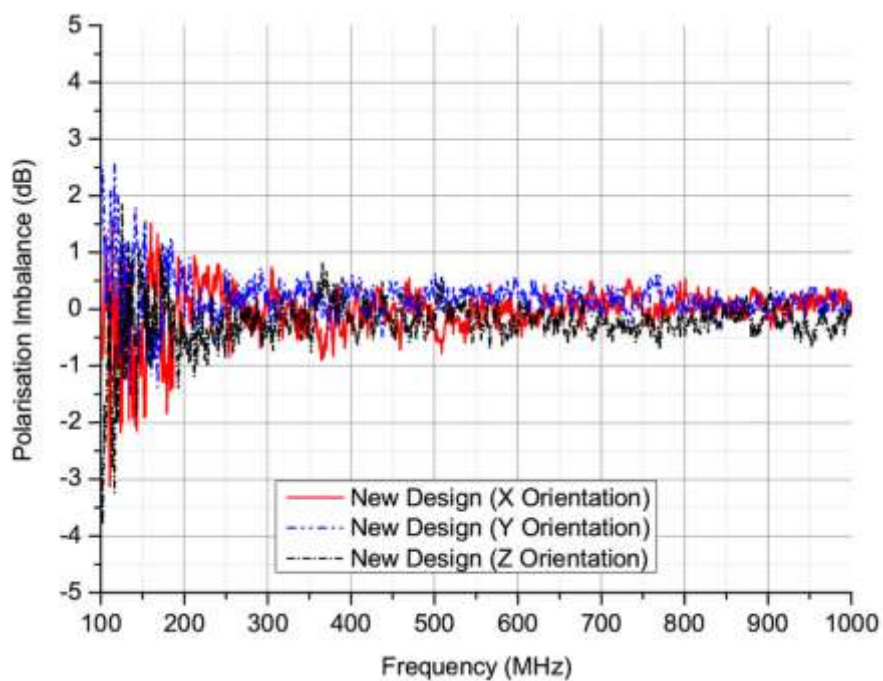


Fig. 5.29: Polarisation Imbalance (dB) for new designs

The Rician K factors for both standard and new designs can be viewed in Fig. 5.30, from which it can be seen that firstly, the proportion of direct power has increased with the additional loading as compared to the unloaded scenario (Fig. 5.25). Irrespective, it can be seen that the new stirrer designs again yield better performance on the whole than a standard design of paddle.

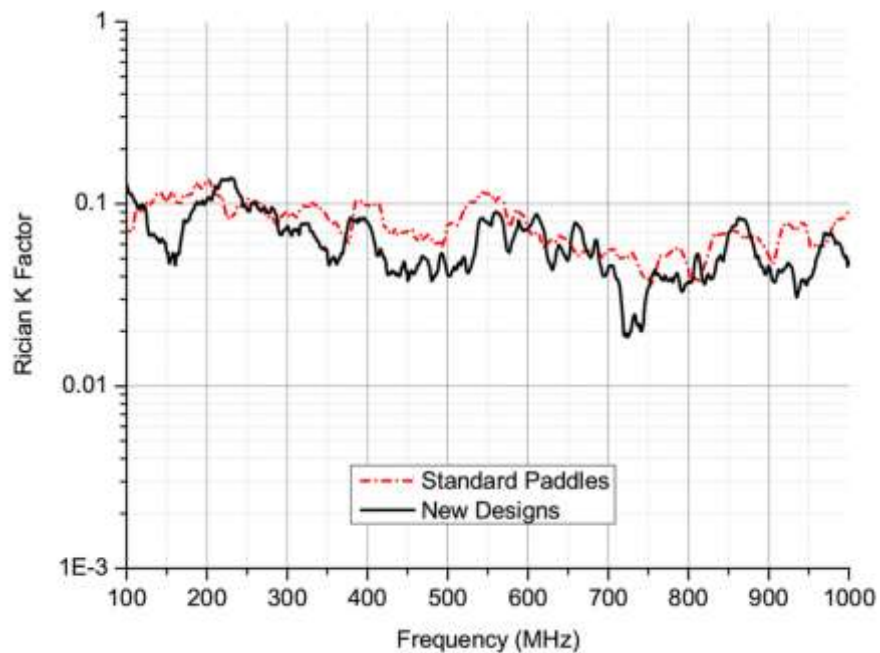


Fig. 5.30: Rician K Factor comparison in loaded chamber

The non line of sight number of independent samples can be viewed next in Fig. 5.31.

From Fig. 5.31 it can be seen that at lower frequencies an increase in the number of independent samples is evident, similar to the unloaded investigation. Overall, it can be seen that the total number of samples that are considered to be independent is lower than for the unloaded case, proving that the mechanical stirring process finds it more difficult to significantly alter the field distribution about an enlarged average mode bandwidth.

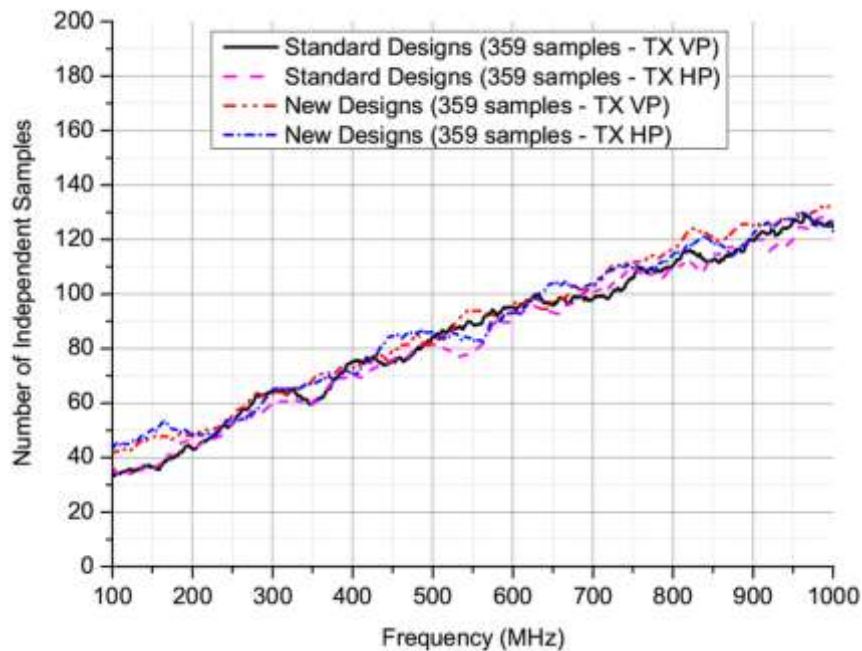


Fig. 5.31: Number of Independent samples comparison in loaded chamber

5.7 Conclusion

In this chapter, a new design of mechanical stirring paddle has been theoretically and numerically developed. Practically, a rigorous assessment has been undertaken to compare the merits of the new design against a standard design of paddle common to most reverberation chambers.

The theoretical idea behind the design has advocated a series of cuts on the paddle structure with a view to lower the resonant capability of the paddle structure by increasing the current path length. In addition, many of these cuts were tried and tested, each with varying lengths in an attempt to enact a broadband enhanced performance. An alternative numerical approach was adopted that yielded an improved design in an efficient manner.

Practical results showed that the theoretical idea worked and performance was improved. The performance aspect was validated by four separate performance indicators whose assessment all came back in favour of the new designs. On the whole, critics could argue that the increase in performance merits in some cases were small; however, it is worth remembering that only one of the principle paddle sets have been subject to modification - the other set stayed as a conventional design. Nevertheless, by this concept validation, there

is evidence enough to promote the idea and also to suggest that if the other principle paddle set was modified, further enhanced results could possibly be obtained.

This point brings us to the first recommendation:

Given the nature of the cuts on the modified paddle, if they were to entirely remain, then the structural rigidity of the paddles should be increased as the paddles had a tendency to flex after movement.

The rigidity could be improved by increasing the plate thickness. However, increasing the plate thickness too much would increase the overall weight which in turn will increase the stress on the motors driving the paddles. It could be possible therefore to limit the number of cuts on each paddle by performing the modification on the other principle paddle set. The reason why this was not performed was that given the horizontal paddle construction, a crane would have been needed to lift the paddles down and the chamber would have been out of commission for a long period of time - the working time frame did not simply allow for this, hence the nature of the design strategy.

The second recommendation brings us to the overall shape of cuts. The manufacturing procedure from the start was envisaged around manual metalwork in the workshop. This selection was made in order to keep costs very low and also because the manufacturing work could be completed immediately.

With the availability of CNC (Computer Numerical Control) milling machines that can be efficiently programmed, the opportunity to create more complex design shapes is possible that manual metal work by hand would struggle to accurately replicate.

With regards to the chamber performance validation in practice, it is clear to see that the procedure adopted provides more of an accurate and robust representation of a chambers' true performance, as multiple performance parameters are compared to benchmark the chamber as opposed to one procedure providing a rough estimate at best. For the EMC community who might not be familiar with the validation procedure adopted in this work, the conventional (standards) chamber validation procedure is presented in Appendix A4. The results issued in this appendix are for illustration purposes only - they have not been used as determining factors with regards to chamber performance in this study, nor is any reliance or significance placed on the results.

At this time, the consensus in thinking is that the new procedures should one day replace (or at the very least add to) the chamber validation protocol in the BS EN 61000-4-21 standards. This decision however will ultimately be down to the community to decide.

5.8 References

- [1] Y. Huang, Z. Jie Tao, and L. Ping, "A novel method to examine the effectiveness of a stirrer," in *Electromagnetic Compatibility, 2005. EMC 2005. 2005 International Symposium on*, 2005, pp. 556-561.
- [2] Y. Huang, N. Abumustafa, Q. G. Wang, and X. Zhu, "Comparison of Two Stirrer Designs for a New Reverberation Chamber," in *Environmental Electromagnetics, The 2006 4th Asia-Pacific Conference on*, 2006, pp. 450-453.
- [3] J. I. Hong, C. S. Huh, "Optimization of Stirrer with Various Parameters in Reverberation Chamber," *Progress In Electromagnetics Research (PIER)*, vol. 104, pp. 15-30, 2010.
- [4] N. Wellander, O. Lunden, and M. Backstrom, "Experimental Investigation and Mathematical Modeling of Design Parameters for Efficient Stirrers in Mode-Stirred Reverberation Chambers," *Electromagnetic Compatibility, IEEE Transactions on*, vol. 49, pp. 94-103, 2007.
- [5] L. R. Arnaut, "Effect of size, orientation, and eccentricity of mode stirrers on their performance in reverberation chambers," *Electromagnetic Compatibility, IEEE Transactions on*, vol. 48, pp. 600-602, 2006.
- [6] J. Clegg, A. C. Marvin, J. F. Dawson, and S. J. Porter, "Optimization of stirrer designs in a reverberation chamber," *Electromagnetic Compatibility, IEEE Transactions on*, vol. 47, pp. 824-832, 2005.
- [7] D. I. Wu and D. C. Chang, "The effect of an electrically large stirrer in a mode-stirred chamber," *Electromagnetic Compatibility, IEEE Transactions on*, vol. 31, pp. 164-169, 1989.
- [8] S. R. Best, "On the resonant properties of the Koch fractal and other wire monopole antennas," *Antennas and Wireless Propagation Letters, IEEE*, vol. 1, pp. 74-76, 2002.
- [9] Y. Huang, "The investigation of chambers for electromagnetic systems," D Phil Thesis, Department of Engineering Science, University of Oxford, 1993.
- [10] "BS EN 61000-4-21:2011," in *Electromagnetic compatibility (EMC) Part 4-21: Testing and measurement techniques — Reverberation chamber test methods*, ed: BSI Standards Publication, 2011.
- [11] P. S. Kildal, X. Chen, C. Orlenius, M. Franzen, and C. S. L. Patane, "Characterization of Reverberation Chambers for OTA Measurements of Wireless Devices: Physical Formulations of Channel Matrix and New Uncertainty Formula," *Antennas and Propagation, IEEE Transactions on*, vol. 60, pp. 3875-3891, 2012.

-
- [12] P. S. Kildal, C. Orlenius, J. Carlsson, U. Carlberg, K. Karlsson, and M. Franzen, "Designing reverberation chambers for measurements of small antennas and wireless terminals: Accuracy, frequency resolution, lowest frequency of operation, loading and shielding of chamber," in *Antennas and Propagation, 2006. EuCAP 2006. First European Conference on*, 2006, pp. 1-6.
 - [13] A. Coates and A. P. Duffy, "Maximum Working Volume and Minimum Working Frequency Tradeoff in a Reverberation Chamber," *IEEE Transactions on Electromagnetic Compatibility*, vol. 49, pp. 719-722, 2007.
 - [14] L. R. Arnaut, "Operation of Electromagnetic Reverberation Chambers with Wave Diffractors at Relatively Low Frequencies," *IEEE Transactions on Electromagnetic Compatibility*, vol. 43, pp. 637-653, 2001.
 - [15] J. R. Taylor, *An Introduction to Error Analysis: The Study of Uncertainties in Physical Measurements*, 2nd ed.: University Science Books, 1997.

Chapter 6: Future Work & Contributions

6.1 Thesis Summary

To briefly summarise the contents of this thesis, it has been further reinforced that the reverberation chamber is an extremely powerful tool in which to conduct antenna measurements. The underpinning theory that governs the facility (from chapter two) has shown that transmission measurements conducted in the facility (if performed correctly), are statistically similar to real life multipath propagation environments (Rayleigh distributed). This condition can serve to prove the suitability of the facility as a multipath emulator. Further, it has also been discussed that providing enough modes are excited, the angle of arrival of plane waves comes from every conceivable direction over a unit sphere with an equal probability. This can provide a simplification in the characterisation of antennas as then their performance is not sensitive to their orientation. For this condition to occur however, the proportion of direct power reaching the receiver has to be crucially minimised.

Chapter three has shown that the measurement of single port antennas can be performed accurately; whether that is under free space equivalent conditions or in conjunction with real human beings used to assess the textile antennas' installed performance. This statement has been verified by confirming very low measurement uncertainties under both operational conditions. New knowledge has been confirmed in this chapter in that for a small sized textile antenna with a small ground plane, the installed (on-body) performance is very sensitive to the conductivity and textile material thickness. In this, a lossier textile antenna measured under free space equivalent conditions was shown to grossly outperform a higher free space efficient textile antenna when placed on-body, in terms of both the efficiency and frequency de-tuning performance. This new information was confirmed for different on-body locations and different proximity distances from the human test subjects.

When this new information was applied to larger ground plane sized textile antennas, the higher efficient antenna in free space retained its higher level of efficiency on-body. Therefore, further new knowledge can be disseminated in that in addition to the textile material conductivity and thickness, the ground plane size of the device is also of crucial importance.

Chapter four charted a distinction between multiport antennas designed for MIMO applications, and more conventional antenna arrays that are not. The reason for this distinction is that from a measurement perspective, the treatment of either case has to differ

in order to realistically characterise the device performance. For the MIMO case, two new single element dual feed planar inverted F antennas were presented. Full measurement procedures were disclosed which supplemented the practical evidence disclosing the antennas excellent performance. Both antennas were confirmed to exhibit high amounts of diversity gain (close to the theoretical two port maximum), very low correlation between their two closely spaced feeds, high levels of channel capacity and high levels of total embedded element efficiency about the centre frequency of operation. These results asserted the claim that the antennas are strong candidates to potentially be employed in an Industrial role.

For the conventional antenna arrays, a new equation was developed that allowed for a simplification in the treatment of the antenna efficiency when measured using a reverberation chamber. A procedure was detailed that allowed for a realistic characterisation of these antenna types, yet remained simple and accurate to perform. The techniques disclosed have the potential to offer a fresh alternative to how the efficiency measurements of conventional antenna arrays are performed.

Chapter five disclosed new designs for the mechanical stirring paddles for use in reverberation chambers. It was shown that a concept of meanderline cuts on the paddle structure can enhance the resonant capability of the paddles enabling them to better perform at lower modal densities where conventional paddle designs do not perform so well. It was shown that the technique is straightforward and cost effective to apply and offered numerous performance enhancements. This statement was confirmed against the backdrop of a more robust / potentially less uncertain chamber calibration procedure, which, at the time of writing, is believed to have the potential to replace or at the very least add to the procedures contained within the BS EN 61000-4-21 standards.

6.2 Future Work

Based upon the conclusions drawn from above and from each consecutive chapter, and taking into account the limitations of the work presented, future work can be carried out in the following areas.

From Chapter 3, the scope can be extended to include different designs of on-body textile antennas. In particular it would be useful to have multiple feed textile antennas in the on-body scenario such that the antennas could be configured to radiate on/off body depending

on the communication scenario, and fading losses in on-body propagation scenarios could also be treated.

In terms of the efficiency measurements in the RC, a very recent communiqué [1] discussed new techniques for measuring the unknown efficiency of antennas without the use of a reference antenna. Three techniques were disclosed: a one antenna method using an S_{11} based approach, a two antenna method using the transmission characteristics (S_{21}), and a three antenna method also using the transmission characteristics.

In each scenario, the chamber path loss was determined from the Q factor. In the one antenna method, approximations were made on the field uniformity that may or may not be evident in different chambers. The two antenna method relied upon having the same transmit and receive antennas. The three antenna method makes no assumptions and does not require the antennas to be the same.

The three antenna method is useful for when no reference antenna is available; however, when reference antennas are available, two more measurements are required using this approach (three antenna method) that obviously takes a longer time. If the one or two antenna method could be validated and honed to work in different RC's without the use of the same antennas this would be advantageous. Furthermore, the power loss deduction from Q factor in [1] assumes that the wall losses are dominant. A technique to relax this constraint may have to be created if this is not the case (for example, when measuring quantities on human beings inside an RC or large arrays with supporting material).

From Chapter 4, the dual feed PIFA's could be scaled down in height further. A 5 mm height co-polarised design has been developed and measured (not included in this thesis) that showed similar diversity gain levels to the 10 mm height. This height would possibly need to be further scaled down to fit with the ultra-slim portable devices that are on the market.

Further, from the measurement procedures for the MIMO characterisation, the deduction of diversity gain and channel capacity without a reference antenna measured power level would also be advantageous. This could be possibly formed by deducing the chamber attenuation from the Q factor approach in [1] and re-deriving the procedure for the measured channel samples with respect to this.

For the array antennas, the efficiency deduction without the reference would again be beneficial. Further, for these designs given the nature of their application, an accurate procedure to measure the noise temperature of the array in the RC would be of great benefit.

Current outdoor techniques suffer from interference - a problem the RC would not have as it is shielded from the outside environment.

From Chapter 5, the technique of the cuts was validated and did provide better performance. However, as a concept validation, only one principle paddle was modified. Further work to modify both sets would be expected to yield even better performance. In addition, by such a modification, fewer cuts could be made on the single paddle structure which would improve its rigidity.

In terms of the RC optimisation, much work still exists. Work on triangular shaped chambers has been performed; however, no information on the optimum cavity shape exists. Once that optimum design was found, the optimum paddle design in that facility also needs to be configured. From the modified paddle sets in this thesis, given no limitations in manufacturing, Koch fractal styles of cut or a hybrid mix of different cuts could perform even better - this should be explored.

6.3 Key Contributions

In this thesis, three main investigation areas exist. The key contributions to new knowledge are detailed as follows:

Chapter 3: Textile Antennas

New knowledge has been obtained that concern the performance textile antennas with small ground planes. In this, a lossier free space textile antenna can outperform a higher efficient free space textile antenna when placed on-body. The reasons for this is that a thinner, higher conductivity textile material will give rise to higher fields inside the human body and thus more power will be lost. In addition, the on-body efficiency performance is proved to be crucially linked to the ground plane dimensions - the prior effect is not witnessed when the ground plane dimensions are increased, hence new knowledge is apparent here where the design of on-body textile antennas are concerned.

New knowledge concerning the performance effects at different human body locations is also discussed as well as the severe effects of bending. New statistical knowledge is disclosed concerning on-body measurements using real human beings as opposed to phantoms, which provides greater confidence in a given sets of results as it is proved that

subtle movements in on-body RC measurements do not affect the measurement repeatability or accuracy, and also that the performance is representative to different human beings.

Chapter 4: MIMO Antennas

The complete practical MIMO characterisation of two new single element dual feed planar inverted F antennas for Bluetooth/WLAN applications has been detailed. Full measurement procedures are also discussed that detail how to acquire each quantity with accuracy. The new antennas have been shown to provide excellent performance despite their small size, in many occasions reaching near theoretically maximum levels. This study and the disclosed results serve to potentially validate the use of the new designs in an industrial capacity.

Chapter 4: (Conventional) Antenna Arrays

A new equation and technique has been developed to simplify the measurements of all excited antenna arrays in the reverberation chamber. This technique is shown to be simple and accurate and provides a strategy that will enable the characterisation of antenna arrays in an RC to be performed more conveniently and more realistic to their true operational scenario. The potential also exists within this technique for the de-embedding of other components (such as baluns) in RC measurements.

Chapter 5: Mechanical Stirring Paddles

A new design of mechanical stirring paddle has been methodically developed and thoroughly tested in practice. The new designs are seen to improve chamber down at lower modal densities where all chambers will have poor performance. This technique has the potential to improve any given reverberation chamber and takes a step further towards the ultimate goal of chamber optimisation. The technique developed is universal in nature meaning that it should work in chambers of any size. The paddles are validated against the backdrop of a more robust chamber characterisation procedure, which has the potential to change the thinking of how a chambers' performance is measured (from a standards perspective).

6.4 References

- [1] C. L. Holloway, H. A. Shah, R. J. Pirkl, W. F. Young, D. A. Hill, and J. Ladbury, "Reverberation Chamber Techniques for Determining the Radiation and Total Efficiency of Antennas," *Antennas and Propagation, IEEE Transactions on*, vol. 60, pp. 1758-1770, 2012.

Appendix A1: Deduction of Non Line of Sight Number of Independent Samples

The purpose of this appendix section is to detail the complete procedure as to how the non line of sight number of independent samples can be calculated in RC measurements. This technique is applied when deducing this quantity for use in the theoretical uncertainty formula and also to determine the stirrer efficiency.

To calculate the non line of sight number of independent samples, the use of the autocorrelation function is considered. The term ‘autocorrelation’ can be defined as the correlation of a signal with itself.

If each sample is a linear power quantity, the offset delta (Δ) at which the autocorrelation has dropped to a given value can be found and the number of independent samples (N_{IND}) determined from:

$$N_{IND} = \frac{N_{MEASURED}}{\Delta} \quad (\text{A1.1})$$

where: $N_{MEASURED}$ is simply the total number of measurement samples.

The procedure to determine delta is described as follows. Firstly, for one specific measured frequency value and assuming 718 measured samples, all the samples obtained from various stirrer increments for a full revolution should be obtained and collated in a one column vector. The column vector is permuted such that the last value in the original vector is placed as the first value in a newly created vector (i.e. vector two). This permuting action continues such that the penultimate value in the original vector is placed first in a newly created third vector and so on. This permuting action continues until a 718 x 718 (assuming one degree mechanical stirring intervals and polarisation stirring) matrix exists; in essence all the values in the original matrix had been permuted to form new vectors in their own right.

This permuting action is detailed as follows:

$$\begin{aligned} &x_1, x_2, x_3, x_4, \dots, x_{N-1}, x_N \\ &x_N, x_1, x_2, x_3, x_4, \dots, x_{N-1} \\ &x_{N-1}, x_N, x_1, x_2, x_3, x_4, \dots, x_{N-2} \end{aligned}$$

And so on, until all samples have been permuted.

Once the permuting of the vectors has been completed, the quantity of delta needs to be found. The quantity delta is a function of the total number of measurement samples and should *not* necessarily be approximated by the $1/e = 0.37$ criterion. This 0.37 criterion is only valid assuming 450 measured samples only [1]. To calculate delta, the theoretical probability density function form of the correlation coefficient (ψ) can be used, as covered in [1] and [2]. In (A1.2), p must be estimated accordingly.

$$\psi(r) = \frac{N-2}{\sqrt{2\pi}} \times \frac{\Gamma(N-1)}{\Gamma(N-0.5)} \times \frac{(1-p^2)^{(N-1)/2} (1-r^2)^{(N-4)/2}}{(1-pr)^{N-3/2}} \times \left[1 + \frac{1+pr}{4(2N-1)} + \dots \right] \quad (\text{A1.2})$$

where: p = expected value of r , Γ is the gamma function, N is the total number of measurement samples and r can be found by [3].

$$r = \frac{\frac{1}{N} \sum_1^n (A_{mn} - \bar{A})(B_{mn} - \bar{B})}{\sqrt{\left(\left(\frac{\sum_1^n (A_{mn} - \bar{A})^2}{N-1} \right) \left(\frac{\sum_1^n (B_{mn} - \bar{B})^2}{N-1} \right) \right)}} \quad (\text{A1.3})$$

where: A = original (unpermuted) vector, B = each permuted vector in turn, $m n$ stand for the row and column vectors and the bar terms above A and B signify the mean.

The pdf function of equation (A1.2) as depicted in Fig. A1.1 will be evident. In this case, Fig. A1.1 has been plotted for 718 samples assuming a value of $p = 0.4601$.

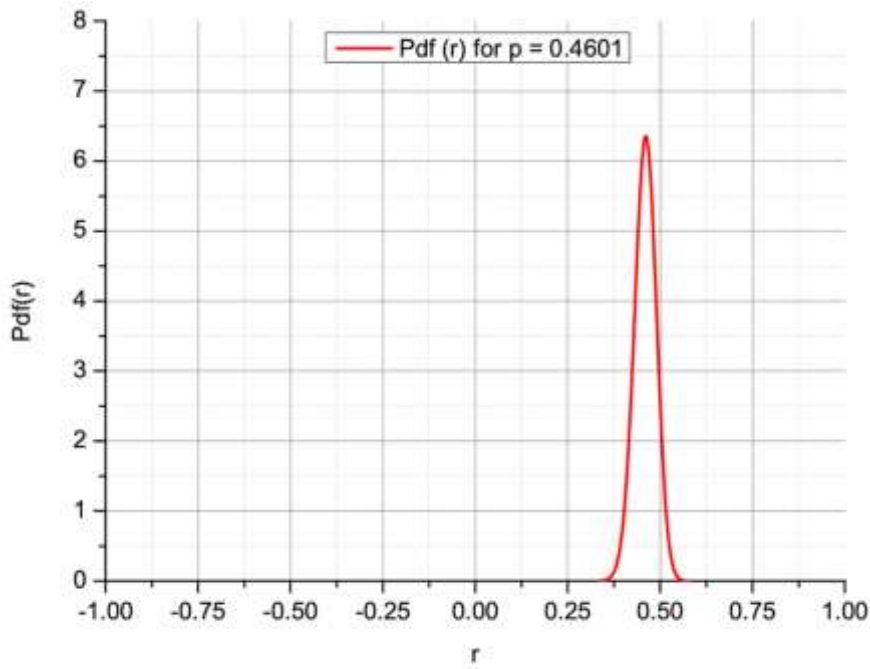


Fig. A1.1: Pdf form of autocorrelation function

The next step concerns the deduction of the probability of occurrence (α) and the formulation of the null hypothesis. Alpha is determined by integrating the pdf form of Fig. A1.1, to determine the probability of occurrence of (r) which is smaller than or equal to the critical value (p_o). Thus:

$$\alpha = \int_{-1}^{p_o} \psi(r) dr \quad (\text{A1.4})$$

The theoretical pdf is integrated until alpha reaches a given confidence interval (usually 0.05 (95% confidence) or 0.01 (99% confidence)). Once that value is reached, it will correspond to a given correlation value. This value must then be tested and either accepted or rejected according to the null hypothesis set out in [1]; thus:

If $r \leq p_o$ the hypothesis must be rejected. If this is the case, the probability that the sample originates from the assumed population is $\leq \alpha$ and p must be re-chosen [1]. Once an acceptable value has been found, it is applied as in Figs. A1.2 and A1.3 to determine delta and the number of independent samples found from equation (A1.1). For 718 samples, p has been determined as 0.4601 and this yields a critical value p_o of 0.394 at alpha = 0.01.

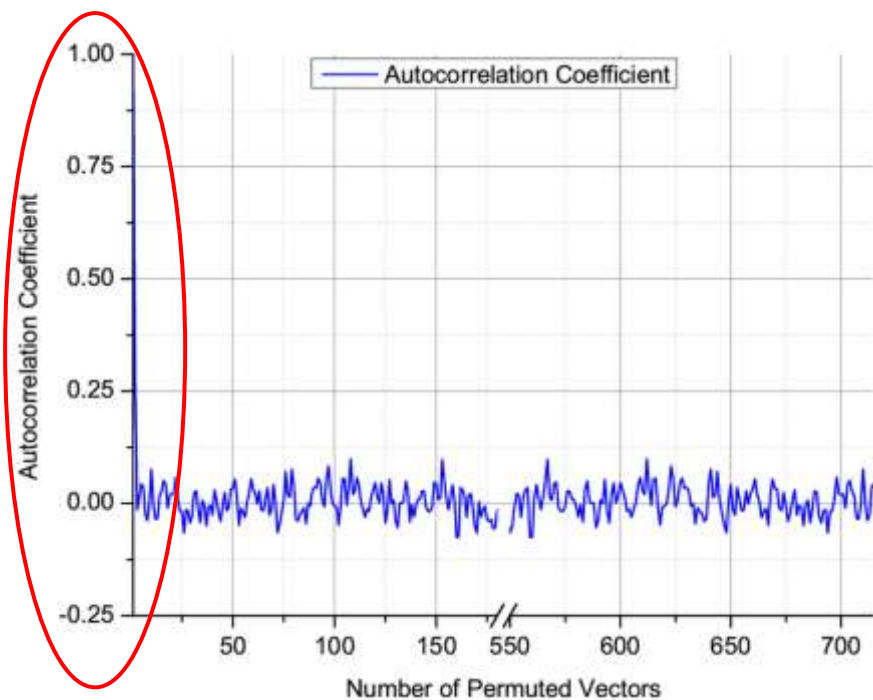


Fig. A1.2: Autocorrelation as a function of number of permuted vectors

Enlarging Fig. A1.3 about the point where the correlation will have dropped to the critical value of 0.394 (deduced for 718 measured samples), the value of delta can be found as shown in Fig. A1.3.

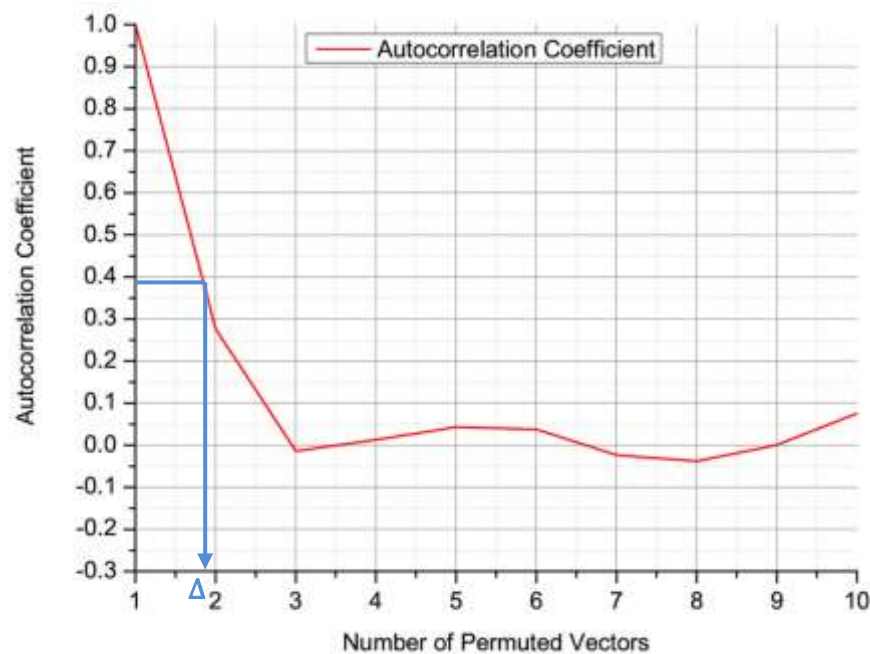


Fig. A1.3: Autocorrelation as a function of ten permuted vectors

- [1] H. G. Krauthauser, T. Winzerling, J. Nitsch, N. Eulig, and A. Enders, "Statistical interpretation of autocorrelation coefficients for fields in mode-stiffed chambers," *EMC 2005: IEEE International Symposium on Electromagnetic Compatibility, Vols 1-3, Proceedings*, pp. 550-555, 2005.
- [2] J. R. Taylor, *An Introduction to Error Analysis: The Study of Uncertainties in Physical Measurements*, 2nd ed.: University Science Books, 1997.
- [3] "BS EN 61000-4-21:2011 Electromagnetic compatibility (EMC). Testing and measurement techniques. Reverberation chamber test methods," ed, 2011.

Appendix A2: Multivariate Normality Test for SIMO Channels

The purpose of this appendix section is to statistically test the measured SIMO channel samples to determine whether they can be reasonably assumed to come from a normal distribution or not. As previously stated back in Chapter 4, if the samples can be confirmed to be normally distributed, it would eliminate a potential source of uncertainty with regards to overestimating the levels of channel capacity, and further reliance can be placed on the measured/calculated values.

Similar to the statistical recommendations in Chapter 2, the Lilliefors test has been applied, and this evidence is compared to scatter plots to re-enforce any conclusions drawn from this analysis. In the Lilliefors test, the null hypothesis has been configured to assess whether the measured SIMO channel samples can be expected to come from a normal distribution and the confidence interval selected in the test is 95%. The test effectively measures the maximum distance from the deduced empirical cdf from the measured data and compares to a theoretical normal distribution having the same mean and standard deviation.

Fig A2.1 details the Lillietest results for the co-polarised PIFA (feed 1) and Fig. A2.2 charts the scatter plot data for feed 1 to re-enforce the evidence from the Lillietest.

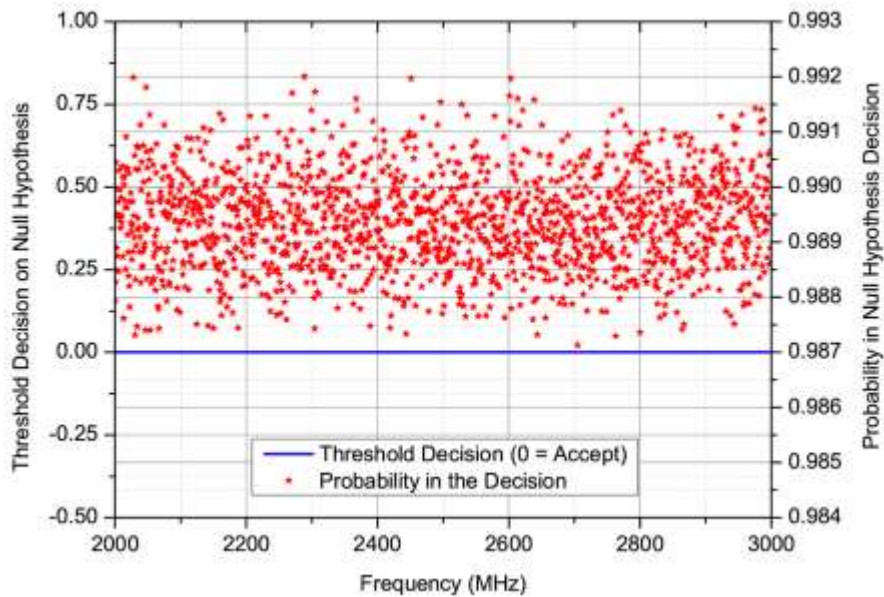


Fig. A2.1: Lillietest decision on normality for co-polarised PIFA feed 1

From Fig. A2.1 it can be seen that the Lillietest has accepted the hypothesis that the samples do come from a normal distribution at a 95% confidence interval.

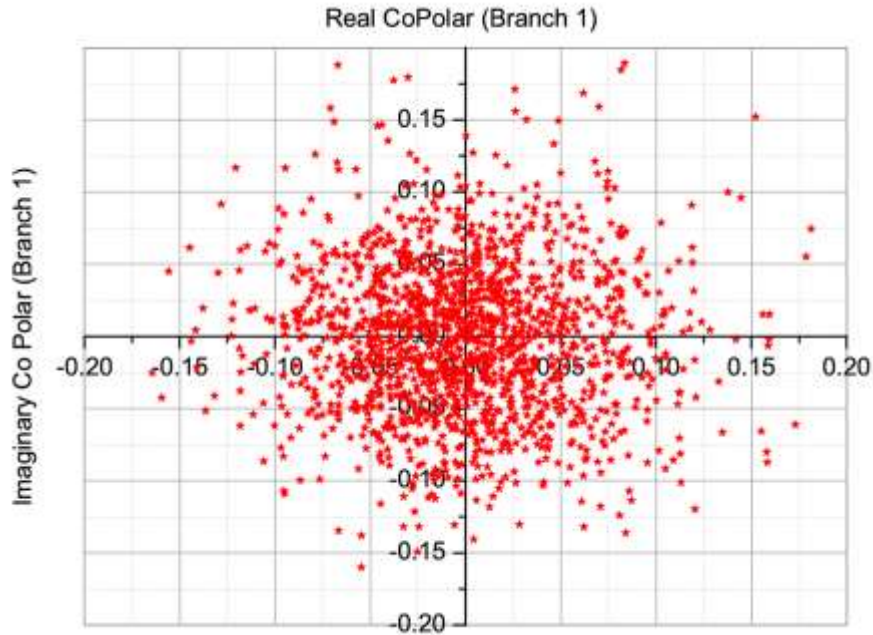


Fig. A2.2: Scatter plot for co-polarised PIFA feed 1

From Fig. A2.2 it can be seen that the vast majority of samples are centred around the (0, 0) axis providing further evidence to re-enforce the Lillietest's decision. Figs. A2.3 and A2.4 detail the evidence obtained for the co-polarised PIFA feed 2.

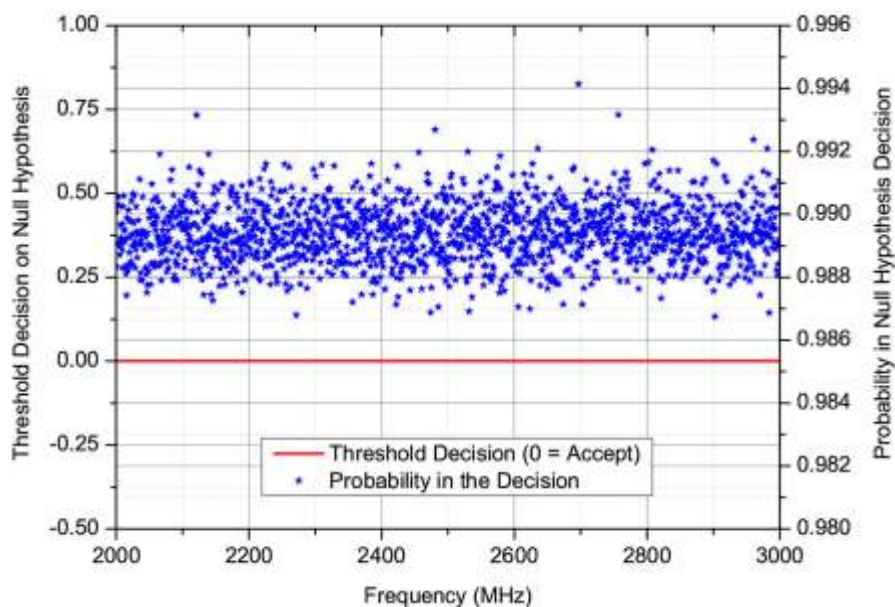


Fig. A2.3: Lillietest decision on normality for co-polarised PIFA feed 2

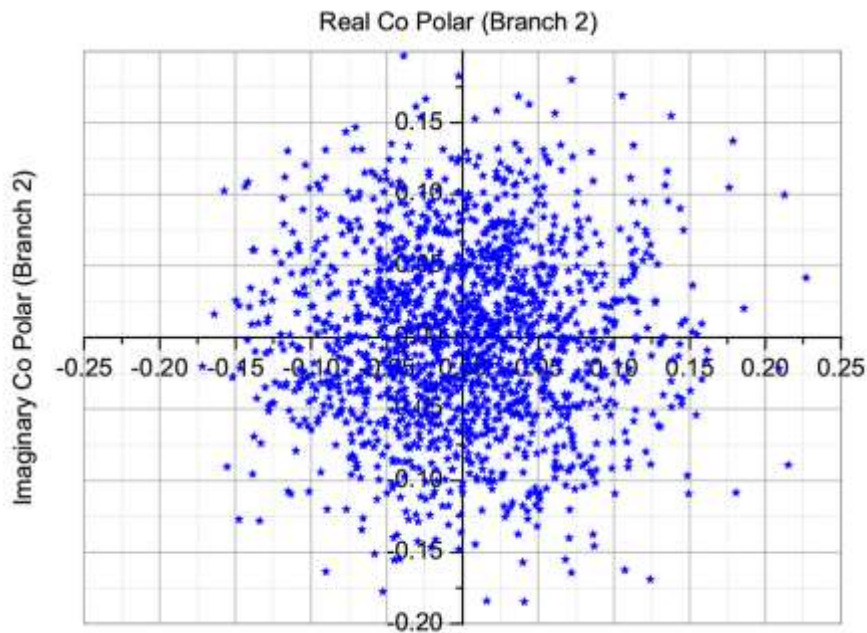


Fig. A2.4: Scatter plot for co-polarised PIFA feed 2

Again, evidence is returned that suggests with a degree of confidence that the measured samples for feed 2 are also normally distributed.

Moving on, Figs. A2.5 and A2.6 detail the evidence obtained for the cross polarised PIFA feed 1.

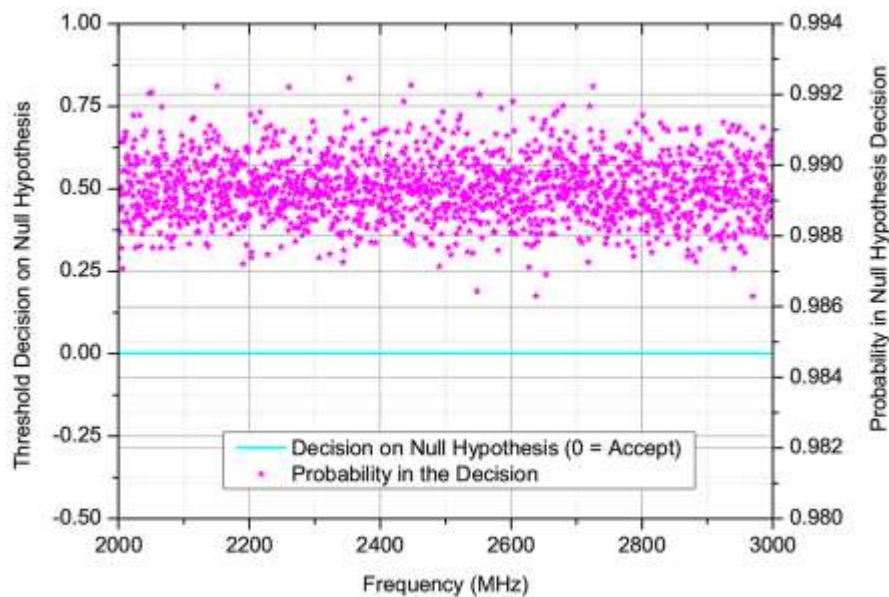


Fig. A2.5: Lillietest decision on normality for cross-polarised PIFA feed 1

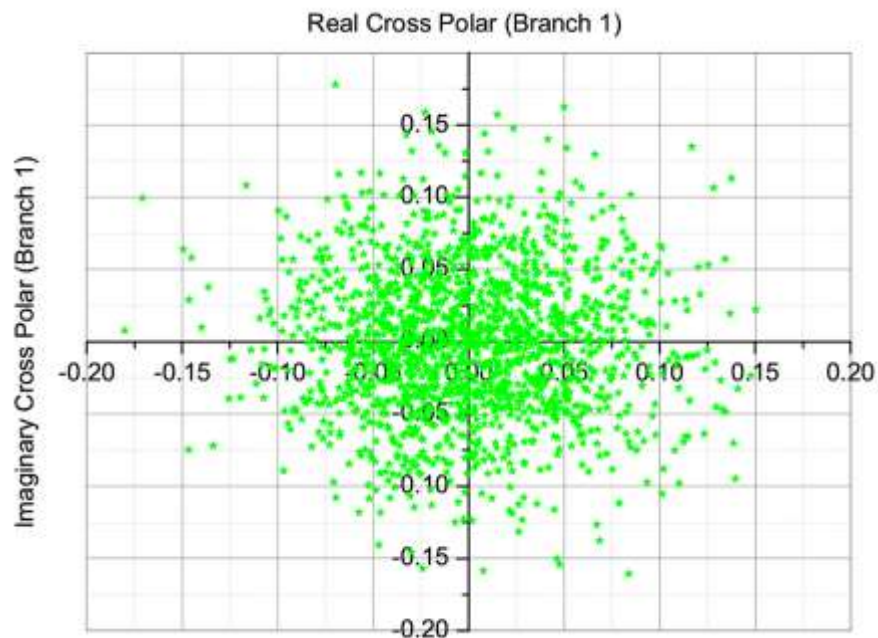


Fig. A2.6: Scatter plot for cross-polarised PIFA feed 1

Likewise, the evidence obtained for the cross polarised PIFA feed 2 is depicted in Figs. A2.7 and A2.8.

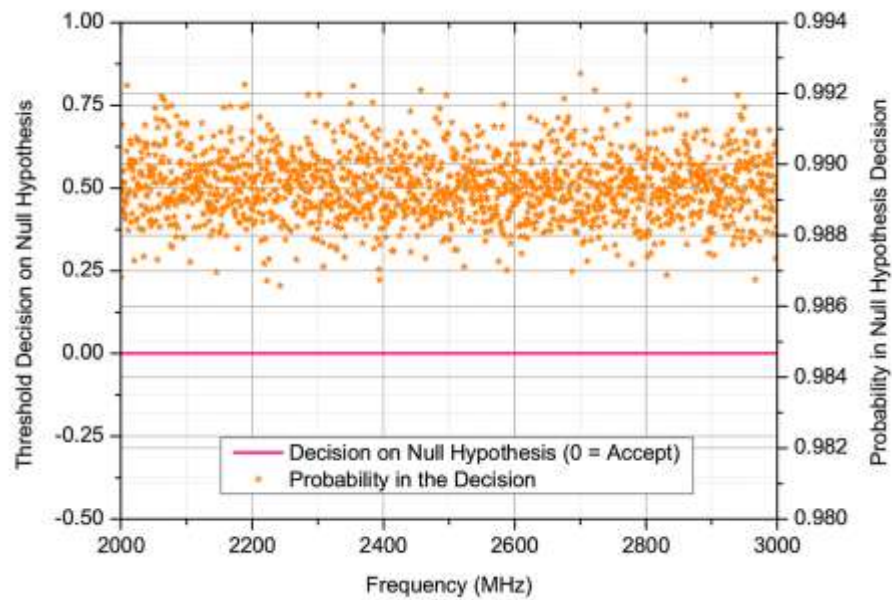


Fig. A2.7: Lillietest decision on normality for cross-polarised PIFA feed 2

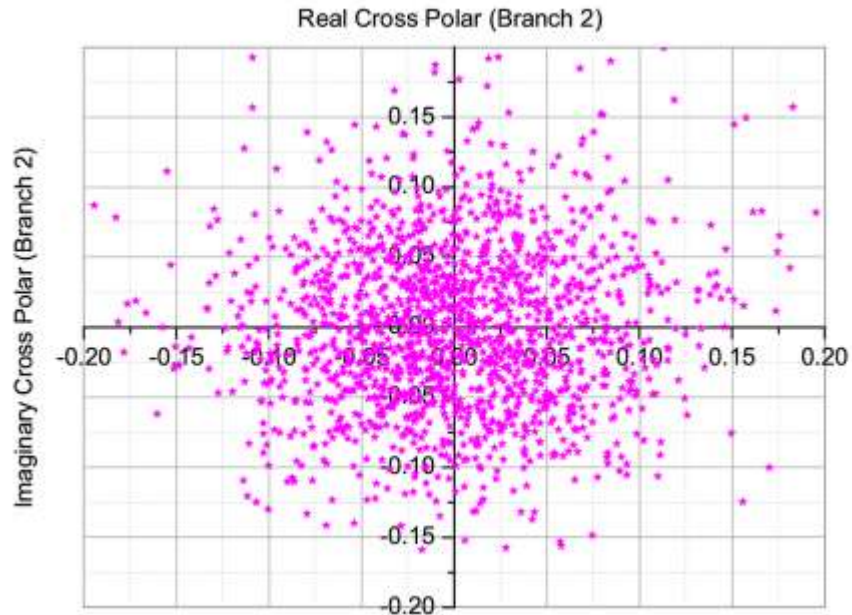


Fig. A2.8: Scatter plot for cross-polarised PIFA feed 2

From the evidence issued in this section it is possible to conclude with a reasonable degree of certainty that the measured channel samples for both PIFAs used in the diversity gain and channel capacity measurements are normally distributed. With regards to the channel capacity calculations, it also serves to provide confidence that the result is accurate and not liable to overestimation as a result of non-normality.

Appendix A3: Surface Current Nature

The purpose of this appendix section is to depict the nature of the induced surface current with respect to the design of mechanical stirring paddles. In this, the section supplies the following evidence:

1. It will depict the specific size of the cuts interacting with a larger wavelength plane wave more effectively than standard designs.
2. It will clearly illustrate the concept of increasing the current path length and increasing the resonant capability - both crucial to the overall design strategy.
3. It clearly shows the manner as to how broadband performance is provided - i.e. different cuts on the paddle surface interact with different sized plane waves to allow for a more efficient operation.
4. Proof is provided that show points (1), (2) and (3) are achieved considering two orthogonal polarisations.

Hence, evidence to further re-enforce why the design strategy of implementing cuts on the paddle surfaces works better at lower modal densities.

The induced surface current has been calculated from a plane wave excitation. The excitation has been configured in two orthogonal polarisations from a direction normal to the plate surface. It is accepted that in operation in the RC, this incoming direction will come from many different angles as the paddles rotate; however, the purpose here is just simply to illustrate the nature of the design strategy and provide further direct evidence to support the technique.

Please note that in order to keep this section concise, the maximum levels of induced current as a function of phase angle has been selected for each frequency, and the overall number of plots is restricted in scope.

Figs. A3.1 (a) - (d) depicts the induced surface current behaviour for the standard paddles and new designs at 115 MHz for vertical and horizontal polarisations respectively. The black lines illustrated on the figure serve to depict the current path length. The paddles have been modelled in full size - i.e. the exact sizes that exist in the real physical chamber.

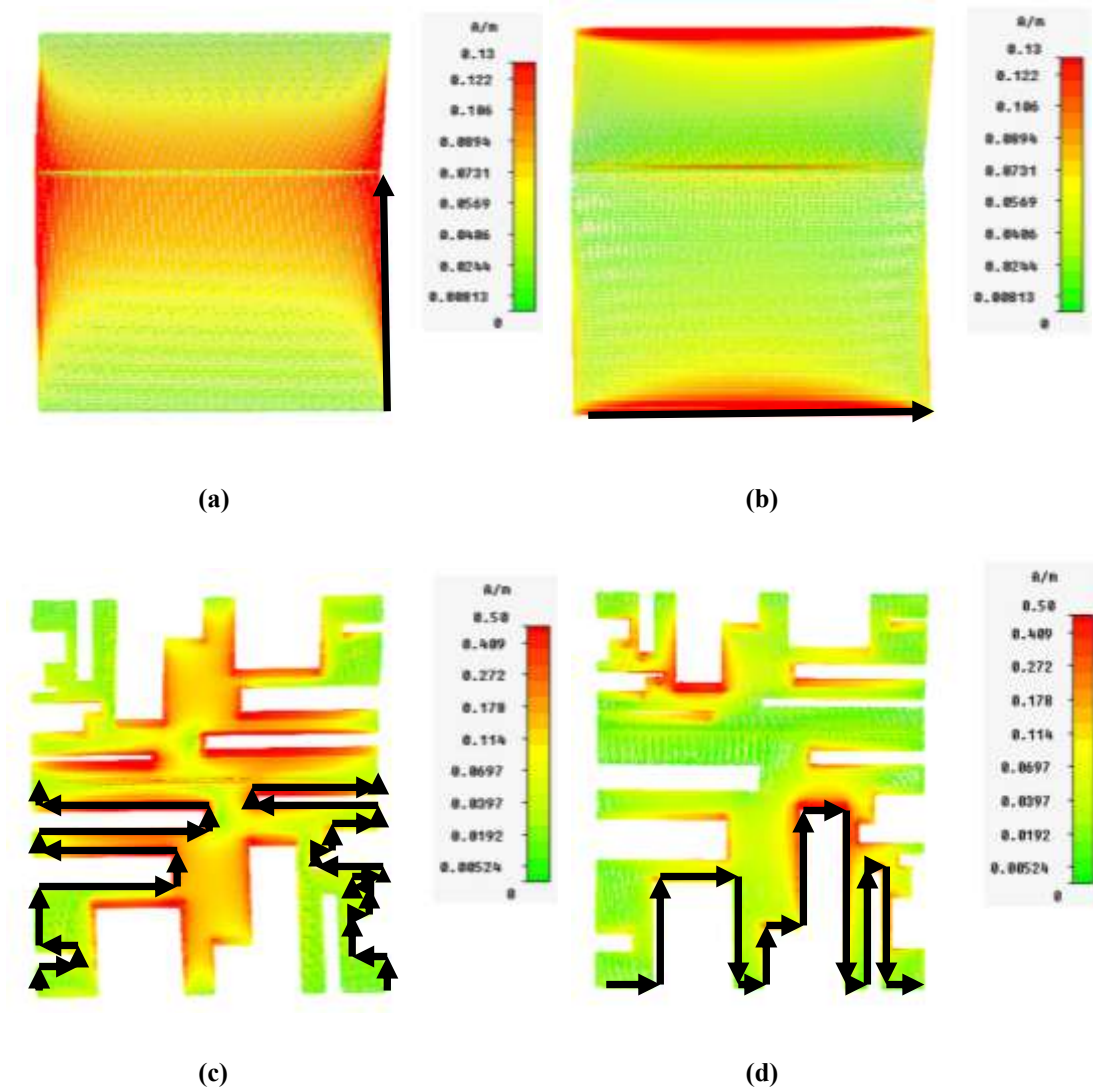


Fig. A3.1: Induced surface current at 115 MHz: (a) Standard paddle vertical polarisation, (b) standard paddle horizontal polarisation, (c) new paddle vertical polarisation and (d) new paddle horizontal polarisation

From Fig. A3.1 (a) - (d) it can be clearly seen how the cuts serve to increase the current path length. From the induced surface for the standard paddles it can be seen that at larger wavelengths, the bulk of the surface current is mainly concentrated around the outer edges of the paddles in both polarisations. This is because these lengths are the largest dimensions on the paddles and the surface current would appear to be seeking a dimension relative in size in order to interact with the paddles sufficiently.

With the new designs, the overall magnitude of the surface current was a lot higher than for the standard paddles - this is believed to be due to the fact that the new paddle approached a condition of resonance more so than the standard designs. Secondly, the surface current can

be seen to be concentrated around the longer length cuts - i.e. these are providing the interaction mechanism between the larger wavelength plane wave and the paddle, which given the overall dimensions of the cuts, would serve to improve the efficiency of the paddles in both polarisations as seen in Chapter 5.

The surface current distributions at 150 MHz can be viewed in Fig. A3.2 (a) to (d).

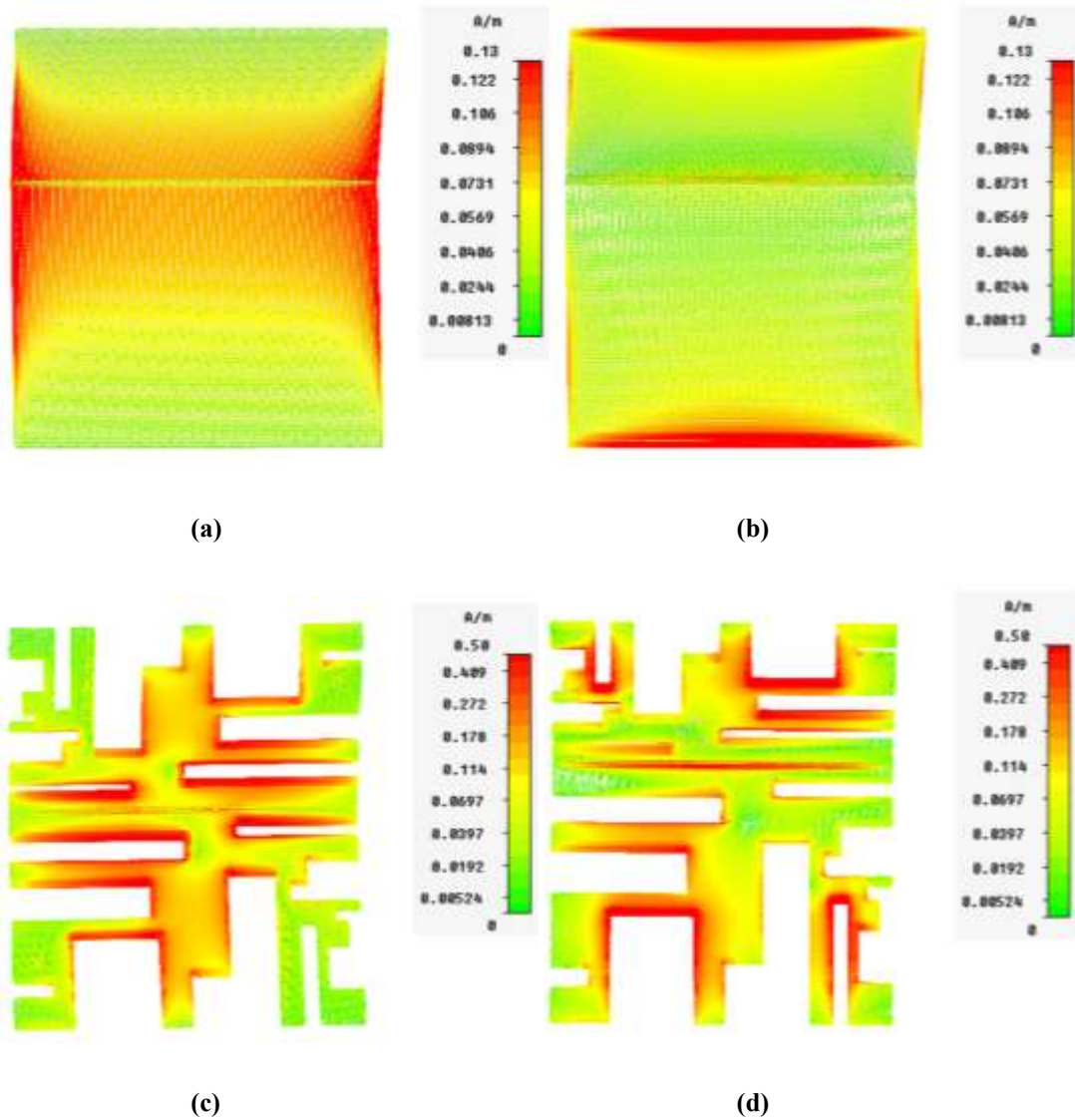


Fig. A3.2: Induced surface current at 150 MHz: (a) Standard paddle vertical polarisation, (b) standard paddle horizontal polarisation, (c) new paddle vertical polarisation and (d) new paddle horizontal polarisation

From Fig. A3.2, it can be seen that the current distribution for the standard paddles are largely the same; that is, minimal interaction is expected at 150 MHz similar to 115 MHz. However, when assessing the nature of the surface current for the new designs, in particular

for the horizontal polarisation, it is seen that the nature of this induced current is remarkably different. More areas on the paddle are seen to be in use; hence, the multiple cuts of different lengths are serving to provide a resonant capability such that the paddle can sufficiently interact with the plane wave at different wavelengths. This offers evidence in support of the theoretical design strategy from Chapter 5.

Fig. A3.3 (a) to (d) illustrates the induced current behaviour at 200 MHz.

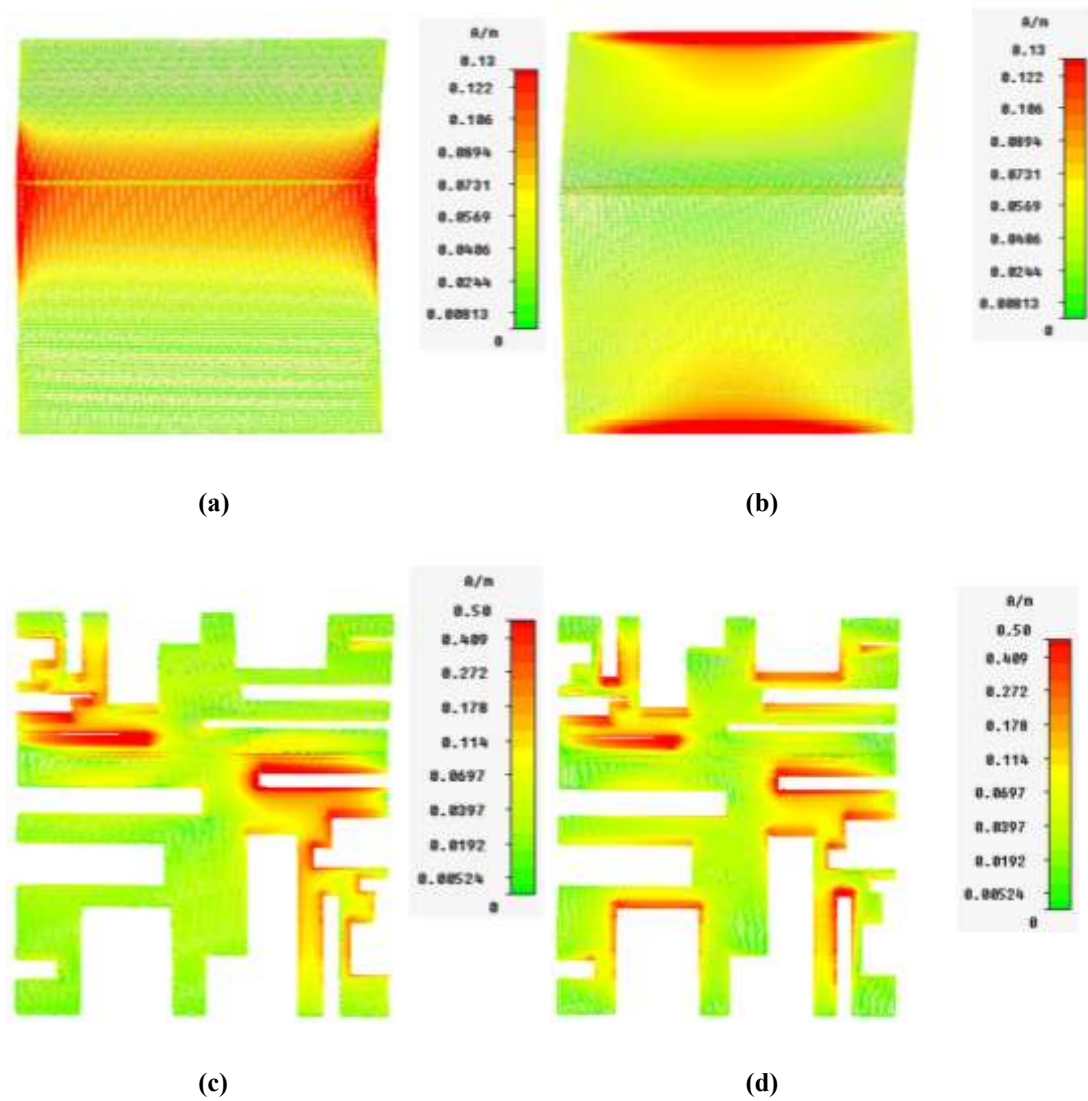


Fig. A3.3: Induced surface current at 200 MHz: (a) Standard paddle vertical polarisation, (b) standard paddle horizontal polarisation, (c) new paddle vertical polarisation and (d) new paddle horizontal polarisation

The surface current at 400 MHz is shown in Fig. A3.4.

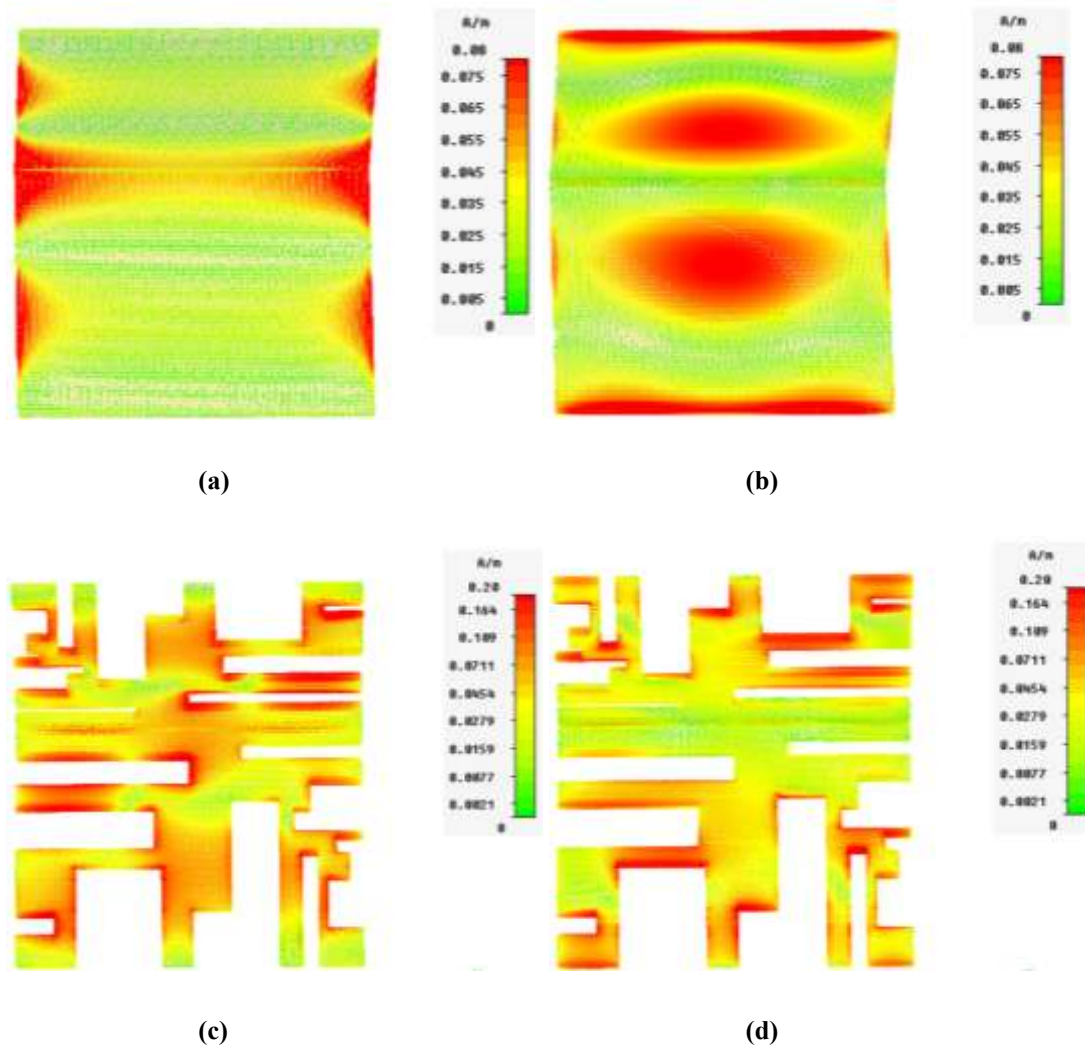


Fig. A3.4: Induced surface current at 400 MHz: (a) Standard paddle vertical polarisation, (b) standard paddle horizontal polarisation, (c) new paddle vertical polarisation and (d) new paddle horizontal polarisation

Appendix A4: BS EN 61000-4-21 Standard Deviation Results

As previously stated, this appendix section details the chamber performance advocated by the BS-EN 61000-4-21 standards. The results issued in this section are merely presented as an illustration for professionals who are familiar with EMC protocols and might not know how to infer / relate to the results presented in Chapter 5. No weight has been attached by this author to the following results with regards to proving the performance of the stirrer designs and no significance on the results is inferred whatsoever for the aforementioned reasons.

Figs. A4.1 and A4.2 detail the standard deviation for the three (separate) cartesian field components and the combined (total) electric field as a function of frequency respectively for the standard stirrer paddles (no cuts) in a unloaded chamber. In each figure, the acceptable limits for field uniformity decreed by the BS-EN 61000-4-21 standards are depicted as a solid green line. The BS EN 61000-4-21 acceptable limits are that the standard deviation should be within 4 dB below 100 MHz, 4 dB at 100 MHz decreasing linearly to 3 dB at 400 MHz, and within 3 dB above 400 MHz.

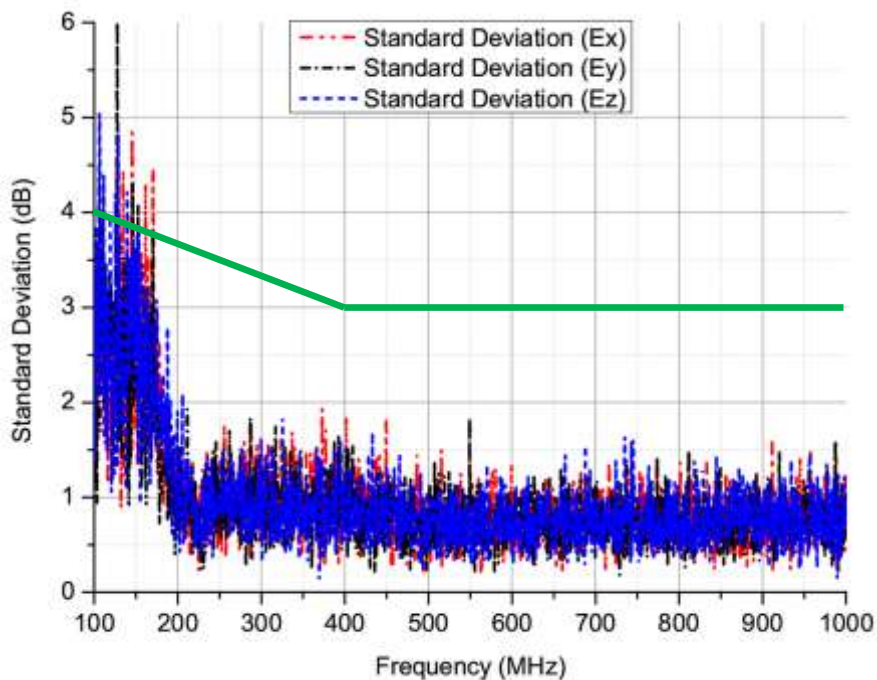


Fig. A4.1: Standard deviation (dB) for 3 cartesian field components from standard stirrer design in unloaded chamber

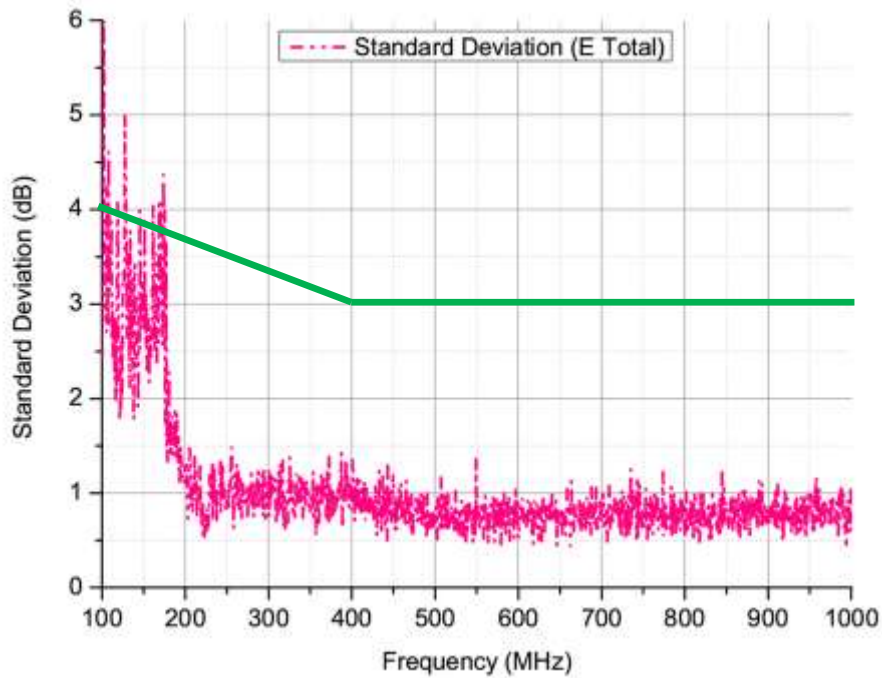


Fig. A4.2: Standard deviation (dB) for total electric field from standard stirrer design in unloaded chamber

From Figs. A4.1 and A4.2, acceptable uniformity is reached at a frequency of 177 MHz.

Moving on to assess the standard paddle design (no cuts) in the loaded chamber, Figs. A4.3 and A4.4 depict the standard deviation for the three (separate) cartesian field components and the combined electric field as a function of frequency respectively.

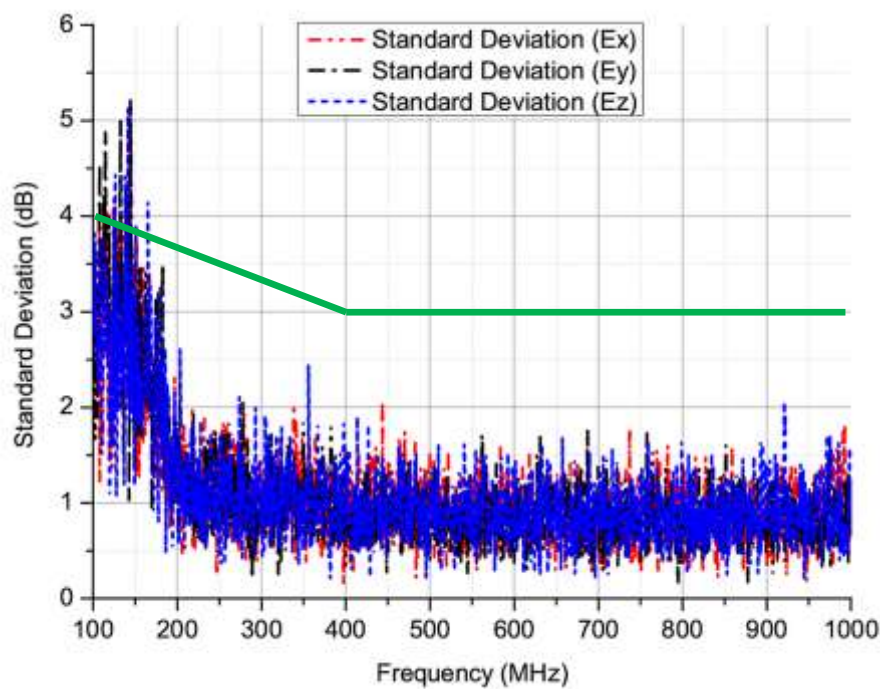


Fig. A4.3: Standard deviation (dB) for 3 cartesian field components from standard stirrer design in loaded chamber

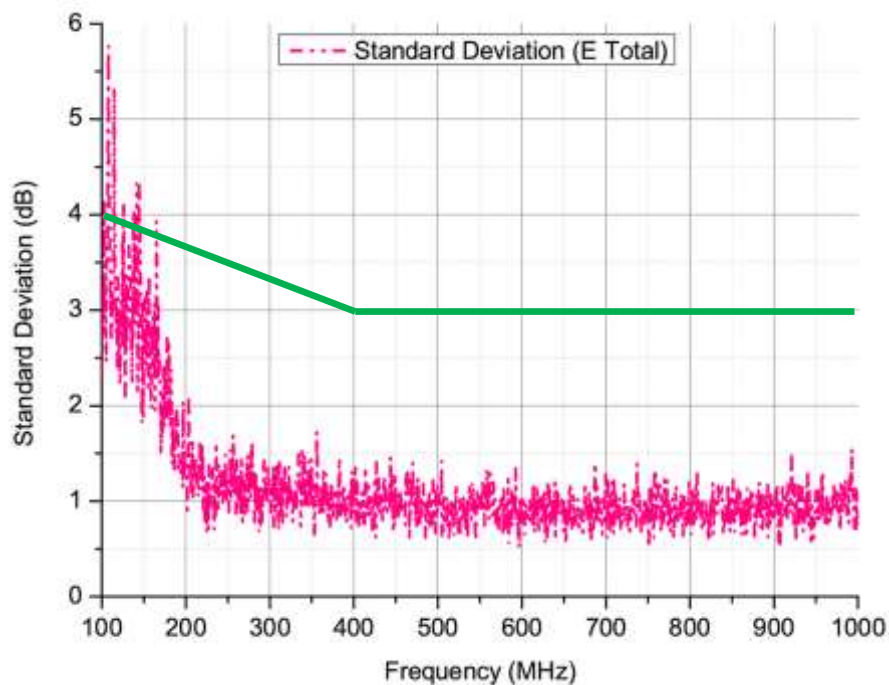


Fig. A4.4: Standard deviation (dB) for total electric field from standard stirrer design in loaded chamber

From Figs. A4.3 and A4.4, acceptable uniformity is reached at a frequency of 170 MHz.

Figs. A4.5 and A4.6 depict the standard deviation performance of the new designs in the unloaded chamber.

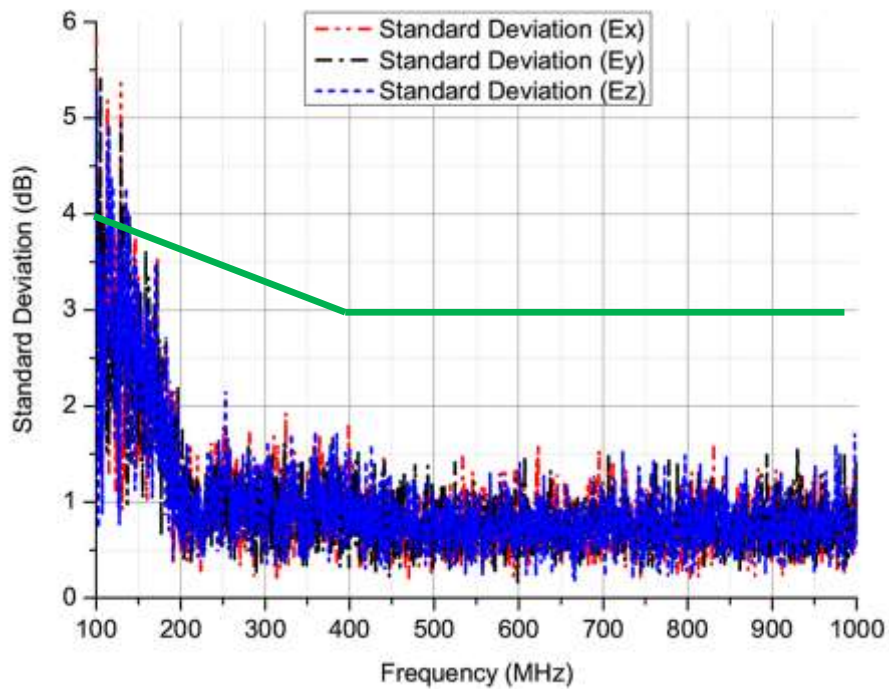


Fig. A4.5: Standard deviation (dB) for 3 cartesian field components from new stirrer design in unloaded chamber

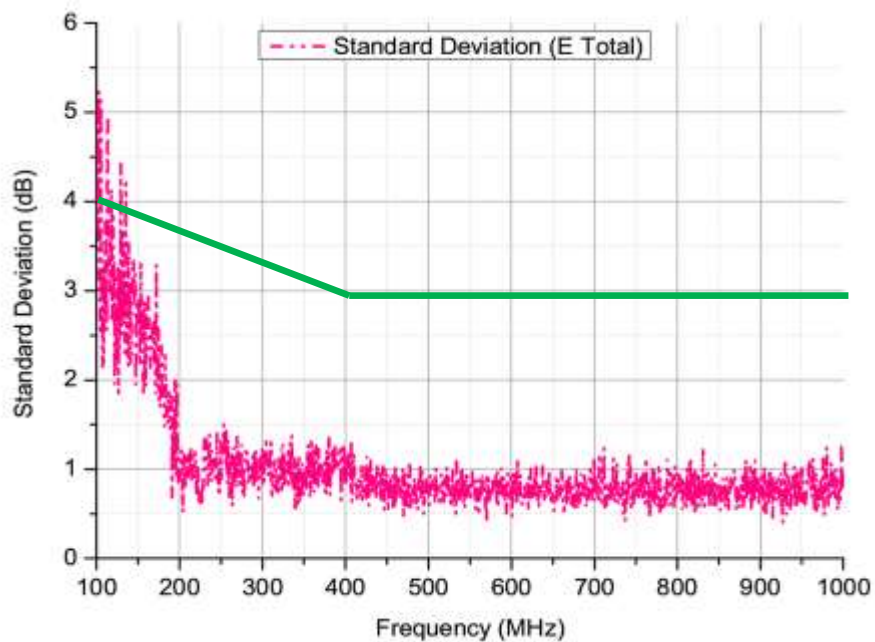


Fig. A4.6: Standard deviation (dB) for total electric field from new stirrer design in unloaded chamber

From Figs. A4.5 and A4.6, acceptable uniformity is reached at a frequency of 139 MHz. The performance of the new designs in the loaded chamber can be viewed in Figs. A4.7 and A4.8.

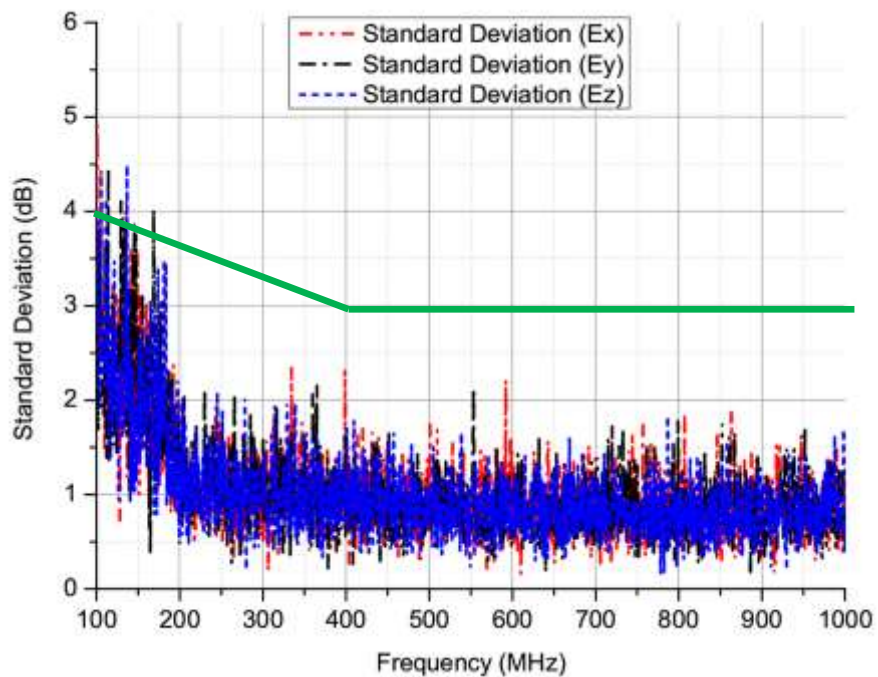


Fig. A4.7: Standard deviation (dB) for 3 cartesian field components from new stirrer design in loaded chamber

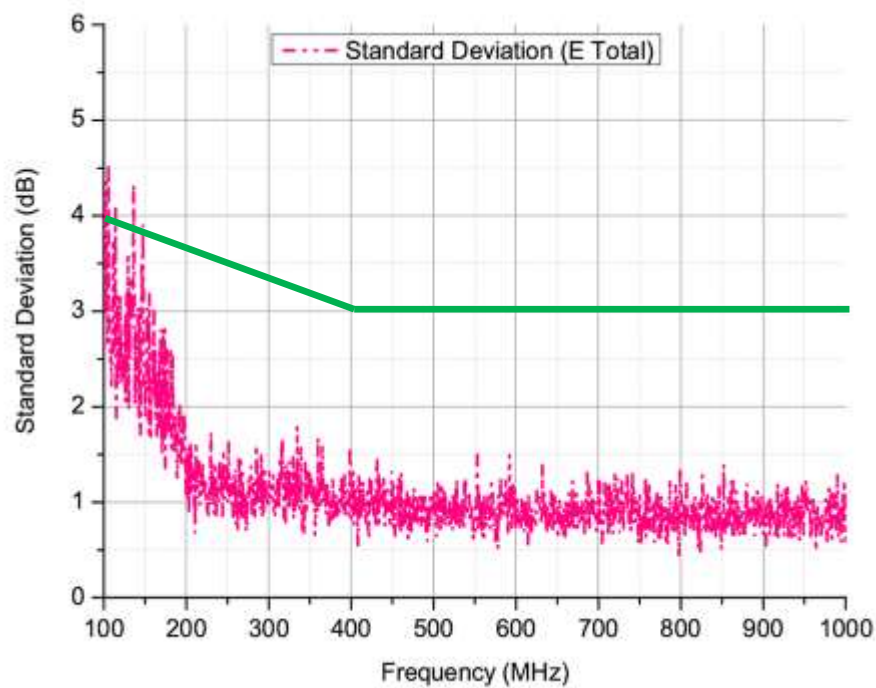


Fig. A4.8: Standard deviation (dB) for total electric field from new stirrer design in loaded chamber

From Figs. A4.7 and A4.8, acceptable uniformity is reached at a frequency of 136 MHz.